

OpenGeoSys
Developer-Benchmark-Book
OGS-DBB 5.04

KOLDITZ, Olaf^{1,3} & SHAO, Hua² (Eds)

Contributed by

BAUER, Sebastian⁶, BEYER, Christof⁶, BLÖCHER, Guido⁸,
BÖTTCHER, Norbert³, CACACE, Mauro⁸, CENTLER, Florian¹,
DELFS, Olaf-Jens¹, DE LUCIA, Marco⁸, DU, Yanliang⁴,
HESSER, Jürgen², GÖRKE, Uwe-Jens¹, KALBACHER Thomas¹,
KOSAKOWSKI, Georg⁷, KRUG, Stefanie², McDERMOTT, Chris⁵,
PARK, Chan-Hee¹, SHAO, Haibing^{1,3}, SINGH, Ashok¹,
SUN, Feng^{1,3}, SUN, Yuanyuan^{1,3}, TARON Joshua¹, THULLNER,
Martin¹,
WANG, Wenqing¹, WATANABE, Norihiro^{1,3}, WU, Yajie¹,
XU, Wenjie^{2,3}

¹Helmholtz Centre for Environmental Research (UFZ)

²Institute for Geosciences and Natural Resources (BGR)

³Technical University of Dresden (TUD)

⁴Center for Applied Geosciences, University of Tübingen (ZAG)

⁵University of Edinburgh (UE), UK

⁶University of Kiel (CAU)

⁷Paul-Scherrer-Institute (PSI), Switzerland

⁸Helmholtz Centre Potsdam (GFZ) German Research Centre for Geosciences

Contents

1	Introduction	12
2	Heat Transport – T-Process	15
2.1	Theory	15
2.2	Linear heat diffusion	16
2.2.1	Problem definition	16
2.2.2	Analytical solution	16
2.2.3	Numerical solution	16
	Model setup	16
	Parameters	17
	Temporal discretisation	17
2.2.4	Results	17
2.3	Linear heat diffusion in a wall	19
2.3.1	Problem definition	19
2.3.2	Analytical solution	19
2.3.3	Numerical solution	19
	Model setup	19
	Parameters	20
2.3.4	Results	20
2.4	Radial heat diffusion	21
2.4.1	Problem definition	21
2.4.2	Model set-up of the 1D numerical model	22
2.4.3	Evaluation method	22
2.4.4	Results	23

2.5	Temperature-dependent thermal properties	23
2.6	Heat transport in a fracture	24
2.6.1	Problem definition	24
2.6.2	Parameters	24
2.6.3	Analytical solution	24
2.6.4	Numerical solution	25
2.6.5	Results	25
2.7	Heat transport in fracture-matrix systems	27
2.7.1	Problem definition	27
2.7.2	Analytical solution	27
2.7.3	Model setup	27
2.7.4	Parameters	28
2.7.5	Results	29
2.8	Heat transport in fracture-matrix systems: 3D case study	31
2.8.1	Problem Definition	31
2.8.2	Initial and boundary conditions	32
2.8.3	Parameters	33
2.8.4	Results	34
2.9	Heat transport with temperature dependent fluid properties	37
2.9.1	Problem definition	37
2.9.2	Model set-up of the 1 D numerical model	37
2.9.3	Validation method	39
2.9.4	Results	39
3	Groundwater flow – H-Proceses	41
3.1	Theory	41
3.2	Linear groundwater flow	42
3.2.1	Flow in an isotropic medium	43
3.2.2	Flow in an anisotropic medium	45
3.2.3	Flow in an isotropic and heterogeneous medium	47
3.3	Confined aquifer	49
3.3.1	Constant source term	49
3.3.2	Channel source term	50

3.3.3	Channel sink term	52
3.3.4	Theis' Problem	54
3.4	Time variant flow	57
3.5	Unconfined aquifer	60
3.5.1	Steady state case	60
4	Fluid property functions	62
4.1	Theory of thermodynamic and transport properties	62
4.1.1	Density	62
4.1.2	Enthalpy	66
4.1.3	Entropy	67
4.1.4	Heat capacity	67
4.1.5	Viscosity	69
4.1.6	Thermal conductivity	70
4.2	Keywords	71
4.2.1	Fluid specification	71
4.2.2	Density model specification	72
4.2.3	Viscosity model specification	73
4.2.4	Thermal conductivity model specification	73
4.2.5	Compressibility model specification	74
4.2.6	Example file	75
4.2.7	Fluid property output	76
4.3	Benchmarks	77
4.3.1	CO ₂ flow with pressure dependent density and viscosity .	77
4.3.2	Non-isothermal single-phase flow	79
4.3.3	Non-isothermal two-phase flow	82
5	Richards flow – H-Proceses	87
5.1	Theory	87
5.1.1	Single continuum	87
5.1.2	Dual continua	88
	Numerical methods	89
5.2	Single Continuum	89

5.2.1	Infiltration in homogenous soil	89
5.2.2	Infiltration in homogenous soil (ST/BC)	91
5.2.3	Infiltration in homogenous soil (BC/BC)	93
5.2.4	Transient infiltration in homogenous soil	95
5.2.5	Nouniform IC of heterogenous soil column (-/BC)	97
5.3	Dual continua	99
5.3.1	Comparison with S1D	99
5.3.2	Classic case: Gerke, etc	101
5.3.3	Discussion	104
5.4	Regional soil model	104
6	Surface Flow – H-Processes	107
6.1	Theory	107
6.2	Benchmarking examples	109
6.2.1	One-dimensional precipitation runoff	109
6.2.2	Two-dimensional precipitation runoff	111
6.2.3	Infiltration excess (Horton) overland flow	112
7	Gas flow	114
7.1	Isothermal compressible flow - H process	114
7.1.1	Theory	114
7.1.2	Examples	115
Compressible flow test	115	
Element test	116	
7.2	Non-isothermal compressible flow - HT process	118
7.2.1	Theory	118
7.2.2	Material functions	119
Air viscosity	120	
Thermal properties	121	
7.2.3	Examples	124
Air flow	124	
7.3	Joule-Thomson process in permeable media - HT process	127

8 Fluid Momentum – H-Process dependent	130
8.1 Theory	130
8.1.1 Velocity Estimation	130
8.1.2 Formulation of Galerkin method to obtain velocity	131
8.2 Test problems for various elements	133
9 Deformation – M-Processes	135
9.1 Theory	135
9.2 Isotropic elasticity	136
9.2.1 Plane strain with uniform loading (2D)	136
9.2.2 Excavation in homogeneous media (2D)	140
9.2.3 Excavation in heterogeneous media (2D)	142
9.2.4 Elastic cube (3D)	145
9.2.5 Given deformation at the top (3D)	147
9.2.6 Given stress at the top (3D)	150
9.2.7 Lubby1: Nonlinear model	152
9.3 Transverse isotropic elasticity	156
9.3.1 Tensile test (2D)	158
9.3.2 Tensile test (3D)	160
9.4 Excavation in homogeneous media (3D)	162
9.5 Elasto-plasticity	165
9.5.1 Plastic plate - von Mises plasticity (2D)	168
9.5.2 Plastic plate - Drucker-Prager plasticity (2D)	171
9.5.3 Plastic plate - Cam-Clay plasticity (2D)	174
9.5.4 Plastic plate - Rotational hardening plasticity (2D)	175
9.6 Creep	178
9.6.1 Creep of a cylindrical sample	178
9.6.2 Creep in salt rock	181
9.6.3 Lubby2: Transient and stationary creep model	187

10 Mass Transport – C-Proceses	191
10.1 Theory	191
10.2 Solute transport with decay	192
10.3 Solute transport with sorption	195
10.3.1 Sorption with linear isotherm (Henry isotherm)	196
10.3.2 Non-linear sorption with Freundlich isotherm	197
10.3.3 Non linear sorption with Langmuir isotherm	200
10.3.4 Solute transport with sorption and decay	202
10.4 Solute transport by diffusion	203
10.4.1 Diffusion: axisymmetric model	204
10.4.2 Diffusion in an anisotropic medium (2 D simulation) . . .	206
10.4.3 Solute transport with matrix diffusion	208
10.4.4 Solute transport with cation exchange	210
10.4.5 1-D Multi-component transport with dissolution and precipitation	214
10.5 1D and 2D conservative transport	215
10.5.1 1D reactive transport	215
10.5.2 2D conservative transport	218
10.5.3 2D conservative transport in heterogeneous media	219
10.6 Radial flow and conservative transport	221
10.6.1 Radial flow - Theiss problem	221
10.6.2 Conservative Transport in radial flow	223
10.7 Reactive Transport	225
10.7.1 Xylene degradation (1D)	225
10.7.2 Competition of TCE- and cis-DCE-degradation for zero valent iron surface (1D)	227
10.7.3 Sequential CHC degradation with isotope fractionation (1D)	231
10.7.4 Degradation network (1D)	235
10.7.5 Mixing Controlled Bioreactive Transport (2D)	242
10.8 Conservative mass transport in unsaturated media	246
11 Random Walk Particle Tracking	248
11.1 Theory	248
11.1.1 Governing Equation	248
11.2 Transport: Advection and Dispersion	251
11.3 Transport: Sorption-desorption and Filtration	252

12 Anisotropy – H or C or HC	258
12.1 Theory	258
12.2 Anisotropic permeability for pressure or hydraulic head	260
12.3 Anisotropic tortuosity for molecular diffusion coefficients	262
12.4 Converting an angle of orientation to tensor	265
13 Surface/Subsurface flow coupling – H-Processes	269
13.1 Theory	269
13.2 Benchmarks examples	270
13.2.1 Horton flow	270
13.2.2 Dunne flow	273
13.2.3 Aquifer recharge from channel	274
13.2.4 Flood at channel junction	277
14 Consolidation – HⁿM-Processes	282
14.1 Theory	282
14.2 Saturated consolidation	283
14.2.1 Poro-elastic column (1D)	283
14.2.2 Poro-elastic cube (3D)	286
14.2.3 Plastic consolidation	289
14.2.4 Dynamic consolidation	290
14.3 Unsaturated consolidation	293
14.3.1 Theory	293
Fluid mass balance	293
Momentum balance	293
Numerical scheme	294
14.3.2 Liakopoulos Experiment	295
14.3.3 DECOVALEX HM test case	300
14.4 Two-phase flow consolidation - H ² M Process	305
14.4.1 Theory	305
Balance equations	305
Swelling models	305
14.4.2 TEP test case	305

Definition	305
Results	307
Benchmark deposit	308
15 Thermo-Mechanics – TM-Processes	309
15.1 Theory	309
15.2 Thermo-Elasticity	311
15.2.1 Thermo-elastic plate (2D)	311
15.2.2 Thermo-elastic cube (3D)	312
15.2.3 Homogeneous material (3 D)	315
Problem definition	315
Model set-up of the 3 D numerical model	315
Evaluation method	316
Results	316
15.2.4 Composite materials (3 D)	317
Problem definition	317
Model set-up of the 3 D numerical model	317
Evaluation method	318
Results	319
15.2.5 Temperature increase in a hollow cylinder	321
Problem definition	321
Model set-up of the 2 D numerical model	322
Evaluation method	322
Results	324
16 Thermo-mechanical consolidation – THM-Processes	326
16.1 Theory	326
16.1.1 Non isothermal flow in porous media	326
16.1.2 Deformation	327
16.1.3 Heat transport	328
16.1.4 Repository in crystalline rock with unsat. bentonite buffer	329

17 Non-isothermal two-phase flow consolidation	335
17.1 Balance equations	335
17.1.1 Non-isothermal two-phase flow	336
17.1.2 Deformation	336
17.1.3 Heat transport	337
17.2 Constitutive equations	337
17.2.1 Density	337
17.2.2 Flux of gaseous mixture	338
17.2.3 Latent heat effects	338
17.3 Test example	338
18 THC-Process	342
18.1 Theory	342
18.2 Repository in crystalline rock with unsat.bentonite buffer	342
Problem definition	342
Model set-up of the 2 D numerical model	343
Evaluation method	344
Results	344
19 Density-dependent Flow – HC or THC	346
19.1 Theory	346
19.1.1 Governing Equation	346
Equation of the Bulk Fluid Density	346
Continuity Equation of Flow	347
Momentum Equation of Flow and Dispersive Flux	347
Contaminant Transport Equation	348
19.2 The Elder Problem	348
20 Isothermal two-phase flow – HH-Process	351
20.1 Isothermal two-phase flow	351
20.1.1 Mass balance equation	351
20.1.2 Pressure-pressure (pp) scheme	353
20.1.3 Pressure-saturation (pS) scheme	354
20.1.4 Liakopoulos experiment	354

20.1.5 Buckley-Leverett problem	358
20.1.6 McWhorter problem	364
20.1.7 Kueper problem	368
A Fluid property equations	372
A.1 Viscosity	372
A.1.1 Carbon dioxide [1]	372
A.1.2 Nitrogen [2]	373
A.1.3 Methane [3] and Ethane [4]	374
A.1.4 Water[5]	376
A.1.5 Propane	378
A.2 Thermal conductivity	380
A.2.1 Carbon Dioxide [6]	380
A.2.2 Nitrogen [2]	381
A.2.3 Methane [7]	382
A.2.4 Ethane [4]	384
A.2.5 Propane [?]	386
A.2.6 Water[8]	387
A.3 Free Helmholtz Energy	389
A.3.1 Theory[9]	389
A.3.2 Water	390
A.3.3 Carbon Dioxide	393
A.3.4 Methane	395
A.3.5 Nitrogen	397
A Density of carbon dioxide	399
A List containing all benchmarks	402

Chapter 1

Introduction

Scopus

The intention of the Developer Benchmark Book (DBB) is twofold:

- DDB provides a collection of test cases which are used for benchmarking the GeoSys code development.
- We recommend the benchmark collection for users as a starting point for their own GeoSys applications.

RockFlow, GeoSys, OpenTHMC, a historical note ...

Looking back to a more than 20 years lasting scientific project as "RockFlow" is amazing ... and at the same time completely impossible to be comprehensive and to be fair ...

RockFlow-1

Somewhen in the mid eighties Dr. Liedtke with the Federal Institute of Geosciences (BGR) was asking Prof. Zielke (Institute of Hydromechanics, University of Hannover) whether the development of a simulation programm for fractured rock is possible. (Never ask a scientist about impossible things). The idea was born (including some funding from the BGR): the development of a computer code based on multi-dimensional FEM. The first name was DURST, which for Germans is not really a good choice (because it means "thirsty"). Later it was renamed into Rockflow: Flow and associated processes in rock. The pioneering work of RockFlow-1 was done in the following four doctoral dissertations [10], [11], [12], [13].

RockFlow-2

The next stages in the early nineties was related to couple the individual RF-1 modules and improve the computational efficiency, e.g. by introducing iterative equation solver. RockFlow-2 was now used in several application projects as waste deposition and geothermal energy ([14],[15]). A "market" for RockFlow in Applied Geoscience was open. From this time the most cited RockFlow paper so far [16] originated (more than 70 times, which is not so bad for a modeling paper).

RockFlow-3

It turned out that the coupling of the different RF modules needed a new code structure. Moreover for the use of grid-adaptive methods dynamic data structures have been necessary. Consequently, in the late nineties a complete re-organization of RF was started. C experience began ... [17], [18]. Major research topics of the RF group had been multi-phase flow [19], grid adaptation [20], reactive transport [21], and deformation processes [22]. Beside the numerical parts geometric modeling and meshing methods became more and more important [23], [24].

GeoSys/RockFlow-4

Tuebingen: Due to the increasing functionality, the RF code became more and more sophisticated and difficult to handle. Consequently, the introduction of object-oriented methods was necessary. RF-4 or now GeoSys was (again) completely re-designed and rewritten in C++ [25], [26]. Several doctoral theses have been prepared in the fields of geotechnical simulation (DECOPALEX project, [27], [28], [29]), contaminant hydrology (Virtual Aquifer project, [30], [31], [32]), geothermal reservoir modeling (Urach Spa project, [33]). Aside computational mechanics progress had been made as well in the pre-processing for numerical analysis [34], [35], [36]. First GeoSys/RockFlow habilitations appeared [37], [38], [39]. As mentioned in the beginning it is impossible to cite everything, other important works in the Tuebingen era are [40], [41], [42].

GeoSys/OpenTHMC

Leipzig: The new challenge for GeoSys is to continue the development as a distributed open-source project, i.e. sharing and widening the knowledge, as people from the GeoSys group got interesting offers. The number of GeoSys-project partners is already quite large (see cover page). At the Helmholtz Center for Environmental Research a new research platform TESSIN is available, which combines high-performance-computing (HPC) and visualization facilities. Post-processing becomes more and more important as more and more information

becomes available, due to high-resolution measurement techniques and HPC itself [43].

Next ...

Benchmarks coming soon ...

- Matrix diffusion (CMCD, GK)
- Thermal signatures in soils and sediments (JOD)
- Gas flow (OK)
- Heat transport in gas flows (OK)
- Two-phase flow and CO₂ stuff (PCH)
- Biodegradation et al (Kiel: CB, SB)
- More overland flow (EK, SF)
- ...

Chapter 2

Heat Transport – T-Process

2.1 Theory

Heat transfer is the passage of thermal energy from a hot to a cold body. Transfer of thermal energy occurs, when a body and its surroundings have not reached thermal equilibrium yet. Heat transfer can occur in three different ways:

- Conduction,
- Advection and
- Radiation.

Conduction takes place when a temperature gradient in a solid or a stationary fluid medium occurs. It runs into the direction of decreasing temperature. The thermal conductivity is defined in order to quantify the ease with which a particular medium conducts. Against it, convection is caused by moving fluids of different temperatures, but in the following only conductive heat flow is considered.

Temperature changes cause a change of fluid density and viscosity which influences again the behaviour of the fluid while flowing through a porous medium and therefore the velocity of heat transport by groundwater flow. The dependence of density on temperature changes is regarded by using the relation given in (2.1.1)

$$\rho(T) = \rho_0 \cdot (1 + \beta_T (T - T_0)). \quad (2.1.1)$$

Here ρ_0 represents the initial density, T the temperature, T_0 the initial temperature and β_T is a constant. The equation for the heat conduction is

$$\frac{\partial T}{\partial t} = \nabla \cdot (\alpha \nabla T), \quad (2.1.2)$$

where T is the temperature and $\alpha = \lambda/c\rho$ is the heat diffusivity constant. For the heat transport the following equation is given:

$$c\rho \frac{\partial T}{\partial t} + c\rho \mathbf{v} \cdot \nabla T - \nabla \cdot (\lambda \nabla T) = Q_T, \quad (2.1.3)$$

where c is the specific heat capacity, ρ is the density, \mathbf{v} is the advection velocity and λ is the thermal conductivity.

2.2 Linear heat diffusion

2.2.1 Problem definition

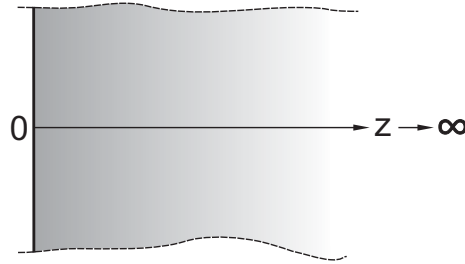


Figure 2.2.1: One side limited domain in cartesian coordinates.

2.2.2 Analytical solution

The one dimensional heat transport in a domain limited just by one side can be derived by (2.2.1)

$$T(x, t) = T_0 \operatorname{erfc} \left(\frac{x}{\sqrt{4\alpha t}} \right), \quad (2.2.1)$$

where T_0 is the initial temperature and $\alpha = \lambda/c\rho$ is the heat diffusivity coefficient of the used material.

2.2.3 Numerical solution

Model setup

The numerical model consists of 60 line elements connected by 61 nodes along the z-axis (figure 2.2.2). The distances of the nodes Δz is one meter. At $z = 0$ m there is a constant temperature boundary condition.

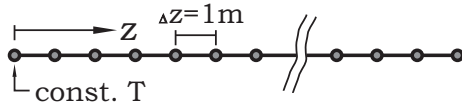


Figure 2.2.2: Spatial discretisation of the numerical model.

Table 2.2.1: Material properties.

parameter	value
density ρ of the solid	$2500 \text{ kg}\cdot\text{m}^{-3}$
heat capacity c	$1000 \text{ J}\cdot\text{kg}^{-1}\cdot\text{K}^{-1}$
thermal conductivity λ	$3.2 \text{ W}\cdot\text{m}^{-1}\cdot\text{K}^{-1}$

Parameters

The material properties for this model setup are given in Tab. 2.2.1. Using these values, the outcome for the heat diffusivity constant $\alpha = \lambda/c\rho$ in (2.1.2) is $\alpha = 1.28 \cdot 10^{-6} \text{ m}^2/\text{s}$.

Temporal discretisation

The *Neumann* stability criteria has to be restrained so that the temperature gradient can't be inverted by diffusive fluxes. Using (2.2.2) the best time step can be estimated by

$$\text{Ne} = \frac{\alpha \Delta t}{(\Delta z)^2} \leq \frac{1}{2}. \quad (2.2.2)$$

With $\Delta z = 1\text{m}$ and $\alpha = 1.28 \cdot 10^{-6} \text{ m}^2/\text{s}$ the outcome for the timestep is $\Delta t \leq 390.625\text{s}$ or 4.5 days respectively.

2.2.4 Results

The following figure (Fig. 2.2.3) show the comparison of the solution of (2.2.1) and the numerical simulation results. It is demonstrated the temperature distribution along the model domain after 2 months, 1 year, 2 years and 4 years.

Table 2.2.2: Benchmark deposit.

Deposit	Version	Date
T\TDiff\TDiff	4.7.03	Jun. 2008

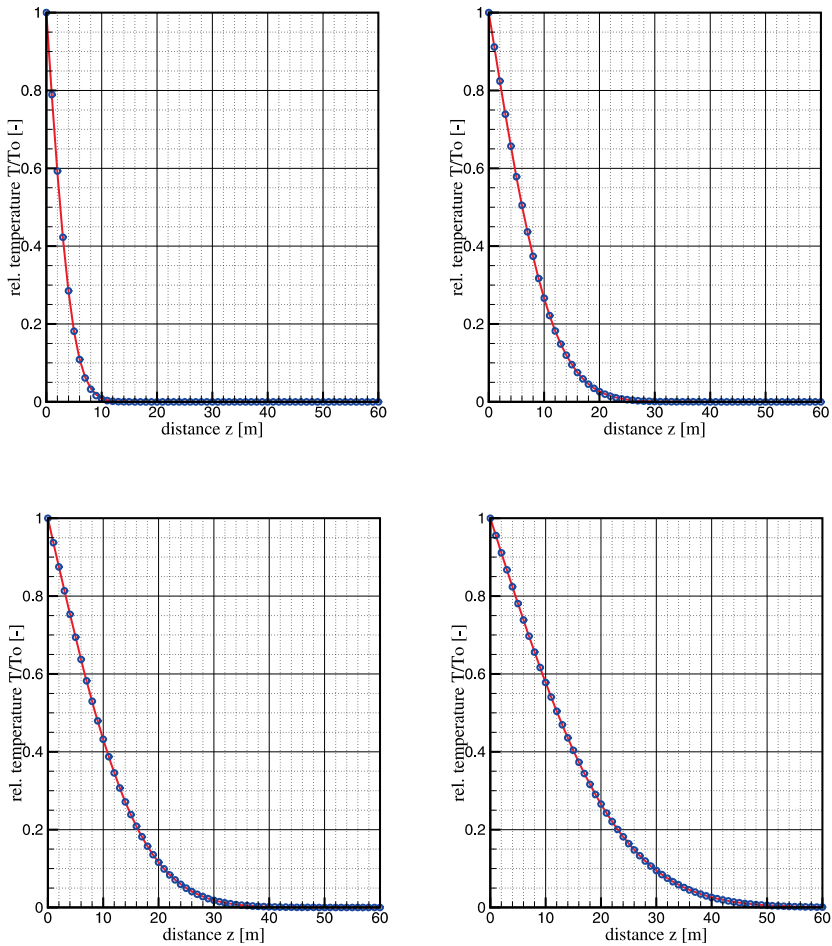


Figure 2.2.3: Temperature distribution along the z-axis after 2 months, 1 year, 2 years and 4 years (from top left to down right).

2.3 Linear heat diffusion in a wall

2.3.1 Problem definition

In the last example there was a domain limited only by one side with a constant temperature at the boundary. The following problem shows the profile of a homogeneous and isotropic wall with a constant heat flow Q_A on the left and a constant temperature T_L on the right boundary (Fig. 2.3.1). This example consists also just of diffusive heat transport.

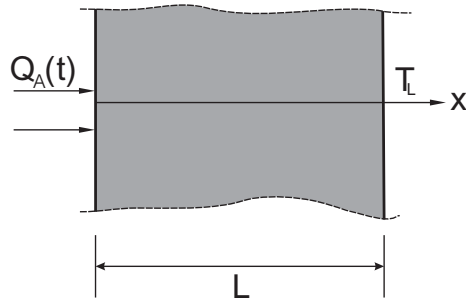


Figure 2.3.1: Heat conduction through a wall.

2.3.2 Analytical solution

A solution for this problem can be found by solving the heat conduction equation (2.1.2) using *Fourier's* method (see [44]). It can be shown:

$$T(x, t) = T_L + \frac{Q_A}{\lambda} (L - x) + \sum_{n=1}^{\infty} \left[-\frac{8L}{(2n-1)^2 \pi^2} \frac{Q_A}{\lambda} \cos \frac{(2n-1)\pi x}{2L} e^{-\frac{(2n-1)^2 \pi^2}{4L^2} \alpha t} \right] \quad (2.3.1)$$

with T_L is the initial temperature, Q_A is the constant heat source, λ is the thermal conductivity and α is the heat diffusivity constant.

2.3.3 Numerical solution

Model setup

The numerical model consists of 40 line elements and 41 nodes along the x-axis (Fig. 2.3.2). The step size Δz is set to 0.1 m. On the left boundary a constant source term is set. The right side obtains a constant temperature.

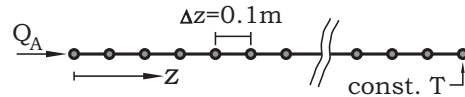


Figure 2.3.2: Boundary conditions and discretisation for the numerical model.

Parameters

Tab. 2.3.1 shows the values of the used material properties. The heat diffusivity constant α outcomes to $\alpha = 3.1 \cdot 10^{-6} \text{ m}^2/\text{s}$.

Table 2.3.1: Material properties.

parameter	value
heat source Q_A	$30 \text{ W} \cdot \text{m}^{-2}$
initial temperatur T_L	$25 \text{ }^\circ\text{C}$
wall thickness L	4 m
density of the solid ρ	$2000 \text{ kg} \cdot \text{m}^{-3}$
thermal capacity c	$900 \text{ J} \cdot \text{kg}^{-1} \cdot \text{K}^{-1}$
thermal conductivity λ	$5.5 \text{ W} \cdot \text{m}^{-1} \cdot \text{K}^{-1}$

2.3.4 Results

The comparison of analytical and numerical solution is presented in Fig. 2.3.3. The figure shows the distribution of the temperatue along the profile of the wall. Due to the thickness of the wall, the heat transport takes very long, after 5.000.000 seconds (≈ 58 days) the temperature distribution becomes staedy-state.

Table 2.3.2: Benchmark deposit.

Deposit	Version	Date
T\TDiff-wall\TDiff-wall	4.7.03	Jun. 2008

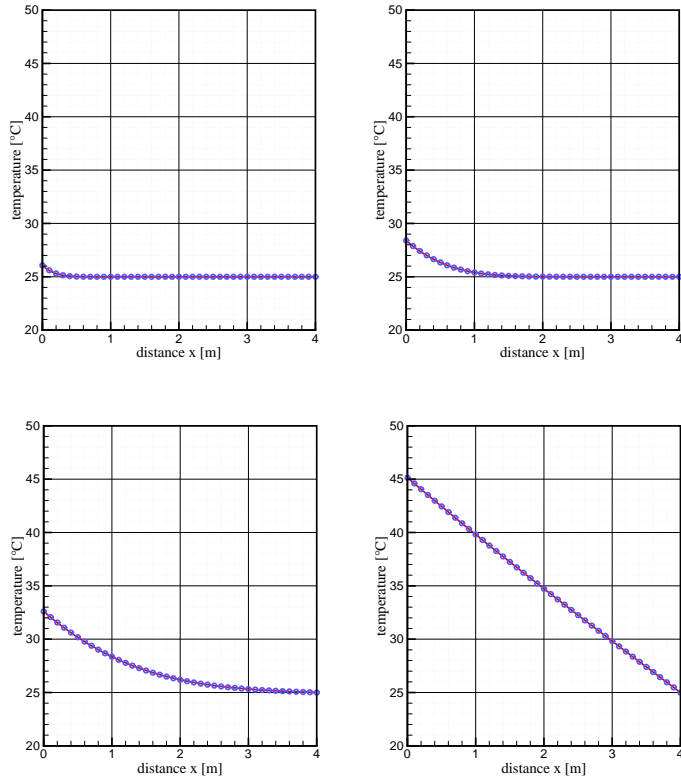


Figure 2.3.3: Temperature distribution along the wall profile after 10.000, 100.000, 500.000 and 5.000.000 seconds (from top left to down right).

2.4 Radial heat diffusion

2.4.1 Problem definition

A slice with a hole in its centre, that means a 2D annulus, which consists of a solid of a constant temperature is exposed to a higher temperature at the surface of its hole. The aim of this calculation is to simulate the heat transfer through this homogeneous solid by the use of an axisymmetric model. Fig. 2.4.1 shows a sketch of the calculation area assuming a homogeneous solid, a constant temperature in the whole body at the beginning and a heating of the slice at the inner surface of the hole .

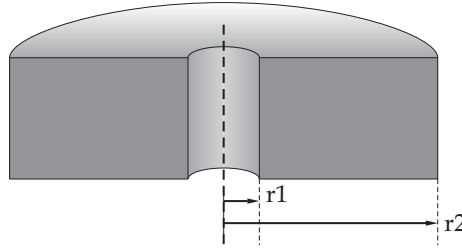


Figure 2.4.1: Calculation area.

2.4.2 Model set-up of the 1D numerical model

The inner radius R_1 of the axisymmetric model is 1 m and the outer radius R_2 is 5 m. The numerical model consists of 40 elements and 41 nodes. The initial temperature in the whole area is 25 °C. At the right boundary of the numerical model a thermal boundary condition is set with a constant value of 25 °C. At the left boundary a source term for heat flux of $q = 30 \text{ W/m}^2$ is defined. Thereby the continuous heating of the solid is simulated. The used parameters of the solid are listed in Tab. 2.4.1. The simulation of 5000 time steps with a constant time step length of 1000 s is done.

Table 2.4.1: Material properties.

parameter	value
density of the solid ρ	$2.0 \text{ t} \cdot \text{m}^{-3}$
thermal capacity c	$900 \text{ J} \cdot \text{kg}^{-1} \cdot \text{K}^{-1}$
thermal conductivity λ	$5.5 \text{ W} \cdot \text{m}^{-1} \cdot \text{K}^{-1}$

2.4.3 Evaluation method

For the heating of the annulus with the inner radius R_1 and the outer radius R_2 the following analytical solution for temperature in dependency on the radius r was used

$$T(r) = \frac{R_1 q}{\kappa} \ln \left(\frac{R_2}{r} \right) + T_0. \quad (2.4.1)$$

Here q represents the heat source, λ the thermal conductivity and T_0 the initial temperature.

2.4.4 Results

The results of the analytical equation for the temperature distribution over the model length are compared to those of the numerical simulation by GeoSys/RockFlow. Fig. 2.4.2 shows the temperature distribution over the radius of the annulus. Obviously, with the axisymmetric model a GeoSys/RockFlow simulation generates comprehensible results that agree well with the analytic solution.

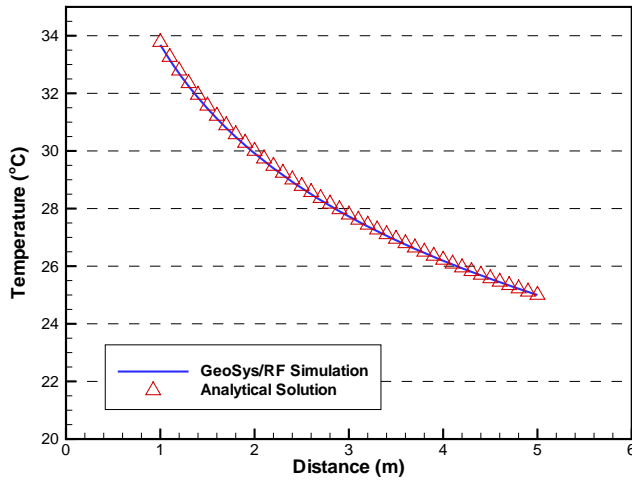


Figure 2.4.2: Temperature distribution over the radius

Table 2.4.2: Benchmark deposit

Deposit	Version	Date
T\heat1d\T_1D_axi	4.7.02	Mar. 2008

2.5 Temperature-dependent thermal properties

For temperature and pressure depending thermal properties see chapter 4 "Fluid property functions".

2.6 Heat transport in a fracture

2.6.1 Problem definition

This problem shows 1D heat transport by advection and diffusion in a 100 m long fracture. The fracture is fully saturated with groundwater, flowing with constant velocity. There is no rock matrix around the fracture which could store heat. Fig. 2.6.1 give a view about the situation.

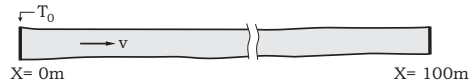


Figure 2.6.1: A fully saturated fracture with flowing groundwater and a constant temperature at the left border.

2.6.2 Parameters

The fracture is described as a porous medium with 100 % porosity, so that no solid material influences the heat transport process. The properties of the fluid are in Tab. 2.6.1. These values cause a diffusivity constant for water of $\alpha =$

Table 2.6.1: Material properties.

parameter	value
density ρ	$1000 \text{ kg} \cdot \text{m}^{-3}$
thermal capacity c	$4000 \text{ J} \cdot \text{kg}^{-1} \cdot \text{K}^{-1}$
thermal conductivity λ	$0.6 \text{ W} \cdot \text{m}^{-1} \cdot \text{K}^{-1}$

$1.5 \cdot 10^{-7} \text{ m}^2/\text{s}$. The groundwater velocity in the fracture is $v = 3.0 \cdot 10^{-7} \text{ m}^2/\text{s}$.

2.6.3 Analytical solution

For 1D-advection/diffusive transport, an analytical solution is given by OGATA & BANKS as

$$T(x, t) = \frac{T_0}{2} \left(\operatorname{erfc} \frac{x - v_x \cdot t}{\sqrt{4\alpha t}} + e^{\frac{v_x \cdot x}{\alpha}} \operatorname{erfc} \frac{x + v_x \cdot t}{\sqrt{4\alpha t}} \right), \quad (2.6.1)$$

where T_0 is the constant temperature at $x = 0$, v is the groundwater velocity and α is the heat diffusivity coefficient of water (see [44],[45]).

2.6.4 Numerical solution

The mesh for the numerical model consists of 501 nodes combining 500 line elements. The distance between the nodes is $\Delta x = 0.2\text{ m}$.

Boundary conditions

- Left border:
 - constant source term (liquid flow) with $Q = 3.0 \cdot 10^{-7}\text{ m}^3/\text{s}$
 - constant temperature with $T = 1^\circ\text{C}$
- Right border:
 - constant pressure with $P = 100,000\text{ kPa}$
- Initial conditions:
 - pressure with $P = 100,000.0\text{ kPa}$ for whole domain
 - temperature $T = 0^\circ\text{C}$ for whole domain
- Time step:
 - $\Delta t = 133,333.0\text{ s}$

With the given parameters, the NEUMANN criteria (2.2.2) results on $\text{Ne} = 0.5$ which guarantees the numerical stability of the diffusion part of the transport process. The *Courant* criteria, given by

$$C = \frac{v_x \cdot \Delta t}{\Delta x} \leq 1 \quad (2.6.2)$$

results to $C = 0.2$.

2.6.5 Results

In Fig. 2.6.2 the comparison of analytical and numerical solution is plotted. The figure shows the temperature breakthrough curve at the end of the fracture at $x = 100\text{ m}$. The numerical results show an acceptable agreement to the analytical solution. In a further step, the diffusion part of the heat transport process was avoided by minimizing the thermal conductivity of the fluid. Fig. 2.6.3 shows the breakthrough curve for only advective heat transport.

Table 2.6.2: Benchmark deposit

Deposit	Version	Date
T\Ogata-Banks\Ogata-Banks	4.7.03	Jul. 2008

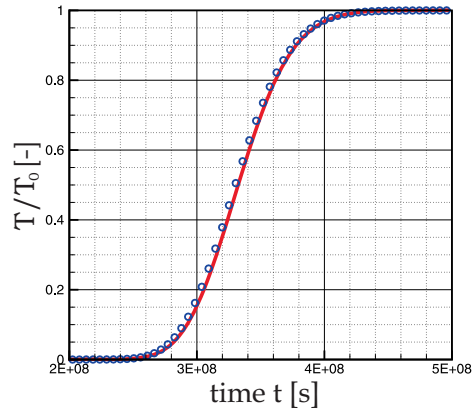
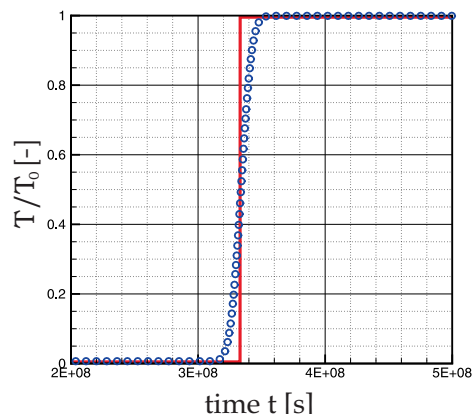
Figure 2.6.2: Temperature breakthrough curve at the point $x = 100$ m.

Figure 2.6.3: Temperature breakthrough curve when diffusion is avoided.

2.7 Heat transport in fracture-matrix systems

2.7.1 Problem definition

Based on the last benchmark example, the heat transport by advection and diffusion in a fracture, this problem is extended by heat diffusion through a rock matrix orthogonal to the fracture (Fig. 2.7.1).

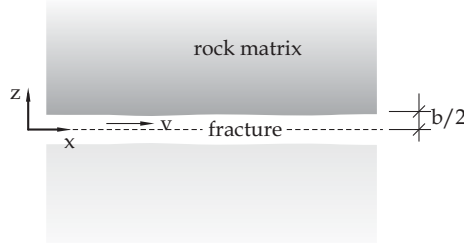


Figure 2.7.1: Heat transport in a fracture-matrix system.

2.7.2 Analytical solution

For this problem an analytical solution is given by LAUWERIER (1955) (see [45]) with following restrictions:

- in the fracture, heat is transported just by advection,
- in the rock matrix, heat transport takes place by diffusion (only along the z-axis).

The LAUWERIER equation is given by

$$T_D = \begin{cases} 0, & t_D < x_D \\ \operatorname{erfc} \left\{ \frac{\beta}{\sqrt{\alpha(t_D - x_D)}} \left[x_D + \frac{1}{2\beta} (z_D - \frac{1}{2}) \right] \right\}, & t_D > x_D, z_D \geq \frac{1}{2} \end{cases} \quad (2.7.1)$$

with the following dimensionless parameters:

$$t_D = \frac{v_x}{b} t, \quad x_D = \frac{x}{b}, \quad z_D = \frac{z}{b}, \quad \alpha = \frac{\lambda^r}{c^r \rho^r} \frac{1}{b v_x}, \quad \beta = \frac{\lambda^r}{c^w \rho^w} \frac{1}{b v_x} \quad (2.7.2)$$

where b is the fracture width, λ is the thermal conductivity, c is the heat capacity, ρ is the density and r and w are rock or water material parameters respectively.

2.7.3 Model setup

The LAUWERIER-problem is formed as a coupling of advective 1D heat transport in x-direction and diffusive 1D heat transport in z-direction. This means, that

nodes in the rock matrix are not influenced by their left or right neighbors. The matrix elements are connected to the fracture elements orthogonally. Fig. 2.7.2 shows a schematical description of the model setup. Because of the symmetry, the numerical model calculates just the domain above the x-axis. Fig. 2.7.3

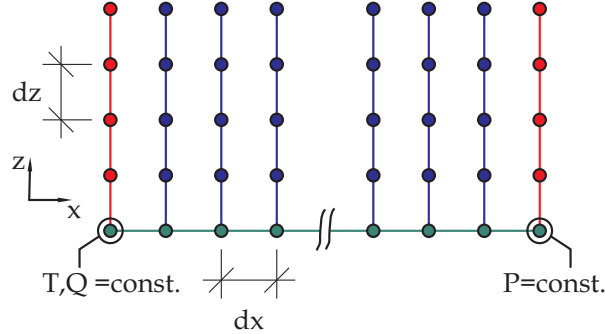


Figure 2.7.2: Alignment of the grid for the numerical model.

shows the positions of observation points which were chosen to evaluate the numerical model by the comparison with analytical solutions.

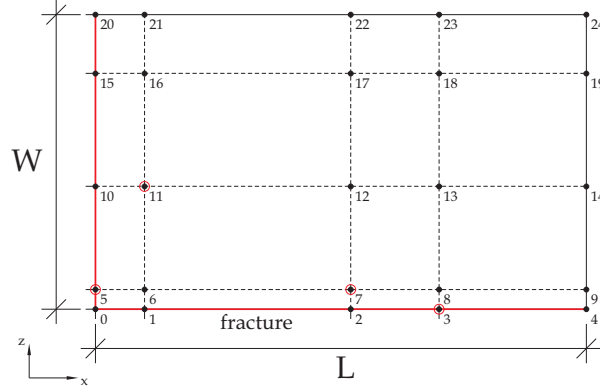


Figure 2.7.3: Positions of observation points for temperature breakthrough curves.

2.7.4 Parameters

The chosen parameters and material properties for this solution are shown in Tab. 2.7.1.

Table 2.7.1: Model parameters for the LAUWERIER-problem.

parameter	value
<i>spatial discretisation</i>	
fracture length L	50 m
matrix width W	63.25 m
step size X Δx	2 m
step size Z Δz	0.1265 m
half of fracture width $b/2$	$1.0 \cdot 10^{-3}$ m
groundwater velocity v_x	$1.0 \cdot 10^{-4}$ m/s
<i>temporal discretisation</i>	
timesteps Δt	$2.0 \cdot 10^5$ s
No. of timesteps	2500
total time	$5.0 \cdot 10^8$ s
<i>material properties – solid</i>	
thermal conductivity λ	$1 \text{ W} \cdot \text{m}^{-1} \cdot \text{K}^{-1}$
heat capacity c	$1000 \text{ J} \cdot \text{kg}^{-1} \cdot \text{K}^{-1}$
density ρ	$2500 \text{ kg} \cdot \text{m}^{-3}$
<i>material properties – fluid</i>	
heat capacity c	$4000 \text{ J} \cdot \text{kg}^{-1} \cdot \text{K}^{-1}$
density ρ	$1000 \text{ kg} \cdot \text{m}^{-3}$

2.7.5 Results

The quality of the numerical results can be shown by temperature distribution curves for several times in the rock matrix. Fig. 2.7.4 shows the temperature profiles for $x = 0$ m at three moments t' . The numerical solution has a very good agreement to the analytical results. Temperature profiles along the fracture at $z = 0$ m are plotted in Fig. 2.7.5. For long simulation times ($t' = 1000; t' = 600$) both solutions fits very well together. For short simulation times, the numerical solution differ slightly from the analytical results. This discrepancy for short simulation times can be examined in Fig. 2.7.6, where temperature breakthrough cures for certain points (see Fig. 2.7.3) is plotted.

Table 2.7.2: Benchmark deposit.

Deposit	Version	Date
T\Lauperier\Lauperier	4.7.03	Jul. 2008

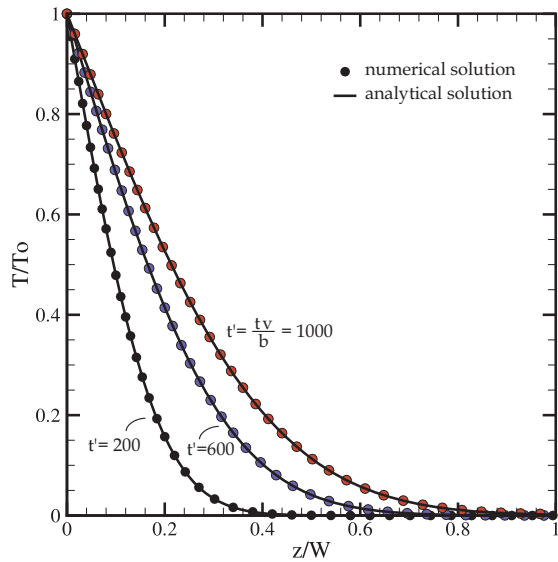


Figure 2.7.4: Temperature distribution orthogonal to the fracture at $x = 0$ at three different times.

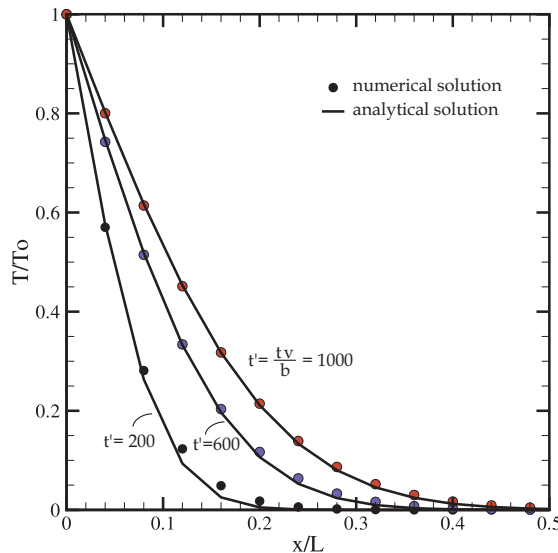


Figure 2.7.5: Temperature distribution along the fracture at three different times.

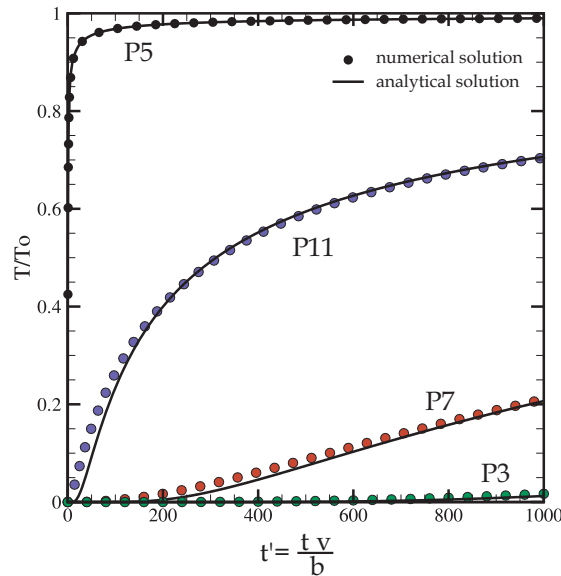


Figure 2.7.6: Temperature breakthrough curves at certain points in the rock matrix.

2.8 Heat transport in fracture-matrix systems: 3D case study

2.8.1 Problem Definition

The following problem deals with simulating fluid flow and heat transport in a 3 dimensional heterogeneous faulted geological system.

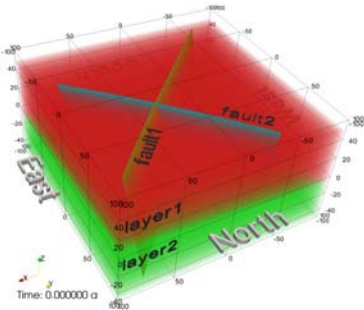


Figure 2.8.1: Sample model consisting of two geological layers cut by a system of two crossing faults.

The model volume consists of two sub-horizontal geological layers, including two dipping faults (Figure 2.8.1). The horizontal north-south and east-west extensions are 200 m, resulting in a horizontal model area of 40,000 m². The two geological layers are vertically bordered by three curved surfaces. The elevation of top, middle and bottom surface is 55 m p_s 5m, 0 m p_s 7 m and -45 m p_s 5 m, respectively. Therefore, an average thickness of 55 m for layer 1 and 45 m for layer 2 is established (Table 2.8.1).

Table 2.8.1: Geometrical attributes of the geological layers and faults.

property	unit	layer1	layer2
average thickness t	[m]	55	45
		fault1	fault2
dip direction	[°]	316.7	225
dip	[°]	80.6	63.2
length l	[m]	233.5	183.8

Both faults are penetrating the two geological layers. Fault 1 has a length of 233 m and is striking North-East, with dip coordinates of 316.7°; 80.6°. Fault 2 has a length of 184 m and is oriented perpendicular to fault 1, having dip coordinates of 225°; 63.2° (Table 2.8.1).

2.8.2 Initial and boundary conditions

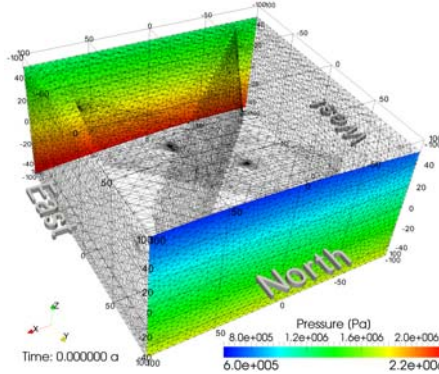


Figure 2.8.2: Pressure boundary condition of the sample model.

During the simulation, a general flow field from the South to the North is generated. Dirichlet (or first-type) boundary conditions for pressure are set along the southern and northern boundaries (Figure 2.8.2). According to the definition of hydrostatic pressure, the pressure at the southern border is constant

at $p(x, y = -100 \text{ m}, z) = \rho g z + 1.75 \cdot 10^6 \text{ Pa}$ and at the northern border at $p(x, y = 100 \text{ m}, z) = \rho g z + 1.25 \cdot 10^6 \text{ Pa}$ (Figure 2.8.2), where ρ [1000 kg/m³], g [9.81 m/s²] and z denotes the fluid density, gravitational acceleration and height of liquid column, respectively. An average hydraulic gradient $\nabla h = 5 \cdot 10^5 \text{ Pa} / 200 \text{ m} = 0.25$ from the South to the North is provided. For the remaining domain, a pressure value of $1.75 \cdot 10^6 \text{ Pa}$ is initialized.

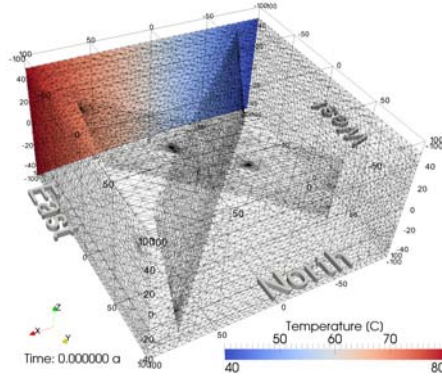


Figure 2.8.3: Temperature boundary conditions of the sample model.

To generate an inflow of hot and cold water from the southern border, Dirichlet boundary conditions for temperature are applied too (Figure 2.8.3). Along the southern border, temperature increases from 40°C to 80°C, in going from West to the East resulting in a temperature profile of $T(x, y = -100 \text{ m}, z) = 0.2^\circ\text{C}/\text{m} * x + 60^\circ\text{C}$ (Figure 2.8.3). For the remaining domain, the initial temperature is set to 60°C.

2.8.3 Parameters

Table 2.8.2 shows the hydraulic properties of the two geological layers.

Table 2.8.2: Porous medium properties of geological layers.

property	unit	layer1	layer2
porosity ϕ	[-]	0.15	0.08
storage β	[1/Pa]	$7 \cdot 10^{-10}$	$7 \cdot 10^{-10}$
permeability k	[m ²]	$2 \cdot 10^{-14}$	10^{-14}

To assure a variation of the hydraulic properties, the upper geological layer was modeled twice as conductive as the lower layer. The permeability k of layer 1 is set to $2 \cdot 10^{-14} \text{ m}^2$ and the porosity ϕ to 0.15. For layer 2 the permeability

k is set to 10^{-14} m^2 and the porosity ϕ to 0.08. The storage of both layers is derived from the bulk compressibility $\beta [1/\text{Pa}]$ of the rock and the embedded fluid. Assuming fissured rocks, the storage is set to $7 \cdot 10^{-10} 1/\text{Pa}$.

In table 2.8.3 the relevant parameters for the system of the two faults are listed.

Table 2.8.3: Medium properties of faults.

property	unit	fault1	fault2
aperture a	[m]	.05	.05
porosity ϕ	[\cdot]	1	1
storage β	[$1/\text{Pa}$]	$4.6 \cdot 10^{-10}$	$4.6 \cdot 10^{-10}$
permeability k	[m^2]	10^{-8}	$5 \cdot 10^{-9}$

The permeability of fault 1 is set to 10^{-8} m and that of fault 2 to $5 \cdot 10^{-9} \text{ m}^2$. The fault transmissivity is defined as the product of the fault permeability k and aperture a . To ensure a high contrast between fault transmissivity and matrix conductivity, the aperture of both faults is set to 0.05 m. To provide free fluid flow in the faults, a porosity value of 1.0 is chosen. The storage in the faults is due to the fluid compressibility only and $\beta = 4.6 \cdot 10^{-10} 1/\text{Pa}$ is assigned.

The simulation time is set to 145 years in order to observe in the simulation the major changes characterizing the temperature field.

2.8.4 Results

After approximately one month a steady state for pressure and velocity field is achieved (Figure 2.8.4).

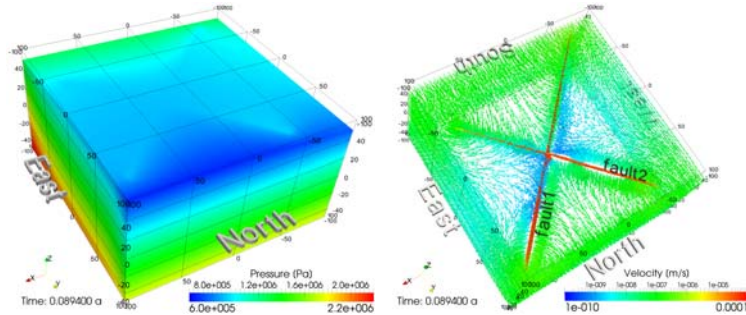


Figure 2.8.4: Simulated steady pressure (2.8.4a) and velocity field (2.8.4b) achieved after approx. 1 month.

Due to the fact that the implemented faults do not cut the southern and northern borders of the model, matrix flow is predominant in these areas. Accordingly, the highest pressure gradients are observed at the northern and southern borders of the model (Figure 2.8.4a). In proximity to the cutting faults, the isobars (surfaces of constant pressure) are sub-horizontal due to high flow rates within the faults. Maximum Darcy velocities of $v = 10^{-4}$ m/s can be observed inside the faults (Figure 2.8.4b). Despite low pressure gradients, high flow rates occur in the fault planes. High values of fluid velocity are the result of the relative high transmissivity of the faults with respects to the surrounding domain.

Figure 2.8.4b shows the stationary flow field. As described above, highest flow velocities can be observed in the fault planes. The applied pressure boundary conditions force a regional flow field from the South to the North. The average velocity at the southern and northern regions is 10^{-7} m/s, with maximum inflow to the faults from the South. In the rest of the domain, outflow from the faults into the rock matrix is pronounced. In the central part of the model, faults act as the predominant flow paths. In contrast, low velocities (less than 10^{-8} m/s) characterize the eastern and western boundaries. An additional important fact is that at the southern edge of fault 1 and fault 2, backward flow from the North to the South occurs. Pressure equalisation within the faults results in higher matrix pressure at this area. This causes drainage of the rock matrix by the fault system.

Figure 2.8.5a-2.8.5d shows the 45°C, 55°C, 65°C and 75°C contours at four different time stages.

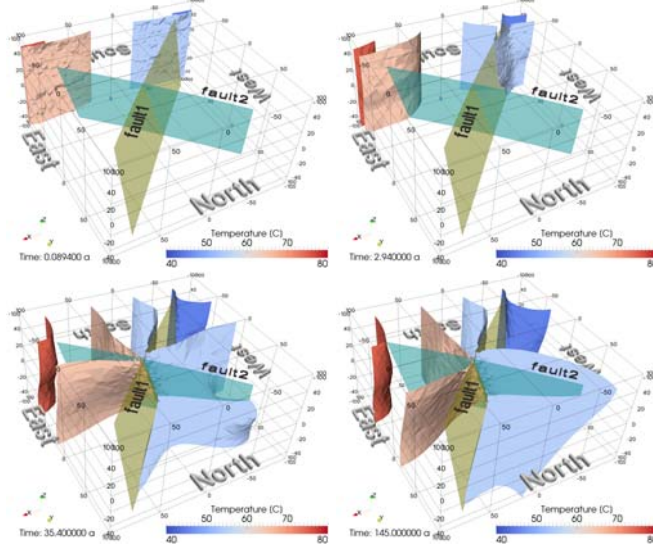


Figure 2.8.5: Temperature contour plots (45°C, 55°C, 65°C and 75°C isosurfaces) at four different time stages.

Before stationary field conditions for pressure and velocity are reached, conductive heat transfer does not affect the initial temperature field significantly (Figure 2.8.5a). After achieving the stationary pressure and velocity field, convective heat transfer (advection plus diffusion) becomes predominant. The cold water front ($T = 55^\circ\text{C}$) enters fault 1 after approx. 4 months (Figure 2.8.5b). Due to the geometry of fault 1 with respects to the southern boundary of the domain, cold water enters fault 1 in the upper part. After 35 years, (Figure 2.8.5c) cold water from fault 1 and hot water from fault 2 are mixed at the fault intersection. The final temperature field (Figure 2.8.5d) shows an average temperature of $T = 55^\circ\text{C}$ in the northern part which is less than the mean initial temperature of 60°C . The depression from the mean value is caused because fault 1 is more conductive than fault 2, which drives higher amounts of cold water into the system.

For a detailed observation of the pressure, velocity and temperature evolution inside the two faults, three observation points were set (Figure 2.8.6a).

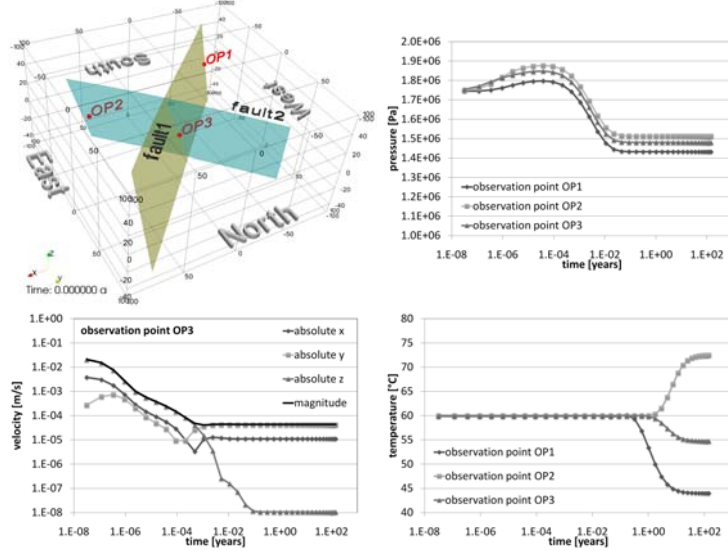


Figure 2.8.6: Location of three observation points within the fault faces (2.8.6a); Simulated pressure (2.8.6b) and temperature (2.8.6d) values at these observation points and simulated velocity components (2.8.6c) at observation point 3.

After starting the simulation the pressure increases at all observation points (Figure 2.8.6b). As shown for observation point 3 (Figure 2.8.6c), the initial magnitude of the velocity is due to vertical flow only. The observed downward flow is forced by the initial pressure conditions in combination with the chosen pressure boundary. Therefore, an initial increase of fluid pressure is observed.

After 1 month, a stationary pressure and velocity field is reached, as indicated by the horizontal lines in Figure 2.8.6b-2.8.6c.

The vertical component of velocity decreases over time from $3 \cdot 10^{-2}$ m/s to 10^{-8} m/s, and the horizontal flow from the South to the North with velocities between 10^{-5} m/s and 10^{-4} m/s becomes dominant. The cold water reaches the fault system at the edge of fault 1 (Figure 2.8.6d) after approx. 4 month. After an additional 17 months, cooling at observation point 3 begins. At the same time, hot water reaches fault 2 first. Due to the lower transmissivity of fault 2, the hot water reaches the intersection point after 10 years, and cooling at observation point 3 stops. Higher amounts of cold water enter the fault intersection (observation point 3) from the more conductive fault 1, causing temperature to decrease to 55°C . This corroborates the observation of the temperature field for the total domain.

In a second run, the same problem described above has been numerically solved using the Flux Corrected Transport (FCT) scheme as implemented in Norihiro's branch of OpenGeoSys version 5. Figure 2.8.7 illustrates the differences regarding numerical oscillations in solving for the transport field with (dashed lines) and without (solid lines) FCT method. Figure 2.8.7a and Figure 2.8.7b show the calculated temperature profiles along the general flow field for two different stages in the simulation. As shown in Figure 2.8.7a, the FCT method seems to reduce the amplitudes of numerical oscillations by a maximum factor of three at the beginning of the simulation. The OGS benchmark files can be found in the subdirectory 2units2faults/FCT.

2.9 Heat transport with temperature dependent fluid properties

2.9.1 Problem definition

A 1D test example for groundwater flow and simultaneous heat transport in the aquifer is made. The aim of the numerical simulation with GeoSys/RockFlow is to determine if the consideration of varying density with temperature changes is possible. The following assumptions will be made:

- Aquifer: homogeneous, saturated, stationary flow
- Fluid flow: incompressible fluid, non-isothermal.

2.9.2 Model set-up of the 1 D numerical model

For the 1-dimensional calculation the calculation area is simplified as a line of a length of 5.2 m. The calculation model includes 25 elements and 26 nodes. The initial pressure in the whole area is 100 kPa and the initial temperature 300 K. As boundary condition a constant pressure of 101 kPa is given at the

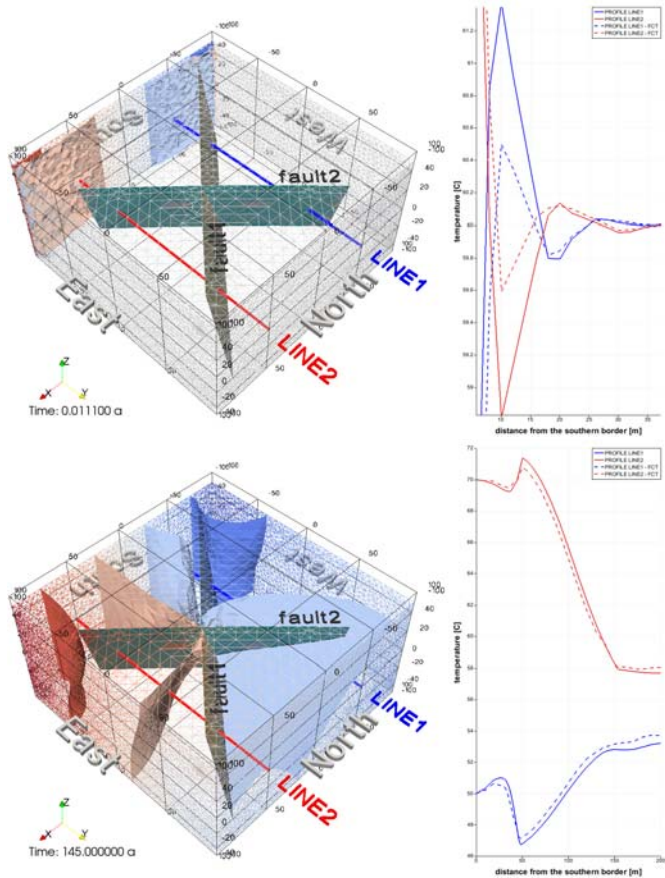


Figure 2.8.7: Simulated temperature along two lines at the beginning (2.8.7a) and at the final simulation time (2.8.7b) with and without flux corrected transport FCT.

left boundary and of 100 kPa at the right boundary. A constant temperature of 400 K is set at the left boundary. The used soil parameters are listed in Tab. 2.9.1. The fluid density is decreasing with increasing temperature. The viscosity, capacity and conductivity of water are set to constant values. The fluid parameters also can be found in Tab. 2.9.1.

Table 2.9.1: Used soil and fluid parameters.

parameter	value
<i>soil parameters</i>	
porosity ϕ	0.01
permeability K	$1.0 \cdot 10^{-11} \text{ m}^2$
density ρ	$2850 \text{ kg} \cdot \text{m}^{-3}$
heat capacity c_s	$1000 \text{ J} \cdot \text{kg}^{-1} \cdot \text{K}^{-1}$
heat conductivity λ_s	$3.2 \text{ W} \cdot \text{m}^{-1} \cdot \text{K}^{-1}$
<i>fluid parameters</i>	
initial density ρ_0	$1000 \text{ kg} \cdot \text{m}^{-3}$
viscosity η	$0.001 \text{ N} \cdot \text{s} \cdot \text{m}^{-2}$
heat capacity c_f	$4000 \text{ J} \cdot \text{kg}^{-1} \cdot \text{K}^{-1}$
heat conductivity λ_f	$0.6 \text{ W} \cdot \text{m}^{-1} \cdot \text{K}^{-1}$

2.9.3 Validation method

In order to find out whether the consideration of varying water density with temperature changes is possible, one simulation run is done with a constant density of 1000 kg/m^3 , which is the initial water density before heating, and one run with a constant density of 900 kg/m^3 , the density after the heating process. The temperature results for a heat transport with varying density have to be in between both temperature evolution curves.

2.9.4 Results

The curve for temperature evolution, which is shown in Fig. 2.9.1 for the right boundary (node 26), shows the expected characteristics. Therefore it can be stated, that the consideration of temperature dependent fluid density is possible.

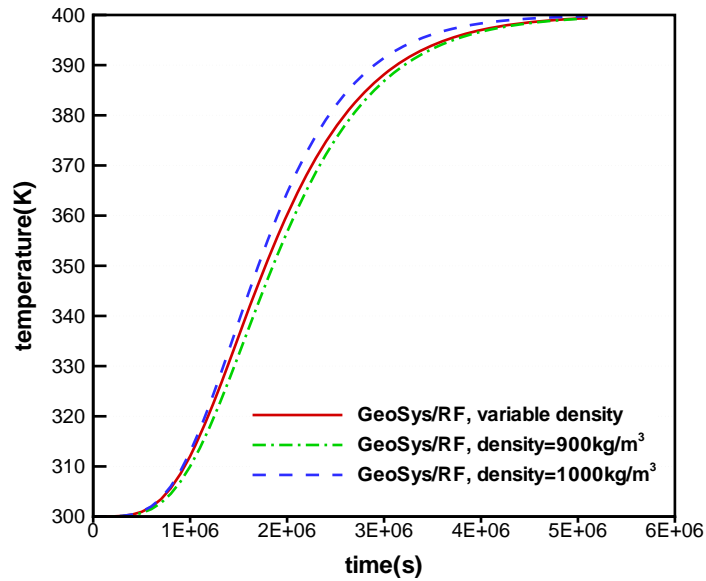


Figure 2.9.1: Temperature evolution with constant and variable fluid densities.

Table 2.9.2: Benchmark deposit

Deposit	Version	Date
\HT_var_density_1D	rf4.7.02	March 2008

Chapter 3

Groundwater flow – H-Processe

This chapter deals with saturated subsurface flow. In the aquifer concept balance equations determine strictly horizontal flow and vertical flow can be included by leakage terms through confining beds. The leakage terms add or subtract water from aquifers overlying and underlying a leaky confining bed according to the aquifer's head difference and a confining bed conductivity. An aquifer which contains a water table is termed unconfined and a completely filled aquifer is termed confined. The governing equations for three-dimensional groundwater, confined, and unconfined aquifer flow are introduced in Sec. 3.1. In Sec. 3.3 the benchmarks for confined and in Sec. 3.5 for unconfined aquifers are introduced. Groundwater flow is solved two- and three dimensionally in the benchmark examples.

3.1 Theory

A three-dimensional description of groundwater flow is given by the mass balance equation

$$S_s \frac{\partial h}{\partial t} - \nabla \cdot \frac{\rho g}{\mu} \kappa \nabla h = q^{ex} \quad (3.1.1)$$

where the head h is the primary variable of groundwater flow and S_s is the specific storage which is assumed to be independent of the head neglecting fluid and soil matrix compression. Use of Darcy's law for momentum balance leads to the fluid density ρ , dynamic fluid viscosity μ , gravity constant g , and aquifer permeability matrix κ . Finally q^{ex} denotes external sources and sinks. Depth integration leads to the two-dimensional Boussinesq equation which describes

unconfined aquifers and reads

$$S_y \frac{\partial h}{\partial t} - \nabla \cdot \frac{\rho g h}{\mu} \kappa \nabla h = q^{ex} \quad (3.1.2)$$

where S_y is the specific yield. For confined aquifers Eq. 3.1.2 becomes

$$S \frac{\partial h}{\partial t} - \nabla \cdot \frac{\rho g L}{\mu} \kappa \nabla h = q^{ex} \quad (3.1.3)$$

where S is the storage and L the aquifer thickness. The aquifer thickness L is taken into account by changing the soil permeability κ in the following benchmark examples. A channel source term can be assigned according to

$$q^{ex} = K_\Lambda \frac{P}{B} \frac{h^{sur} - h^{sub}}{a} \quad (3.1.4)$$

where K_Λ is the channel bed conductivity, B the channel width, a the channel bed thickness, and h^{sur} the channel flow head. The wetted perimeter $P = 2(h^{sur} - z^{sur}) + B$ for rectangular channel where z^{sur} is the height of the top of the channel bed. Groundwater head h is taken into account by

$$h^{sub} = \max(h, z^{sur}). \quad (3.1.5)$$

Leakage terms between adjacent aquifers can be defined accordingly.

3.2 Linear groundwater flow

Theory

Water flow in a saturated porous medium is influenced by the pressure gradient over a given distance and the hydraulic conductivity of the aquifer. By Darcy's Law (equ. 3.2.1) the flow rate by considering these influences can be calculated.

$$v_f = k_f \cdot i \quad (3.2.1)$$

with

- v_f – flow rate (m/s),
- k_f – hydraulic conductivity (m/s),
- i – pressure gradient (-).

The hydraulic conductivity is calculated by the following relation.

$$k_f = \frac{\kappa \cdot \rho \cdot g}{\mu} \quad (3.2.2)$$

with

κ – permeability (m^2)

ρ – density of the fluid ($\text{kg}\cdot\text{m}^{-3}$)

g – gravity constant ($\text{m}\cdot\text{s}^{-2}$)

μ – dynamic viscosity of the fluid ($\text{Pa}\cdot\text{s}$)

By using the law of continuity the discharge through a defined cross section can be calculated.

$$Q = v_f \cdot A \quad (3.2.3)$$

with

Q – discharge (m^3/s)

A – cross section (m^2)

Layered soil material is possibly less permeable in one direction than in the direction perpendicular to it. In this case the input of different values for the permeability κ in dependence on the direction of anisotropy is possible in RockFlow.

3.2.1 Flow in an isotropic medium

Problem definition

This test example for groundwater flow is taken from the RockFlow Tutorial A (Maßmann, 2004). The aim of this example is to simulate the stationary groundwater flow in a homogeneous aquifer. Figure 3.2.1 shows a sketch of the calculation area.

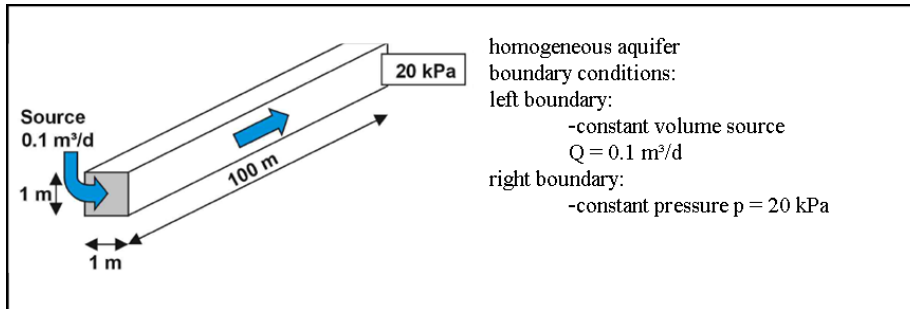


Figure 3.2.1: Calculation area: homogeneous aquifer (Maßmann, 2004)

Assumptions

Aquifer: homogeneous, saturated, stationary flow

Model set-up of the 1 D numerical model

For the 1-dimensional calculation the calculation area is simplified as a line of a length of 100 m. The calculation model includes 100 elements and 101 nodes. As boundary condition the source volume of the fluid phase of $0.1 \text{ m}^3/\text{d}$ is given at the left border of the calculation area and the constant pressure of 20 kPa at the right boundary. The used parameters of the soil are listed in table 3.2.1.

parameter	value	unit
porosity Φ	0.2	–
permeability κ	$1.0 \cdot 10^{-12}$	m^2

Table 3.2.1: Used parameters

Evaluation method

The constant flow rate v_f is calculated by using equation 3.2.3. In order to calculate the pressure at the left border of the calculation model, Darcy's Law is applied in the following way. The second relation (eq. 3.2.4) shows that the pressure gradient is linear.

$$i = \frac{Q}{k_f \cdot A} = \frac{Q}{K \cdot \frac{\rho \cdot g}{\eta} \cdot A} = \frac{1.157 \cdot 10^{-6} \frac{\text{m}^3}{\text{s}}}{9.81 \cdot 10^{-6} \frac{\text{m}}{\text{s}} \cdot 1 \text{ m}^2} \quad \text{and} \quad p_{\text{left}} = p_{\text{right}} + \rho \cdot g \cdot i \cdot l \quad (3.2.4)$$

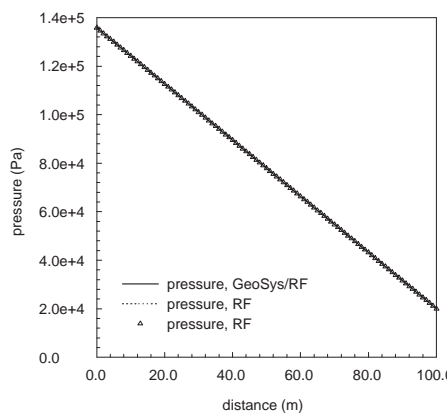


Figure 3.2.2: Pressure distribution over the distance of 100 m

Results

In figure 3.2.2 you can find the pressure distribution over the whole length of the 1 D model that was calculated by GeoSys/RockFlow. In addition, the analytically calculated pressure distribution is depicted in this figure. These pressure values match the numerical results well.

Benchmark	Problem type	Path in benchmark deposit
h_sat_flow_1d	H	benchmarks \H\sat_1D

3.2.2 Flow in an anisotropic medium

Problem definition

The aim of this example is to simulate the stationary groundwater flow in an anisotropic porous medium. In order to consider the anisotropy of permeability, a 2 D numerical model was built which contains a higher permeability in the vertical than in the horizontal direction.

Assumptions

Aquifer: anisotropic, saturated, stationary flow

Model set-up of the 2 D numerical model

For the 2-dimensional simulation, the cube consisting of a porous medium is simplified as a square with an area of 1 m². The calculation model includes 736 triangular elements and 409 nodes. At the left corner at the bottom of the model a constant pressure of 1000 Pa is specified along two polylines of the length of 0.3 m (3.2.3). At the top and the right border the pressure is set to 0 in order to create a pressure gradient. As the porous medium is assumed to be anisotropic, which influences the groundwater flow, the values for permeability are equal to $1.0 \cdot 10^{-15}$ m² in x-direction and $1.0 \cdot 10^{-14}$ m² in y-direction.

parameter	value	unit
porosity Φ	0.2	–
permeability κ_x	$1.0 \cdot 10^{-15}$	m ²
permeability κ_y	$1.0 \cdot 10^{-14}$	m ²

Table 3.2.2: Used parameters

Evaluation method

This test example is not made up to introduce a new process, but it shows the possibility for the GeoSys/RockFlow user to give a specific permeability for each

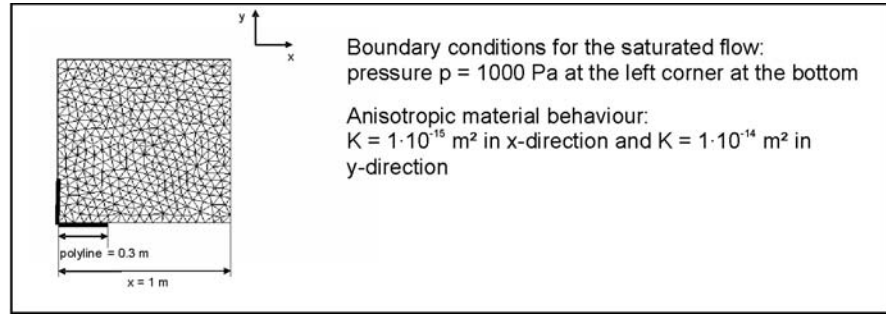


Figure 3.2.3: Calculation model (2 D)

direction. Therefore, the interpretation of GeoSys/RockFlow results comprises merely the comparison between pressure distributions due to anisotropic groundwater flow that were simulated by the use of RockFlow and GeoSys/RockFlow. This comparison is possible because both versions are developed separately concerning anisotropy of soils.

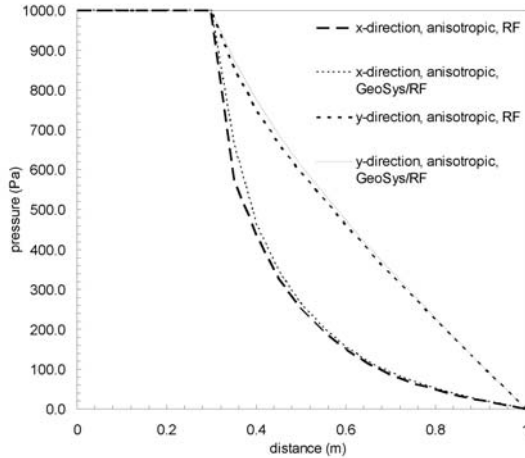


Figure 3.2.4: Pressure distribution caused by anisotropic saturated flow

Results

In figure 3.2.4 the horizontal and vertical pressure distributions of an anisotropic groundwater model which is made using the program code RockFlow are depicted next to the pressure distributions of the described anisotropic model. While presuming an anisotropic medium, an inhomogeneous pressure field is developing, because the groundwater is not able to spread out uniformly. This can be recognized at the different curve gradients in x- and y-direction. There

are slight differences between the curve characteristics of the RockFlow and the GeoSys/RockFlow simulation results. These differences are due to different element types (square in the RockFlow model) and the resulting differing x- or y-coordinates. Therefore, the pressure distributions that are obtained by the simulation with GeoSys/RockFlow are evaluated to be correct.

Benchmark	Problem type	Path in benchmark deposit
H_sat_flow_K_ortho	H	benchmarks \H\sat_2D

3.2.3 Flow in an isotropic and heterogeneous medium

Problem definition

The aim of this example is to simulate the stationary groundwater flow in an isotropic and heterogeneous porous medium. In order to consider the heterogeneous of permeability, a 2 D numerical model was built. The heterogeneous distribution of permeability is showed in 3.2.5.

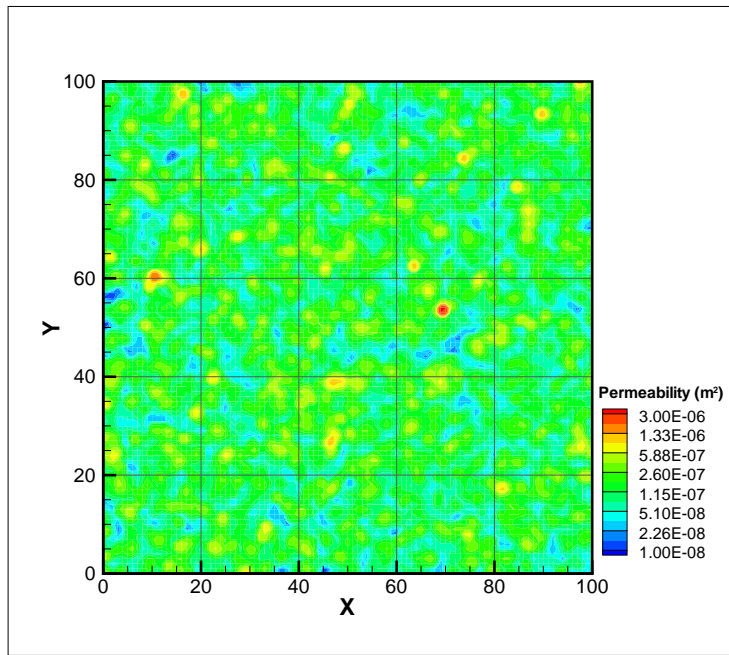


Figure 3.2.5: Calculation model(2 D): heterogeneous permeability distribution

Assumptions

Aquifer: isotropic, heterogeneous, saturated, stationary flow

Model set-up of the 2 D numerical model

For the 2-dimensional simulation, the cube consisting of a porous medium is simplified as a square with an area of 10000 m². The calculation model includes 10000 quad elements and 10201 nodes. At the left boundary a constant head of 10 m and the right boundary a constant head of 9 m are specified in order to create a pressure gradient.

Results

In figure 3.2.6 the horizontal and vertical head distributions of a groundwater flow in a heterogeneous medium are depicted responding to the distribution of the permeability.

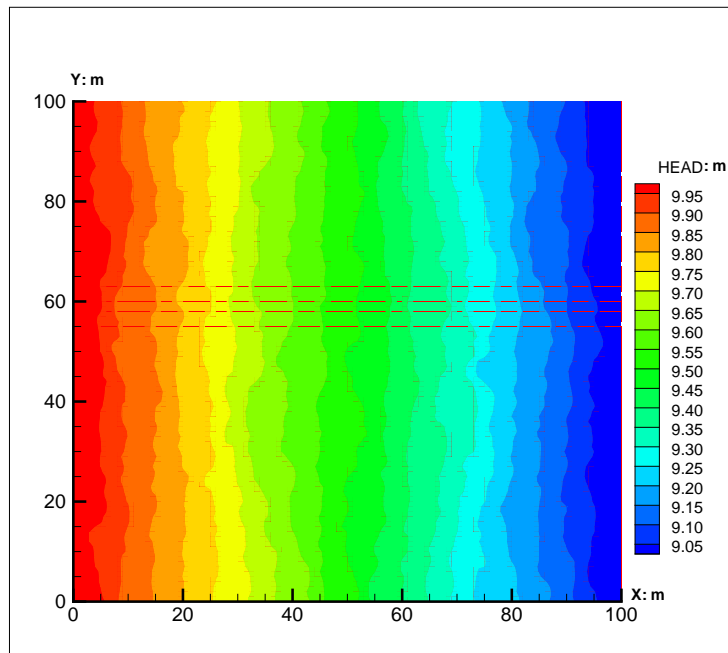


Figure 3.2.6: Head distribution responded to isotropic and heterogeneous medium

Benchmark	Problem type	Path in benchmark deposit
2D1P-GWFlow	H	benchmarks \H\HetGWFlow

3.3 Confined aquifer

3.3.1 Constant source term

Problem definition

These examples deal with an aquifer which is subject to a constant recharge line source. [46] presented an analytical solution for a constant line source on an infinite domain which reads for the groundwater head at the source

$$h = q^{ex} \sqrt{\frac{\mu t}{\pi \rho g k L S_y}}. \quad (3.3.1)$$

The aquifer size is $20m \times 10m$ with the source term at one boundary (See Fig. 3.3.2). The simulation time is $30min$.

Initial and boundary conditions

Initial groundwater head is $0m$. The source term is $2 \times 10^{-4}m/s$, groundwater head is 0 at the opposite boundary, and at the remaining part no-flow is imposed.

Material properties

For the spatial discretization 24×12 quadrants or hexahedra are used. The hexahedra have a height of $1m$. Material parameters are given in Tab. 3.3.1.

Table 3.3.1: Parameters for the constant source term examples

Parameter	Symbol	Setting	Unit
Storage	S	0.2	–
Specific storage	S_s	0.2	$1/m$
Viscosity	μ	1×10^{-3}	$Pa \cdot s$
Thickness	L	1	m

Results

Simulation results are compared with the analytical solution in Fig. 3.3.1

Benchmark deposit

Benchmark	Problem type	Path in benchmark deposit
$q\text{-}quad$	H	benchmarks\GROUNDWATER_FLOW\
$q\text{-}hex$	H	benchmarks\GROUNDWATER_FLOW\

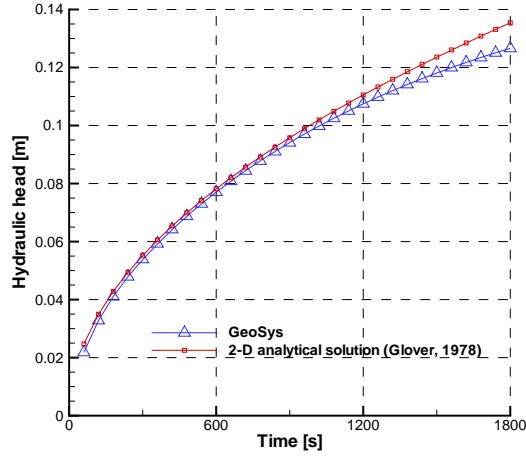


Figure 3.3.1: Results and analytical solution for confined aquifer with line source term

3.3.2 Channel source term

Problem definition

For these examples the source term of the previous examples (Sec. 3.3.1) is substituted by a corresponding channel source term (Eqn. 3.1.4). The channel is assumed to be not affected by the water loss and the exchange flux is independent of the groundwater head. Therefore, the source term represents a steady and uniform channel located above the aquifer. The cross-section of the channel is rectangular. The setup, spatial discretization, and calculated water head are shown in Fig. 3.3.2. The simulation time is 30min.

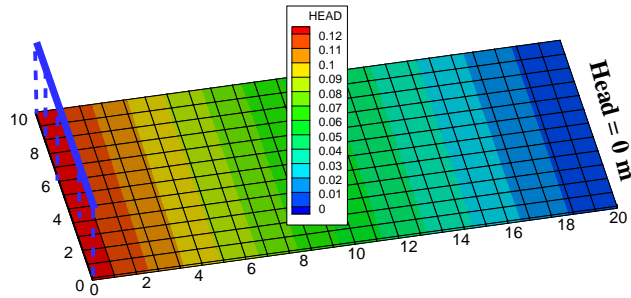


Figure 3.3.2: Computational domain and (channel) source term location

Initial and boundary conditions

The initial groundwater head is $0m$. The channel source term is the boundary condition at one side, at the opposite boundary the head is fixed 0 . At the remaining boundaries no-flow is imposed.

Material properties

For the spatial discretization either 24×12 quadrants or hexahedra are used as well prisms which are generated by cutting the hexahedra in two parts. The hexahedra or prism height is $1m$. The time step is $1min$. Simulation parameters for the aquifer and the channel source term are given in Tab. 3.3.3.

Table 3.3.2: Parameters for channel source term examples

Parameter	Symbol	Setting	Unit
Aquifer			
Storage	S	0.2	—
Specific storage	S_s	0.2	$1/m$
Viscosity	μ	1×10^{-3}	$Pa \cdot s$
Thickness	L	1	m
Channel source term			
Head	h^{sur}	4	m
Bed top location	z^{sur}	1	m
Width	B	14	m
Conductivity	K_A	1×10^{-6}	m/s
Thickness	a	0.3	m

Results

Comparison of simulation results and analytical solution is given in Fig. 3.3.3 for quadrants and in Fig. 3.3.4 for hexahedra.

Benchmark deposit

Benchmark	Problem type	Path in benchmark deposit
<i>riv1-quad</i>	H	benchmarks\GROUNDWATER_FLOW\
<i>riv1-pris</i>	H	benchmarks\GROUNDWATER_FLOW\
<i>riv1-hex</i>	H	benchmarks\GROUNDWATER_FLOW\

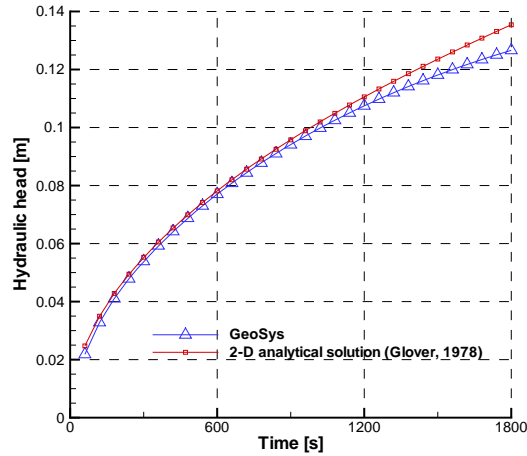


Figure 3.3.3: Results with quadratic elements and analytical solution for confined aquifer below uniform and steady channel

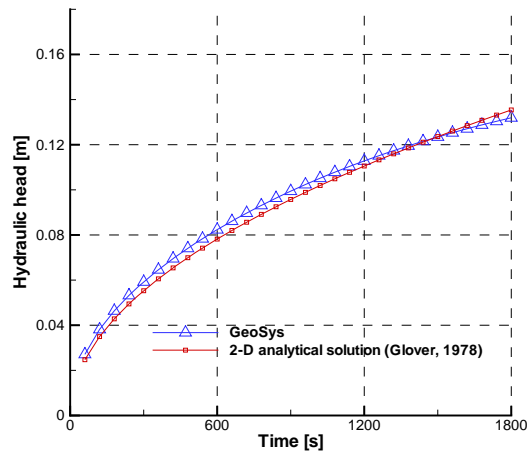


Figure 3.3.4: Results with hexahedral and prismatic elements compared with the analytical solution for confined aquifer below uniform and steady channel

3.3.3 Channel sink term

Problem definition

For this example the channel of the previous examples (Sec. 3.3.2) is located such that flow from the aquifer to the channel takes place. Therefore, the source

term represents a steady and uniform rectangular channel located in the aquifer. The setup is shown in Fig. 3.3.2. The simulation time is 30min .

Initial and boundary conditions

Initial groundwater head is 0m . The channel source term is the boundary condition at one side, at the opposite boundary the head is 0. At the other boundaries no-flow is imposed.

Material properties

The domain is discretization with 24×12 quadrants. The time step size is 1min . Simulation parameters for the aquifer and the channel source term are given in Tab. 3.3.3.

Table 3.3.3: Parameters for the channel sink term example

Parameter	Symbol	Setting	Unit
Aquifer			
Storage	S	0.2	—
Specific storage	S_s	0.2	$1/\text{m}$
Viscosity	μ	1×10^{-3}	$\text{Pa} \cdot \text{s}$
Thickness	L	1	m
Channel source term			
Head	h^{sur}	-0.5	m
Bed top location	z^{sur}	-0.7	m
Width	B	59.6	m
Bed conductivity	K_Λ	1×10^{-6}	m/s
Bed thickness	a	0.3	m

Results

Simulation results are shown in Fig. 3.3.5.

Benchmark deposit

Benchmark	Problem type	Path in benchmark deposit
<i>riv2_hex</i>	H	benchmarks\GROUNDWATER_FLOW\

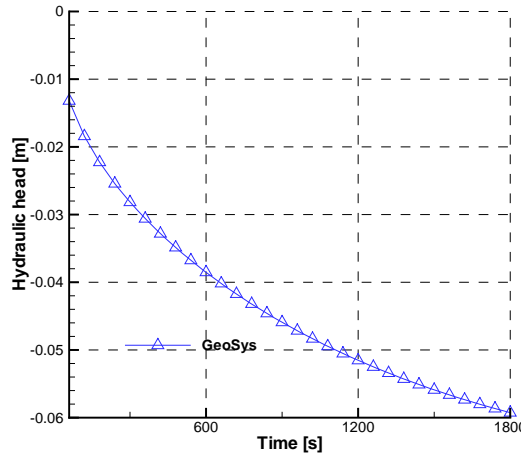


Figure 3.3.5: Results by GeoSys for confined aquifer with a constant channel sink term

3.3.4 Theis' Problem

Problem definition

Theis' problem examines the transient lowering of the water table induced by a pumping well. Theis' fundamental insight was to recognize that Darcy's law is analogous to the law of the flow of heat by conduction, hydraulic pressure being analogous to temperature, pressure-gradient to thermal gradient.

Assumptions

Aquifer: confined, infinite areal extend, homogeneous, isotropic, uniform thickness, horizontal piezometric surface;

Well: constant discharge rate, well penetrates the entire thickness, well storage effects can be neglected.

Analytical solution

The analytical solution of the drawdown as a function of time and distance is expressed by equation 3.3.2:

$$h_0 - h(t, x, y) = \frac{Q}{4\pi T} W(u) \quad (3.3.2)$$

$$u = \frac{(x^2 + y^2)S}{4Tt} \quad (3.3.3)$$

where:

symbol	property	unit
h_0	constant initial hydraulic head	L
Q	constant discharge rate	$L^3 T^{-1}$
T	aquifer transmissivity	$L^2 T^{-1}$
t	time	T
x,y	the coordinate at any point	L
S	aquifer storage	-

Initial and boundary conditions

Parameters/conditions	OpenGeoSys
Initial conditions	$h(0,r)=0$
Sink, well pumping rate	$Q = 1.22329 \times 10^3 m^3 d^{-1}$
Boundary conditions	$h(t,304.8m)=0$
flow materials	
-Hydraulic conductivity	$9.2903 \times 10^{-4} ms^{-1}$
-storage coefficient	$S=0.001$
-storage compressibility	0
-wellbore radius	0.3048m

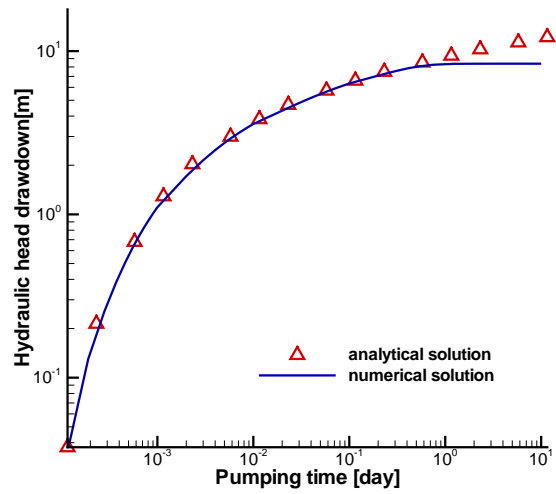


Figure 3.3.6: Calculated drawdowns at a distance of 9.639m from the well.

Results

Fig. 3.3.6 shows the comparison of analytically and numerically calculated drawdown of hydraulic head versus time at the distance of $r = 9.639$ m from the well.

Benchmark deposit

Benchmark	Problem type	Path in benchmark deposit
<i>h_quad_axisym</i>	H	benchmarks\H\Theis_1D\

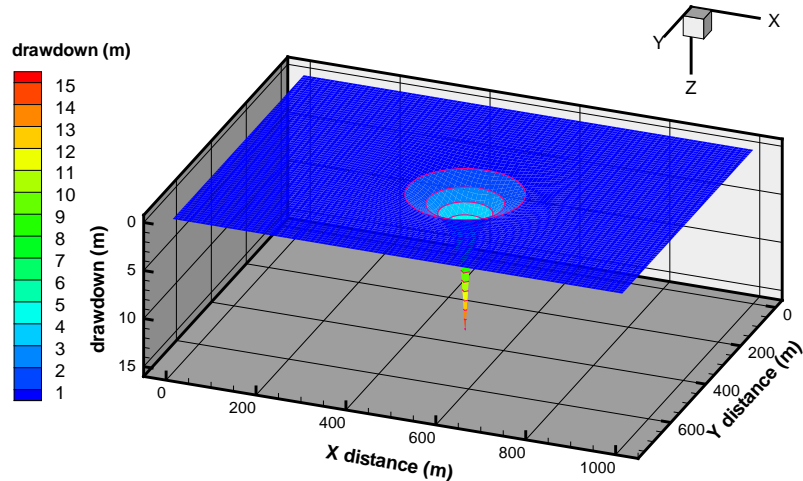


Figure 3.3.7: Cone of depression at the end of the simulation.

2D application

The 2D application is solved in the following situation:

parameters	description	values	unit
Q	discharge rate	1000	$m^3 d^{-1}$
S	specific storage	1.0×10^{-5}	m^{-1}
T	transmissivity	1000	$m^2 d^{-1}$
B	thickness of aquifer	20	m

The aquifer horizontal domain size is $1000\text{m} \times 750\text{ m}$ with the pumping well at the location coordinate (500,375).The discretization of space is $10\text{m} \times 10\text{m}$ grid. The simulation time is 0.00175 day and the time step is 1.036 sec. The boundary condition is 0.0 drawdown. The cone of depression induced by the pumping well at the end of the simulation is plotted in Fig. 3.3.7.

Benchmark deposit

Benchmark	Problem type	Path in benchmark deposit
<i>h_quad_axisym</i>	H	benchmarks\H\Theis_2D\

3.4 Time variant flow

This benchmark is set up to test the implementation of time variant boundary conditions for the GROUNDWATER_FLOW process. These boundary conditions allow to simulate flow and transport in a flow field, which changes gradient and direction according to user specified functions.

The setup of the model domain is depicted in Figure 3.4.1. The model geometry is designed by 4 corner nodes (gli nodes 0 through 3), which are connected along the model edges by one polyline each. To induce a time variant flow field, time functions are generated externally and are connected to the corner gli nodes. The polyline names and location and the names of the time functions are shown in Figure 3.4.1.

To connect the time functions with the boundary condition, the boundary condition has to be specified along a polyline. The distribution type is LINEAR followed by the number of nodes of the polyline (2) and then by two lines specifying the gli node number, the value at this node and the name of the time function. The value of the time function at the corresponding time is then multiplied by the specified value at the nodes and interpolated to all mesh nodes found along the polyline. This is performed in each timestep. In the case shown here, this was applied for all four boundary condition polylines along the four model area sides.

```
#BOUNDARY_CONDITION
$PCS_TYPE
GROUNDWATER_FLOW
$PRIMARY_VARIABLE
HEAD
$GEO_TYPE
POLYLINE BCLEFT
$DIS_TYPE
LINEAR 2
0 1.0 BC_left_low
```

3 1.0 BC_left_high

The model area is 184 m in x direction and 64 m in y direction. Boundary conditions are placed along all four sides of the model area. Hydraulic conductivity is 0.00215 m s^{-1} , the storage coefficient is set to 0. Initial conditions are a head of 2.0239 m everywhere.

The benchmark tests at the same time the application of a heterogeneous distribution of the hydraulic conductivity. This is achieved by setting in the *.mmp file:

```
$PERMEABILITY_TENSOR
ISOTROPIC 1.0
$PERMEABILITY_DISTRIBUTION
2d_het_a_kfhet
```

The file `2d_het_a_kfhet` contains the heterogeneous distribution of the hydraulic conductivity, and is generated using an geostatistical simulator. The file contains information on the `$MSH_TYPE`, the `$MMP_TYPE` and specifies options for the interpolation of the values onto the elements of the specified mesh (`$DIS_TYPE`). Under the keyword `$DATA` the actual values are specified as x - y - parameter values, where parameter is the hydraulic conductivity. The end of the data set is marked using the keyword `#STOP`.

```
#MEDIUM_PROPERTIES_DISTRIBUTED
; Specify mesh, for which data is read
$MSH_TYPE
GROUNDWATER_FLOW
$MMP_TYPE
PERMEABILITY
; give interpolation option: NEAREST_VALUE or GEOMETRIC_MEAN
$DIS_TYPE
NEAREST_VALUE
$CONVERSION_FACTOR
1.0
; X, Y, Z, nof field values
$DATA
33.00 35.00 0 1.0903602235e-004
25.00 37.00 0 8.4356781197e-005
125.00 21.00 0 5.7274327695e-005
...
```

The result of the simulation is shown in Figures 3.4.2 in top view. The full contours show the piezometric head isolines after the first five time steps, the black and red lines show head isolines from a succession of time steps. It can be seen, that the flow field is turned and directed upwards (black isolines) and back again (red isolines) during the simulation. Figure 3.4.3 shows the time variant

head in an observation well at $x=20$ m and $y=28$ m. The rise and fall of the piezometric head due to the time variant flow field can be clearly seen, as well as the initial jump from the initial head to the time variant head.

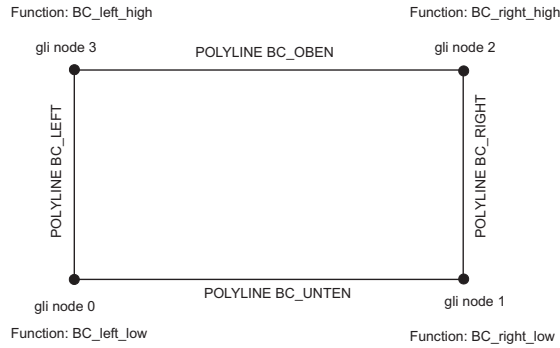


Figure 3.4.1: Model setup for the time variant flow

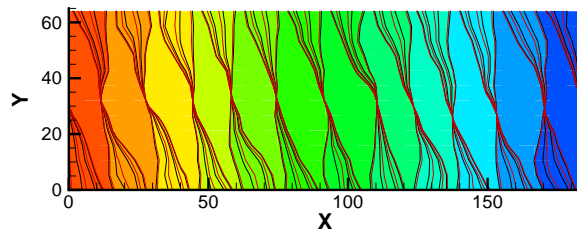


Figure 3.4.2: Model results for the time variant heads in top view

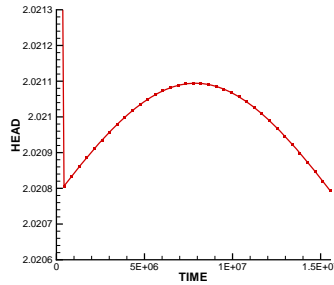


Figure 3.4.3: Model results at one observation well

Benchmark	Type	Path
transient_flow	H	benchmarks\GROUNDWATER_FLOW\transient_flow

3.5 Unconfined aquifer

3.5.1 Steady state case

Problem definition

In these examples the aquifer consists of a small strip with the size of $100m \times 2m$ (see Fig. 3.5.1). At both ends the head is fixed and constant recharge is imposed on the whole domain which leads to steady state flow. This setting allows comparison with an analytical solution.

Initial and boundary conditions

Initial groundwater head is $0m$. At one end of the strip the head is 1 at the other 5 . At the top a source term of $1.0 \times 10^{-8}m/s$ and at the remaining parts no-flow is imposed.

Material properties

For the spatial discretization 100 equal quadrants and 410 triangles or prisms are used. In latter case the three-dimensional groundwater Eqn. 3.1.2 is solved with elements adapting to the water height. One time step with the size of 100s is used. The specific storage $S_s = 0m^{-1}$ or specific yield $S_y = 0$ and a permeability κ of $1 \times 10^{-9}m^2$ is used.

Results

Comparison of simulation results for prisms and analytical solution is shown in Fig. 3.5.1.

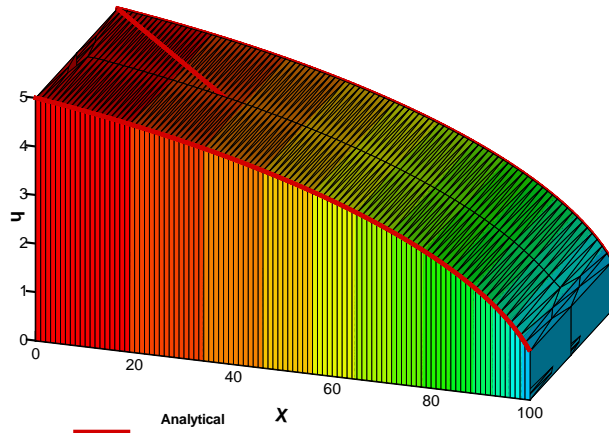


Figure 3.5.1: Results of unconfined aquifer benchmark example by GeoSys with prisms

Benchmark deposit

Benchmark	Problem type	Path in benchmark deposit
<i>uc_quad</i>	H	benchmarks\GROUNDWATER_FLOW\
<i>uc_tri</i>	H	benchmarks\GROUNDWATER_FLOW\
<i>uc_pris</i>	H	benchmarks\GROUNDWATER_FLOW\

Chapter 4

Fluid property functions

4.1 Theory of thermodynamic and transport properties

4.1.1 Density

In subterranean oil and gas reservoirs, properties of gases and liquids strongly depend from environmental pressure and temperature conditions. Equations of state (EOS) may be used to describe the relationship of volume, pressure and temperature of a real fluid. The knowledge of a fluids volume or its density is essential to estimate further thermodynamic properties. The first EOS for real gases, which was based on the ideal gas law, was presented by Johannes Diderik VAN DER WAALS in 1873 [47]. In 1910 he received the Nobel prize for the development of the equation

$$p = \frac{RT}{V_m - b} - \frac{a}{V_m^2} \quad (4.1.1)$$

where p is the pressure, R is the gas constant, T is the temperature, V_m is the molare volume and a and b are correcting parameters.

Following three different EOS will be described, which are implemented in version GeoSys (4.10.00), based on the VAN DER WAALS-equation (4.1.1).

Redlich-Kwong equation of state (RKEOS) The Equation of REDLICH and KWONG from 1949 (4.1.2) represents just a little improvement of the van der Waals equation [48]. It is given as

$$p = \frac{RT}{V_m - b} - \frac{a}{T^{0.5} V_m (V_m + b)}. \quad (4.1.2)$$

Its results are satisfactory only for temperatures above the critical point (see Tab. 4.1.1).

Table 4.1.1: Fluid properties used in equations of state, where ω is the acentric factor, T_c and p_c are temperature und pressure at the critical point and R ist the gas constant.

substance	ω [-]	T_c [K]	p_c [MPa]	R [J/kg/K]
Carbon dioxide	0.239	304.13	7.38	188.9
Ethane	0.099	305.32	4.87	276.5
Methane	0.011	190.56	4.60	518.3
Water	0.344	647.10	22.06	461.5

Equation (4.1.2) can be recasted as a cubic equation in terms of volume

$$V_m^3 - \frac{RT}{p} V_m^2 - \left(\frac{RTb}{p} - \frac{a}{T^{0.5}p} + b^2 \right) V_m - \frac{ab}{T^{0.5}p} = 0. \quad (4.1.3)$$

This equation yields to one or three real roots depending on the number of phases in the system. In the two-phase region, the largest positive root represents the molar volume of the gas phase while the smallest root corresponds to the volume of the liquid phase. The correcting terms a and b are given as

$$a = 0.4275 \frac{R^2 T_c^{2.5}}{p_c} \quad (4.1.4)$$

and

$$b = 0.0866 \frac{RT_c}{p_c} \quad (4.1.5)$$

where T_c and p_c are Temperature and pressure at the critical point (see Tab. 4.1.1). Figs. 4.1.1 and 4.1.2 show the results of the RKEOS for several substances at four different temperatures in comparison to other equations of state.

Peng-Robinson equation of state (PREOS) D. Y. PENG and D. B. ROBINSON presented an improvement of the RKEOS in 1975 [49]. The proposed equation is also a two-constant van der Waals-Type equation and combines simplicity and accuracy. The PREOS is very simple to solve and gives satisfying results within the whole fluid region of a gas. It is given in the form

$$p = \frac{RT}{V_m - b} - \frac{a(T_c) \cdot \alpha(T_r, \omega)}{V_m^2 + 2 \cdot bV_m - b^2} \quad (4.1.6)$$

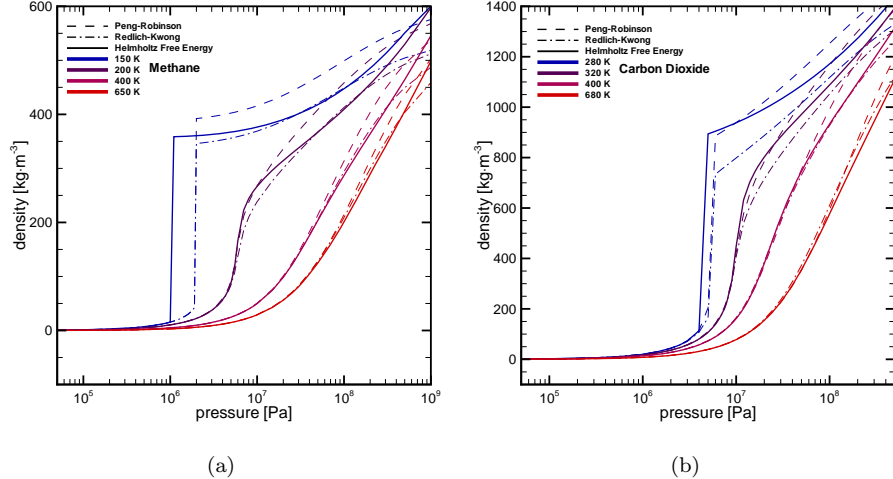


Figure 4.1.1: Density of CH₄ (a) and CO₂ (b) derived by different EOS. There stand — for the HELMHOLTZ Free Energy, - - - for the PREOS and - · - - for the RKEOS. The colours refer to different temperatures (blue - 280 K, violet - 320 K, pink - 400 K, red - 680 K).

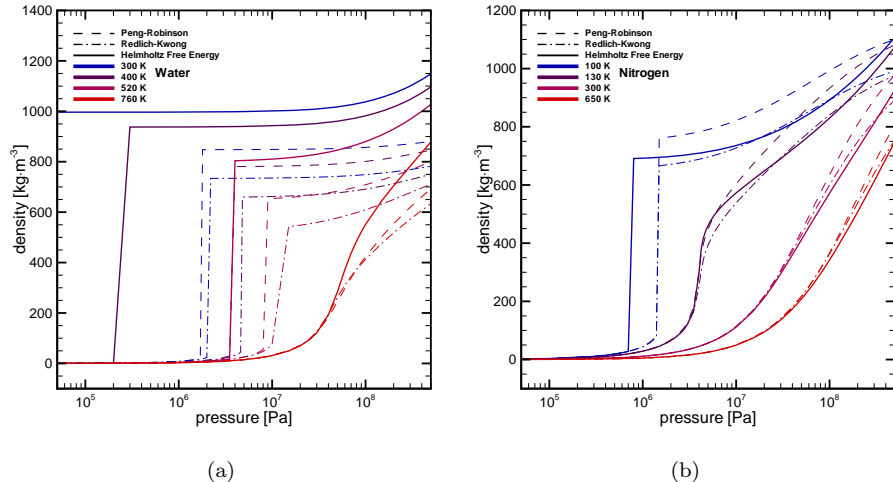


Figure 4.1.2: Density of H₂O (a) and N₂ (b) derived by different EOS. There stand — for the HELMHOLTZ Free Energy, - - - for the PREOS and - · - - for the RKEOS. The colours refer to different temperatures (blue - 280 K, violet - 320 K, pink - 400 K, red - 680 K).

where a and b are correcting terms. They can be derived by

$$a(T_c) = 0.45724 \frac{R^2 T_c^2}{p_c} \quad (4.1.7)$$

and

$$b(T_c) = 0.07780 \frac{RT_c}{p_c} \quad (4.1.8)$$

for the particular fluids under specification of pressure and temperature at the critical point. Parameter $\alpha(T_r, \omega)$ is a dimensionless function of reduced temperature T_r and acentric factor ω . It is given as

$$\alpha = (1 + (0.37464 + 1.54226 \omega - 0.26992 \omega^2) (1 - T_r^{0.5}))^2 \quad (4.1.9)$$

for $\omega \leq 0.49$ and

$$\alpha = (1 + (0.379642 + (1.48503 - (1.164423 - 1.016666 \omega) \omega) \omega) (1 - T_r^{0.5}))^2 \quad (4.1.10)$$

for $\omega > 0.49$.

Tab. 4.1.1 shows acentric factors and critical parameters for different real gases. The resulting density distribution of the PREOS is shown in Figs. 4.1.1 and 4.1.2 at four different temperatures.

Fundamental equations For highly precise results it is necessary to adapt fundamental equations based on the free energy. The HELMHOLTZ free energy is given as

$$\frac{f(\rho, T)}{RT} = \phi(\delta, \tau) = \phi^o(\delta, \tau) + \phi^r(\delta, \tau) \quad (4.1.11)$$

in dependence from density ρ and temperature T in its dimensionless form. These dimensionless parts are given as the terms $\delta = \rho/\rho_c$ and $\tau = T_c/T$, whereas ρ_c and T_c are density and temperature at the critical point (see Tab. 4.1.1). The HELMHOLTZ free energy provides relations between density, temperature and all thermodynamic properties of a fluid, which are expressed in the parameter ϕ^o as the ideal gas part and ϕ^r as the residual part. For their derivatives in the short forms like ϕ_δ^r , $\phi_{\delta\delta}^r$, ϕ_τ^r , $\phi_{\tau\tau}^r$, $\phi_{\delta\tau}^r$, ϕ_τ^o , $\phi_{\tau\tau}^o$ it is referred to [50].

Many authors used the approach of HELMHOLTZ free energy to develop EOS for different substances, e. g. :

- SPAN&WAGNER [50], [51], [52] for carbon dioxide and for nitrogen,

- PRUSS&WAGNER [53], [54] for water,
- BÜCKER&WAGNER [55] for ethane and
- SETZMANN&WAGNER [56] for methane.

The fundamental equation (4.1.11) according to WAGNER et al. ([50],[53],[55], and [56]) is one of the most precise EOS at present. The Equation and its derivatives can be used to describe all thermodynamic properties of a pure substance depending on density and temperature. So it is necessary to solve the relationship between density, pressure and temperature iteratively, as (4.1.12) shows

$$\frac{p(\delta, \tau)}{\rho RT} = 1 + \delta \frac{\partial \phi^r}{\partial \delta}. \quad (4.1.12)$$

For water, the equation became international standard for the IAPWS¹ since 1995. Certainly, the equation is complicated to solve and requires long computing time. Therefore, in the version of GeoSys (4.10.00) it is possible to choose between an iterative solving algorithm and an interpolation of density values out of a database.

The semi-empirical fundamental equation (4.1.11) has to be fitted to measurement data by computer algorithms for each substance. Depending on the fluid, there are up to 200 adjusting coefficients to ensure a very accurate fit to the real gas behaviour. For each substance, (4.1.11) has separate ranges of validity, which are shown in Tab. 4.1.2.

Table 4.1.2: Ranges of validity of the free HELMHOLTZ equation (4.1.11) for several fluids valid from the melting point up to the indicated values.

substance	T [K]	p [MPa]	reference
Carbon dioxide	216	1100	[50], [51]
Nitrogen	1000	2200	[52]
Ethane	520	30	[55]
Methane	625	1000	[56]
Water	1273	1000	[53], [54]

4.1.2 Enthalpy

The specific enthalpy h is the whole amount of energy of a fluid. It consists of the internal energy and the volume changing work. It can be expressed by deviations of the free HELMHOLTZ energy as

¹International Association for the Properties of Water and Steam

$$\frac{h(\delta, \tau)}{RT} = 1 + \tau (\phi_\tau^o + \phi_\tau^r) + \delta \phi_\delta^r. \quad (4.1.13)$$

4.1.3 Entropy

The entropy s represents which plenty of the energy of a system is potentially available to do work and which plenty of it is potentially defined as heat. In classical thermodynamics, the validity for the entropy is the thermodynamical system in equilibrium. The following equation is given for the entropy:

$$\frac{s(\delta, \tau)}{R} = \tau (\phi_\tau^o + \phi_\tau^r) - \phi^o - \phi^r. \quad (4.1.14)$$

4.1.4 Heat capacity

The specific heat capacity of a fluid is defined as the amount of heat which is needed to increase the temperature of a fluid of 1 kg by 1 K. In thermodynamics, it is distinguished between a heat capacity at constant pressure, the isobaric heat capacity, and a heat capacity at constant volume, the isochoric heat capacity. Both can be expressed in terms of free HELMHOLTZ energy, like the following equations show:

isobaric heat capacity

$$\frac{c_p(\delta, \tau)}{R} = -\tau^2 (\phi_{\tau\tau}^o + \phi_{\tau\tau}^r) + \frac{(1 + \delta \phi_\delta^r - \delta \tau \phi_{\delta\tau}^r)^2}{(1 + 2\delta \phi_\delta^r + \delta^2 \phi_{\delta\delta}^r)} \quad (4.1.15)$$

isochoric heat capacity

$$\frac{c_v(\delta, \tau)}{R} = -\tau^2 (\phi_{\tau\tau}^o + \phi_{\tau\tau}^r). \quad (4.1.16)$$

Due to the high number of adjusting coefficients, the properties based on the HELMHOLTZ free energy may be seen as very accurate. On the other hand, the iterative solution of (4.1.12) takes long computing times, so for long-term simulations or for simulations with a high number of elements, it would be better to use the VAN DER WAALS-type equations of REDLICH-KWONG or PENG-ROBINSON. These cubic equations are easy to solve and lead to results very fast. Figs. 4.1.3 and 4.1.4 illustrate, in which range of temperature and pressure those simple EOS may be used. Here, thermodynamical properties of carbon dioxide based on temperature and density are shown calculated by different EOS. In general, if temperature rises while pressure is declining, the behaviour of a fluid approaches to that of the ideal gas and the cubic equations of state

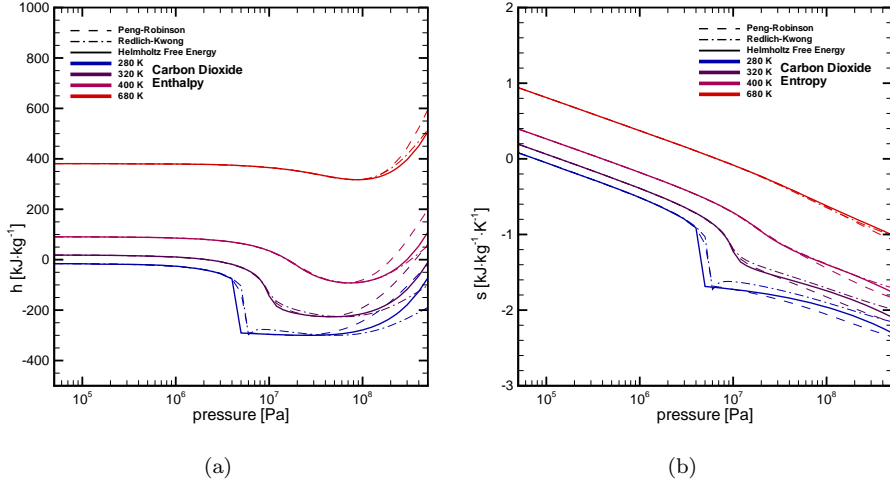


Figure 4.1.3: Enthalpy (a) and entropy (b) of CO_2 based on different EOS. There stand — for the HELMHOLTZ Free Energy, - - - for the PREOS and - · - - for the RKEOS. The colours refer to different temperatures (blue - 280 K, violet - 320 K, pink - 400 K, red - 680 K).

give suitable results. For instance, the resulting entropy and enthalpy values of carbon dioxide at low pressures and high temperatures are identical, regardless of the density model they are based on (see Fig. 4.1.3(a) and 4.1.3(b)). In the liquid and the dense supercritical region, the results based on different EOS diverge increasingly.

In addition, in the vicinity of the saturation curve, the results based on the VAN DER WAALS-type EOS may show large variations compared to the fundamental equation based curves (HELMHOLTZ free energy). Particularly, this becomes apparent from Figs. 4.1.4(a) and 4.1.4(b), where the heat capacities of CO_2 are given. The heat capacities at 400 K and 680 K (in the supercritical region of CO_2 , where no phase boundary exists) are identical, independent from according density model. Within the two-phase region at 280 K and 320 K, a strong deviation at the phase boundary can be seen.

For water, the cubic EOS are not suitable. Water is a high critical fluid, so its properties are too complex to be described by simple approaches. As we can see in Fig. 4.1.2(a), the RKEOS, as well as the PREOS equation give viable results only at pressures below 1 MPa and at high temperatures. Therefore it is recommended to use the fundamental equation of the HELMHOLTZ free energy to estimate the density of water.

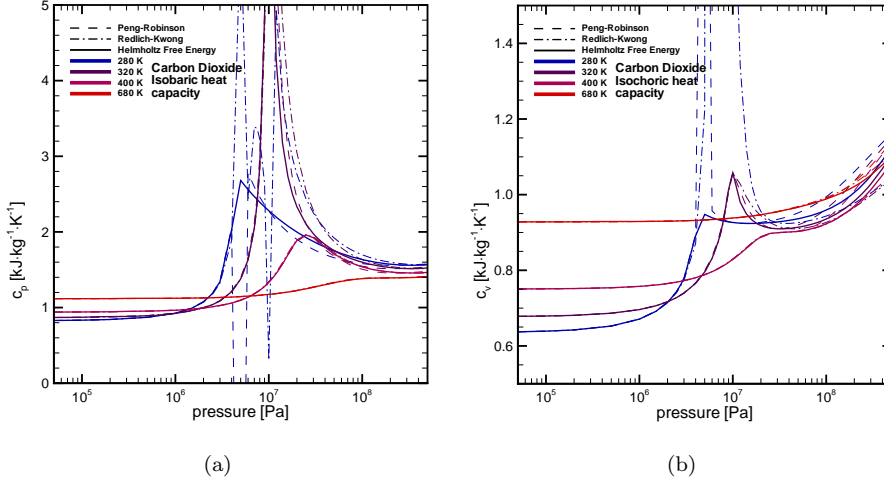


Figure 4.1.4: Isobaric heat capacity (a) and isochoric heat capacity (b) of CO_2 based on different EOS. There stand — for the HELMHOLTZ Free Energy, - - - for the PREOS and - - - - for the RKEOS. The colours refer to different temperatures (blue - 280 K, violet - 320 K, pink - 400 K, red - 680 K).

4.1.5 Viscosity

Many authors developed correlation equations for viscosity η of fluids at a density ρ and a temperature T . Those correlation equations may be composed of two or three terms, like

$$\eta(\rho, T) = \eta_0(T) + \eta_{ex}(\rho, T) \quad (4.1.17)$$

or

$$\eta(\rho, T) = \eta_0(T) + \Delta\eta(\rho, T) + \Delta\eta_c(\rho, T). \quad (4.1.18)$$

In the two-term form, the viscosity correlation consists of a zero-density limit viscosity $\eta_0(T)$ at a temperature T , and an excess contribution viscosity $\eta_{ex}(\rho, T)$ at a density ρ and a temperature T . This type of correlation function is used (among others) by FRIEND et al. [3] or STEPHAN et al. [2]. The formulation can be enhanced by a term describing the viscosity in the immediate vicinity of the critical point, $\Delta\eta(\rho, T)$ (4.1.18), as described in FENGHOUR et al. [1] or HUBER et al. [5]. An overview about the used viscosity correlations for several substances is given in Tab. 4.1.3. To show an example, Fig. 4.1.5(a) portrays the resulting viscosities for carbon dioxide based on densities of different EOS.

Table 4.1.3: Ranges of T and p validity for viscosity correlations for several substances.

substance	T [K]	p [MPa]	reference
Carbon dioxide	200–1500	≤ 300	[1]
Nitrogen	70–1100	≤ 100	[2]
Ethane	90–625	≤ 30	[4]
Methane	91–600	≤ 100	[3]
Water	273–1173	≤ 100	[5]

4.1.6 Thermal conductivity

Similar to the correlations between viscosity and T and p , the thermal conductivity λ can be expressed by an equation consisting of the following three parts (see [6]): A conductivity in the limit of zero-density $\lambda^0(0, T)$, where only two-body interaction occurs, a term $\Delta_c\lambda(\rho, T)$ which enhances the property function in the critical region of the fluid, and finally $\Delta\lambda(\rho, T)$ which represents the contribution of all other effects to the thermal conductivity at elevated densities including many-body collisions, molecular-velocity correlations and collisional transfer. This equation is

$$\lambda(\rho, T) = \lambda^0(T) + \Delta\lambda(\rho) + \Delta_c\lambda(\rho, T). \quad (4.1.19)$$

Fig. 4.1.5(b) shows the thermal conductivity of carbon dioxide at four temperatures based on different EOS. In Tab. 4.1.4 the ranges for the validity of T and p concerning thermal conductivity correlations for several substances are shown.

Table 4.1.4: Ranges of T and p validity for thermal conductivity correlations for several substances.

substance	T [K]	p [MPa]	Reference
Carbon dioxide	200–1000	≤ 100	[1]
Nitrogen	70–1100	≤ 100	[2]
Ethane	≤ 600	≤ 70	[7]
Methane	≤ 200	≤ 600	[7]
Water	≤ 800	≤ 100	[8]

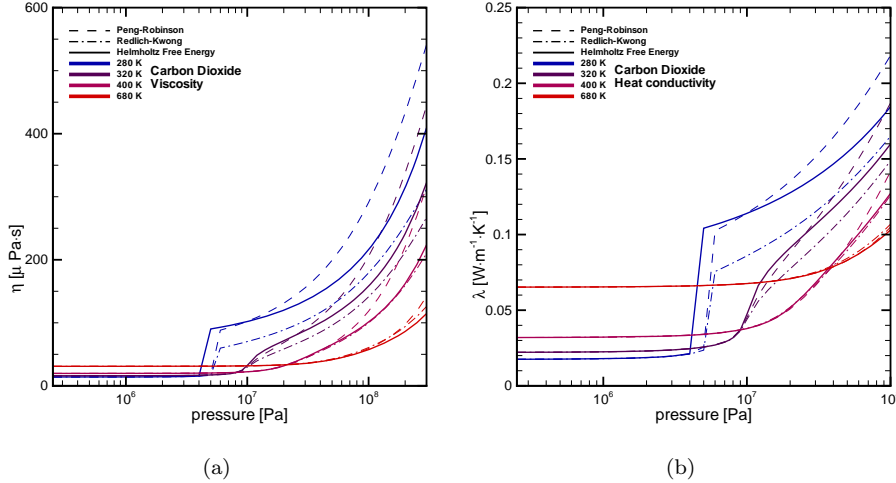


Figure 4.1.5: Viscosity (a) and thermal conductivity (b) of CO_2 based on different EOS. There stand — for the HELMHOLTZ Free Energy, - - - for the PREOS and - · - - for the RKEOS. The colours refer to different temperatures (blue - 280 K, violet - 320 K, pink - 400 K, red - 680 K).

4.2 Keywords

4.2.1 Fluid specification

The new fluid property functions are working for specific substances. So, it is necessary to specify the desired fluid in the *.MFP-file. This has the advantage, that there is no need to know or to look-up fluid properties like initial density or viscosity for a specific pressure or temperature condition. The subkeyword **\$FLUID_NAME** identifies the substance. Since GeoSys version 4.10.02, four substances are defined: CO_2 , H_2O , CH_4 and N_2 . By defining the fluid name, all necessary coefficients, parameters and critical values are called by the source code to solve the EOS and the fluid property functions.

Example: In MFP-file, write:

```
#FLUID_PROPERTIES
$FLUID_TYPE
LIQUID
$FLUID_NAME
CARBON_DIOXIDE
```

The first letter of the fluid name identifies the substance, so 'C' would be sufficient define the substance clearly as CO₂. Table 4.2.1 shows all available substances and their identifiers.

Table 4.2.1: Fluid substances and their identifiers.

Identifier	Substance
W	Water
C	Carbon dioxide
M	Methane
N	Nitrogen

4.2.2 Density model specification

With these specified substances, it is possible to choose between different equations of state, which are described in detail in section 4.1.1. In addition to former ones, a selection of new density models is available since GeoSys version 4.10.00. The referring density model identifiers are shown in table 4.2.2. These density models determine the fluid density depending on pressure and temperature. If multiple phases or components are defined, an optional argument name can be specified behind the density model identifier.

Example: (MFP-file)

```
$FLUID_NAME
CARBON_DIOXIDE
$DENSITY
12 PRESSURE_W TEMPERATURE1
```

This example sets up density model 12 (PREOS), where PRESSURE_W and TEMPERATURE1 serve as property function arguments. If the optional argument specification is omitted, the default argument names are PRESSURE1 and TEMPERATURE1. So, especially for multiphase-flow examples, the declaration of arguments can be important. For isothermal problems, it is possible to define a reference temperature behind the density model identifier.

Example: (MFP-file)

```
$FLUID_NAME
CARBON_DIOXIDE
$DENSITY
13 400 PRESSURE2
```

In this case, the temperature argument for the equation of state is a constant value of 400 K, regardless if heat transport considered or not.

Table 4.2.2: Density model identifiers

Identifier	Density model
10	Lookup-table
11	REDLICH&KWONG
12	PENG&ROBINSON
13	HELMHOLTZ free energy

4.2.3 Viscosity model specification

For viscosity, several correlation functions were presented by different authors (see section 4.1.5), but there is only one new viscosity model identified by no. 9. When viscosity model is 9, the right correlation function is chosen automatically by the fluid name (see section 4.2.1). If no fluid name is specified, the default substance will be carbon dioxide. For viscosity model 9, the same arguments as for density models 11 to 13 can be given.

Example: (MFP-file)

```
#FLUID_PROPERTIES
$FLUID_TYPE
LIQUID
$FLUID_NAME
CARBON_DIOXIDE
$VISCOSITY
9 400 PRESSURE2
```

4.2.4 Thermal conductivity model specification

The thermal conductivity correleations depending on temperature and pressure can be switched on by identifier '3'.

Example: (MFP-file)

```
$HEAT_CONDUCTIVITY
3 PRESSURE2
```

The **heat conductivity model 3** handles the same arguments as **viscosity model 9**. in section ??, the correlation functions for all implemented substances are described and referenced.

4.2.5 Compressibility model specification

Since GeoSys version 4.10.02, a fluid can be considered as compressible or incompressible due to temperature and pressure². The compressibility of a fluid depends on the slope of the density function surface (see (4.3.2) on page 85). This slope can be determined by

- a constant value
- a lookup-table
- the difference quotient
- the analytical derivation of the equation of state

or can be set to zero to treat the fluid as incompressible. In GeoSys version 4.10.02, only the constant value and the difference quotient alternatives are available. This difference quotient is a simple and fast way to approximate the slope of the density function:

$$\frac{\partial \rho_\alpha}{\partial p_\alpha} \approx \frac{\Delta \rho_\alpha}{\Delta p_\alpha} = \frac{\rho_\alpha \left(p_\alpha + \frac{\Delta p_\alpha}{2}, T \right) - \rho_\alpha \left(p_\alpha - \frac{\Delta p_\alpha}{2}, T \right)}{\Delta p_\alpha}. \quad (4.2.1)$$

A comparable equation determines the slope of the density function in terms of temperature. The compressibility model can be defined for each individual phase. The new subkeyword \$COMPRESSIBILITY requires two lines of arguments: The first line defines the fluids compressibility due to pressure, the second one the compressibility due to temperature. Each argument line has to start with the compressibility model identifier. The meaning of the second argument depends on the chosen identifier (see Table 4.2.3). The following example defines carbon dioxide as compressible due to pressure changes using a numerical approximation of its equation of state (model 3, first line); the pressure difference Δp , which is used to determine the difference quotient (see (4.2.1)) is set to 1 Pa. Furthermore, the example defines the fluid as incompressible due to temperature changes (model 0, second line).

²only in global pressure-saturation formulation

Example: (MFP-file)

```
$FLUID_NAME
CO2
$COMPRESSIBILITY
3 1
0
```

Table 4.2.3: Compressibility model identifiers

Identifier	Argument	Compressibility model
0	-	incompressible
1	$\frac{\Delta\rho}{\Delta p}$ or $\frac{\Delta\rho}{\Delta T}$	constant slope
2	-	lookup-table
3	Δp (eq. 4.2.1) or ΔT	difference quotient
4	-	analytical derivation

4.2.6 Example file

The following listing of an MFP-file defines a two-phase or a two-component scenario with H₂O and CO₂ as involved fluids.

Water is incompressible due to pressure changes, but its density depends on temperature. The chosen equation of state is the fundamental HELHOLTZ free energy equation, which is the only EOS which returns accurate density values for water, but takes long computing time. The viscosity and the thermal conductivity of water is determined by the IAPWS formulation for scientific use [5], [8]. No pressure or temperature argument names are defined for water, so the default PRESSURE1 and TEMPERATURE1 variables are used for fluid no. 1.

The example file considers carbon dioxide as compressible due to pressure and temperature, where the temperature depending density changes are approximated by a constant slope ($2.5 \text{ kg} \cdot \text{m}^{-3} \cdot \text{T}^{-1}$). CO₂ is a much less complex than water, so a simple PREOS is precise enough for density determination. For viscosity and thermal conductivity, the formulations of FENGHOUR et al. [1] are chosen. For this second fluid, the argument name PRESSURE2 has to be declared.

Example: (MFP-file)

```

#FLUID_PROPERTIES
$FLUID_TYPE
LIQUID
$FLUID_NAME
WATER
$COMPRESSIBILITY
0
3 1
$DENSITY
13
$VISCOSITY
9
$HEAT_CONDUCTIVITY
3
#FLUID_PROPERTIES
$FLUID_TYPE
GAS
$FLUID_NAME
CO2
$COMPRESSIBILITY
3 1
1 2.5
$DENSITY
12 PRESSURE2
$VISCOSITY
9 PRESSURE2
$HEAT_CONDUCTIVITY
3 PRESSURE2
#STOP

```

4.2.7 Fluid property output

Fluid properties can be written in the output-file using the subkeyword \$MFP_VALUES in *.OUT-file. This was only possible for one single phase or component. Since GeoSys version 4.10.02, it is possible to define the number of the phase, whose properties shall be given out. This can be done by writing the phase number directly behind the respective fluid property.

Example: (OUT-file)

```

$MFP_VALUES
DENSITY1
HEAT_CONDUCTIVITY1
DENSITY2
VISCOSITY2

```

This example writes density and thermal conductivity of the first, and density and viscosity of the second defined fluid into the respective output-file.

4.3 Benchmarks

4.3.1 CO₂ flow with pressure dependent density and viscosity (H-process)

Problem definition

This benchmark shows the distribution of pressure along a 1D soil profile for different fluid property models (see Fig. 4.3.1). Two wells, one injection well and one production well are placed with a distance of 400 m. CO₂ is dumped by the injection well at a pressure of 7 MPa, at the production well there is a pressure of 6.5 MPa. The temperature along the profile shall be constant at 400 K.

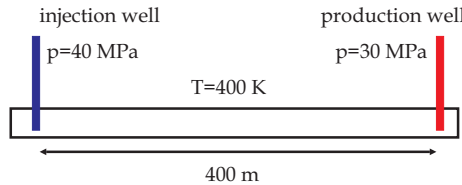


Figure 4.3.1: Problem definition

Model setup

For this case the model area is reduced to a very simple 1D problem. The mesh consists of 200 line elements with a constant length of 2 m. The injection well on the left side is represented as a constant boundary pressure of 40 MPa, the right boundary has a constant pressure of 30 MPa for the whole domain. Initial conditions are a temperature of 400 K and a pressure of 30 MPa. The used material is a porous medium with a porosity of $n_e = 10\%$ and a density of $\rho = 2500 \text{ kg m}^{-3}$.

Fluid properties

Two different cases show the influence of non linear fluid properties. A constant viscosity of $\eta = 0.001 \text{ Pas}$ in the first simulation is set. For the second simulation, the CO₂ viscosity is calculated by a constant temperature and a pressure depending density. The calculation is based on data tables with $\rho p T$ -data calculated by (4.1.11) and on the data set of $\rho p T$ -data shown in the appendix in Tabs. ?? to ??.

Results

The pressure distribution for the first simulation with the constant viscosity decreases linearly along the profile. When viscosity and density are variable values the pressure distribution curve shows a non-linear behaviour like in Fig. 4.3.2.

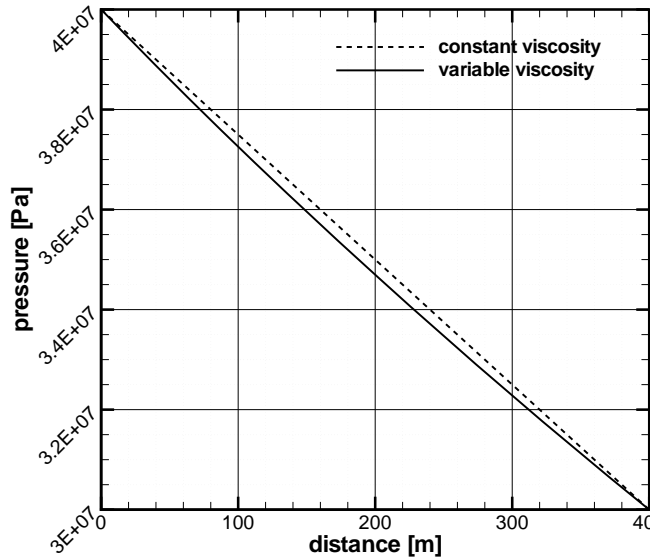


Figure 4.3.2: Pressure distribution along the soil profile

Benchmark deposit

Table 4.3.1: Benchmark location in the repository.

Benchmark	Problem type	Path in benchmark deposit
CO2-FLOW	H	benchmarks\GROUNDWATER_FLOW\CO2-FLOW

4.3.2 Non-isothermal single-phase flow of different fluids with variable fluid properties (HT-process)

Problem definition

The aim of this test case is to show the functionality of different equations of state and transport property correlations for different fluids. Because of that, the model setup from section ?? was extended by non-isothermal conditions. At the beginning of the infiltration, the residing fluid within the reservoir has a temperature of 400 K. At the point of injection, a constant temperature of 300 K is defined. During the infiltration process, the reservoir will cool down and the residing fluid will change its properties. In case of CO₂ as working fluid, there will be a phase change during the injection process regarding the CO₂ phase diagram in Fig. 4.3.3. Note that this example shows just the fluid behavior related to temperature and pressure conditions. No physically based phase change is simulated here, only the fluid property functions are tested.

This example is simulated for four different substances (CO₂, CH₄, H₂O, and N₂). For each substance, three different EOS are tested, so that this test case consists of twelve model set ups. Tab. 4.3.2 gives an overview about the used fluid property correlations.

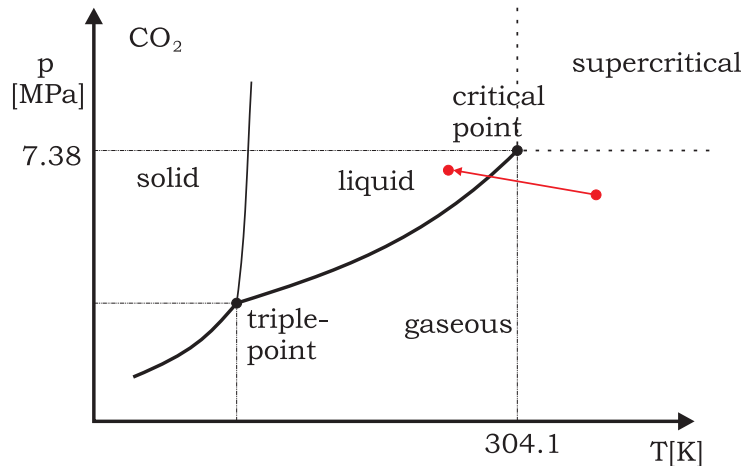


Figure 4.3.3: Phase diagram of carbon dioxide. The two extreme conditions (400 K at 6.5 MPa and 300 K at 7 MPa) are crossing a phase boundary of CO₂, so a phase change from hot gas to liquid state will be forced.

Table 4.3.2: Set-up names and referring correlation functions

working fluid	model name	density	viscosity
Methane CH ₄	CH4-RK	[48]	Friend, 1989 [3]
	CH4-PR	[49]	
	CH4-HE	[56]	
Carbon dioxide CO ₂	CO2-RK	[48]	Fenghour, 1998 [1]
	CO2-PR	[49]	
	CO2-HE	[50]	
Water H ₂ O	H2O-RK	[48]	IAPWS, 1998 [5]
	H2O-PR	[49]	
	H2O-HE	[54]	
Nitrogen N ₂	N2-RK	[48]	Stephan, 1987 [2]
	N2-PR	[49]	
	N2-HE	[52]	

Model setup

The 1D model domain of this test case consists of 200 line elements with a length of 0.5 m. There is an injection well on the left, and a production well on the right side (see Fig. 4.3.4). The thermal properties of the porous medium was all set to zero, so that no heat is stored or transported by the solid material. The fluid pressure on the left hand side (injection point) is $p = 7 \text{ MPa}$, on the right hand side the pressure is $p = 6.5 \text{ MPa}$. Tab. 4.3.3 gives an overview about the model specifications.

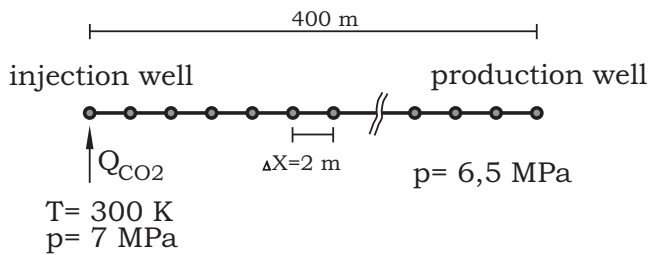


Figure 4.3.4: Model setup

Results

Fig. 4.3.5 shows the distribution of the fluid density and its viscosity after a simulation time of 50 000 seconds. At this time, the phase border has moved 175 m

Table 4.3.3: HT-benchmark specifications

parameter	symbol	value
<i>spatial discretisation</i>		
model dimension:		1D
no. of Elements:		200
length :	L	100 m
step size:	δx	0.5 m
<i>initial conditions</i>		
temperature:	T	400 K
pressure:	p	6.5 MPa
<i>boundary conditions</i>		
pressure (left):	p	7.0 MPa
pressure (right):	p	6.5 MPa
temperature (left):	T	300 K
<i>temporal discretisation</i>		
timesteps:	Δt	10 000 s
no. of timesteps:		30
total time:	t	30 000 s
<i>fluid properties</i>		
density:	ρ	simulated
viscosity:	η	simulated
heat capacity	c	$40 \text{ W}\cdot\text{m}^{-1}\cdot\text{K}^{-1}$
heat conductivity	λ	$0.06 \text{ J}\cdot\text{m}^{-1}\cdot\text{K}^{-1}$
<i>reservoir properties</i>		
thermal conductivity	λ	-
heat capacity:	c	-
density:	ρ	-

away from the injection well. At this point, the density jumps from $475 \text{ kg} \cdot \text{m}^{-3}$ down to $220 \text{ kg} \cdot \text{m}^{-3}$. The stepwise dropping of density between 175 m and 300 m is caused by the interpolation of database values. A higher resolution of density values in the database should solve this problem. The "saw teeth" and the offset between 60 m and 120 m is also caused by the interpolation, but this time the problem is deeper. Here, the interpolation takes place between liquid and gaseous density values. To solve this problem, the FCT-reading function has to be enhanced by a switch which avoids a interphase interpolation.

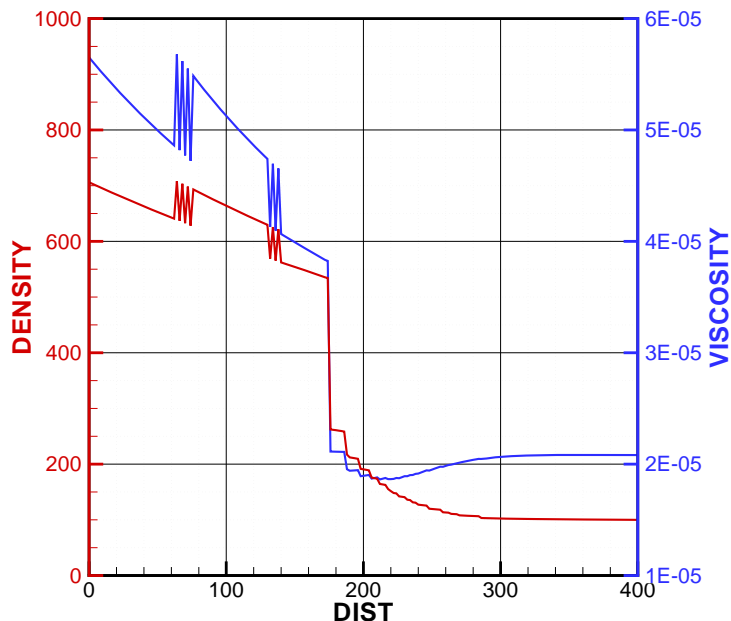


Figure 4.3.5: This is still a dummy graphic, the correct result plot follows soon...

4.3.3 Non-isothermal two-phase flow of compressible fluids (H^2T -process)

Intro

In this test case, compressible two-phase flow of real gases is considered. The transport properties of the fluids are determined by accurate constitutive correlations (see sections 4.1.5 and 4.1.6). With the chosen conditions of pressure and temperature, the gases are in a supercritical state. Using equations of state for determining the density changes due to pressure and temperature, the compressibility of the gases can be considered. This test case can be applied for simplified

CO_2 storage applications as enhanced gas recovery. CO_2 displaces methane of a depleted gas reservoir (see Fig. 4.3.6). Because of its different chemical polarities, CO_2 and CH_4 are not (completely) miscible (in supercritical state), so two-phase flow can be assumed. Pressure of carbon dioxide and saturation of methane are chosen as independent variables. Different temperatures at the injection point and within the reservoir lead to non-isothermal conditions. The test case shows the saturation development of CO_2 in the vicinity of the injection point and the resulting fluid properties of the involved substances due to pressure and temperature conditions.

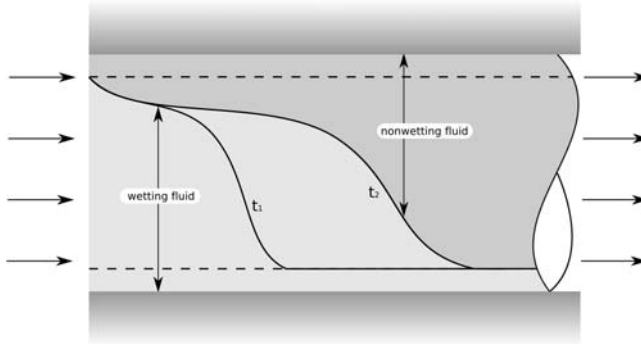


Figure 4.3.6: Schematic drawing of 1D-two phase flow problem: CO_2 is treated as a wetting fluid and displaces the non-wetting methane from the 1D-model domain.

Problem definition

Initially, a 1D gas reservoir in a depth of 3500 m is nearly fully saturated with methane at a pressure of $p_{\text{CH}_4} = 50$ bar and a temperature of $T = 400$ K. The model domain has a length of $L = 5$ m (see Fig. 4.3.7). At $x = 0$ m, CO_2 with a temperature of $T = 350$ K is pumped into the aquifer and displaces the residing methane. To show the influence of temperature to fluid properties clearly, the temperature is forced to grow linearly with the distance from the injection point. Time steps at the beginning of the simulation are very short (0.1 s), and are growing longer up to 100 s. Tab. 4.3.4 shows all relevant model specifications.

Governing equations

The governing equation for two phase flow in porous media can be written as:

$$\phi \frac{\partial S_\alpha \rho_\alpha}{\partial t} = \operatorname{div} \left(\rho_\alpha \frac{k_{r\alpha}}{\mu_\alpha} \mathbf{K} \{ \nabla p_\alpha - \rho \mathbf{g} \} \right) + \rho_\alpha q_\alpha. \quad (4.3.1)$$

Table 4.3.4: Parameters used in the H²T-benchmark test example

parameter	symbol	value
<i>spatial discretisation</i>		
element type		1D
domain length	L	5 m
element number		260
<i>temporal discretisation</i>		
timestep size	Δt	0.1 s to 100 s
timestep number		580 [-]
total time	t	10 000 s
<i>material properties</i>		
density	ρ	2500 kg·m ⁻³
<i>CO₂ properties</i>		
density	$\rho(p, T)$	PREOS [49]
viscosity	$\eta(\rho, T)$	FENGOUR [1]
thermal conductivity	λ	-
<i>CH₄ properties</i>		
density	$\rho(p, T)$	PREOS [49]
viscosity	$\eta(\rho, T)$	FRIEND [3]
thermal conductivity	λ	-
<i>initial conditions</i>		
CH ₄ saturation	S_{CH_4}	0.99 [-]
<i>boundary conditions</i>		
CH ₄ saturation	S_{CH_4}	0 [-]
CO ₂ pressure	p_{CO_2}	5.495 MPa
temperature left	T	380 K
temperature right	T	420 K
(temperature rises linearly from left to right border)		
<i>medium properties</i>		
porosity	ϕ	0.03 [-]
intrinsic permeability	\mathbf{K}	$1 \cdot 10^{-12} \text{ m}^2$
residual CO ₂ saturation	S_{r,CO_2}	0.01 [-]
residual CH ₄ saturation	S_{r,CH_4}	0 [-]
capillary pressure	$p_c(S_{\text{eff}})$	Brooks&Corey
relative permeability	$k_r(S_{\text{eff}})$	Brooks&Corey
soil distribution index	λ	2
entry pressure	p_d	5 000 Pa

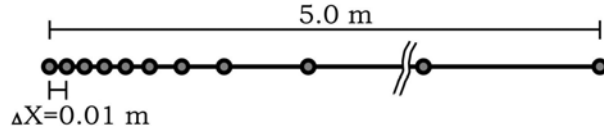


Figure 4.3.7: Model domain consisting of 1D-line elements with growing lengths.
The length of the first element (at the injectoin point) is 1 cm.

In the actual test case, no source terms are considered ($q_\alpha = 0$). Since we consider a horizontal 1D-problem, the z coordinate doesn't change, so the gravity term can be neglected as well. We also handle no changes of porosity due to deformation or precipitation, so porosity ϕ can be treated as constant. Regarding this assumptions, we can expand (4.3.1) to the following formulation:

$$\phi \frac{\partial S_\alpha}{\partial t} + \phi \frac{S_\alpha}{\rho_\alpha} \left(\frac{\partial \rho_\alpha}{\partial p_\alpha} \frac{\partial p_\alpha}{\partial t} + \frac{\partial \rho_\alpha}{\partial T} \frac{\partial T}{\partial t} \right) = \operatorname{div} \left(\rho_\alpha \frac{k_{r\alpha}(S_\alpha)}{\mu_\alpha(p_\alpha, T)} \mathbf{K} \nabla p_\alpha \right) \quad (4.3.2)$$

for both phases α . At the present state, density change due to temperature is not considered yet, so

$$\phi \frac{\partial \rho_\alpha}{\partial T} = 0, \quad (4.3.3)$$

and (4.3.2) reduces to

$$\phi \frac{\partial S_\alpha}{\partial t} + \phi \frac{S_\alpha}{\rho_\alpha} \frac{\partial \rho_\alpha}{\partial p_\alpha} \frac{\partial p_\alpha}{\partial t} = \operatorname{div} \left(\rho_\alpha \frac{k_{r\alpha}(S_\alpha)}{\mu_\alpha(p_\alpha, T)} \mathbf{K} \nabla p_\alpha \right). \quad (4.3.4)$$

The compressibility of fluids due to temperature change will be shown in one of the next benchmarks.

Constitutive equations

A general equation of state for pure substances by PENG&ROBINSON [49] was chosen to determine the densities of carbon dioxide and methane. The viscosity of both fluids is computed by correlations from Fenghour et al. [1] for CO_2 and Friend et al. [3] for CH_4 . Both density and viscosity correlations depend on pressure and temperature conditions and are described in detail in sections 4.1.1 and 4.1.5.

Results

The functionality of the fluid property functions can be evaluated by comparing the simulation results with constant fluid property models... In comparison with the H2T-McWhorter problem (20.1.6), the plume of the wetting fluid ...

Table 4.3.5: Benchmark deposit

Deposit	Version	Date
GROUNDWATER_FLOW\EOS\H2T	4.10.02	Oct. 2009

Chapter 5

Richards flow – H-Processes

5.1 Theory

5.1.1 Single continuum

Richards equations are used to describe water movement in unsaturated zone, which is the portion of the subsurface above the ground water table. Pressure p based formation, that select the unknown primary variable as p , is solved.

$$n \frac{\partial S^l}{\partial p^l} \frac{\partial p^l}{\partial t} - \nabla \cdot \left(- \frac{k_{\text{rel}}^l \mathbf{k}}{\mu^l} (\nabla p^l - \rho^l \mathbf{g}) \right) = \frac{Q_{\rho^l}}{\rho^l} \quad (5.1.1)$$

Constitutive equations are described as:

Saturation:

$$\theta = nS \quad (5.1.2)$$

$$S_{\text{eff}} = \frac{S - S_r}{S_{\max} - S_r} \quad (5.1.3)$$

Pressure:

$$p_c = -p^l \quad (5.1.4)$$

van Genuchten model

$$p_c = \frac{\rho g}{\alpha} (S_{\text{eff}}^{-1/m} - 1)^{1/n} \quad (5.1.5)$$

$$m = 1 - \frac{1}{n} \quad (5.1.6)$$

Permeability: Relationship of hydraulic conductivity and permeability:

$$\mathbf{k} = \frac{\mu}{\rho g} \mathbf{K} \quad (5.1.7)$$

van Genuchten model [van Genuchten, 1980]

$$k_{\text{rel}} = S_{\text{eff}}^{1/2} \left[1 - (1 - S_{\text{eff}}^{1/m})^m \right]^2 \quad (5.1.8)$$

Tangent approximation is applied for capacity coefficient $M = \frac{\partial S^l}{\partial p^l}$, and combined with mass-lumping matrix to reduce oscillation and improve numerical stability. Picard iteration scheme is used for nonlinear iterations.

5.1.2 Dual continua

In structured porous media the water movement can be described by dual-porosity model, which is composed by coupled Richards equations of matrix and fracture continua, respectively, which are combined by additional transfer and specific storage terms.

$$n \frac{\partial S_m^l}{\partial p_m^l} \frac{\partial p_m^l}{\partial t} - \nabla \cdot \left(\frac{k_{\text{rel}}^l \mathbf{k}_m}{\mu^l} (\nabla p_m^l - \rho^l \mathbf{g}) \right) = \frac{Q_{\rho^l m}}{\rho^l} + \frac{\Gamma^l}{w_m} \quad (5.1.9)$$

$$n \frac{\partial S_f^l}{\partial p_f^l} \frac{\partial p_f^l}{\partial t} - \nabla \cdot \left(\frac{k_{\text{rel}}^l \mathbf{k}_f}{\mu^l} (\nabla p_f^l - \rho^l \mathbf{g}) \right) = \frac{Q_{\rho^l f}}{\rho^l} - \frac{\Gamma^l}{w_f} \quad (5.1.10)$$

Relationship of preferential factors w_m and w_f is:

$$w_m + w_f = 1 \quad (5.1.11)$$

Transfer term is given as follows:

$$\Gamma^l = \alpha^* K_\alpha (p_f^l - p_m^l) R^l \quad (5.1.12)$$

The first-order exchange coefficient α^* [1/s] is derived from the properties of the fractures network, which also define the average size and form of the matrix blocks as $A^* \beta / D$, where A^* is the fracture/matrix interface area per bulk volume of rock [m^3/m^3], β is a shape factor, and D is the average fracture spacing [m](or average matrix block size). K_α is the hydraulic conductivity at the interface between fracture and matrix continua, usually define K_α as the unsaturated hydraulic conductivity of the matrix rock, because the much smaller matrix permeability is the limiting factor for fracture-matrix flow. Interface reduction factor R^l is set to the fracture liquid saturation S_f^l . The saturation of whole system is:

$$S = S_m w_m + S_f w_f \quad (5.1.13)$$

Numerical methods

There are two numerical methods used to solve dual-continua model: partitioned and monolithic, which are given as the following descriptions.

Partitioned

In the partitioned scheme, two coupled Richards equations are solved one after another: one primary variable is given as known value when the other is solved, and the system error is controlled by the first primary variable.

Monolithic

All the primary variables are assembled in one matrix and solved as unknown variables in the same time in monolithic scheme.

5.2 Single Continuum

Single continuum model is based on Eq. 5.1.12.

5.2.1 Infiltration in homogenous soil

Problem definition

This case is a numerical modelling of classical experiment of Warrick et al's(1971)[?]. The solution is Richards equation combining with uniform initial condition, fixed boundary condition without source term, and curve descriptions of homogenous media properties.

As for the dimension extension, line, triangle, quadrilateral, hexahedra, prism and tetrahedra mesh are used, and distinctions of different special discretization are presented in right of Fig. 5.2.1. Here, we present temporal evolution of the capillary pressure at the some point.

Initial and boundary conditions

The uniform initial condition in the whole domain, the saturation is 0.455, and meanwhile the pressure is -21500 Pa. Boundary condition at the top is saturated, accordingly pressure is 0, and pressure equals -21500 Pa at bottom in the simulation period. Details are illustrated in left of Fig. 5.2.1.

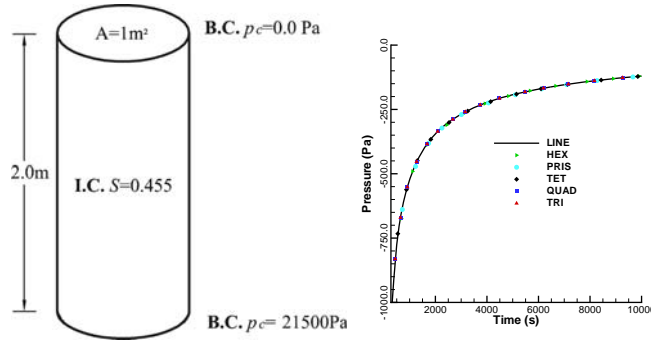


Figure 5.2.1: Illustration of numerical model and element test.

Material properties

Homogenous material properties are assumed within the whole domain. Table 5.2.1 gives the parameters.

Table 5.2.1: Parameters in simulation

items	setting
Porosity	0.38
Capillary pressure	$p(S)$ Curve in Fig. 5.2.2(l)
Relative permeability	k_{rel} Curve in Fig. 5.2.2(r)
Permeability tensor (m^2)	9.35e-12

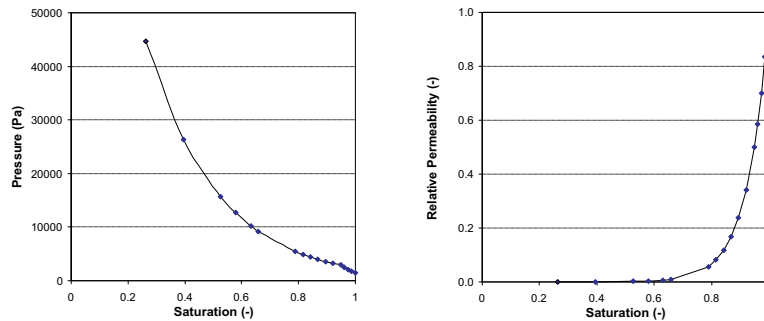


Figure 5.2.2: Relationship of capillary pressure-saturation and relative permeability-saturation

Results

Fig. 5.2.3 shows the distribution of saturation. Symbols in the Fig.5.2.3 are observations of Warrick et al's(1971)[?].

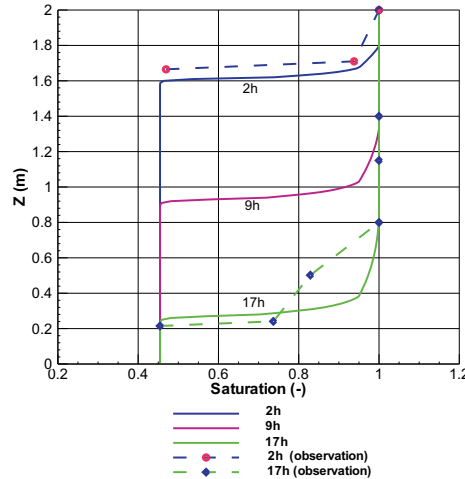


Figure 5.2.3: Saturation comparison of observed (symbol and dashed) and simulated (solid)

Fig. 5.2.4 shows the distribution of saturation by triangle and quadrilateral mesh respectively, the symbol-solid lines are 1D results. When the mesh densities are identical, the results are same; otherwise, there are distinctions.

Benchmark deposit

Benchmark	Problem type	Path in benchmark deposit
<i>h_us_line_warrick</i>	H	benchmarks\h_us\wet\
<i>h_us_quad</i>	H	benchmarks\h_us\wet\
<i>h_us_tri_freebc</i>	H	benchmarks\h_us\wet\

5.2.2 Infiltration in homogenous soil (ST/BC)

Problem definition

Numerical results compare with experimental measurements of Abeele et al.(1981). The soil column is 6m long and the diameter is 3m. The problem is defined as uniform initial condition, continuous infiltration treated as source term at top, van Genuchten homogenous material and constant mesh density.

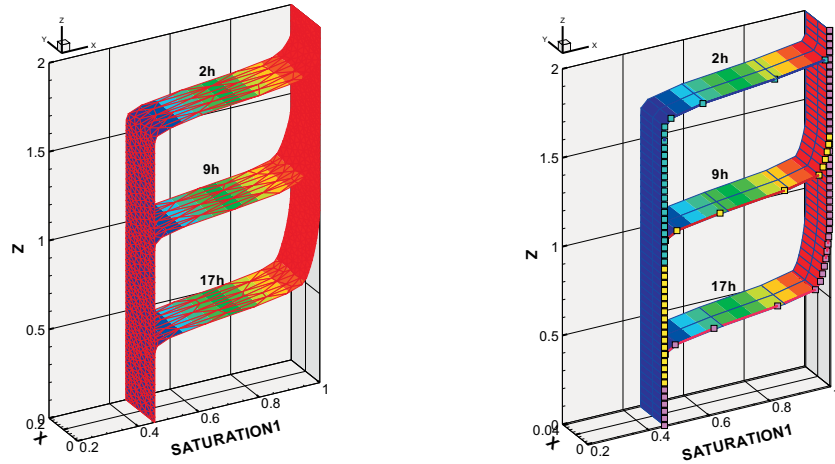


Figure 5.2.4: Saturation simulation by triangle(l) and quadrilateral (r) mesh comparison with 1D mesh (symbol-solid)

Initial, boundary conditions and source term

The initial condition of pressure is -71000pa, and continuous source term at the top is $2.314e-6$ m/s. Details are illustrated in Fig. 5.2.5.

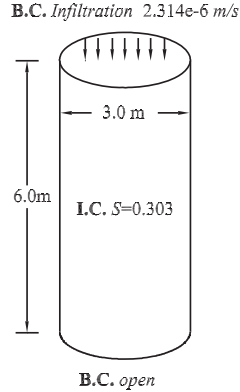


Figure 5.2.5: Illustration of numerical model

Material properties

Homogenous material properties are assumed within the whole domain. Table 5.2.2 gives the parameters.

Table 5.2.2: Parameters in simulation

Parameter	Value	Unit
Porosity	0.33	-
Saturated permeability k_s	2.95e-13	m^2
S_r^l	0.0	-
S_{max}^l	1.0	-
α	1.43	$1/m$
n	1.506	-

Results

Fig. 5.2.6 shows the distribution of saturation. Left side in Fig.5.2.6 is the result of reference [57].

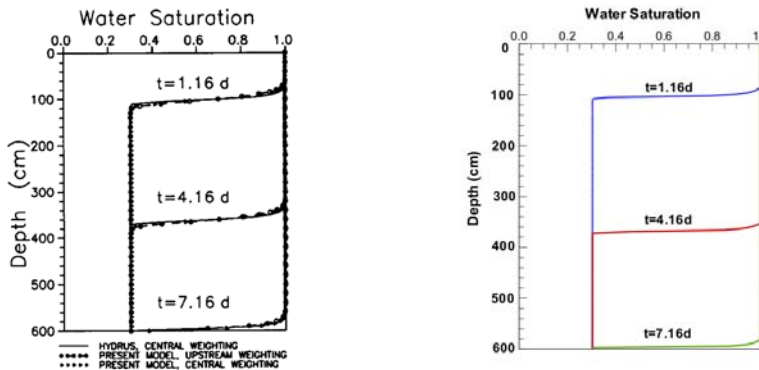


Figure 5.2.6: Saturation simulation by [57] and GeoSys

Benchmark deposit

Benchmark	Problem type	Path in benchmark deposit
<i>h_us_line_forsyth</i>	H	benchmarks\h_us\wet\

5.2.3 Infiltration in homogenous soil (BC/BC)

Problem definition

Numerical results compare with classical experimental measurements of Celia et al.(1990). The soil column is 0.6m long. The problem is defined as uni-

form initial condition in water head, fixed water head at top, van Genuchten homogenous material and constant mesh density.

Initial, boundary conditions and source term

The initial condition of pressure is -10m, and boundary conditions at top and bottom are -0.75m and -10m. Details are illustrated in Fig. 5.2.7.

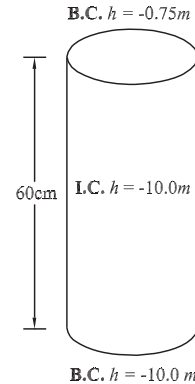


Figure 5.2.7: Illustration of numerical model

Material properties

Homogenous material properties are assumed within the whole domain. Table 5.2.3 gives the parameters.

Table 5.2.3: Parameters in simulation

Parameter	Value	Unit
Porosity	0.368	-
Saturated permeability k_s	9.35247e-12	m^2
S_r^l	0.277	-
S_{max}^l	1.0	-
α	3.35	$1/\text{m}$
n	2	-
Gravity constant g	9.807	m/s^2
Liquid density ρ	998.2	kg/m^3

Results

Fig. 5.2.8 shows the distribution of saturation. Left side in Fig.5.2.8 is the result of reference. In GeoSys/RockFlow the tangent approximation is used.

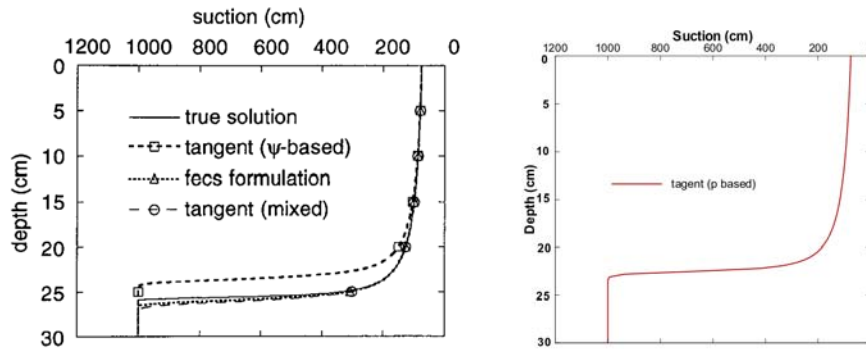


Figure 5.2.8: Suction distribution simulation by [58] and GeoSys at 6 hours

5.2.4 Transient infiltration in homogenous soil

Problem definition

This study case comes from David Kuntz in Tübingen, and it is compared with the numerical solutions of Min3P. It is a 0.25 length soil column with an artificial transient water discharge at top. Three points are selected at different location of the column, and the saturation evolution are presented. The description of model is shown in Fig. 5.2.9.

Initial, boundary conditions and source term

The initial condition is set by restart file. Artificial transient infiltration source term at top instead of boundary condition,which is shown in Fig. 5.2.10. Fixed boundary condition at bottom as pressure equal -31800Pa.

Material properties

Homogeneous material is defined by van Genuchten parameters and Table 5.2.4 gives the parameters.

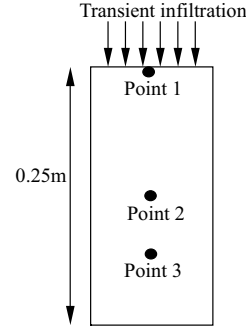


Figure 5.2.9: Illustration of numerical model

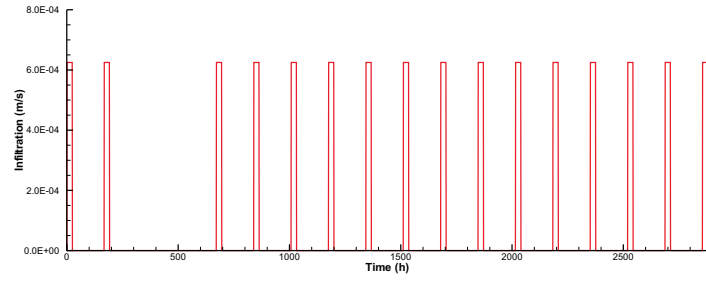


Figure 5.2.10: Discharge serial at the top

Table 5.2.4: Parameters in simulation

Parameter	Value	Unit
Porosity	0.406	-
Saturated permeability k_s	9.35247e-12	m^2
S_r^l	0.056	-
S_{max}^l	1.0	-
α	4.56	$1/m$
m	0.254	-
Gravity constant g	9.8	m/s^2
Liquid density ρ	1000	kg/m^3

Results

The vertical distributions of saturation at some moments are shown in Fig.5.2.11.

Three points, which locate at (0,0,0.25),(0,0,0.10) and (0,0,0.05) respectively, are selected to see the time evolution of saturation and compare with those by

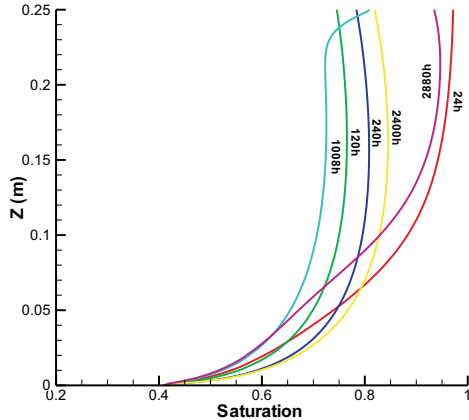


Figure 5.2.11: Saturation distributions

Min3p. Fig.5.2.12 shown the results.

Benchmark deposit

Benchmark	Problem type	Path in benchmark deposit
Transient	H	benchmarks\h_us\wet\

5.2.5 Nonuniform IC of heterogenous soil column (-/BC)

Problem definition

The case is from DECOVALEX. Heterogenous horizontal soil column starts at nonuniform status, and results show the interruptions at the interface of two material.

Initial and boundary conditions

Heterogeneous initial condition setting is loaded by restart file, and fixed boundary condition is at the end. Details are illustrated in Fig. 5.2.13.

Material properties

The heterogeneous soil column consists of two kinds material: bentonite and rock. The van Genuchten parameters of rock are shown in Tab.5.2.5, and as for

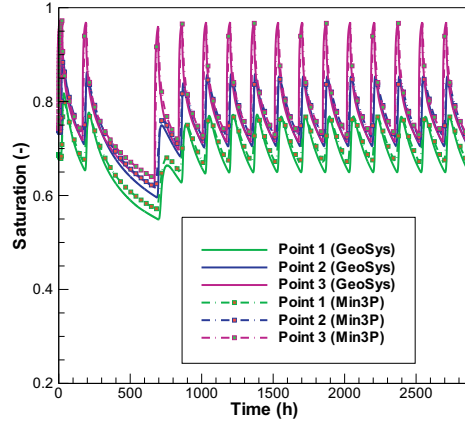


Figure 5.2.12: comparison of saturation time evolutions three points

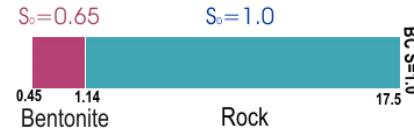


Figure 5.2.13: Illustration of numerical model

bentonite the curves in Fig. 5.2.14 are used in the simulation.

Table 5.2.5: Parameters in DECOVALEX

Parameter	Rock	Bentonite	Unit
Porosity	0.41	0.01	-
Saturated permeability k_s	1.03e-17	2.0e-21	m^2
S_r^l	0	-	-
S_{max}^l	1.0	-	-
α	6.673	-	$1/m$
n	0.6	-	-

Results

Fig. 5.2.15 shows the distribution of saturation and pressure.

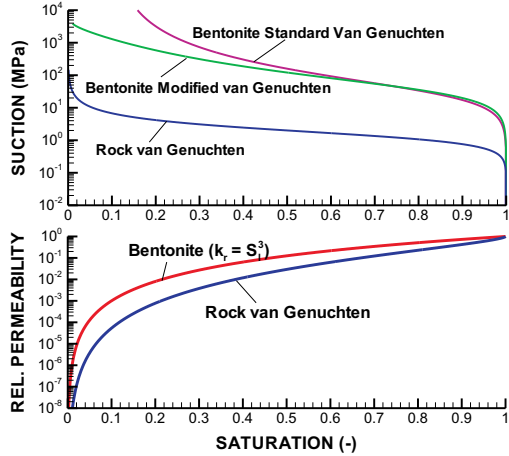


Figure 5.2.14: Characteristic Curves for bentonite and granite rock

Benchmark deposit

Benchmark	Problem type	Path in benchmark deposit
1d_ho	H	benchmarks\h_us\wet\

5.3 Dual continua

Dual continua model is based on Eq. 5.1.9 and 5.1.10.

5.3.1 Comparison with S1D

Problem definition

The simple case is defined by Vogel (2007)[59]. Numerical results compare with HYDRUS for single continua and S1D for dual continua model.

Initial and boundary conditions

The initial conditions for both matrix and fracture continuum are identical as a gradient pressure distribution, which are $p_{top}^l = -27440Pa$ and $p_{bottom}^l = -21560Pa$. The boundary conditions for both continua are also identical as fixed BC at top $p_{top}^l = 98Pa$ and free drainage at bottom. Details are illustrated in Fig. 5.3.4.

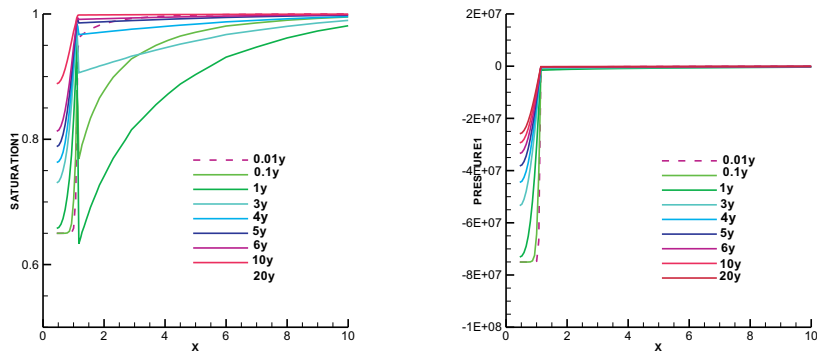


Figure 5.2.15: Saturation and pressure distribution

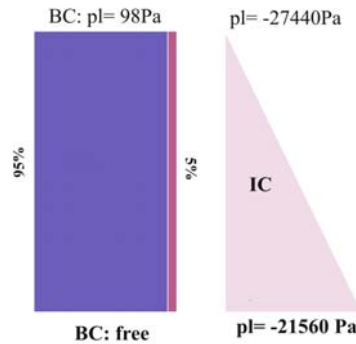


Figure 5.3.1: Illustration of numerical model

Material properties

Table 5.3.1 gives the parameters

Table 5.3.1: Parameters in simulation

Soil type	Items	Setting
Matrix continuum	Preferential factor	0.95
	Porosity	0.498
	S_r^l	0.0
	S_{max}^l	1.0
	$\alpha (1/m)$	1.8
	n	1.8
	Saturated permeability($1/m^2$)	2.32368E-13
Fracture continuum	Preferential factor	0.05
	Porosity	0.6
	S_r^l	0.0833
	S_{max}^l	1.0
	$\alpha (1/m)$	5.6
	n	2.68
	Saturated permeability($1/m^2$)	1.09000E-11
Transfer	Transfer coefficient($1/m^2$)	500

Results

Fig. 5.3.2 shows the pressure distribution comparison of single continuum at the time of 20 min and 30 min, which are calculated by GeoSys/RlockFlow (lines) and HYDRUS (symbols) respectively. The solid lines are pressure fronts of matrix, and the dash lines are fracture. The comparisons of dual-continua model results are shown in Fig. 5.3.3. The blue lines are the outcomes without transfer term, and the red lines by GeoSys/RockFlow and symbols by S1D show the exchange effects within two continua. Since matrix continuum is the dominant part in whole system, and the influence on matrix is less than that on fracture.

Benchmark deposit

Benchmark	Problem type	Path in benchmark deposit
<i>dual_vl</i>	H	benchmarks\h_us\dual\

5.3.2 Classic case: Gerke. etc

Problem definition

The section is a dual continua model comparison of GeoSys/RockFlow with the paper work of Gerke(1993)[60].

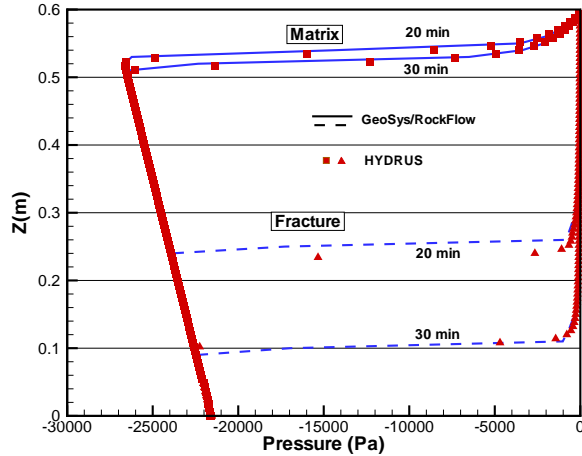


Figure 5.3.2: Pressure comparison of two single continua

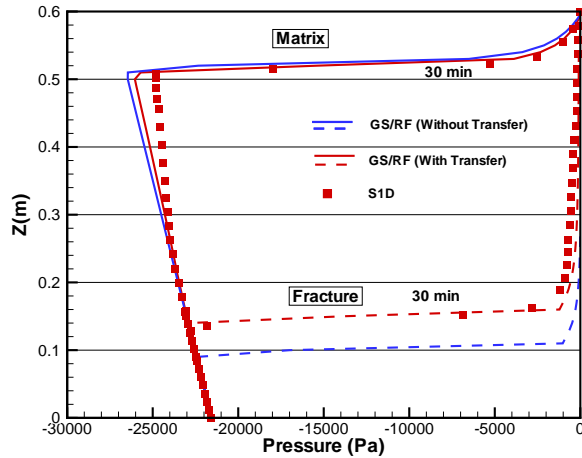


Figure 5.3.3: Pressure comparison of DPM

Initial and boundary conditions

The initial conditions for both matrix and fracture continuum are identical, which are set as $h_m^l = h_f^l = -10m$ and $p_m^l = p_f^l = -9800Pa$ in GeoSys/RockFlow. The infiltration exclusively goes into the fracture pore part, matrix continuum gets water from transfer. Details are illustrated in Fig. 5.3.4.

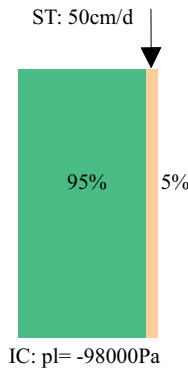


Figure 5.3.4: Illustration of numerical model

Material properties

Table 5.3.2 gives the parameters

Table 5.3.2: Parameters in simulation

Soil type	Items	Setting
Matrix continuum	Preferential factor	0.95
	Porosity	0.5
	S_r^l	0.21052
	S_{max}^l	1.0
	α (1/m)	0.05
	n	1.5
	Saturated permeability(1/m ²)	1.2419E-14
Fracture continuum	Preferential factor	0.05
	Porosity	0.5
	S_r^l	0.0
	S_{max}^l	1.0
	α (1/m)	5.6
	n	10
	Saturated permeability(1/m ²)	2.3596E-11
Transfer	Transfer coefficient(1/m ²)	$0.01 \times 0.5[K(p_m) + K(p_f)]$

Results

Fig. 5.3.5 shows simulated pressure and saturation profiles during infiltration at some time steps.

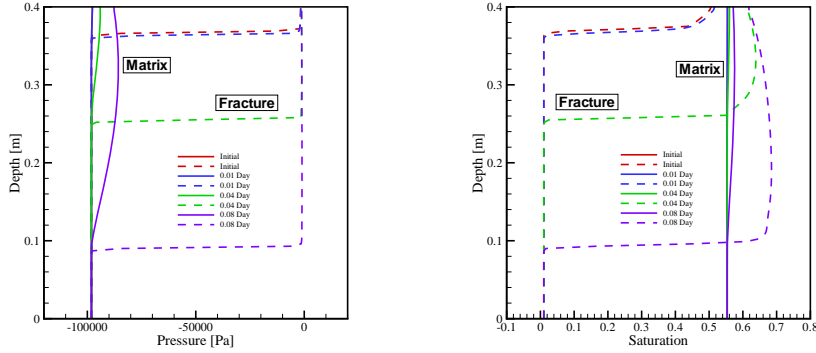


Figure 5.3.5: Simulated pressure and saturation profiles of the matrix (solid lines) and fracture (dashed lines)

Benchmark deposit

Benchmark	Problem type	Path in benchmark deposit
<i>dual_van</i>	H	benchmarks\h_us\dual\

5.3.3 Discussion

The pressure evolution of fracture continuum in 5.3.1 calculated by GeoSys/RlockFlow is a little slower than that by HYDRUS.

The distributions of saturation and pressure in 5.3.2 are different from the paper. The saturation of fracture is $S \in [0, 0.05]$ in [60].

5.4 Regional soil model

Problem definition

For the large scale area, soil represent significant diversification of moisture content with respect to the meteorologic changing such as precipitation and evapotranspiration as well as its physically-based continuum mechanics. Coupled hydrologic model with global climate model (GCM) is developed to research the impact of climate variabilities to vadose zone. The responses and water budget of alterations in timing and distribution of precipitation on the unsaturated zone are focused on by deterministic physically-based RSM, which is flexible and adaptable to extent one dimensional vertical column to three dimensional

spatial area according to the heterogenous characteristics of climatological conditions, soil properties, geographic elevation, which is shown in Fig.5.4.1.

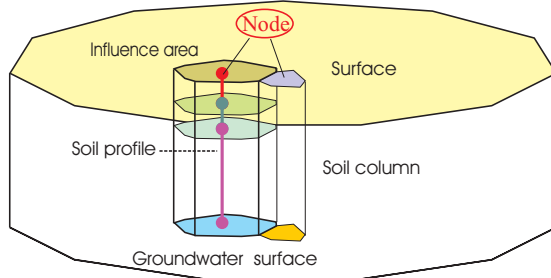


Figure 5.4.1: Concept of regional soil model

Initial and boundary conditions

Initial condition in the whole domain is set as: $P^l = -9000.0 \text{ Pa}$, and the top BC is set as pure infiltration serial in 2000 year in Beerze-Reusel basin, which is described by functions (FCT).

Material properties

The soil materials are from Beerze-Reusel drainage basin. There are several different soil types representing sand, loam and peat soils formed during the pleistocene, and those soil compose 5 kinds of soil profile type, which are defined the vertical structure of soil column. The soil water characteristic curves (SWCC) are given to describe the different soil properties (Fig. 5.4.2, left), for complete SSWC descriptions for the investigation area can be found in [61].

Results

The saturation evolutions of selected soil columns are shown in Fig. 5.4.2 (right).

Benchmark deposit

Benchmark	Problem type	Path in benchmark deposit
AT_5	H	benchmarks\h_us\RSM

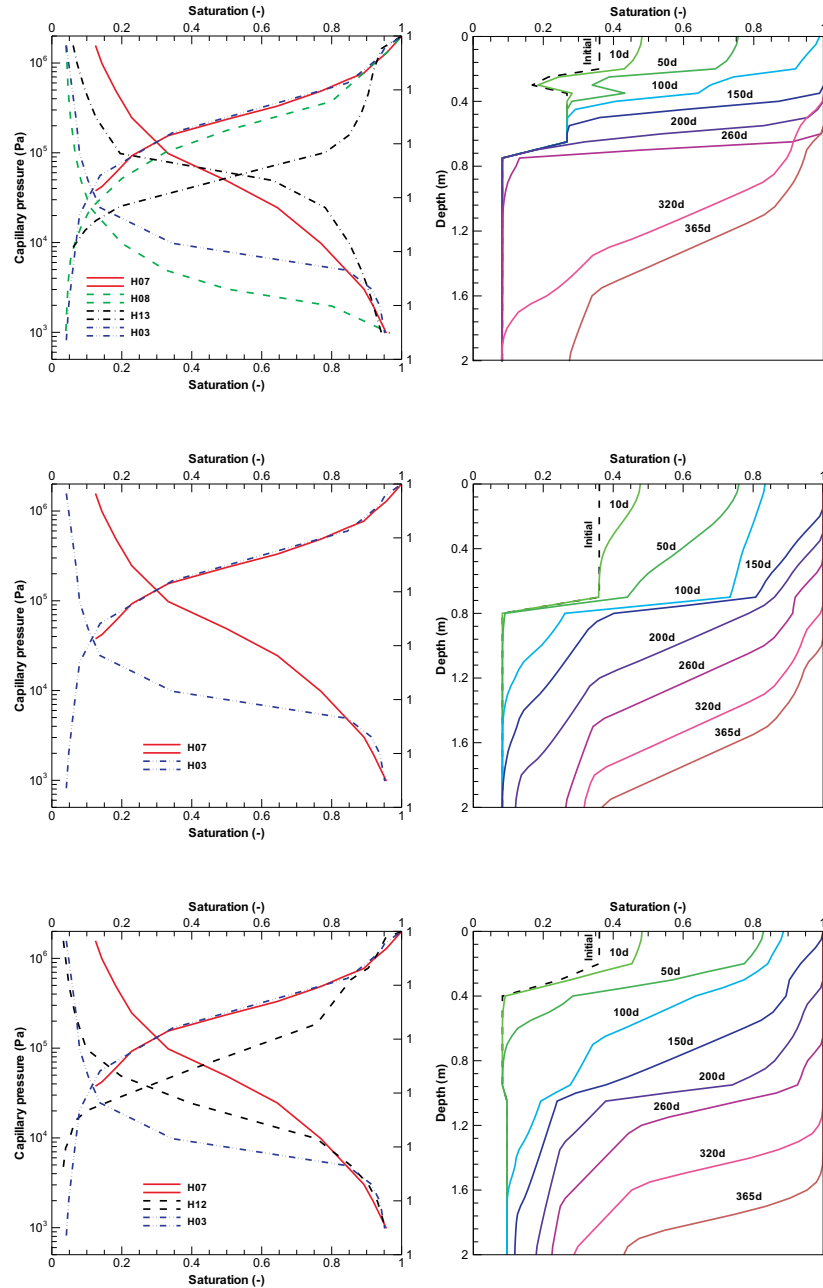


Figure 5.4.2: Soil water characteristic curves (SWCC) (left) and time evolution of water saturation in selected soil columns (right)

Chapter 6

Surface Flow – H-Processes

This chapter deals with surface flow. Surface flow or overland flow is a thin sheet of water flow which occurs when soil is infiltrated to full capacity and excess water, from rain, snowmelt, or other sources flows over the land. Generally, it causes a gathering of the runoff into discrete stream channels. The governing equations are introduced in Sec. 6.1 and the benchmarks in Sec. 6.2. Surface flow is solved one- and two-dimensionally in the benchmark examples.

6.1 Theory

Overland flow can be described by the diffusive and kinematic wave approximations of the Saint-Venant equations. The diffusive wave equation [62] is given by

$$\phi_a \frac{\partial H_a}{\partial t} + \bar{\nabla} \cdot (H \mathbf{q}) = q_s \quad (6.1.1)$$

where surface water depth H_a is used as a primary variable in the overland flow calculation, H is the mobile water depth, $\bar{\nabla}$ is two-dimensional Nabla-Operator and q_s is the source/sink term. $0 \leq \phi_a(H_a) \leq 1$ is the surface porosity which is unity for flow over a flat plane and varies between zero and unity for flow over an uneven surface. Surface roughness is parameterized with the immobile water depth a such that the surface water depth is given by $H_a = H + a$ (see Fig. 6.1.1).

Empirical resistance to flow relationships leads to [63]

$$\mathbf{q} = -\frac{CR^l}{S_s^{1-j}} \bar{\nabla} h \quad (6.1.2)$$

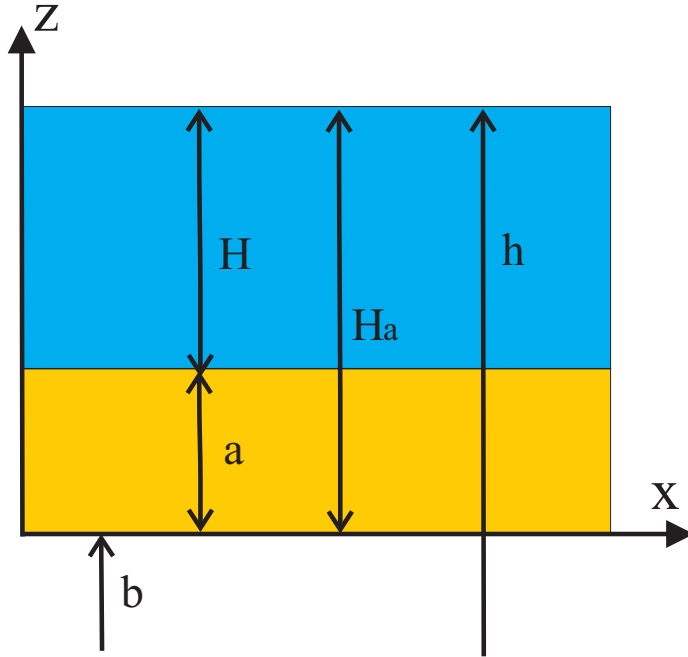


Figure 6.1.1: The diagram for the relationships of surface water depth, mobile/imobile water depth and surface water head

where

$$S_s = \left[\left(\frac{\partial h}{\partial x} \right)^2 + \left(\frac{\partial h}{\partial y} \right)^2 \right]^{1/2} \quad (6.1.3)$$

where h is the surface water head and given by $h = H_a + b$ where b is the bottom elevation. For overland flow, the resistance to flow relationship considers only the bottom friction such that the hydraulic radius is given by $R = H$.

The surface bottom friction parameters C , j , l are evaluated from the Darcy-Weisbach relationship. The turbulent Chézy relationship is obtained with $j = l = 1/2$ and $C = C_t$ is the Chézy coefficient. Correspondingly, $j = 1$, $l = 2$ can lead to the laminar Chézy relationship. $j = 1/2$, $l = 2/3$ and $C = 1/n$ can lead to the Manning relationship, where n is Manning coefficient.

For one-dimensional description of rivers, Eq. 6.1.2 becomes [64]

$$\mathbf{q} = -\frac{CR^l}{|\partial h/\partial x|^{1-j}} \frac{\partial h}{\partial x} \quad (6.1.4)$$

where the hydraulic radius R is determined by the flow cross-section A_F and the wetted perimeter P , i.e. $R = A_F/P$.

For overland flow, the source/sink term is given by $q_s = q_p - q_d$, where q_p is the precipitation rate, and outflow at the lower boundary q_d is determined by normal depth, or critical depth.

$$q_d^{norm} = CS_o^j H^l \quad (6.1.5)$$

$$q_d^{crit} = \sqrt{gH^3} \quad (6.1.6)$$

The infiltration source-terms can be calculated with the Green-Ampt model.

$$q_d^{GA} = K \left(\frac{H - \Psi}{\tilde{a}} \right) \quad (6.1.7)$$

where K is the effective hydraulic conductivity, Ψ is the effective capillary drive, and \tilde{a} is the location of the wetting front.

6.2 Benchmarking examples

6.2.1 One-dimensional precipitation runoff

Problem definition

These examples are based on the study by [65] which compared solutions given by the Saint-Venant equations and its diffusive wave and kinematic wave approximations. The simulation parameters are given by [62]. Constant precipitation is applied for 4min to an initially dry plane with a length of 100m and a slope of 0.01 . The flow is assumed to continue uniformly at the lower domain boundary.

Initial and boundary conditions

The initial water depth is $1 \cdot 10^{-4}\text{m}$. The precipitation value is $4 \cdot 10^{-3}\text{m/s}$. A normal depth boundary condition is assigned to the outlet and no-flow to the remaining boundary.

Material properties

The time step size is 1s . The domain is discretized with line or quadrilateral elements. The line elements have a length of approximately 1m throughout and the quadrilaterals $1\text{m} \times 1\text{m}$. For bottom friction Manning's relationship is used. Simulation parameters and fluid characteristics are given in Tab. 6.2.1.

Table 6.2.1: Parameters and fluid characteristics for one-dimensional precipitation runoff examples

Parameter	Symbol	Setting	Unit
Manning coefficient	n	5.48×10^{-2}	$s/m^{1/3}$
Immobile depth	a	0	m

Results

A comparison of GeoSys with Hydrosphere and MODFLOW-Surface as well as solutions with the Saint-Venant and kinematic wave equations are shown in Fig. 6.2.1

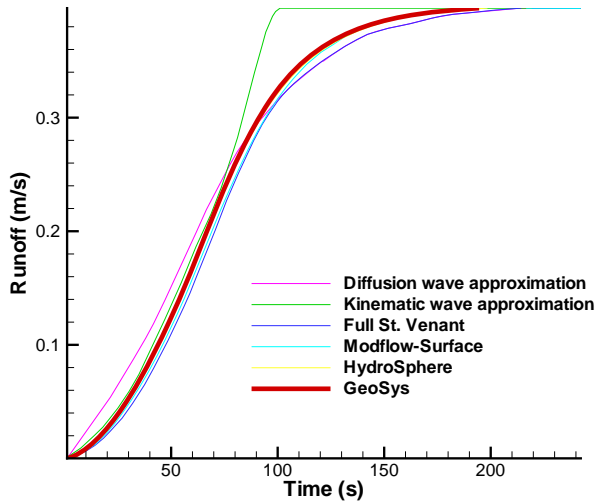


Figure 6.2.1: Results for one-dimensional precipitation runoff examples

Benchmark deposit

Benchmark	Problem type	Path in benchmark deposit
<i>govin_line</i>	H	benchmarks\OVERLAND_FLOW\
<i>govin_quad</i>	H	benchmarks\OVERLAND_FLOW\

6.2.2 Two-dimensional precipitation runoff

Problem definition

These examples are based on the study by [66] and consider two-dimensional surface flow on a V-catchment subject to constant precipitation for 90min and no-precipitation for additional 90min. At the catchment base the surface roughness is reduced to generate a channel region. At the channel outlet the water is leaving free-falling. Because of symmetry the computational domain involves only one half of the catchment which is a hillslope with the size of 1000m × 800m.

Initial and boundary conditions

The initial water depth is $1 \cdot 10^{-4} m$ and the precipitation $3 \cdot 10^{-6} m/s$. At the channel outlet a critical depth boundary condition and at the residual boundary no-flow is assigned.

Material properties

The domain is discretized with quadrilateral and triangular elements. Former have a size of $100m \times 100m$ and $10m \times 100m$ at the channel region. Triangles are generated by cutting the quadrilaterals into halves. Friction is described by Manning's relationship. The parameters are given in Tab. 6.2.2.

Table 6.2.2: Parameters for two-dimensional precipitation runoff examples

Parameter	Symbol	Setting	Unit
Manning coefficient	n	1.5×10^{-2}	$s/m^{1/3}$
Immobile depth	a	0	m

Results

Results of GeoSys, Hydrosphere and a semianalytical solution are compared in Fig. 6.2.2

Benchmark deposit

Benchmark	Problem type	Path in benchmark deposit
<i>gian_tri</i>	H	benchmarks\OVERLAND_FLOW\
<i>gian_quad</i>	H	benchmarks\OVERLAND_FLOW\

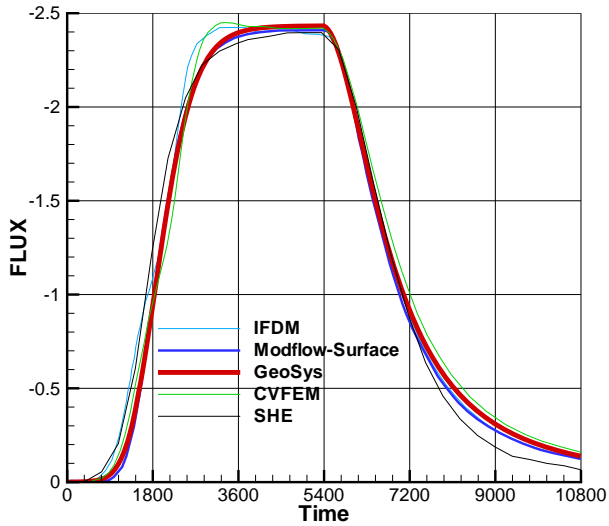


Figure 6.2.2: Results for two-dimensional precipitation runoff example

6.2.3 Infiltration excess (Horton) overland flow

Problem definition

This example is based on the soil flume experiments by [67]. The computational domain consists of an inclined plaine with a length of $12.2m$, a width of $0.051m$ and a slope of 0.01 . Light oil was applied on initially drained sand and generated Horton overland flow. Infiltration is calculated by the Green-Ampt approach for homogeneous soil. The simulation time is $900s$. Sec. 13.2.1 deals with simulations of the experiments by [67] with overland/soil flow coupling.

Initial and boundary conditions

The initial water depth is 1×10^{-6} . Precipitation of $6.944 \times 10^{-5} m/s$ and the Green-Ampt source term are imposed on the surface. A critical depth boundary condition is assigned at outlet and no-flow at the remaining boundary.

Material properties

For discretization a string of quadrants with a length of $12.2cm$ is used and a time step of $2s$. For bottom friction the laminar Chézy relationship is used. Fluid, surface structure, friction, and infiltration parameters are given in Tab. 6.2.3.

Table 6.2.3: Parameters for Horton overland flow simulation

Parameter	Symbol	Setting	Unit
Kinematic viscosity	ν	1.47×10^{-3}	m^2/s
Density	ρ	755.6	kg/m^3
Laminar Chézy coefficient	C	430000	$1/ms$
Immobile depth	a	1×10^{-3}	m
Conductivity	K	2.3×10^{-5}	m/s
Effective capillary drive	Ψ	0.13	m

Results

The outflow hydrograph by GeoSys is compared with the experimental data in Fig. 6.2.3.

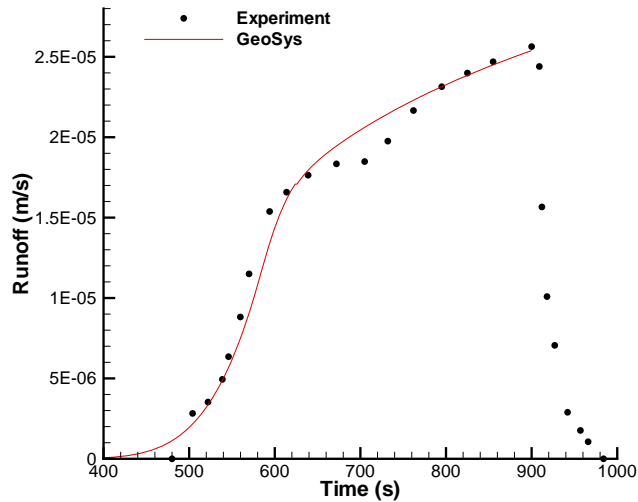


Figure 6.2.3: Measurements and simulation results by Geosys for the outflow hydrograph in the Horton overland flow example

Benchmark deposit

Benchmark	Problem type	Path in benchmark deposit
Wool_quad	H	benchmarks\OVERLAND_FLOW\

Chapter 7

Gas flow

7.1 Isothermal compressible flow - H process

The subject of this chapter is the movement of gases in porous media. In contrast to groundwater hydraulics, gas flow is more complicated because of its compressibility. Significant variations in air density and viscosity can result also from temperature fluctuations (so-called Klinkenberg effect). According to the kinetic theory of gases, its viscosity should not depend on the pressure. This is not necessarily the case for conditions typically existing in natural gas reservoirs [68]. At a fixed temperature, the viscosity of gas can vary by tens of percents as the formation pressure changes by a few Mega Pascale. Another problem concerns the evidence of turbulent flow which results in additional friction effects. The present verificational study is constrained to isothermal gas flow, where analytical solutions exist. Non-isothermal effects are considered in section 7.2. Simulation of compressible flows in porous media is necessary for different applications such as air movement in soils, gas production or CO₂ storage if carbondioxide is injected in a gaseous state.

7.1.1 Theory

The theory of gas seepage was developed first by [69], [70], and [71], who worked out a number of analytical approximations to solve the nonlinear problem. To this end, a number of general assumptions must be introduced, e.g. gravitational forces are neglected, no phreatic surfaces are formed, and idealized material properties must be assumed. The state of the compressible fluid within a considered closed system may be isothermal (const. temperature), adiabatic (const. heat content), or polytropic (const. change of heat content). The equation of gas flow in a porous medium can be derived from the mass balance of fluid (gas)

mass

$$\frac{\partial n\rho}{\partial t} + \nabla \cdot (\rho n\mathbf{v}) = Q_\rho \quad (7.1.1)$$

where ρ is gas density, \mathbf{v} is velocity vector, n is porosity and Q_ρ is a fluid mass density source/sink term. The equation of state for an ideal gas (7.1.2) represents its compressibility and expansivity due to pressure and temperature changes, respectively.

$$\rho = \frac{p}{R_{\text{air}} T} \quad (7.1.2)$$

where p is gas pressure, R_{air} is the specific gas constant which is for air is equal to 287 J/(kgK) and T is temperature in Kelvin. Therefore, the ideal gas density at atmospheric pressure and $T = 293 \text{ K}$ is

$$\rho = \frac{101325 \text{ Pa}}{287 \text{ J/(kgK)} 293 \text{ K}} = 1.20433 \frac{\text{kg}}{\text{m}^3} \quad (7.1.3)$$

For isothermal flow, i.e. $T = T_0$ we have

$$n \frac{\partial p}{\partial t} + \nabla \cdot (pn\mathbf{v}) = R_{\text{air}} T_0 Q_\rho \quad (7.1.4)$$

In addition with the momentum balance equation, which can be expressed in form of an extended Darcy's law for non-linear flow.

$$n\mathbf{v} = -\frac{\mathbf{k}}{\mu} \nabla p \quad (7.1.5)$$

where \mathbf{k} is permeability tensor, μ is fluid viscosity, the gas mass balance equation reads as

$$n \frac{\partial p}{\partial t} - \nabla \cdot (p \frac{\mathbf{k}}{\mu} \nabla p) = R_{\text{air}} T_0 Q_\rho \quad (7.1.6)$$

which is a non-linear equation with respect to gas pressure p .

7.1.2 Examples

Two test examples for isothermal gas flow are presented. The first test case is dealing with 1-D compressible flow in a porous media where an analytical solution exists for the steady state (sec. 7.1.2). The second example shows the advantages of object-orientation in finite element implementation (sec. 7.1.2).

Compressible flow test

We consider a simple 1-D test example where gas is injected at constant pressure into the porous medium. The material parameters are summarized in Tab. 7.2.1.

Property	Symbol	Value	Unit
Model length	L	100	m
Cross section area	A	1	m^2
Porosity	n	0.35	—
Permeability	k	2.7×10^{-11}	m^2
Gas dynamic viscosity	μ	1.76×10^{-5}	$Pa\ s$
Initial condition	p_I	101325	Pa
Boundary conditions	p_1, p_2	$101325, 3 \times 10^6$	Pa
Time step	Δt	$1, 10, 10^2, 10^3, 10^4$	s
Space step	Δx	1	m

Table 7.1.1: Model parameters

For isothermal flow with Dirichlet boundary conditions, i.e. $p(0, t) = p_1$ and $p(100, t) = p_2$, there exists an analytical solution,

$$p(x) = \sqrt{(p_2^2 - p_1^2) \frac{x}{x_2 - x_1} + p_1^2} \quad (7.1.7)$$

which is used for verification of the present numerical solution. Fig. 7.1.1 shows the comparison of present numerical solution with analytical. Steady state is reached after about 1.0×10^4 s.

According to Darcy's law (7.1.5) the volumetric gas flux at reference conditions can be approximated as follows

$$Q_0 = A \frac{T_0}{T^* p_0} \frac{k}{\mu} \frac{(p_2^2 - p_1^2)}{2(x_2 - x_1)} \quad (7.1.8)$$

Benchmark repository

Problem type	Repository path	Files	Version
H_GAS	benchmarks\h_gas\gas_flow	h_gas_line	4.10.07

Element test

This example is presented first of all for code verification of all element types implemented, i.e. lines, triangles, quads, tetrahedra, triangle prisms and hexahedra [72]. We consider a non-linear problem, flow of a compressible fluid through the porous medium. In this case the hydraulic conductivity is pressure dependent.

The discretizations with different element types is shown in Fig. 7.1.2. The initial gas pressure distribution is equal to $1.01325 \times 10^5\ Pa$, everywhere in the model domain. There are Dirichlet boundary condition set at left $p^g(x = 0m)$

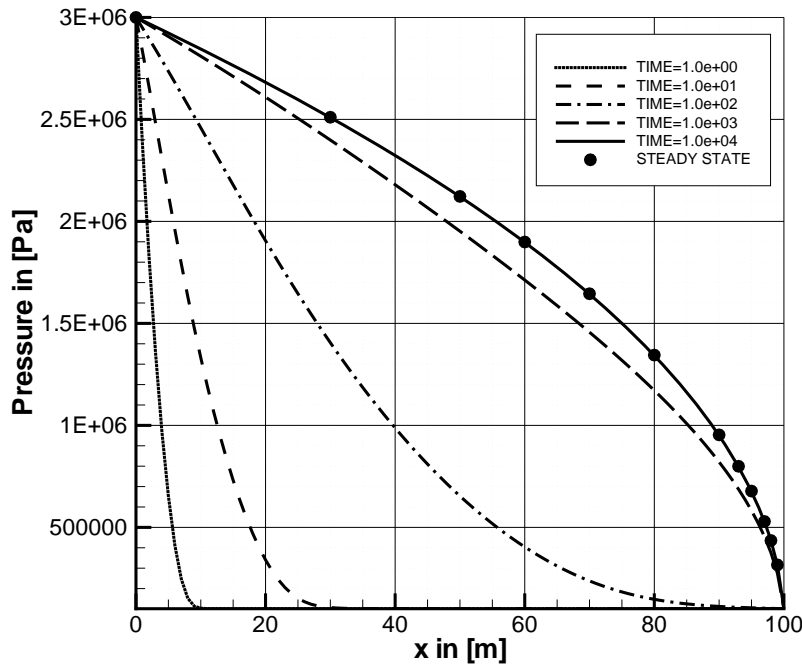


Figure 7.1.1: Comparison of analytical (circles) and numerical solutions

$= 9.5500 \times 10^4 \text{ Pa}$, and right hand side $p^g(x = 100m) = 1.01325 \times 10^5 \text{ Pa}$, respectively, in order to extract gas from the domain. The material parameters of the fluid and the porous medium are given in Tab. 7.1.2.

Property	Symbol	Value	Unit
Model length	L	0.05	m
Cross section area	A	1	m^2
Viscosity	μ	1.78×10^{-5}	Pa s
Porosity	n	0.005	—
Permeability	k	2.77×10^{-19}	m^2
Time step	Δt	3×10^2	s
Space step	Δx	0.005	m

Table 7.1.2: Material parameters

Fig. 7.1.3 depicts the temporal evolution of gas pressure at the observation point at the outlet. The numerical results of all implemented element types compare very well. Small deviation occur from different numbers of Gauss integration

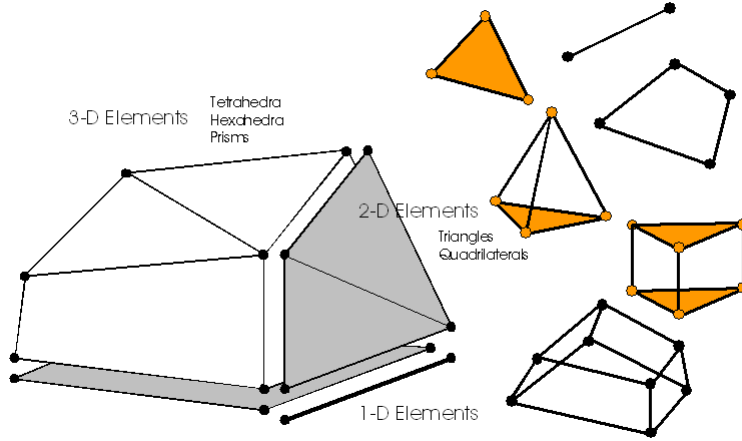


Figure 7.1.2: Different element types

points.

Benchmark repository

Problem type	Repository path	Files	Version
H_GAS	benchmarks\h_gas\element_test	h_gas_*	4.10.07

7.2 Non-isothermal compressible flow - HT process

7.2.1 Theory

For non-isothermal flow we have to account for temperature changes in the ideal gas law (7.1.2).

$$\frac{\partial \rho}{\partial t} = \frac{\partial}{\partial t} \left(\frac{p}{R_{\text{air}} T} \right) = \frac{1}{R_{\text{air}} T} \frac{\partial p}{\partial t} - \frac{p}{R_{\text{air}} T^2} \frac{\partial T}{\partial t} \quad (7.2.1)$$

The fluid mass balance equation is then given by

$$n \frac{1}{T} \frac{\partial p}{\partial t} - n \frac{p}{T^2} \frac{\partial T}{\partial t} - \nabla \cdot \left(\frac{p}{T \mu} \mathbf{k} \nabla p \right) = R_{\text{air}} Q_\rho \quad (7.2.2)$$

For heat transport there is an advective term due to air flow. The heat transport equation is as follows.

$$c \rho \frac{\partial T}{\partial t} + c^g \rho^g n \mathbf{v}^g \cdot \nabla T - \nabla \cdot [\lambda \nabla T] = Q_T \quad (7.2.3)$$

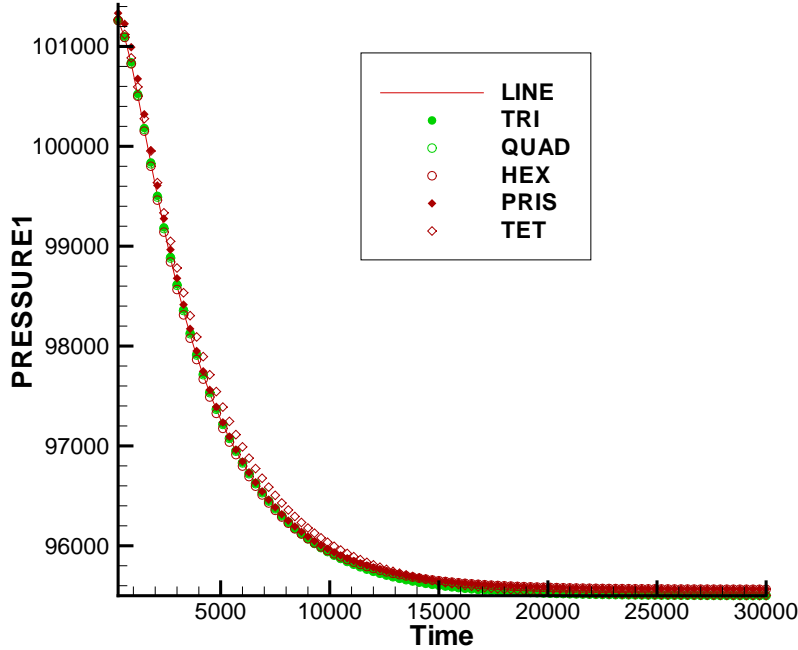


Figure 7.1.3: Evolution of gas pressure at the outlet observation point

with $c\rho = n(c^g\rho^g) + (1 - n)c^s\rho^s$, heat capacity of porous medium and $\lambda = n\lambda^g + (1 - n)\lambda^s$, heat conductivity of porous medium. Superscripts g, s denote gas and solid phases of the porous medium, respectively. Using the ideal gas law (7.1.2), density of the porous medium is given by

$$\rho = n \frac{p}{R_{\text{air}} T} + (1 - n)\rho^s \quad (7.2.4)$$

7.2.2 Material functions

For non-isothermal air flow and heat transport we have to consider in addition to the ideal gas law (7.1.2) the pressure and temperature dependencies of air viscosity $\mu^g(p, T)$ (section 7.2.2), specific heat capacities $c^g(p, T)$ and heat conductivities $\lambda^g(p, T)$ (section 7.2.2) as well ([73]).

Air viscosity

The Reichenberg viscosity model ([74]) is used for the non-isothermal flow of air. The pressure and temperature dependencies of air viscosity are shown in Fig. 7.2.1.

$$\mu^g(p, T) = \mu_0(T) \left(1 + \frac{Ap_r^{3/2}}{Bp_r + (1 + Cp_r^D)^{-1}} \right) \quad (7.2.5)$$

with the following parameters:

$$\begin{aligned} p_r &= p/p_{\text{crit}} & T_r &= T/T_{\text{crit}} \\ A &= \frac{\alpha_1}{T_r} \exp(\alpha_2 T_r^a) & B &= A(\beta_1 T_r - \beta_2) \\ C &= \frac{\gamma_1}{T_r} \exp(\gamma_2 T_r^c) & D &= \frac{\delta_1}{T_r} \exp(\delta_2 T_r^d) \\ p_{\text{crit}} &= 33.9 \times 10^4 \text{ Pa} & T_{\text{crit}} &= 126.2 \text{ K} \\ \alpha_1 &= 1.9824 \times 10^{-3} & \alpha_2 &= 5.2683 & a &= -0.5767 \\ \beta_1 &= 1.6552 & \beta_2 &= 1.2760 \\ \gamma_1 &= 0.1319 & \gamma_2 &= 3.7035 & c &= -79.8678 \\ \delta_1 &= 2.9496 & \delta_2 &= 2.9190 & d &= -16.6169 \end{aligned} \quad (7.2.6)$$

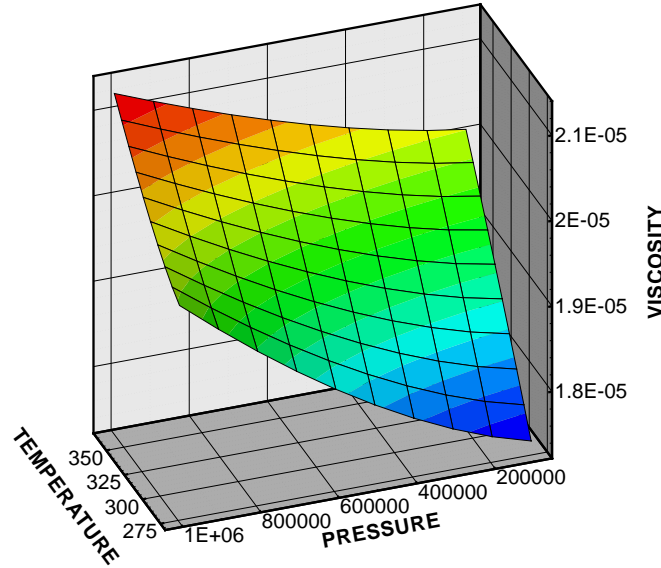


Figure 7.2.1: Air viscosity as a function of temperature (in Kelvin) and pressure (in Pa)

Thermal properties

Beside the hydraulic characteristics such as air viscosity, the thermal properties of the gas and solid, such as heat capacity and thermal conductivity are important for heat transport. As an example, Fig. 7.2.2 depicts the thermal properties of the gaseous phase. Fig. 7.2.2 (left) shows the temperature dependence of specific heat capacity of air at atmospheric pressure corresponding to equation (7.2.7) from [75] and compared with experimental data by [76]. Fig. 7.2.2 (right) illustrates the temperature dependence of thermal conductivity of air at atmospheric pressure corresponding to equation (7.2.8) from [75] and compared with experimental data by [76]. The pressure dependency of thermal properties can be neglected in the present pressure regimes.

$$c^g = 1.0613 - 4.3282 \times 10^{-4}T + 1.0234 \times 10^{-6}T^2 - 6.4747 \times 10^{-10}T^3 + 1.3864 \times 10^{-13}T^4 \quad (7.2.7)$$

$$\lambda^g = 7.488 \times 10^{-3} - 1.7082 \times 10^{-4}T + 2.3758 \times 10^{-7}T^2 - 2.2012 \times 10^{-10}T^3 + 9.46 \times 10^{-14}T^4 - 1.579 \times 10^{-17}T^5 \quad (7.2.8)$$

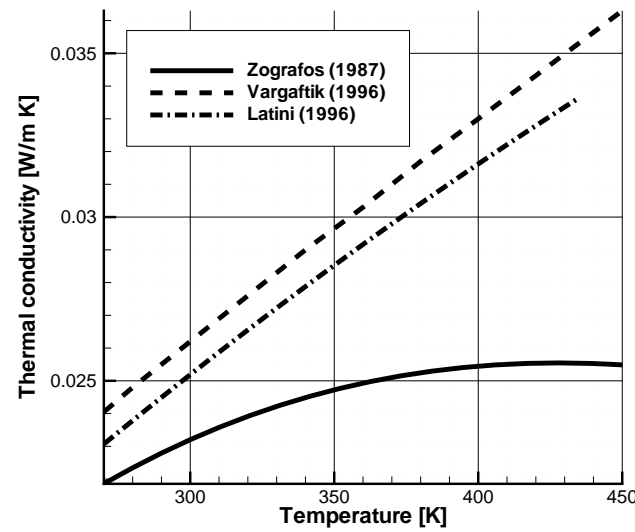
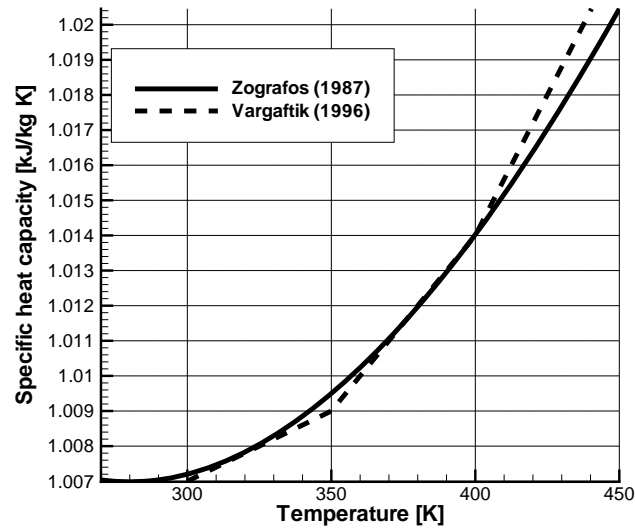


Figure 7.2.2: Thermal properties of air: Heat capacity (top), thermal conductivity (bottom)

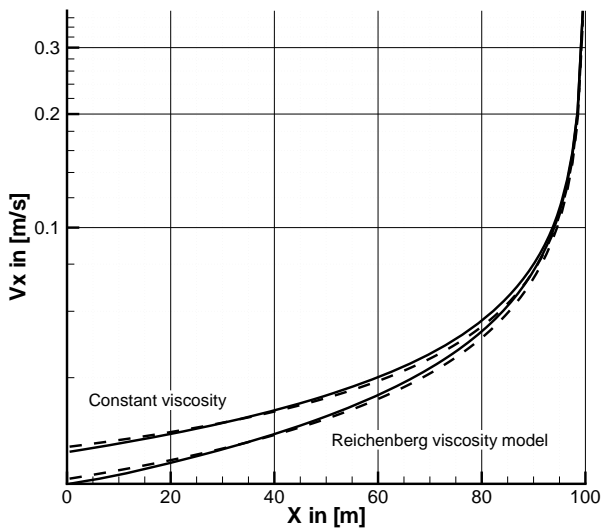
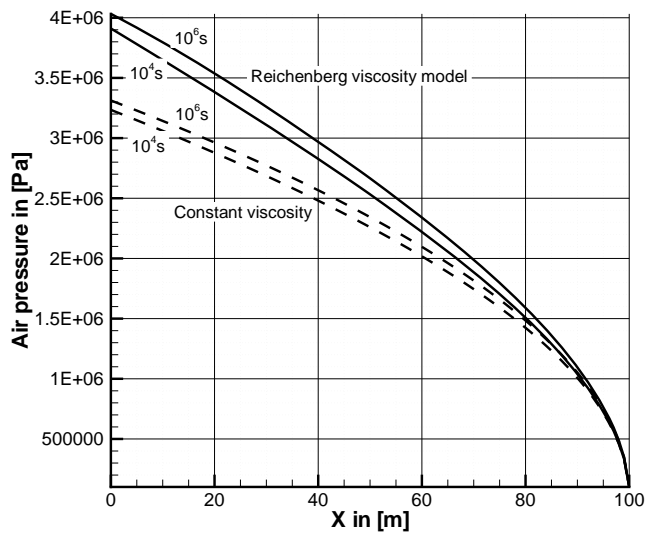


Figure 7.2.3: Hydraulic profiles evolution: Air pressure (top), Air velocity (bottom)

7.2.3 Examples

Air flow

We consider the same test example definition as for isothermal gas flow in sec. 7.1. Now we use temperature dependent fluid properties according to the Reichenberg model described in section 7.2.2. The model parameters are summarized in Tab. 7.2.1.

Property	Symbol	Value	Unit
Model length	L	100	m
Cross section area	A	1	m^2
Porosity	n	0.35	—
Densities	ρ^g, ρ^s	(7.1.2), 2650	kg/m^3
Permeability	k	2.7×10^{-11}	m^2
Dynamic gas viscosity	μ	(7.2.5)	$Pa\ s$
Initial condition	p_I	101325	Pa
Boundary condition	p_1	101325	Pa
Injection rates	Q^p	1 – 10	kg/s
Heat dispersion length	α_L, α_T	1, 0.1	m
Heat conductivities	λ^g, λ^s	(7.2.8), 2.5	$W/(mK)$
Heat capacities	c^g, c^s	(7.2.7), 2300	$J/(kgK)$
Time step	Δt	10^4	s
Space step	Δx	1	m

Table 7.2.1: Model parameters

Fig. 7.2.3 show the air pressure (left) and velocity distributions (right) along the soil profile. Simulations were run with constant viscosities and those corresponding to the Reichenberg model (section 7.2.2) which takes pressure and temperature changes into account.

The corresponding temperature profiles for different air injection rates are depicted in Fig. 7.2.4. The different shapes of the thermal profile curves indicate the transition between diffusion (left) and advection dominated regimes (right). Fig. 7.2.5 shows the temporal evolution of air pressure profiles for non-isothermal gas flow. In order to see the non-isothermal effects we plotted the analytical steady state solution for isothermal flow along with present numerical solution for non-isothermal flow. As a consequence of the viscosity increase resulting from the Reichenberg model the steady state pressure is larger for non-isothermal conditions.

Benchmark repository

Problem type	Repository path	Files	Version
H_GAS	benchmarks\h_gas\nonisothermal_gas_flow	h_gas_line	4.4.04(OK)

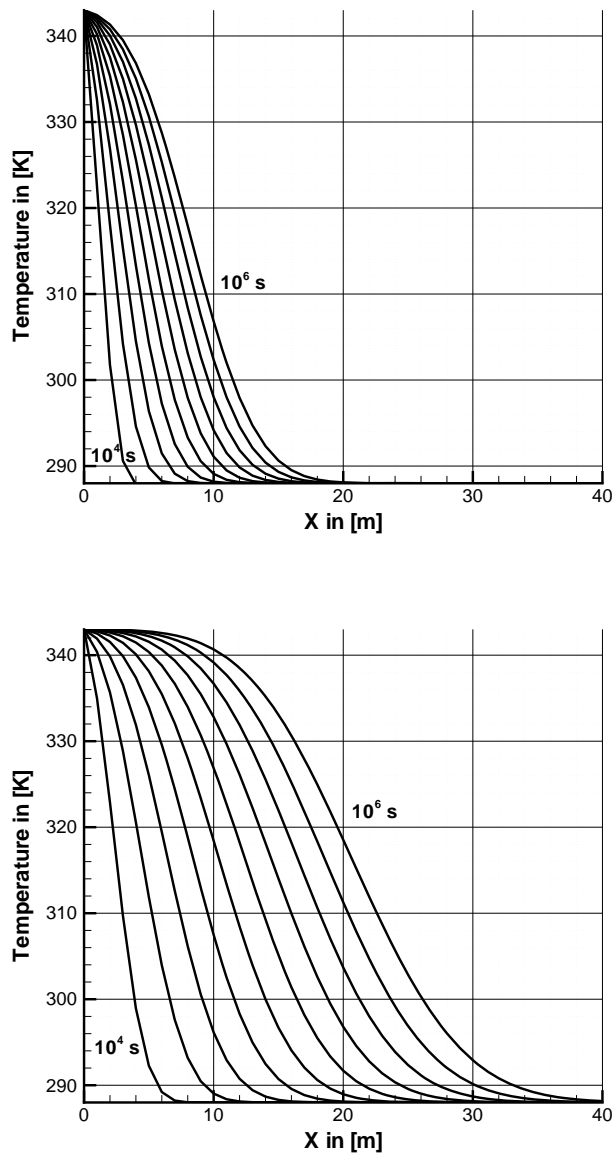


Figure 7.2.4: Air temperature profiles evolution. $1\text{kg}/\text{s}$ air injection rate (top), $10\text{kg}/\text{s}$ air injection rate (bottom)

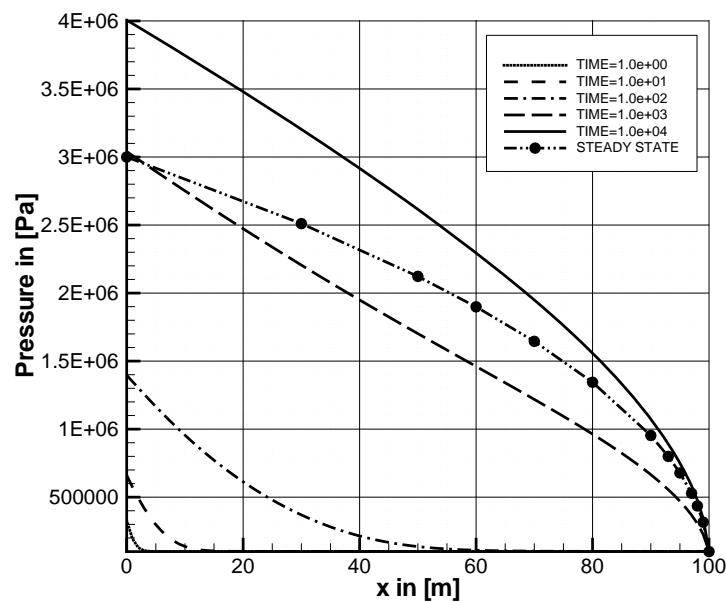


Figure 7.2.5: Temporal evolution of air pressure profiles for non-isothermal gas flow

7.3 Joule-Thomson process in permeable media - HT process

Theory

Flow in permeable media is not an isothermal process because there is a temperature change resulting from fluid expansion and viscous dissipation heating. Interests of this problem is to use the energy balance equation with heat transfer related with expansion and viscous dissipation for prediction of temperature profiles. For gas phase with only one component as carbon dioxide, we can start from the thermal energy balance as the following form

$$(\rho c_p)_{\text{eff}} \frac{\partial T}{\partial t} + c_p^g \rho^g \mathbf{u} \cdot \nabla T - \nabla \cdot [\kappa_{\text{eff}} \nabla T] = n \beta_T T \frac{\partial p}{\partial t} + (\beta_T T - 1) \mathbf{u} \cdot \nabla p + Q_T \quad (7.3.1)$$

In the following we develop an analytical solution for one-dimensional (**1D**) steady energy balance equation. The pressure relationship is described by Darcy law as:

$$u_x = -\frac{\mathbf{k}}{\mu} \frac{\partial p}{\partial x} \quad (7.3.2)$$

In a one-dimensional Cartesian coordinate (x-direction), steady energy balance becomes

$$c_p^g \rho^g u_x \frac{\partial T}{\partial x} - \beta_T T u_x \frac{\partial p}{\partial x} + u_x \frac{\partial p}{\partial x} - \kappa_{\text{eff}} \frac{\partial^2 T}{\partial x^2} = 0 \quad (7.3.3)$$

Substituting Eq. (7.3.2) into Eq.(7.3.3) and rearranging give

$$\frac{\partial^2 T}{\partial x^2} - \frac{c_p^g \rho^g}{\kappa_{\text{eff}}} u_x \frac{\partial T}{\partial x} - \frac{\mu \beta_T}{\mathbf{k} \kappa_{\text{eff}}} u_x^2 T + \frac{\mu}{\mathbf{k} \kappa_{\text{eff}}} u_x^2 = 0 \quad (7.3.4)$$

Solving the second order ordinary differential equation (7.3.4) gives

$$T = L_+ \exp(m_+ x) + L_- \exp(m_- x) + \frac{1}{\beta_T} \quad (7.3.5)$$

where

$$m_{p_s} = u_x \left(\frac{c_p^g \rho^g}{\kappa_{\text{eff}}} p_s \sqrt{\left(\frac{c_p^g \rho^g}{\kappa_{\text{eff}}} \right)^2 + \frac{4 \beta_T \mu}{\mathbf{k} \kappa_{\text{eff}}}} \right)$$

and L_+ and L_- are integration constants to be determined by boundary conditions.

Problem definition

The test benchmark problem for Joule-Thomson cooling processes has been solved. Problem is formulated for the expansion occurs during injection of compressed cryogenic CO₂ in a one-dimensional (**1-D**) horizontal column. We assume that column is a permeable media which is filed with CO₂ at low pressure.

Finite element solution has been obtained through solving the mass and energy balance equations. Within a time step mass balance equation for pressure is solved with temperature changes in return the energy balance equation, i.e. Eq. (7.3.1) is then solved for temperature with obtained fluid velocity. This is so called staggered approach and executed until solution become steady. Model geometry and conditions has shown in Fig. 7.3.1

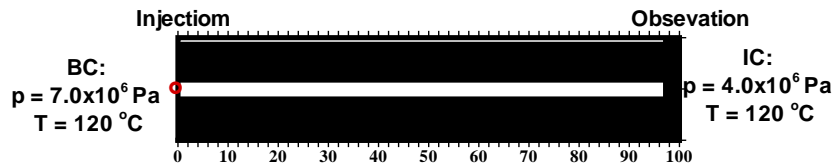


Figure 7.3.1: Model geometry and conditions

Results

Based on the above discussion OpenGeoSys (OGS) capable to show the Joule-Thomson process in carbon sequestration with enhanced gas recovery (CSEGR) related problems. In Fig. 7.3.2 we have presented comparison of temperature profile produced from OGS with those of analytical solution, i.e. Eq. (7.3). In this figure ‘without solid matrix’ mean the case where we do not account heat provide by solid matrix by setting $c_p^s = 0, \kappa^s = 0$ whereas case ‘with solid matrix’ mean we have accounted heat provided by solid matrix. The physical

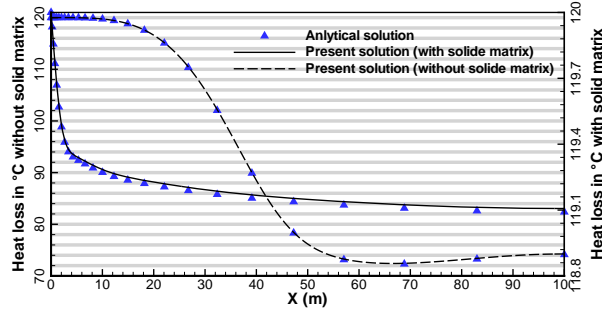


Figure 7.3.2: Comparison of present solution (FEM) with analytical solution due to Eq. (7.3).

domain has been discretized in hundred line element which size is varying between $\delta x = 0.4$ m to $\delta x = 4.3498$ m. This helps to capture the sharp gradient of temperature present near the injection point. Concerning to the time step size, at beginning of the simulation $\delta t = 1$ s with step by step increasing it reaches to $\delta t = 9.0 \times 10^4$ s after 14 time steps.

Figure shows that as we inject CO₂ (at temperature 120°C which is lower than inversion temperature $\approx 1227^\circ\text{C}$), its pressure falls with high gradient. It means as expansion starts, the average distance between molecules grows. Because of intermolecular attractive forces, expansion causes an increase in the potential energy of the gas. As no external work is extracted and process is adiabatic, the total energy of the gas remains constant because of the conservation of energy. The increase in potential energy thus implies a decrease in kinetic energy and therefore temperature falls.

Table 7.3.1: Model parameters

Meaning	Symbol	Value
Column radius	L	100 (m)
Porosity	n	0.35 (-)
Densities	ρ^g, ρ^s	$\frac{pM}{z_{sc}RT}, 2460 (\text{kg m}^{-3})$
Permeability	\mathbf{k}	$2.7 \times 10^{-11} (\text{m}^2)$
Dynamic viscosity	μ	$1.9836 \times 10^{-5} (\text{Pa s})$
Heat conductivities	κ^g, κ^s	$0.026374, 2.5 (\text{W m}^{-1}\text{K}^{-1})$
Heat capacities	c_p^g, c_p^s	$1.067 \times 10^3, 1.2 \times 10^3 (\text{J kg}^{-1}\text{K}^{-1})$

Benchmark deposit

Benchmark	Problem type	Path in benchmark deposit
JTCooling	H-GAS	JT-Cooling

Chapter 8

Fluid Momentum – H-Process dependent

8.1 Theory

8.1.1 Velocity Estimation

For accurate simulation in groundwater, an accurate calculation of the groundwater velocity is a prerequisite. Generally, there are two approaches for calculation of velocities. The first is local element-based, while the second is global-node-based. The first is commonly used in numerical models while the latter is often neglected due to additional computational burden. Several methods based on the first approach have been described in the literature [77, 78, 79, 80]. However, the second approach is much less common and was used by e.g. [81, 82, 83]. In handling continuous velocity estimation on elemental boundaries, the mixed finite element method is also introduced in the literature [82, 84]. In this method, the normal component of the velocity field is continuous at elemental boundaries. Velocity is estimated on each edge of an element. Mixed finite element methods [85, 86] as well as the node-based velocity estimation get increased attention from modelers because of the need for accuracy and continuity. More specifically, the node-based velocity estimation can provide independence from element geometry under the same formation of the FEM's and easiness to interpolate velocity at any location in elements from the known velocity on nodes (i.e., position). In one of the scientific graphical software [87], nodes defined as positions are used for interpolation to have continuous values while elements defined as connections are not used for interpolation so that the values associated to the connections are discrete. Since the velocity estimation can be separated technically from the RWPT method if velocity fields are given, easy adaptation for various types of elements as well as a variety of choices for interpolation techniques in treating velocity as position-dependent data lead to considerable

advantages and become a standard method in scientific graphical software such as OpenDX[87].

The global node based method for velocity interpolation is used, due to the advantages discussed previously. The global-node-based velocity method uses the momentum equation of flow (the Darcy equation) as for the element-based velocity. The momentum balance equation for variable-density fluid flow in a porous medium in terms of hydraulic head, h (L) can be given as [77, 78, 79, 80, 81, 83]

$$\vec{q} = \phi \vec{v} = -\frac{\hat{k} \rho_0 \vec{g}}{\mu} \left(\nabla h + \left(\frac{\rho - \rho_0}{\rho_0} \right) \vec{e} \right) \quad (8.1.1)$$

where \vec{q} is the Darcy velocity vector, ϕ is the porosity, \vec{v} is the velocity vector, \hat{k} is the tensor of permeability of a porous medium, ρ_0 is the reference density, ρ is the density, \vec{g} is the gravitational vector, μ is viscosity, and \vec{e} is the unit vector against the gravitational direction.

Given the hydraulic head and the fluid density at element nodes, the global-node-based velocity can be obtained by applying the Galerkin method to Equation (8.1.1) for each velocity component. This global node based velocity is continuous and smooth so that it can further be used for interpolation at any location inside of elements.

8.1.2 Formulation of Galerkin method to obtain velocity

Equation 8.1.1 can be rewritten in a simplified form as

$$\vec{q} = -\hat{K}(\nabla h + \lambda_C C \vec{e}) \quad (8.1.2)$$

where $\hat{K} = \frac{\hat{k} \rho_0 \vec{g}}{\mu}$ is the hydraulic conductivity, $\lambda_C = \frac{\rho - \rho_0}{\rho_0}$ is the relative density difference term, and C is the relative concentration.

Substitution of the known approximate hydraulic head field and relative density difference term in Equation 8.1.2 yields

$$\begin{aligned}
q_x &= -K_{xx} \frac{\partial}{\partial x} \left(\sum_{i=1}^N \hat{h}_k \omega_k \right) - K_{xy} \frac{\partial}{\partial y} \left(\sum_{i=1}^N \hat{h}_k \omega_k \right) \\
&\quad - K_{xz} \left[\frac{\partial}{\partial z} \left(\sum_{i=1}^N \hat{h}_k \omega_k \right) + \sum_{i=1}^N \hat{C}_k \omega_k \right] \\
q_y &= -K_{yx} \frac{\partial}{\partial x} \left(\sum_{i=1}^N \hat{h}_k \omega_k \right) - K_{yy} \frac{\partial}{\partial y} \left(\sum_{i=1}^N \hat{h}_k \omega_k \right) \\
&\quad - K_{yz} \left[\frac{\partial}{\partial z} \left(\sum_{i=1}^N \hat{h}_k \omega_k \right) + \sum_{i=1}^N \hat{C}_k \omega_k \right] \\
q_z &= -K_{zx} \frac{\partial}{\partial x} \left(\sum_{i=1}^N \hat{h}_k \omega_k \right) - K_{zy} \frac{\partial}{\partial y} \left(\sum_{i=1}^N \hat{h}_k \omega_k \right) \\
&\quad - K_{zz} \left[\frac{\partial}{\partial z} \left(\sum_{i=1}^N \hat{h}_k \omega_k \right) + \sum_{i=1}^N \hat{C}_k \omega_k \right]
\end{aligned} \tag{8.1.3}$$

where w is the basis function and N is the number of nodes in an element.

The residual function for the darcy velocity in x direction in Equation 8.1.3, which is the same for y and z direction, can be written as,

$$\begin{aligned}
R(x, y, z, t) &= q_x + K_{xx} \frac{\partial}{\partial x} \left(\sum_{i=1}^N \hat{h}_k \omega_k \right) + K_{xy} \frac{\partial}{\partial y} \left(\sum_{i=1}^N \hat{h}_k \omega_k \right) \\
&\quad + K_{xz} \left[\frac{\partial}{\partial z} \left(\sum_{i=1}^N \hat{h}_k \omega_k \right) + \lambda_C \left(\sum_{i=1}^N \hat{C}_k \omega_k \right) \right]
\end{aligned} \tag{8.1.4}$$

The Galerkin method weighs this residual over the whole domain using basis functions as the weighing function to yield

$$\begin{aligned}
&\int_{\Omega} \left[q_x + K_{xx} \frac{\partial}{\partial x} \left(\sum_{i=1}^N \hat{h}_k \omega_k \right) + K_{xy} \frac{\partial}{\partial y} \left(\sum_{i=1}^N \hat{h}_k \omega_k \right) \right. \\
&\quad \left. + K_{xz} \left[\frac{\partial}{\partial z} \left(\sum_{i=1}^N \hat{h}_k \omega_k \right) + \lambda_C \left(\sum_{i=1}^N \hat{C}_k \omega_k \right) \right] \right] \omega_i d\Omega = 0
\end{aligned} \tag{8.1.5}$$

When the approximate solution of each velocity is substituted in the velocity term, the equation yields the following form:

$$\begin{aligned}
& \int_{\Omega} \left(\sum_{j=1}^N \hat{q}_x \omega_j \right) \omega_i d\Omega + \int_{\Omega} \left[K_{xx} \frac{\partial}{\partial x} \left(\sum_{i=1}^N \hat{h}_k \omega_k \right) + K_{xy} \frac{\partial}{\partial y} \left(\sum_{i=1}^N \hat{h}_k \omega_k \right) \right. \\
& \left. + K_{xz} \left[\frac{\partial}{\partial z} \left(\sum_{i=1}^N \hat{h}_k \omega_k \right) + \lambda_C \left(\sum_{i=1}^N \hat{C}_k \omega_k \right) \right] \right] \omega_i d\Omega = 0
\end{aligned} \tag{8.1.6}$$

The element matrix of integrals can be written in the following form:

$$[\mathbf{A}^e]\{\hat{\mathbf{q}}_x\} = \{\mathbf{B}^e\} \tag{8.1.7}$$

where

$$[\mathbf{A}^e] = \int_{\Omega} \omega_j \omega_i d\Omega^e \tag{8.1.8}$$

$$\begin{aligned}
\{\mathbf{B}^e\} = & - \int_{\Omega} \left[K_{xx} \frac{\partial}{\partial x} \left(\sum_{i=1}^N \hat{h}_k \omega_k \right) + K_{xy} \frac{\partial}{\partial y} \left(\sum_{i=1}^N \hat{h}_k \omega_k \right) \right. \\
& \left. + K_{xz} \left[\frac{\partial}{\partial z} \left(\sum_{i=1}^N \hat{h}_k \omega_k \right) + \lambda_C \left(\sum_{i=1}^N \hat{C}_k \omega_k \right) \right] \right] \omega_i d\Omega^e = 0
\end{aligned} \tag{8.1.9}$$

By solving Equation 8.1.7, velocity in each direction for all nodes can be obtained. The same method can also be applied to pressure-based darcy equation. Further, the method is independent of element types and works for one, two, and three dimensions. In this way, the continuous velocity on every node for density-driven flow can be obtained.

8.2 Test problems for various elements

Benchmark name: *1d_line, 1d_tri, 1d_quad, 1d_tet, 1d_pri, 1d_hex*.

Purpose: Comparison of the result with simple analytical solution

- one directional constant velocity;
- Homogeneous media: Table ?? gives the parameters;
- fixed BC of 9810 Pa at the left end and 0 Pa at the right end;

Geometry and mesh: a 100m long saturated aquifer.

Table 8.2.1: Parameters in simulation

items	setting
Porosity	1.0
Permeability tensor (m^2)	1.000000e-12
Soil density kg/m^3	2.0e3

Model description: The hydraulic conditions is provided in Fig. 8.2.1

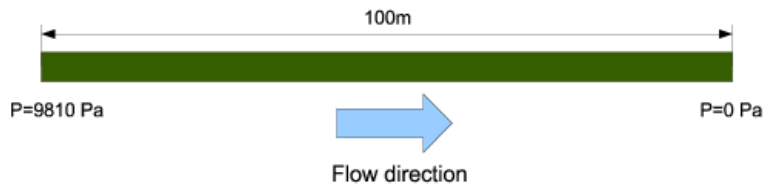


Figure 8.2.1: 1D Flow Description

Results: No matter what element type is used for the problem, the pressure distribution and velocity field should be same as provied in Fig.8.2.2.

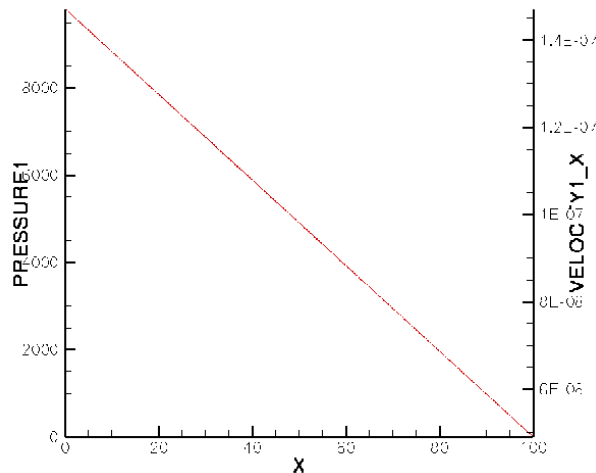


Figure 8.2.2: pressure and velocity

Chapter 9

Deformation – M-Processes

9.1 Theory

Pure deformations in any media can be described by the momentum balance equation in the terms of stress as

$$\nabla \cdot \boldsymbol{\sigma} + \rho g = 0 \quad (9.1.1)$$

where $\boldsymbol{\sigma}$ is stress tensor, ρ is the solid density. In the present implementation, the traditional sign convention for stress and fluid pressure is used. Displacement \mathbf{u} is the primary variable to be solved by substituting the constitutive law for stress-strain behavior

$$\begin{aligned} \boldsymbol{\sigma} &= \mathbb{C} \boldsymbol{\epsilon} \\ \boldsymbol{\epsilon} &= \frac{1}{2} (\nabla \mathbf{u} + (\nabla \mathbf{u})^T) \end{aligned} \quad (9.1.2)$$

with \mathbb{C} , a forth order material tensor and $\boldsymbol{\epsilon}$, the strain. Superscript T means the transpose of matrix. The deformation problem can be considered as a boundary value problem with boundary conditions given by

$$\boldsymbol{\sigma} : \mathbf{n} = \mathbf{t} \quad \text{or} \quad \mathbf{u} = \mathbf{u}_\Gamma, \quad \forall \mathbf{x} \in \partial\Omega \quad (9.1.3)$$

where \mathbf{n} is the normal to the portion of domain surface on where the traction boundary condition \mathbf{t} is prescribed, \mathbf{u}_Γ is the described displacement boundary values.

For 2D problems, we restrict the analysis under the assumption of plane strain.

9.2 Isotropic elasticity

We consider linear elasticity, i.e. using the generalized Hook's law:

$$\mathbb{C} := \lambda \delta_{ij} \delta_{kl} + 2\mu \delta_{ik} \delta_{jl} \quad (9.2.1)$$

where δ is the Kronecker delta, μ is the shear modulus, $\lambda = 2\mu\nu/(1-2\nu)$ is the so called Lamé constant with Poisson ratio ν .

The elastic deformation is a reversible process. The related material behaviour is called elasticity. The Hooke's linear elastic law (Eqns. 9.2.2 to 9.2.4) describes the elastic behaviour of solids. The elastic strain ε is directly proportional to the effective stress σ .

$$\varepsilon_x = \frac{1}{E} \cdot (\sigma_x - \nu \cdot (\sigma_y + \sigma_z)) \quad (9.2.2)$$

$$\varepsilon_y = \frac{1}{E} \cdot (\sigma_y - \nu \cdot (\sigma_x + \sigma_z)) \quad (9.2.3)$$

$$\varepsilon_z = \frac{1}{E} \cdot (\sigma_z - \nu \cdot (\sigma_x + \sigma_y)) \quad (9.2.4)$$

with

ε_i – strains,

σ_i – stresses in Pa,

E – Young's modulus in Pa,

ν – Poisson's ratio.

The Poisson's number μ can be derived by the following relation.

$$\mu = -\frac{\varepsilon_x}{\varepsilon_x} = -\nu$$

The following examples are utilized to verify the functionality of the software dealing with elastic deformation problems.

9.2.1 Plane strain with uniform loading (2D)

Problem definition

This example deals with calculations of a part of the whole rock mass. This can be done when there are special conditions concerning symmetry, structure of the rock mass and material behaviour. To simulate an initial state of stress in different depths, a pressure at least at one boundary has to be put on which represents the load of the overburden. In addition to this the stresses decrease with depth because of the gravity and the density of the rock mass (Fig. 9.2.1).

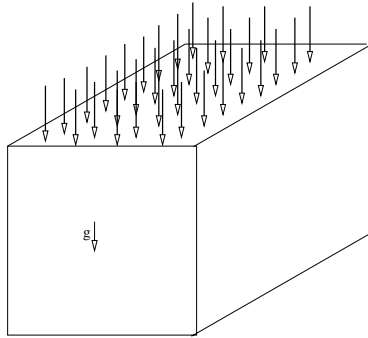


Figure 9.2.1: Conceptual model of elastic foundation

The calculation area has a size of $50m \times 50m$ (length and height) and the problem is simplified under the condition of plane strain. The quadrilateral mesh is illustrated in Fig. 9.2.2, one corner of which is finely meshed in order that it can be used directly to conduct an elastic excavation simulation in a coming example.

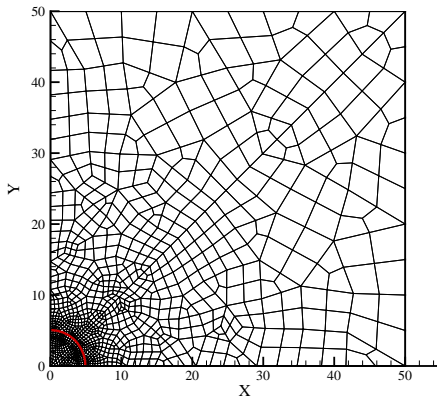


Figure 9.2.2: Special discretization: 1150 quadrilateral elements, 1101 nodes

Initial and boundary conditions

Initial conditions are not required for this problem. As for boundary conditions, the top boundary is prescribed with a uniformly distributed pressure of $23.75MPa$. Such kind of boundary conditions are so called traction bound-

ary in the context of mechanics, they are treated as Neumann type boundary condition. More detailed boundary conditions are illustrated in Fig. 9.2.3.

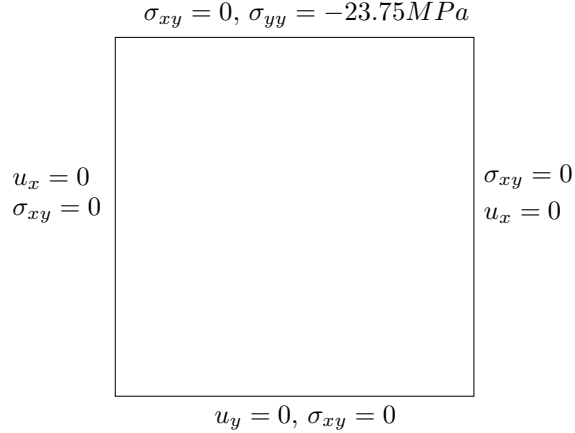


Figure 9.2.3: Boundary conditions

Material properties

Homogeneous material properties are assumed within the whole domain. Table 9.2.1 gives the parameters.

Property	Value	Unit
Young's modulus	25	GPa
Poisson's ratio	0.3	—
Density	2500	kg/m^3

Table 9.2.1: Material parameters

Results

For this simple elastic problem, we have an analytic solution given by

$$\sigma_{yy} = -23.75 - \rho h [\text{MPa}] \quad (9.2.5)$$

where ρ is the solid density and h is the height from top to bottom boundary.

Fig. 9.2.4 (left) shows the distribution of vertical stress in the domain, which implies that the discretization error is very small. Fig. 9.2.4 (right) shows a linear variation of stress σ_{yy} along with height.

The numerical result of σ_{yy} at the bottom boundary is -24.97MPa, which is very close to the analytic solution, $\sigma_{yy} = -25.0 \text{ MPa}$. This proves the correction of the numerical scheme.

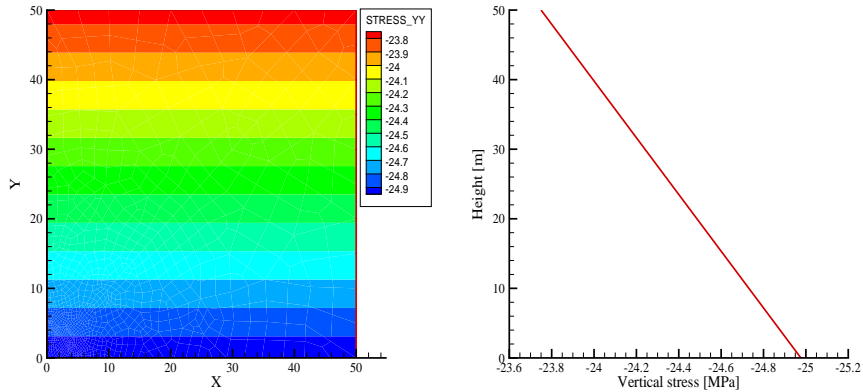


Figure 9.2.4: Result of vertical stress, σ_{yy} (MPa). Left: domain distribution.
Right: Vertical profile

Benchmark deposit

Benchmark	Problem type	Path in benchmark deposit
<i>m-drift</i>	M	benchmarks\M\

9.2.2 Plain strain with uniform loading - Excavation in homogeneous media (2D)

Problem definition

This is the second step of the simulation described in the above section, Section 9.2.1. A long round tunnel is built in the rock mass and this is depicted in Fig. 9.2.5. The deformation due to the excavation is simulated under the assumption of plane strain, same initial condition and material parameters given in Section sec:el2d.

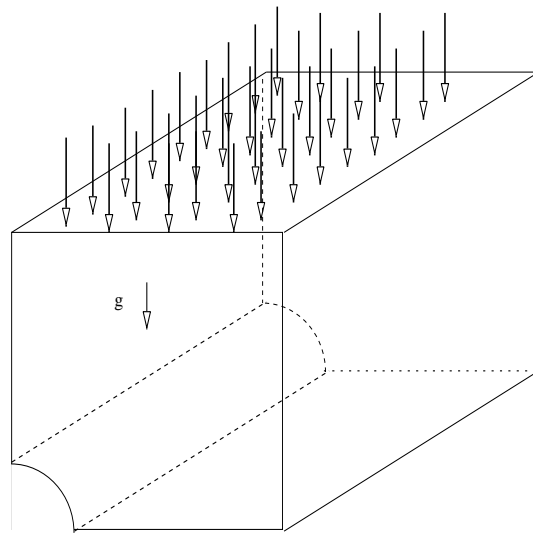


Figure 9.2.5: Excavation in rock mass

Initial and boundary conditions

The tunnel has a radius of 5m. The released loading approach is applied to simulate the excavation.

Results

We use the same mesh as given in the above section to conduct the simulation. Fig. 9.2.7 shows the distribution of vertical displacement and stresses in the domain after excavation.

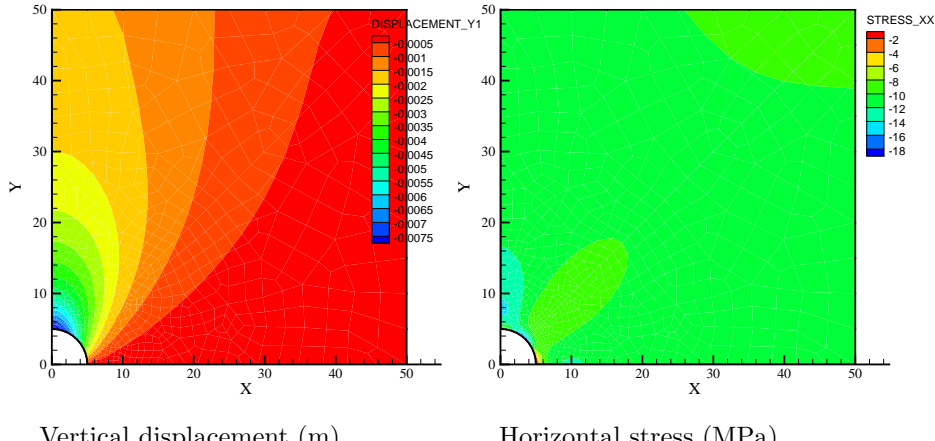


Figure 9.2.6: State variables after excavation

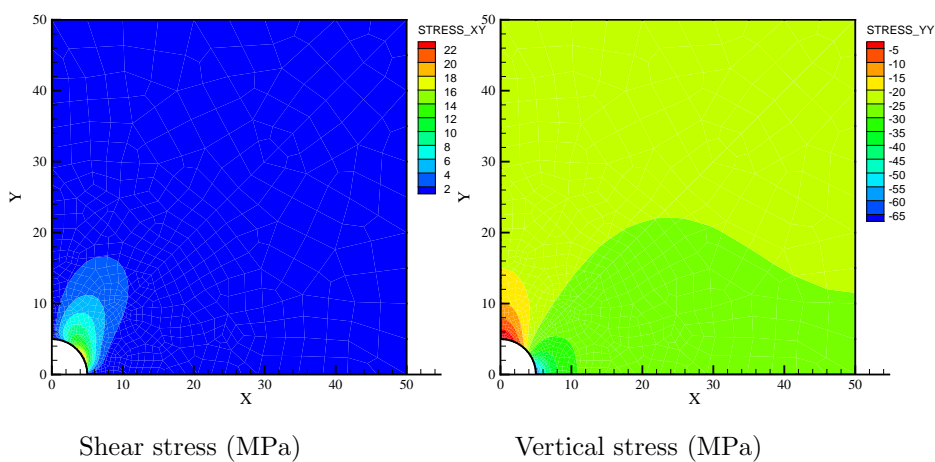


Figure 9.2.7: State variables after excavation

Benchmark deposit

Benchmark	Problem type	Path in benchmark deposit
<i>m_drift</i>	M	benchmarks\M\

9.2.3 Plain strain with uniform loading - Excavation in heterogeneous media (2D)

Problem definition

Again, we analyze the deformation of the excavation problem defined in Section 9.2.2. Contrary to homogeneous case, we use function defined initial stress and assume four different material domains make up the geometry (Fig. 9.2.8).

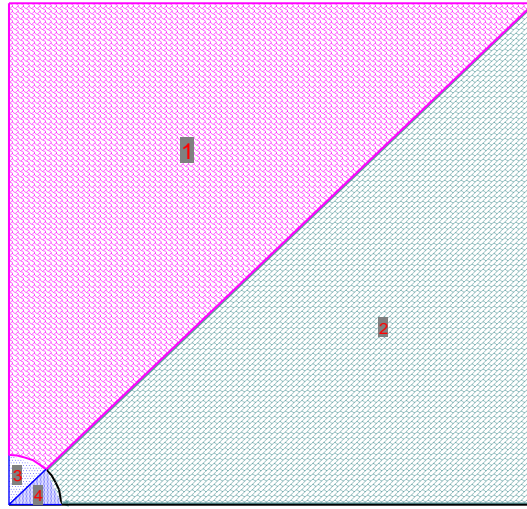


Figure 9.2.8: Excavation in heterogeneous rock mass

Initial and boundary conditions

The initial stresses are assumed linearly distributed within a material domain. The expressions of these distribution are given in

Material (Fig. 9.2.8)	σ_{xx}	σ_{yy}	Expression
			σ_{zz}
1	$23.75 + 0.2y$	$23.75 + 0.2y$	$23.75 + 0.2y$
2	$24.75 + 0.5y$	$24.75 + 1.3y$	$24.75 + 0.5y$
3	$26.75 + 10.0x + 12.0y$	$26.75 + 20.0x + 16.0y$	$26.75 + 10.0x + 12.0y$
4	$27.75 + 10.0x + 14.0y$	$27.75 + 20.0x + 18.0y$	$27.75 + 10.0x + 14.0y$

Table 9.2.2: Initial stress expression (negative value, kPa)

Material properties

As depicted in Fig. 9.2.8, the domain consists of four different materials denoted by 1, 2, 3 and 4. Hereby, we assume only Young's modulus differs from each other of materials (Table 9.2.3).

Property	Value	Unit
Young's modulus	1:25, 2:26.0, 3:30.0, 4:28.0	GPa
Poisson's ratio	0.3	—
Density	2.5	kg/m^3

Table 9.2.3: Parameters

Results

Fig. 9.2.9 shows the distribution of displacements after excavation.

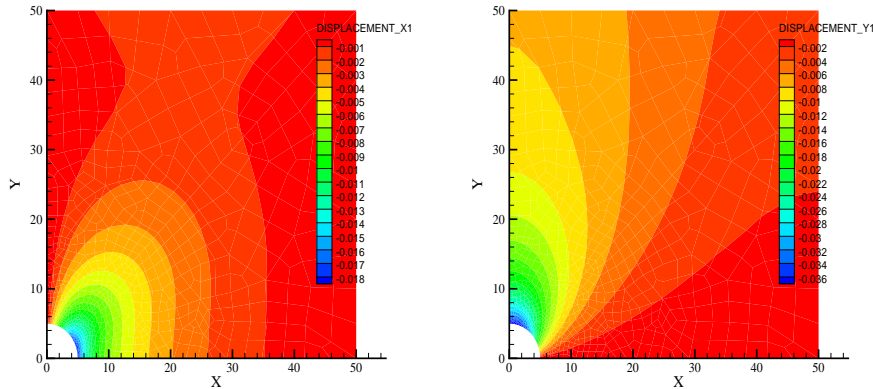


Figure 9.2.9: Distribution of displacement (m)

Fig. 9.2.10 shows the distribution of stresses after excavation.

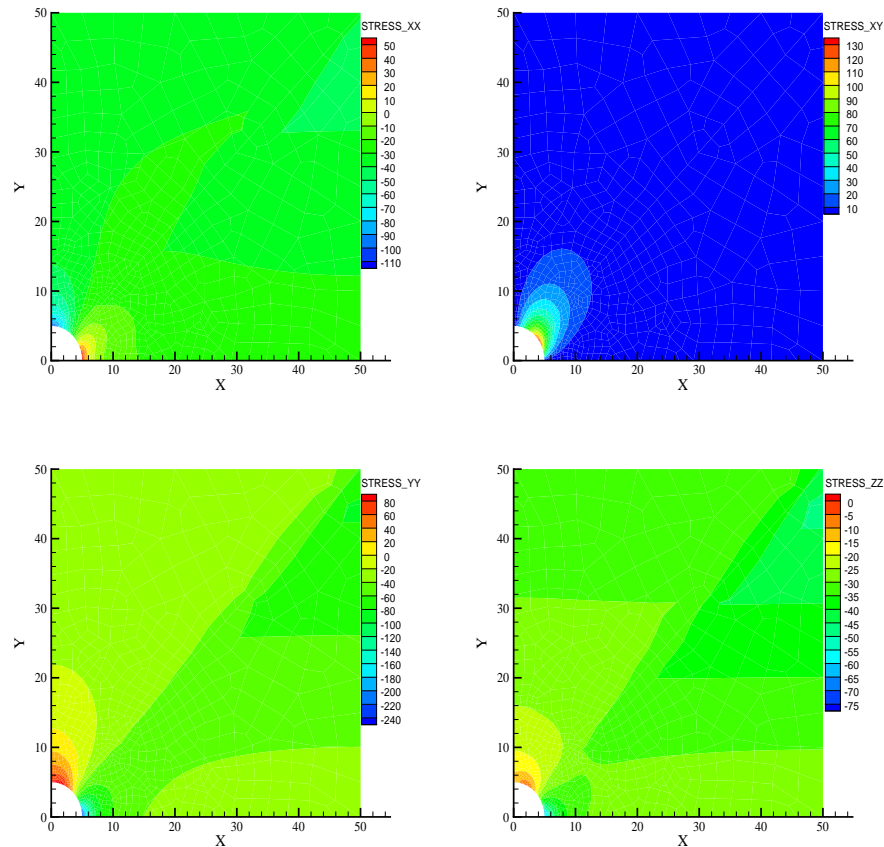


Figure 9.2.10: Distribution of stresses (kPa)

Benchmark deposit

Benchmark	Problem type	Path in benchmark deposit
<i>m_drift_init</i>	M	benchmarks\M\

9.2.4 Elastic cube (3D)

Problem definition

We consider deformation in a cubic domain under linearly distributed pressure (Fig. 9.2.11). The size the domain is $1m \times 1m \times 1m$. The deformation is assumed being elastic.

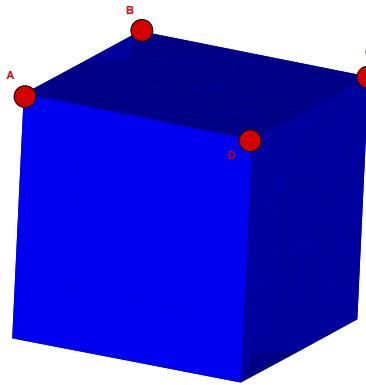


Figure 9.2.11: A block with linear distributed pressure on the top surface

Initial and boundary conditions

Normal translation on the vertical surfaces, which contains vertex A, D and which contains vertex B, C, and on the bottom surface is restricted. On the top surface, a linear distributed pressure is prescribed in the manner of point-wise as:

- Vertex A: $1.0Pa$
- Vertex B: $1.0Pa$
- Vertex C: $0.0Pa$
- Vertex D: $0.0Pa$

The pressure at any point on the top surface is obtained by a linear interpolation before face integration. This is done by programm automatically.

Material properties

The material properties are homogenous with the domain and they are listed in Table 9.2.4

Property	Value	Unit
Young's modulus	2.0×10^7	Pa
Poisson's ratio	0.4	–

Table 9.2.4: Material parameters of cubic domain

Results

A deformed domain is depicted in Fig. 9.2.12, which demonstrated that the results are consistent with the prescribed boundary condition.

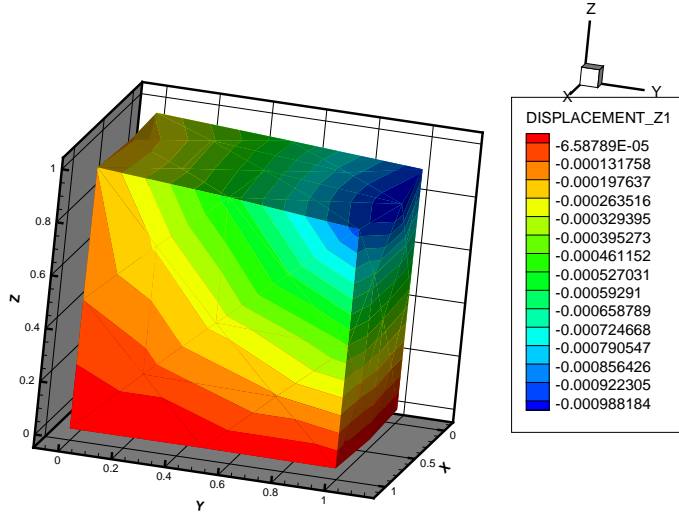


Figure 9.2.12: Deformed cubic domain

Benchmark deposit

Benchmark	Problem type	Path in benchmark deposit
<i>m_brick_l</i>	M	benchmarks\M\

9.2.5 Given deformation at the top (3D)

Problem definition

A quarter of an elastic cylinder is compressed at the top. The deformation that is caused by a uniform vertical stress is given as boundary condition. The aim is to calculate the stress in z -direction which is caused by this deformation and to get to know the resulting deformations in each direction.

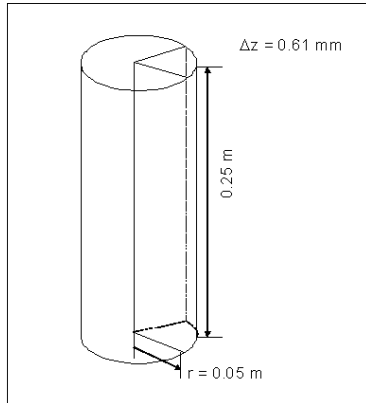


Figure 9.2.13: Calculation area: a quarter of a cylinder

Assumptions

Solid: homogeneous, isotropic, finite dimensions, constant deformation, linear elastic material behaviour

Model set-up of the 3D numerical model

For the 3-dimensional simulation the calculation area is exclusively out of a quarter of a cylinder. The model includes 4000 elements and 4947 nodes. Deformations in x -direction are suppressed in the $y - z$ -plane. Deformations in y -direction are suppressed in the $x - z$ -plane and deformations in z -direction are inhibited at the bottom of the quarter cylinder. At the top of the model a mechanical boundary condition is set with a constant displacement of 0.61 mm. The elastic deformation of the solid is not time-dependent. The used material parameters are shown in Tab. 9.2.5.

symbol	quantity	value
ρ	density of the solid	$2.5 \text{ t} \cdot \text{m}^{-3}$
E	Young's modulus of the solid	7 GPa
ν	Poisson ratio	0.3

Table 9.2.5: Material parameters

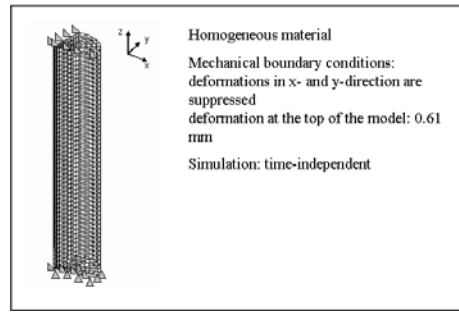


Figure 9.2.14: Calculation model (3D)

Evaluation method

In order to solve the equations of the Hooke's law, there are some constraints that have to be considered: the stresses in x - and y -direction are equal to zero, because the body can expand into radial direction. Thus the Hooke's equations can be simplified as follows:

$$\varepsilon_z = \frac{\Delta z}{z} = \frac{1}{E} \cdot \sigma_z \quad (9.2.6)$$

$$\varepsilon_x = \varepsilon_y = \frac{1}{E} \cdot (-\nu \cdot \sigma_z) \quad (9.2.7)$$

Results

With the given strain in z -direction, the stress σ_z is calculated by Eqn. 9.2.6.

$$\frac{\Delta z}{z} = \frac{-6.1 \cdot 10^{-4} \text{ m}}{0.25 \text{ m}} = -2.44 \cdot 10^{-3} \quad \text{and} \quad \sigma_z = -2.44 \cdot 10^{-3} \cdot 7 \cdot 10^9 \text{ Pa} = -1.71 \cdot 10^7 \text{ Pa}$$

In this way, the strains in x - and y -direction are known.

$$\varepsilon_x = \varepsilon_y = \frac{1}{7 \cdot 10^9 \text{ Pa}} \cdot (-0.3 \cdot -1.71 \cdot 10^7 \text{ Pa}) = 7.32 \cdot 10^{-4}$$

The numerical results meet exactly the analytical solutions. This is sketched in Fig. 9.2.15, where the strains and the resulting stress along a polyline from top to bottom of the quarter cylinder can be found. That means both RockFlow and GeoSys/RockFlow are able to calculate the state of stresses for the 3D elastic deformation.

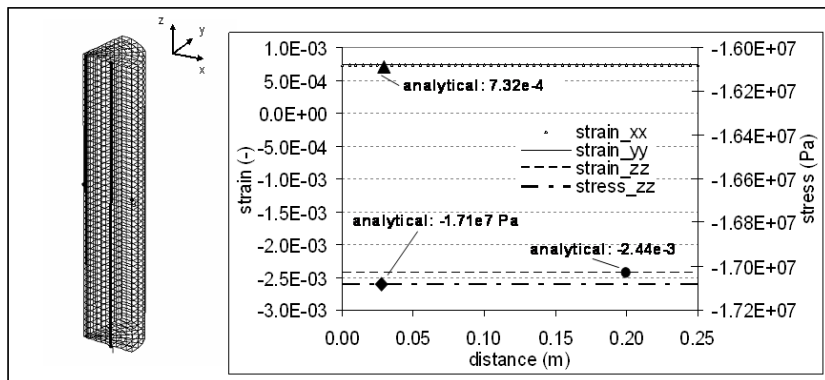


Figure 9.2.15: Strains and stress in z -direction as the result of deformation

Path in the benchmark deposit	Used code	Used version	Date of simulation run
\M\elastic_deformation\displacement\displ_Geosys/RF\m_e_displacement_3Du	GeoSys/RockFlow	RockFlow 4, rf4-507	Dec. 2007

9.2.6 Given stress at the top (3D)

Problem definition

This example is the inverse of the precedent one. The quarter cylinder is deformed by a given stress, while this time the resulting deformation is unknown. In order to check out easily whether the simulated results correspond to the analytical solutions, the value of the effective stress in z -direction on top of the calculation model is the same as in the above described example.

Assumptions

Solid: homogeneous, isotropic, finite dimensions, constant deformation, linear elastic material behaviour

Model set-up of the 3D numerical model

The calculation model has the same properties as the model of the precedent example. At the top of the model a load of $-1.71 \cdot 10^7$ Pa was set as constant source term. The simulation with both RockFlow and Geosys/RockFlow needs the input of the load as source term in z -direction at the single nodes under consideration of each element node. The input is done as single forces, not as the common stresses. The displacement boundaries are the same as in the precedent example except the z -displacement on the top of the model. The used material parameters are shown in Tab. 9.2.5.

Results

The analytical solution and results are identical to the previous example. The calculated displacement as a result of the constant load on the top amounts to $6.1 \cdot 10^{-4}$ m. The numerical results that are shown in Fig. 9.2.16 meet the analytical solutions well.

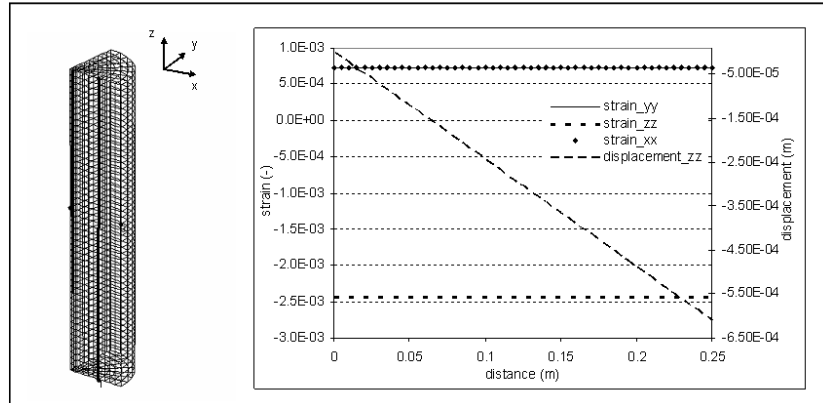


Figure 9.2.16: Strains and displacement in z -direction

Path in the benchmark deposit	Used code	Used version	Date of si- mulation run
\M\elastic_deformation\stress\stress_Geosys RF\m_e_stress_3Du	GeoSys/RockFlow	RockFlow 4, rf4-507	Dec. 2007

9.2.7 Lubby1: Nonlinear model

The Lamé constants defined for Hooke's fourth-order elastic material tensor (9.2.1) can be expressed by the Young's modulus E , the Poisson's ratio ν and the shear modulus G (so-called *engineering constants*) which can be obtained experimentally.

$$\mu = \frac{E}{2(1+\nu)} = G \quad (9.2.8)$$

$$\lambda = \frac{E\nu}{(1+\nu)(1-2\nu)} = \frac{2G\nu}{(1-2\nu)} \quad (9.2.9)$$

In many technical applications considering small strains, the elastic material parameters are assumed to be constant, and the stress-strain curves are nearly linear. However, the typical response of certain geological materials to monotonic loading (without load reversal) shows a nonlinear stress-strain behavior. Considering only elastic effects during load application, Hooke's law cannot be used to describe the observed material properties. Therefore, so-called pseudo-elastic constitutive models are frequently used for the analysis of nonlinear stress-strain curves, particularly in soil and rock mechanics. In a generalized manner, they are based on the assumption of an explicit stress-strain relation considering a stress- and strain-dependent material matrix:

$$\sigma = \mathcal{C}(\sigma, \varepsilon) \cdot \varepsilon^e. \quad (9.2.10)$$

Based on the so-called *Lubby1* model (cf. [88]), a nonlinear elastic approach with strain-dependent Young's modulus

$$E(\varepsilon_v) = \frac{E_0}{1 + a \varepsilon_v^n} \quad (9.2.11)$$

but constant Poisson's ratio is proposed. Here, ε_v is the equivalent strain, and E_0 , a as well as n are material parameters. The equivalent strain is defined by

$$\varepsilon_v = \sqrt{\frac{2}{3} \varepsilon^e \cdot \varepsilon^e}. \quad (9.2.12)$$

Problem definition

Triaxial short-term compression under axisymmetric conditions is carried out to verify the nonlinear elastic isotropic material model (modified Lubby1 approach). For the calculation, the cross-section of a cylindrical sample with a radius of 30 mm and a height of 120 mm is studied. The loading in principal axes includes a radial pressure as well as an axial displacement, and is realized in two steps. It is resulting in a homogeneous stress-strain state. Details of the model (geometry, mesh, boundary conditions) according to K.-H. Lux and F. Werunsky (unpublished report, 2008) are presented in Fig. 9.2.17.

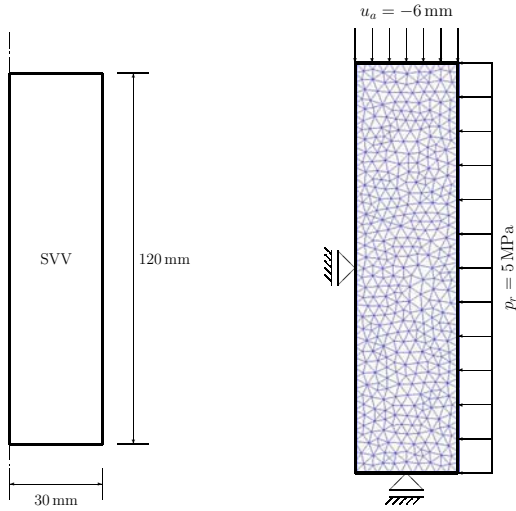


Figure 9.2.17: Triaxial compression of a cylindrical sample. Axisymmetric model. Left: Geometry. Right: Finite element grid and boundary conditions.

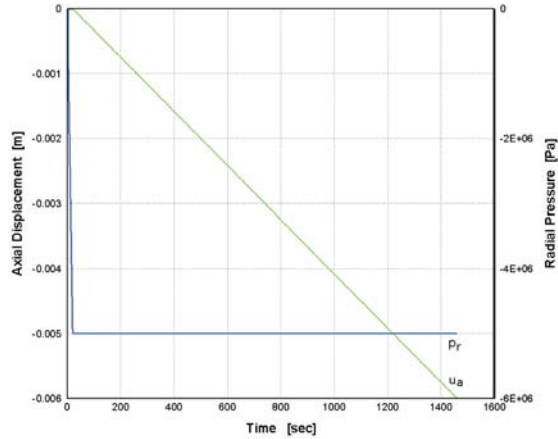


Figure 9.2.18: Triaxial compression of a cylindrical sample. Loading history for short-term experiments. Radial casing pressure (stress rate $\dot{\rho}_r = 0.25 \text{ MPa}\cdot\text{s}^{-1}$) with subsequent axial displacement (strain rate $\dot{\varepsilon}_a = 3.47 \cdot 10^{-5} \text{ s}^{-1}$).

Initial and boundary conditions

Initial conditions do not have to be given for the problem under consideration. As the bottom edge is fixed in vertical direction, the left-hand edge is fixed in

horizontal direction for symmetry reasons (axis of rotation). On the right-hand edge initially a radial casing pressure of 5 MPa is applied within 20 seconds with a constant stress rate. While keeping constant this radial pressure, a subsequent stroke-driven axial compressive loading is applied within the following 1 440 seconds with a constant strain rate. The maximum axial displacement is 6 mm which corresponds to a 5% reduction of the sample's height (for the complex loading history cf. Fig. 9.2.18).

Material properties

The material parameters referring to the modified Lubby1 relation (9.2.11) are summarized in Tab. 9.2.6. Within this context, the initial Young's modulus and the Poisson's ratio are close to values known for rock salt.

Property	Value	Unit
Poisson's ratio ν	0.335	–
initial Young's modulus E_0	21 400	MPa
factor a in (9.2.11)	2 750	–
exponent n in (9.2.11)	1.0	–

Table 9.2.6: Material parameters

Results

The representation of the axial stress vs. the axial strain in Fig. 9.2.19 shows on exemplarily chosen material parameters the noticeable difference between the linear (Hooke's model) and the nonlinear (modified Lubby1 model) elastic models even at small strains. Within the context of the studied case, the stress response will be overestimated by a multiple using the linear Hooke's law.

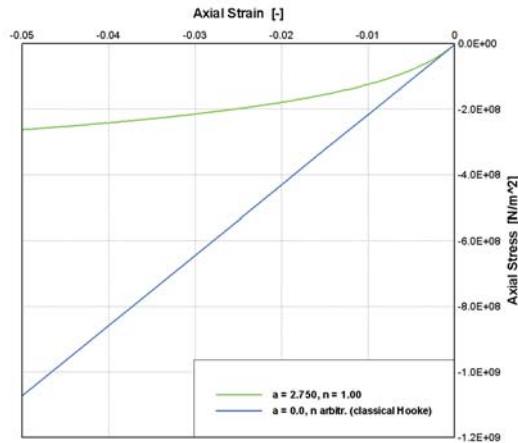


Figure 9.2.19: Triaxial compression of a cylindrical sample. Stress-strain curves regarding the axial load response. Comparison of linear elastic (Hooke) and nonlinear elastic (modified Lubby1 (9.2.11)) material models.

Benchmark deposit

Benchmark	Problem type	Path in benchmark deposit
<i>m_triax_lubby1</i>	M	benchmarks\M\

9.3 Transverse isotropic elasticity

If the material properties are independent of orientations and directions of the technical or natural object under consideration, the material behavior is called *isotropic*. Otherwise, the material is known as *anisotropic* one. Anisotropy is closely connected with distinguished orientations in the material structure. Among others, fiber-reinforced and layered materials are typical anisotropic materials.

From the point of view of modeling and numerical simulation special cases of anisotropy like *orthotropy* are of particular interest. Orthotropic materials are characterized by mutually orthogonal two-fold axes of rotational symmetry. A special class of orthotropic materials represent the so called *transverse isotropic* materials. They are characterized by a plane of isotropy featuring the same material properties independent of the direction of observation within this plane, and different material properties in the direction normal to this plane. Within this context, the normal to the plane of isotropy can be considered as the direction of anisotropy. Most of layered materials, biological membranes as well as rocks (e.g. sandstone, shale) are typical materials which can be considered as transverse isotropic ones.

In case of transverse isotropy, the Hooke's law (9.2.1) has to be modified establishing a unit vector \mathbf{a} which defines the direction perpendicular to the plane of isotropy (normal vector, direction of anisotropy – defining, e.g., the direction of a single fiber family of a fiber-reinforced material).

$$\begin{aligned} \sigma_{ij} = & \lambda \delta_{ij} \varepsilon_{kk} + 2\mu_T \varepsilon_{ij} \\ & + 2 (\mu_L - \mu_T) (a_i \varepsilon_{jl} a_l + a_l \varepsilon_{li} a_j) \\ & + \alpha (a_i a_j \varepsilon_{kk} + a_k \varepsilon_{kl} a_l \delta_{ij}) \\ & + \beta a_k \varepsilon_{kl} a_l a_i a_j \end{aligned} \quad (9.3.1)$$

Linear elastic transverse isotropic material is characterized by 5 independent material parameters like λ , μ_T , μ_L , α and β given in Eqn. (9.3.1). In some cases these parameters are called *invariants* of the transverse isotropic elastic Hooke's law. They can be defined w.l.o.g. by the following (engineering) elastic constants which can be obtained experimentally:

E_i	–	Young's modulus within the plane of isotropy,
ν_i	–	Poisson's ratio within the plane of isotropy,
E_a	–	Young's modulus w.r.t. the direction of anisotropy,
ν_{ia}, ν_{ai}	–	Poisson's ratio w.r.t. the direction of anisotropy,
G_a	–	shear modulus w.r.t. the direction of anisotropy.

There exist some relations between these parameters.

$$G_i = \frac{E_i}{2(1 + \nu_i)} = \mu_i \quad (\text{shear modulus within the plane of isotropy}) \quad (9.3.2)$$

$$\nu_{ai} = \nu_{ia} \frac{E_a}{E_i} \quad (9.3.3)$$

As mentioned above, the invariants of the transverse isotropic elastic Hooke's law can be expressed by the presented elastic parameters.

$$\begin{aligned} \lambda &= \frac{E_i(\nu_i + \nu_{ia}\nu_{ai})}{\tilde{D}} \\ \mu_T &= G_i \\ \mu_L &= G_a \\ \alpha &= \frac{E_i(\nu_{ai}(1 + \nu_i - \nu_{ia}) - \nu_i)}{\tilde{D}} \\ \beta &= \frac{E_a(1 - \nu_i^2) - E_i[(\nu_i + \nu_{ia}\nu_{ai}) + 2(\nu_{ai}(1 + \nu_i - \nu_{ia}) - \nu_i)]}{\tilde{D}} \\ &\quad - 4G_a + 2G_i \\ \text{with } \tilde{D} &= 1 - \nu_i^2 - 2\nu_{ia}\nu_{ai} - 2\nu_{ia}\nu_i\nu_{ai} \\ &= (1 + \nu_i)(1 - \nu_i - 2\nu_{ia}\nu_{ai}) \end{aligned}$$

The coordinates of the material tensor for linear elastic transverse isotropic material are defined as follows:

$$\begin{aligned} C_{ijkl} &= \lambda \delta_{ij} \delta_{kl} + 2\mu_T \delta_{ik} \delta_{jl} \\ &\quad + 2(\mu_L - \mu_T) (a_i \delta_{jk} a_l + a_k \delta_{il} a_j) \\ &\quad + \alpha (a_i a_j \delta_{kl} + a_k a_l \delta_{ij}) \\ &\quad + \beta a_i a_j a_k a_l \end{aligned} \quad (9.3.4)$$

Tension of a quadratic plate according to Schröder [89], Kohlmeier [90] and Fiolka [91] is carried out to verify the linear elastic transverse isotropic material model. The model definition and the results are presented in the following examples.

9.3.1 Tensile test (2D)

Problem definition

The first example for transverse isotropic elasticity is the twodimensional simplification of the tension of a quadratic plate under plane strain conditions according to Schröder [89] and Kohlmeier [90]. Within this context, a laminated material structure perpendicular to the plane under consideration is assumed. The direction of anisotropy within this plane, which is defined by a vector \mathbf{a} is perpendicularly oriented to the material layers. During simulation, the direction of anisotropy is rotated counterclockwise starting with an angle φ of $\varphi = 0^\circ$ and ending with $\varphi = 180^\circ$. Consequently, as in *OpenGeoSys* the direction of anisotropy is assumed to be directed parallel to the local \bar{y} -axis, and the angle of rotation is defined as the rotation between the global x -axis and the local \bar{x} -axis, the input angle changes in the range of $\varphi = -90^\circ \dots 90^\circ$.

The quadratic plate has an edge length of $l = 10$ mm, and was analyzed using triangular and rectangular elements respectively. For details of the model (geometry, boundary conditions, material orientation) see Fig. 9.3.1.

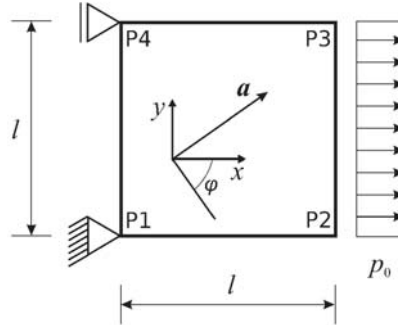


Figure 9.3.1: Tensile test. Model definition according to Kohlmeier [90]. Vector \mathbf{a} defines the direction of anisotropy.

Initial and boundary conditions

Initial conditions do not have to be given for the problem under consideration. The left-hand edge is fixed in horizontal direction. To avoid rigid body motions, the left lower corner node is fixed in both vertical and horizontal directions. A distributed tension load of $p_0 = 0.2$ MPa is applied at the right-hand edge.

Material properties

The material parameters are summarized in Tab. 9.3.1.

Property	Value	Unit
Young's modulus E_i	561.12	MPa
Young's modulus E_a	1311.83	MPa
Poisson's ratio ν_i	0.6032	—
Poisson's ratio ν_{ia}	0.1838	—
shear modulus G_a	375.0	MPa

Table 9.3.1: Material parameters

Results

The numerical results obtained with *OpenGeoSys* are compared to values given in [90]. They include displacement coefficients of various corner nodes of the plate depending on the anisotropy direction, and show a good agreement (cf. Fig. 9.3.2).

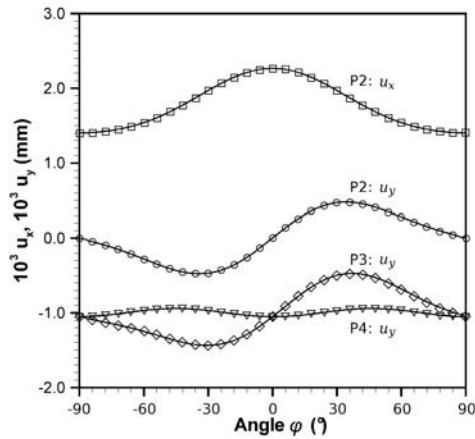


Figure 9.3.2: Tensile test. *OpenGeoSys* results (symbols) at length $l = 10$ mm and an edge load of $p_0 = 0.2$ MPa compared to the reference solution given by Schröder [89] and Kohlmeier [90] (continuous lines).

Benchmark deposit

Benchmark	Problem type	Path in benchmark deposit
<i>m-e-transiso_2D</i>	M	benchmarks\M\

9.3.2 Tensile test (3D)

Problem definition

To verify the linear elastic transverse isotropic material model in the three dimensional case, the tensile test analyzed in Sec. 9.3.1 was simulated using a rectangular sample with an edge length $l = 10\text{ mm}$ and a height $h = 1\text{ mm}$. According to the twodimensional case, a vertically arranged laminated material structure is assumed. The direction of anisotropy, which is defined by a vector \mathbf{a} is perpendicularly oriented to the material layers. During simulation, the direction of anisotropy is rotated counterclockwise in the xy -plane from $\varphi = 0^\circ$ to $\varphi = 180^\circ$.

Within the context of the different opportunities offered by the input structure of *OpenGeoSys* to define the anisotropy direction, the coefficients of the unit normal vector which is parallel to the direction of anisotropy are given as $n_x = \cos \varphi$, $n_y = \sin \varphi$, and $n_z = 0$. Considering the case that the basis vectors of the local Cartesian coordinate system for transverse isotropic materials are provided by consecutive rotations of the plane of isotropy about the global $y(x_2)$ -axis and the $\bar{x}(\bar{x}_1)$ -axis of the once rotated system, the angle α has a constant value of 90° , whereas the angle β changes from 0° to -180° . Using the angles known from applications in structural geology to generate the constitutive rotation matrices, the dip ϕ has the constant value of 90° , and the azimuth varies from $90^\circ \dots 0^\circ$ (for $0^\circ \leq \varphi \leq 90^\circ$) and $360^\circ \dots 270^\circ$ (for $90^\circ \leq \varphi \leq 180^\circ$) respectively.

For details of the model (geometry, boundary conditions, material orientation) see Fig. 9.3.3.

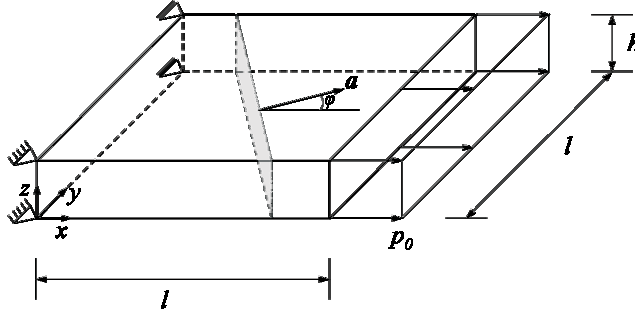


Figure 9.3.3: Tensile test. Threedimensional model definition according to Fiolká [91]. Vector \mathbf{a} defines the direction of anisotropy.

Initial and boundary conditions

The initial and boundary conditions are the same as described for the two dimensional example (cf. Sec. 9.3.1). The plane strain condition assumed for

the twodimensional case was realized preventing any displacement in z -direction on the upper and lower boundary surfaces of the sample.

Material properties

The material parameters are given in Tab. 9.3.1, as in the twodimensional case (cf. Sec. 9.3.1).

Results

The results in the corresponding corner nodes of the sample are exactly the same as presented in Fig. 9.3.2 (cf. Sec. 9.3.1).

Benchmark deposit

Benchmark	Problem type	Path in benchmark deposit
<i>m-e_transiso_3D</i>	M	benchmarks\3D\elasticity

9.4 Excavation in homogeneous media (3D)

Problem definition

A long round tunnel is build in the rock mass. The tunnel is 9 m lang and its radius is 0.33 m. We analyze the distribution of displacement and stresses after the excavation. Different with the above section there is no plain strain at top the model. Fig. 9.4.1

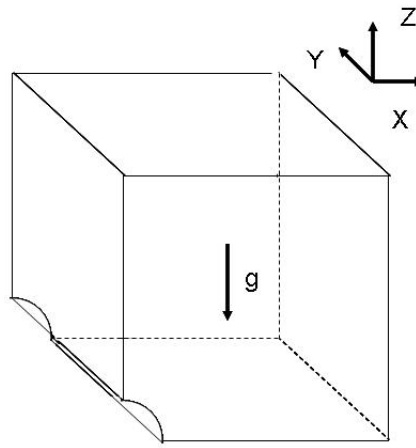


Figure 9.4.1: Conceptual model of elastic foundation

Initial and boundary conditions

The initial conditions are not required in this case. More detailed boundary conditions are illustrated in Fig. 9.4.2.

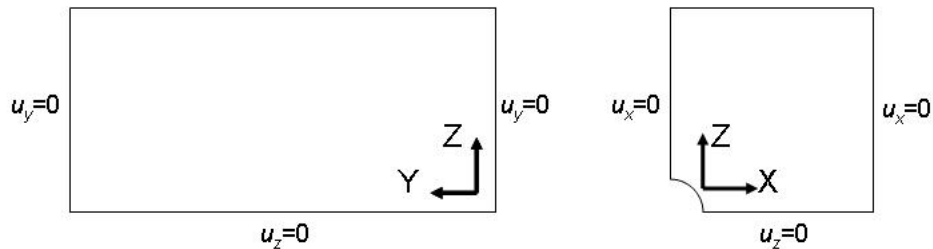


Figure 9.4.2: Boundary conditions

Material properties

Property	Value	Unit
Young's modulus	8	GPa
Poisson's ratio	0.2	—
Density	2500	kg/m^3

Table 9.4.1: Parameters

Results

Fig. 9.4.3 and 9.4.4 show the distribution of displacements and stresses after excavation.

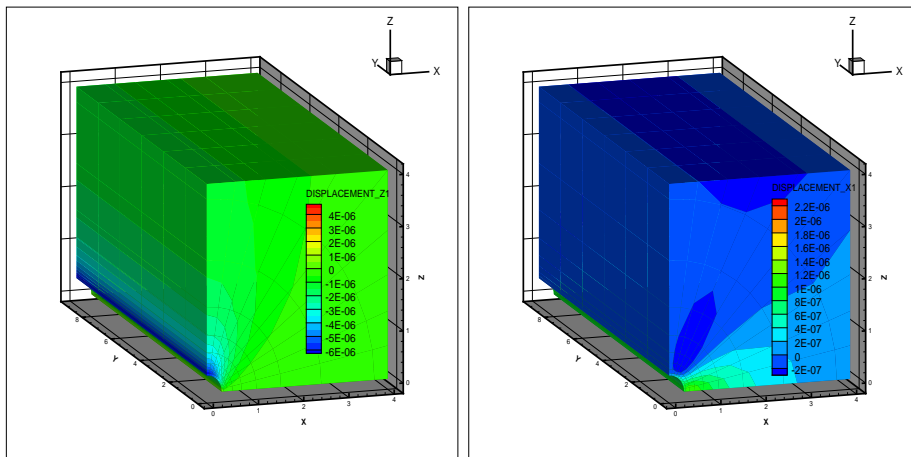


Figure 9.4.3: Distribution of displacement (m)

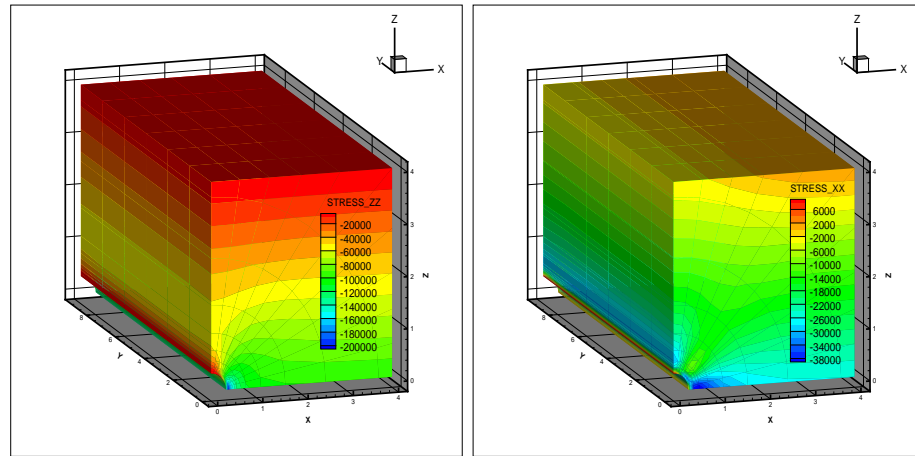


Figure 9.4.4: Distribution of stresses (Pa)

Fig. 9.4.5 shows the radial and tangential stresses in the X and Z direction. The results are compared to values obtained with FLAC3D version 3.10 and they are well matched. Nevertheless the results of tangential stresses at tunnel's boundary are not correct. This problem will be solved later.

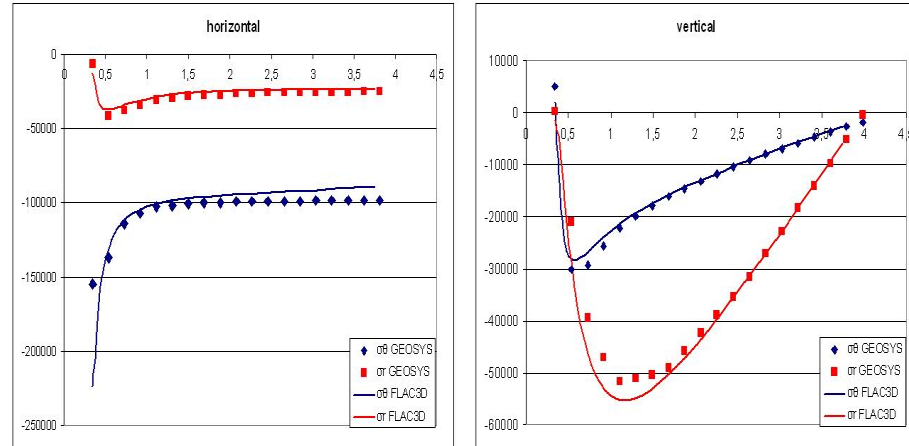


Figure 9.4.5: Distribution of stresses (Pa)

Benchmark deposit

Benchmark	Problem type	Path in benchmark deposit
3d_excav	M	benchmarks\M\excavation\3D_EX

9.5 Elasto-plasticity

Plasticity is a property of a material to undergo a non-reversible change of shape in response to an applied force. During the elasto-plastic deformation, the onset of plasticity is determined by a yield criterion and post-yield deformation is governed by the yield criterion and a plastic potential. To illustrate features of elasto-plasticity deformation, we consider a uniaxial test of stress depicted in Fig. 9.5.1.

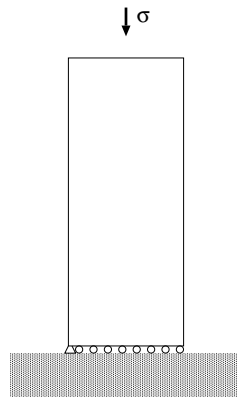


Figure 9.5.1: Uniaxial test

This means only one direction has non-zero stress and strain, e.g. $\sigma = \sigma_{yy}$ and $\epsilon = \gamma_{yy}$. Different material exhibits different elasto-plastic behavior. Fig. 9.5.2 depicts a typical

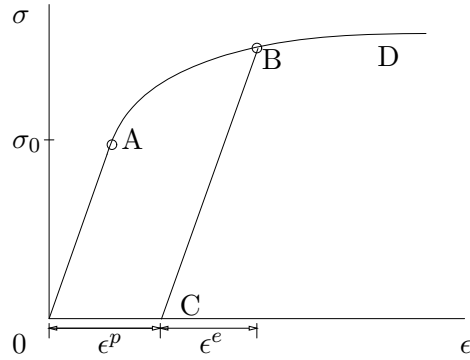


Figure 9.5.2: Stress-strain curve of 1D problems

stress-strain curve of the uniaxial test. If load σ is gradually increased, a corresponding point in (σ, ϵ) plane are moving from 0 to A. Up to A, stress reaches a value σ_0 , so called yield stress. If the load is removed gradually before its reaches the yield value, the point follows the line from A to 0. On the other

hand, if the load is continually increased after stress is bigger than σ_0 , the material experiences plastic deformation. Assuming the curve is extended from A to B during load acting. If we remove the load gradually, the point will not take the way its from, i.e. from B to A to 0. On the contrary, it will move from B to C linearly. Furthermore, if the load is applied again, the point will take the path from C → B → D.

This implies that: i) The unloading is elastic and there is still strain ϵ^p left after the load being removed, Therefore, the plastic deformation is irreversible; ii) The strain is admissible to be decomposed into several components, e.g. $\epsilon = \epsilon^e + \epsilon^p$; iii) The relationship of stress-strain is history dependent curve. Based on the last point and the Hook's law, the constitutive equation for the 1D deformation problem can be described as

$$\sigma_{yy} = E\epsilon_{yy}^e = E(\epsilon_{yy} - \epsilon_{yy}^p) \quad (9.5.1)$$

where E is so called Young's modulus. If the stress-strain is monotonic increasing after yielding, the material shows hardening behavior. For some porous media, softening behavior may be observed and its stress-strain curve looks like what depicted in Fig. 9.5.3.

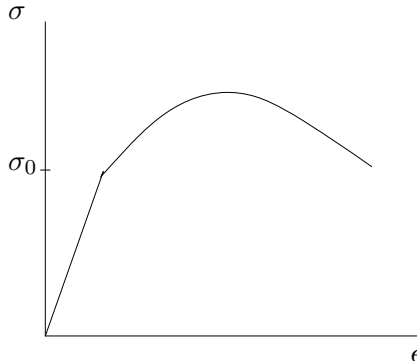


Figure 9.5.3: Softening

For the constitutive equation, the case of more than one direction have non-zero stress and strain are much more complicated. A yield function f and a plastic potential g are introduced to establish a constitutive equation. Normally, the variables of the two functions are the first, second or third stress invariant σ_v , II or III. If we cast the yield functions to the principal stress space, we get the yield surfaces. Fig. 9.5.4 depicts three typical yield surfaces of porous media.

If the stress path of any point locates inside the surface, the point undergoes elastic deformation. Otherwise, the stress status is determined by the Kuhn-Tucker criterion for the loading or unloading:

$$\dot{f} \leq 0, \quad \dot{\lambda}_p f = 0, \text{ or, } \dot{\lambda}_p \geq 0 \quad (9.5.2)$$

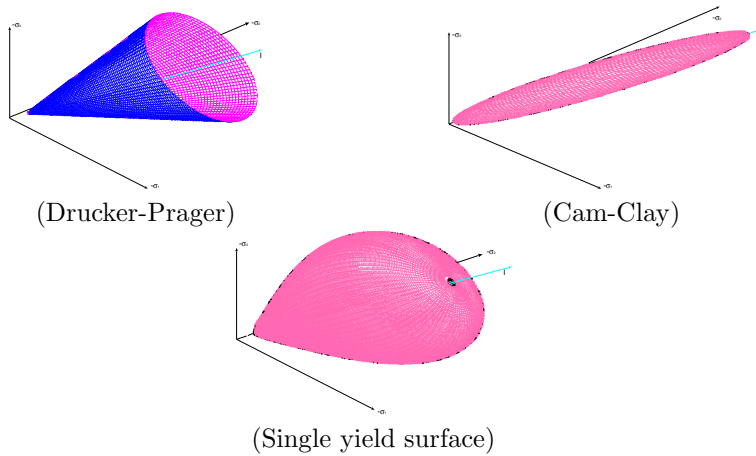


Figure 9.5.4: Yield surface

is then used to check the yield status.

Since the stress path in plastic deformation is history dependent, we describe the constitutive equations in the sense of increment of stress and strain. Considering the generalized Hook's law (9.2.1), the relationship of incremental stress tensor $d\sigma$ and incremental strain tensor $d\varepsilon$ the relationship of stress and strain obeys the generalized Hook's law:

$$d\sigma = \mathbf{D}d\varepsilon^e = \mathbf{D}(d\varepsilon - d\varepsilon^p) \quad (9.5.3)$$

From the definition of plastic potential surface g , and normality law, it is possible to express the generalized plastic strain increment if the potential surface is smooth. Since $d\varepsilon^p$ lies parallel to the normal to g at σ , we may write

$$d\varepsilon^p = d\lambda_p \frac{\partial g}{\partial \sigma} \quad (9.5.4)$$

where $d\lambda_p$ is non-negative factor, plastic multiplier. Equation (9.5.4) is so called flow rule. Hence, the general elasto-plastic constitutive equation is given by

$$d\sigma = \mathbf{D}d\varepsilon^e = \mathbf{D}(d\varepsilon - d\lambda_p \frac{\partial g}{\partial \sigma}) \quad (9.5.5)$$

The flow rule is associative if $f \equiv g$. Otherwise, it is non-associative. Typical plastic models, i.e. yield functions and plastic potentials are described below.

Drucker-Prager model

This model is a function of the two stress invariants and hardening parameter. Its yield function takes the form

$$f(\boldsymbol{\sigma}, \kappa) = \|\mathbf{s}\| + \alpha\sigma_v - y(\kappa) = 0 \quad (9.5.6)$$

$$g(\boldsymbol{\sigma}, \kappa) = \|\mathbf{s}\| + \beta\sigma_v - y(\kappa) = 0 \quad (9.5.7)$$

where α is a coefficient related to the internal frictional angle, $y(\kappa)$ is the yield stress depending on the hardening parameter.

Cam-Clay model

Similar to the Drucker-Prager model, the Cam-Clay model is a function of both of the first and the second stress invariants. The generalized Cam-Clay model reads:

$$f = q^2 + M^2 p_s (p_s - p_{scn}) = 0 \quad (9.5.8)$$

where $q = \sqrt{3/2} = \|\mathbf{s}\|$, $p_s = \sigma_v/3$ the mean stress, M is the slope of the critical state line in a $q - p_s$ diagram and p_{scn} is the isotropic preconsolidation pressure. The rate of p_{scn} is given by

$$\frac{dp_s}{d\epsilon_v^p} = \frac{(1+e)p_s}{\lambda_c - \kappa_c} \quad (9.5.9)$$

with e the void ratio, ϵ_v^p the volume plastic strain, λ_c the virgin compression index and λ_c the swelling/recompression index.

The model also describes the nonlinear elastic behavior of the clay-like media before plastic yielding occurs, in which the bulk modulus K is dependent of stress status as

$$K = \frac{1+e}{\kappa_c} p_s = 0 \quad (9.5.10)$$

with $\mu = 3(1-2\nu)K/(2(1+\nu))$.

9.5.1 Plastic plate - von Mises plasticity (2D)

Problem definition

This is a typical plane strain benchmark for von Mises plasticity, which is defined in [92]. We first analyze this example to compare the behavior of two approaches

on pure plastic deformation problems. In the present simulation, a quarter of plate is taken due to the symmetry of the problem. The model set-up is depicted in Fig. 9.5.5. The radius of the hole is 10mm. Two points as point 1 and point 2 are specified to monitor the evolution of variables. Point 1 is at one third of the distance from point 3 to point 4.

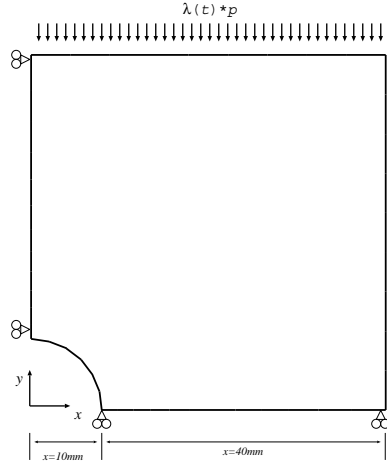


Figure 9.5.5: Stretched steel plate with a hole: one quarter

Boundary conditions

Traction boundary condition, $p = 100N/mm^2\lambda(t)$ is prescribed on the top with $\lambda(t)$, the time dependent scaling factor. The case of cycling loading is investigated with a scaling function depicted in Fig. 9.5.6, in which, $\lambda_{max} = 4.1$.

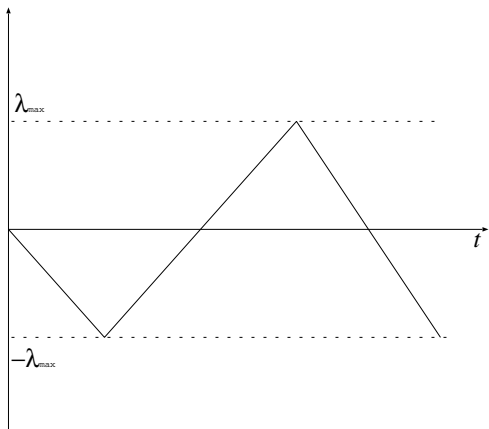


Figure 9.5.6: Time dependent load factor

The domain is triangulated as depicted in Fig. 9.5.7.

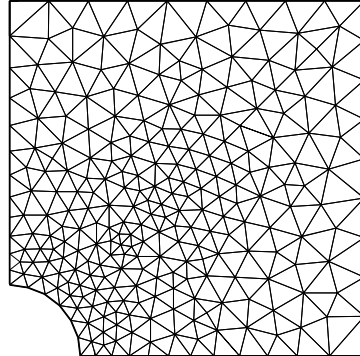


Figure 9.5.7: Mesh: 269 nodes and 484 elements

Material properties

The domain is assumed in homogeneous state. Table 9.5.1 gives the material parameters[92].

Table 9.5.1: Material properties

Property	Value	Unit
Young's modulus	206900	N/mm^2
Poisson's ratio	0.29	—
Initial yield stress	450	N/mm^2
Hardening modulus	0.0	kPa

Results

The loading takes 60 steps with constant increment of $\lambda_{max}/10$. The similar distribution of plastic strain and vertical stain given in Fig.9.5.8 shows implies the behavior of von Mises plasticity.

The evolution of horizontal displacements at point 1 and point 2 along with periodic load factor $\lambda(t)$ are shown on Fig.

9.5.9.

Benchmark deposit

Benchmark	Problem type	Path in benchmark deposit
<i>m-mises</i>	M	benchmarks\M\

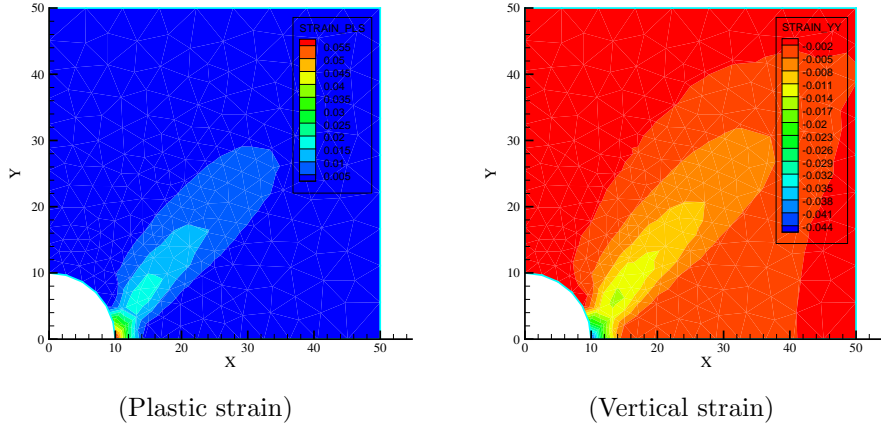
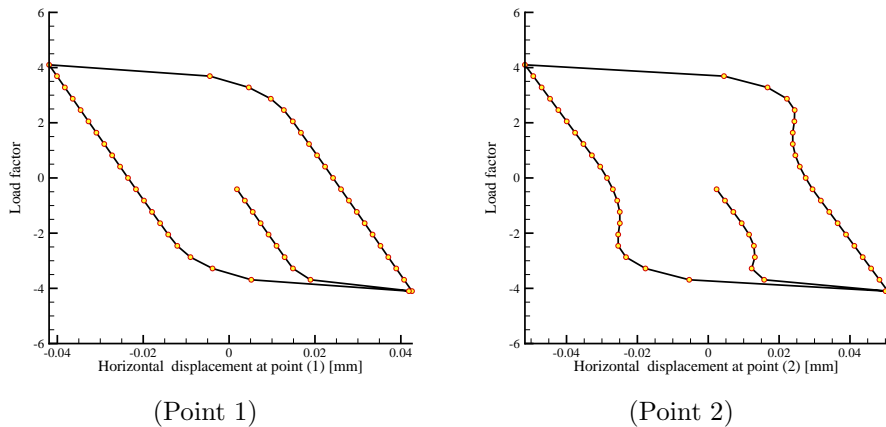
Figure 9.5.8: Distribution of plastic strain and vertical strain at $\lambda_{max}/10$ 

Figure 9.5.9: Evolution of horizontal displacement vs load factor

9.5.2 Plastic plate - Drucker-Prager plasticity, enhanced strain element (2D)

Problem definition

In this application, we analyze a plane strain biaxial failure deformation problem with triangle and quadrilateral elements, correspondingly. We use an enhanced strain approximation to simulate the displacement discontinuity after failure appears. Neighbor relationships of an element object are essential data for

constructing the deforming mesh and to determinate the propagation orientation of the discontinuity in the failure analysis.

From the view point of bifurcation theory, strain localization is a bifurcation phenomenon, which takes place when the velocity field moves away from the branch of continuous solutions and takes a new path of discontinuous solutions. If standard finite element is applied to this problem, we have to refine mesh adaptively near the localization area. Otherwise, the system equation is ill-posed. The strong discontinuity approach with enhanced strain element avoids the ill-posed system equations and therefore avoid mesh sensitive of the analysis [93].

The set-up of the biaxial compression problem as proposed by [94] is shown in Fig. 9.5.10. The geometry of the specimen is simplified to a rectangle with size of $1\text{m} \times 3\text{m}$.

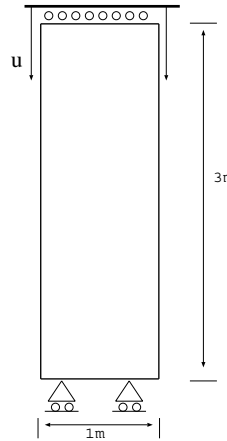


Figure 9.5.10: Plane strain biaxial test

Boundary conditions

The bottom of the specimen is placed on horizontal roll supporters. While the top of it is only allowed to a vertical down movement u_z . Both lateral sides are considered to be traction free.

Material properties

The non-associative flow rule is adopted for the Drucker-Prager model. All material parameters are given in Table (9.5.2)

Parameter	Unit	Value
Young's modulus	kPa	2×10^4
Poisson ratio	-	0.4
Parameter α	-	0.233345 (30° friction angle)
Parameter β	-	0.141421 (16.53° dilatancy angle)
Initial stress σ_0	kPa	29.69 (20 of initial cohesion)
Hardening modulus H	kPa	100
Localized softening modulus H_δ	kPa	-1000, varying

Table 9.5.2: Material parameters of the plane strain biaxial test

Results

Fig. 9.5.11 shows the deformed sample exhibiting localization. Fig. 9.5.12 depicts the stress reaction at the top surface due to the displacement load. The results agrees with what given in [94]

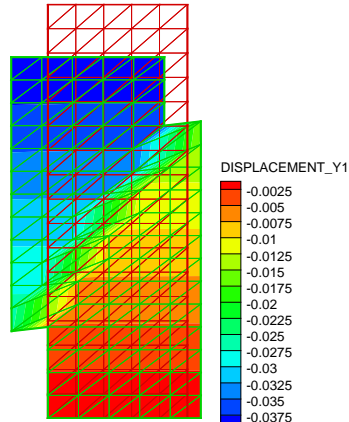


Figure 9.5.11: Vertical reaction of the top

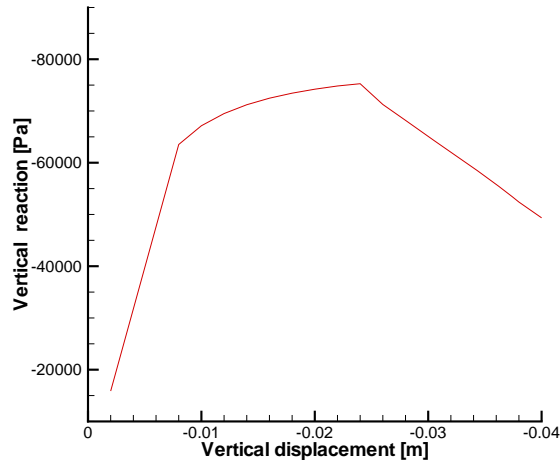


Figure 9.5.12: Vertical reaction of the top

Benchmark deposit

Benchmark	Problem type	Path in benchmark deposit
<i>m_sdc</i>	M	benchmarks\ M\

9.5.3 Plastic plate - Cam-Clay plasticity (2D)

Problem definition

This example is generally applied to verify a critical state plastic mode, i.e. Cam-Clay model. We consider a quarter of the cylindrical sample of 5cm in diameter and 10cm in length.

Initial and Boundary conditions

The bottom surface is roller supported. A vertical down displacement is prescribed to make an axial strain of 50%. The movement in the radial direction on the top surface is allowed. The cylindrical surface is traction free.

Material properties

Table 9.5.3 shows the material parameters.

Meaning	Value	Unit
Poisson ratio	0.3	—
Slope of the critical state line	1.2	—
Virgin compression index	0.2	—
swelling/recompression index	0.02	—
Initial preconsolidation pressure	60.0	--
Initial void ratio	1.5	--

Table 9.5.3: Solid material properties

Results

The problem is axisymmetrical. A relationship between von Mises type stress, the second stress invariant, and the axial strain is illustrated in Fig. 9.5.13. The results agrees with what given in [95].

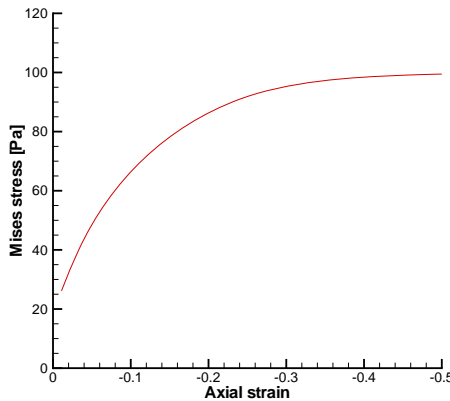


Figure 9.5.13: Axial strain vs von Mises type stress

Benchmark deposit

Benchmark	Problem type	Path in benchmark deposit
<i>m_cc_quad_s & m_cc_tri_s</i>	M	benchmarks\M\

9.5.4 Plastic plate - Rotational hardening plasticity (2D)

Problem definition

This example is a plane strain compression test on a material with both isotropic and rotational hardening behaviour.

The geometry of the specimen used is 0.34 m height and 0.1 m width. We denote by σ_x the stress acting on the both lateral sides of the specimen and by σ_y the stress applied to the top side of the specimen. The set-up of the problem is shown in Fig. 9.5.14.

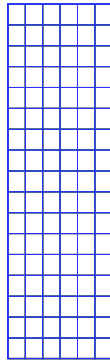


Figure 9.5.14: Plane strain biaxial test: rotational hardening

A vertical down displacement load is applied on the top boundary.

Material properties

Assume all initial stresses are zero. The material properties of the rotational hardening model are defined in Table 9.5.4

Results

The output of the results in a specified point, i.e. a center of a finite element close to the geometrical center of the domain (Fig. 9.5.14), is used to analyze the model behavior. Fig. 9.5.15 shows the varying of vertical stress along with vertical displacement at the top boundary.

Benchmark deposit

Benchmark	Problem type	Path in benchmark deposit
<i>m_ssy_quad</i>	M	benchmarks\M\

Parameter	Unit	Value
Young's modulus	Pa	1e+08
Poisson ratio	-	0.3
α_0	-	0.0
β_0	-	0.26
δ_0	m^2/N	3.5e-07
ε_0	m^2/N	1.0e-7
κ_0	N/m^2	0.0
γ_0	-	0.0
m_0	-	0.569
$\hat{\alpha}$	-	0.0
$\hat{\beta}_0$	-	0.29
$\hat{\delta}_0$	m^2/N	8.81e-9
$\hat{\varepsilon}_0$	m^2/N	1.5e-8
$\hat{\kappa}_0$	N/m^2	0.0
$\hat{\gamma}_0$	-	0.0
\hat{m}_0	-	1.0
ψ_1	-	0.55
ψ_2	-	-0.26
C_h	-	0.81e-3
C_d	-	0.60e-3
b_r	-	100.0
m_r	-	-3.0

Table 9.5.4: Material parameters of rotational hardening model

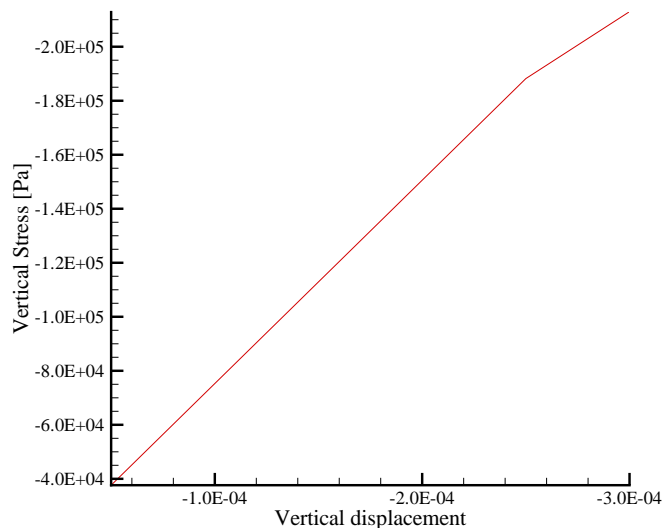


Figure 9.5.15: Vertical stress vs vertical displacement

9.6 Creep

Creep is a time-dependent and/or temperature-dependent deformation process of a solid body under the influence of a constant load. Creep is a phenomenon of time effect to deformation such that the tendency of a material to move or to deform is permanent to relieve stresses. Similar to plastic potential, a creep potential F_c is introduced to describe the constitutive equations.

Usually, a stationary creep model is sufficient to describe the creep phenomena in geological media, such as soil and rock. Norton's model reads that the creep potential F_c can be expressed by a function of the first stress invariant σ_v as

$$F_c = \frac{\alpha}{n+1} \sigma_v^{n+1} \quad (9.6.1)$$

where α and n are material parameters, which have to be determined by experiments. Assuming the total strain increment $d\boldsymbol{\varepsilon}$ is admissible to be decomposed in several portions contributed by different physical reactions such elasticity, plasticity and creep, it can be written as

$$d\boldsymbol{\varepsilon} = d\boldsymbol{\varepsilon}^e + d\boldsymbol{\varepsilon}^p + d\boldsymbol{\varepsilon}^c \quad (9.6.2)$$

Similar to the plastic flow rule, we can derive the strain rate resulting from creep as

$$d\boldsymbol{\varepsilon}^c = \frac{\partial F_c}{\partial \boldsymbol{\sigma}} = \left(\frac{3}{2}\right)^{(n+1)/2} \alpha \|\mathbf{s}\|^{n-1} \mathbf{s} \quad (9.6.3)$$

Applying explicit Euler's method to equation (9.6.3), the increment of the strain by creep is obtained from

$$\Delta\boldsymbol{\varepsilon}^c = \left(\frac{3}{2}\right)^{\frac{n+1}{2}} \alpha \|\mathbf{s}^k\|^{n-1} \mathbf{s}^k \Delta t \quad (9.6.4)$$

where \mathbf{s}^k is the deviatoric stress of the previous time step k and Δt is the time step size. Using the generalized Hook's law, the stress change deduced by the creep stain increment is

$$\Delta\boldsymbol{\sigma}^c = \mathbf{D}^e \Delta\boldsymbol{\varepsilon}^c \quad (9.6.5)$$

with \mathbf{D}^e the elastic material tensor.

9.6.1 Creep of a cylindrical sample

Problem definition

In this example, creep is considered in a thick cylinder subjected a constant normal pressure at the inner face. The boundary conditions are as follows: $p = 2.515$ MPa at the inner surface and zero normal stress at the outer surface, no displacements in axial direction. The inner radius of the cylindrical sample is 4

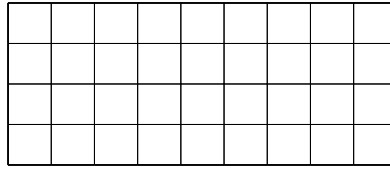


Figure 9.6.1: Mesh for thick cylinder undergoes creep deformation

mm, the outer radius is 6.4 mm and the height is 1 mm. Quadrilateral elements are adopted for meshing (Fig. 9.6.1).

We assume that the initial stress is homogeneously distributed in the domain as $\sigma_r^0 = \sigma_\theta^0 = \sigma_z^0 = -50$ Pa. The parameters of the Norton creep model are given in Tab. 9.6.1.

Symbol	Meaning	Value	Unit
α	Norton model parameter 1	6.415×10^{-10}	–
n	Norton model parameter 2	4	–
ν	Poisson ratio	0.48	–
E	Young's modulus	1.378×10^5	MPa

Table 9.6.1: Material parameters of the Norton creep model

Results

Figs. 9.6.2 and 9.6.3 give the distribution of the first stress invariant and radial displacement along radial direction and the comparison with pure elastic solution. They demonstrated that \mathbf{s} at inner surface decreases about 26% after steady state of creep reached. While radial displacements increase about 200%. The results can be compared with Balley's analytical solution, which reads for rate of radial displacement as

$$\dot{u}_r = \alpha \frac{3^{\frac{n+1}{2}}}{2n^n} \frac{r_a^2 r_b^2 p^n}{(r_b^{2/n} - r_a^{2/n})r}$$

and for the steady state of first stress invariant

$$\sigma_v = \frac{2\sqrt{3}}{2n} \frac{p (r_b/r)^{\frac{2}{n}}}{(r_b/r_a)^{2/n} - 1}$$

Benchmark deposit

Benchmark	Problem type	Path in benchmark deposit
<i>m_crp_tri</i>	M	benchmarks\M\

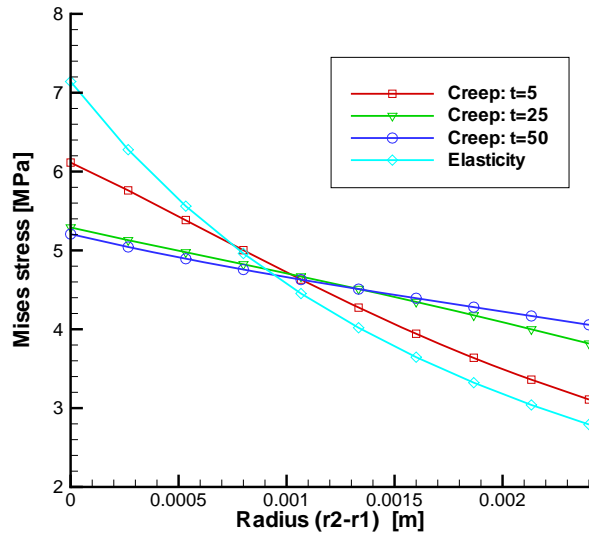


Figure 9.6.2: First stress invariant profiles during creep at different times, $t = 5, 25, 50$ sec, and comparison to elastic solution

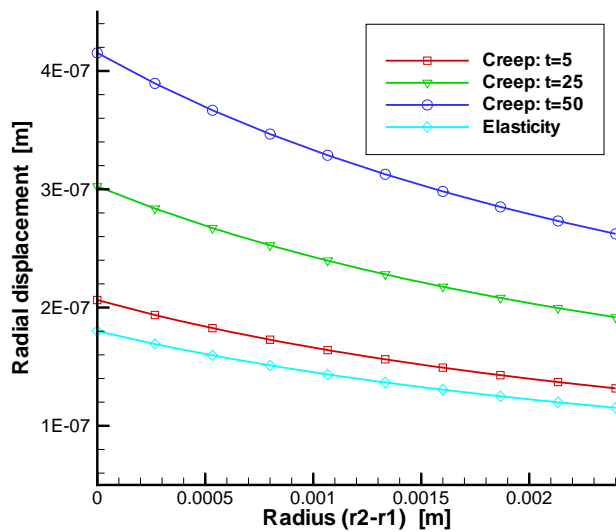


Figure 9.6.3: Radial displacement profiles during creep at different times, $t = 5, 25, 50$ sec, and comparison to elastic solution

9.6.2 Creep in salt rock

Several models exists for the evaluation of the effect of stationary creep in rock salt, i.e the strain variation with time is calculated. One of those models is the BGra-model (9.6.6), which is valid for loads between 5 and 25 MPa in a temperature range of 22-200°C (Hunsche and Schulze, 1994).

$$\dot{\epsilon}^c = A e^{-\frac{Q}{RT}} \left(\frac{\sigma}{\sigma^*} \right)^n \quad (9.6.6)$$

Table 9.6.2 depicts the symbols of equation (9.6.6), their meaning and parameter values.

Symbol	Meaning	Value	Unit
$\dot{\epsilon}$	Strain rate		1/d
σ	Effective stress		MPa
A	Material constant	0.18	1/d
Q	Activation energy	54	kJ/mol
R	Gas constant	8.31447215	J/(K mol)
n	Material constant	5	—
σ^*	Reference effective stress	1	MPa

Table 9.6.2: Creep model, symbols and material values

Example 1: Temperature dropping (relaxation)

Problem definition In a sample of rock salt a stress relaxation is caused by a temperature decrease of 30 K. The aim of the example is to calculate the resulting strain variation with time within the solid body by the use of the stationary creep model BGra (9.6.6). The results of the simulation using an axial symmetric calculation model and a 3D model are compared afterwards.

Assumptions	Heat	Constant temperature in the whole body at the beginning (330 K), temperature decrease of 30 K
	Solid	Homogenous, finite dimensions, no deformation at the boundaries in z-direction at the bottom and the top

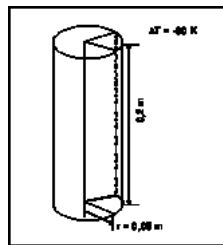


Figure 9.6.4: Core sample model

For the 2D numerical simulation a cylindrical core sample as shown in Fig. 9.6.4 is selected. The 2D numerical model is an axial symmetric one in the x-z-plane (see Fig. 9.6.5). The dimensions of this 2D model are: 0.05 m radius (x-direction) and 0.2 m of height. A relatively coarse mesh consisting of 228 triangular elements and 139 nodes is used. Vertical deformations at the top and the bottom are suppressed (no displacement boundary conditions). The initial temperature in the whole area is 330 K. At the top and the bottom of the model thermal boundary conditions are set with a temperature of 300 K. Thereby the stress relaxation during the cooling down is simulated. The used parameters of the solid represent the material behavior of rock salt are given in Tab. 9.6.2. The calculation is divided in 360 time steps with a constant time step length of 1 day.

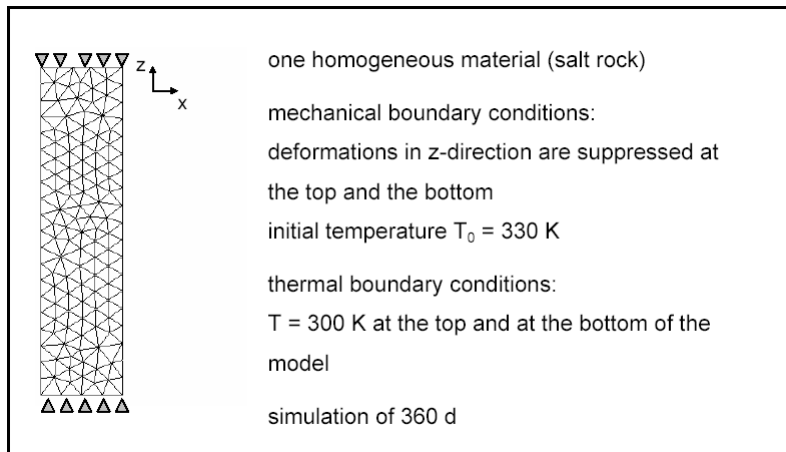


Figure 9.6.5: Numerical axisymmetrical model

Table 9.6.3 depicts the values of material properties for the thermo-mechanical creep model.

Symbol	Meaning	Value	Unit
T_0	Initial temperature (before cooling down)	330	K
T	Temperature after cooling down	300	K
E	Young's modulus	25	GPa
ν	Poisson ratio	0.27	–
α	Thermal expansion coefficient	4×10^{-5}	1/K
c	Thermal capacity	1	J/(kg K)
λ	Thermal conductivity	100	W/(m K)

Table 9.6.3: Material parameters of the thermo-mechanical creep model

Analytical solution In order to evaluate the numerical results of the relaxation problem, the analytical solution of equation (9.6.7) (Eickemeier 2007, personal communication) for the difference of effective stresses within one time step can be applied.

$$\Delta\sigma_{i+1} = \frac{(\dot{\varepsilon}_1^c - A(\sigma/\sigma^*)^n)E_q\Delta t}{1 - E_q/\sigma^*A^*\Delta t\xi n(\sigma/\sigma^*)^{n-1}} \quad (9.6.7)$$

and

$$A^* = Ae^{-Q/RT} \quad (9.6.8)$$

where the initial strain rate $\dot{\varepsilon}_1^c$ in this case is zero, E_q in general is the weighted Young's modulus of the steel plates and the salt rock sample (in this case we consider only salt rock), $\xi = 0.5$.

For the analytical solution of the equation (9.6.7) the vertical stress before the last time step is considered. Time step increment is $\Delta t = 1$ d. The calculation is done for node 705 of the 3D model (Fig. 9.6.6), which is located at point $(x,y,z)=(0.05,0,0.12)$. The calculated stress difference σ_{i+1} has to be identical to the numerical result.

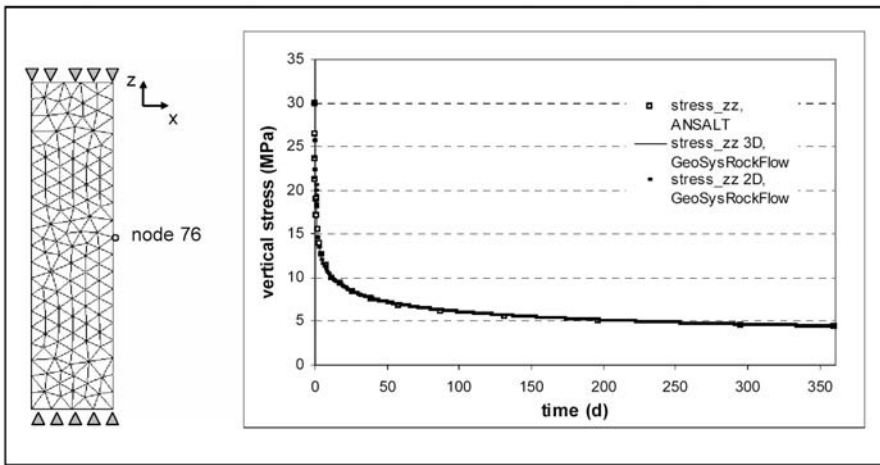


Figure 9.6.6: Comparison of numerical results (GeoSys/RockFlow vs ANSALT) for vertical stresses

Results The comparison of the stress increment σ_{i+1} which was obtained by the use of equation (9.6.7) is identical to the value (of vertical stresses) at node 705 (at the same location as node 76, see Fig. 9.6.6) of the 3D numerical calculation. Both stress increments σ_{i+1} obtained by GS/RF and ANSALT are equal to 3.05×10^{-3} MPa. Additionally, the numerical results for vertical stresses of the 2D simulation at node 76 are compared to the results that were obtained by simulating the creep process by the FE programme ANSALT (Nipp 1988) and also to the results of the 3D simulation with GS/RF at node 705. The

comparison of the results of GS/RF in 2D and 3D with the ANSALT findings are depicted in Fig. 9.6.6.

The input data and boundary conditions for each calculation model are identical. Also the results show a good accordance. That means, the creep simulation (2D and 3D) of GS/RF by using the implemented BGra model provides correct results.

Benchmark deposit

PCS type	MSH type	Files	Version	Date	Author
TM	axial-symmetry	BGRa	4.4.10(WW)	13.03.07	BGR
TM	axial-symmetry	creep3d	4.4.10(WW)	13.03.07	BGR

Example 2: Creep under constant load

Problem definition In the same example that is described in section 9.6.2 the creep process is now assumed to be caused by a constant load at the bottom of the solid and a constantly high temperature at the same time. The aim of this example is to calculate the resulting strain variation with time by using the stationary creep model BGra (9.6.6).

We specify the initial and boundary conditions for the 2D numerical model. For the simulation with GS/RF almost the same calculation models (2D and 3D) as in the precedent creep example were selected. Only the height of the solid is 0.25 m instead of 0.2 m. The initial temperature in the whole area is 373.15 K. There is a constant load of 5 MPa at the bottom of the model as boundary condition. The calculation is divided in 100 time steps with a constant time step length of 1 day.

Analytical solution In order to find out, whether the numerical solutions of GeoSys/RockFlow accord to the results of the BGra model (9.6.6), the input parameter A is compared to the A , which results from the simulation run. For this calculation equation (9.6.6) is converted to the following expression.

$$A = \frac{\dot{\varepsilon}^c}{e^{-Q/RT} \sigma_{\text{eff}}} \quad (9.6.9)$$

with

$$\begin{aligned} \sigma_{\text{eff}} &= \frac{1}{\sqrt{2}} \sqrt{(\sigma_1 - \sigma_2)^2 + (\sigma_2 - \sigma_3)^2 + (\sigma_3 - \sigma_1)^2} \\ \dot{\varepsilon} &= \frac{\varepsilon_{\text{eff}}(t + \Delta t) - \varepsilon_{\text{eff}}(t)}{\Delta t} \\ \varepsilon_{\text{eff}} &= \frac{\sqrt{2}}{3} \sqrt{(\varepsilon_1 - \varepsilon_2)^2 + (\varepsilon_2 - \varepsilon_3)^2 + (\varepsilon_3 - \varepsilon_1)^2} \end{aligned} \quad (9.6.10)$$

For these calculation steps the stresses of the regarded time period have to be constant. Equations (9.6.11) are solved for node 25 (see Fig. 9.6.7) of the 2D numerical model. The last time step at $t = 100$ days of the simulation run was considered.

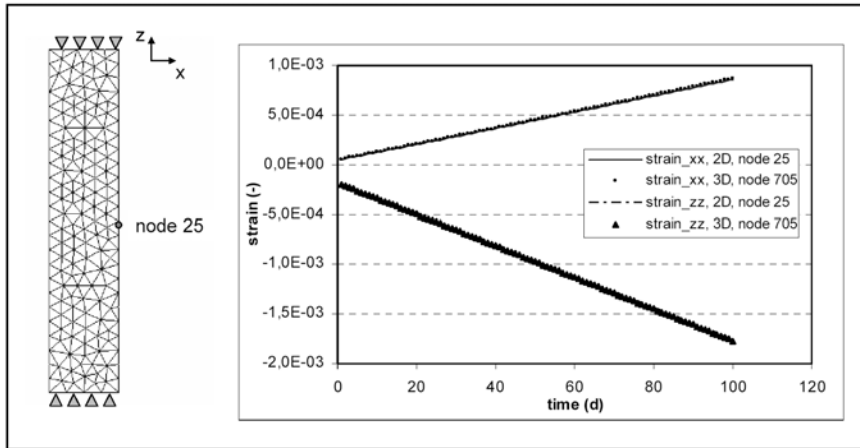


Figure 9.6.7: Comparison of 2D and 3D numerical results for strains (x- and z-directions)

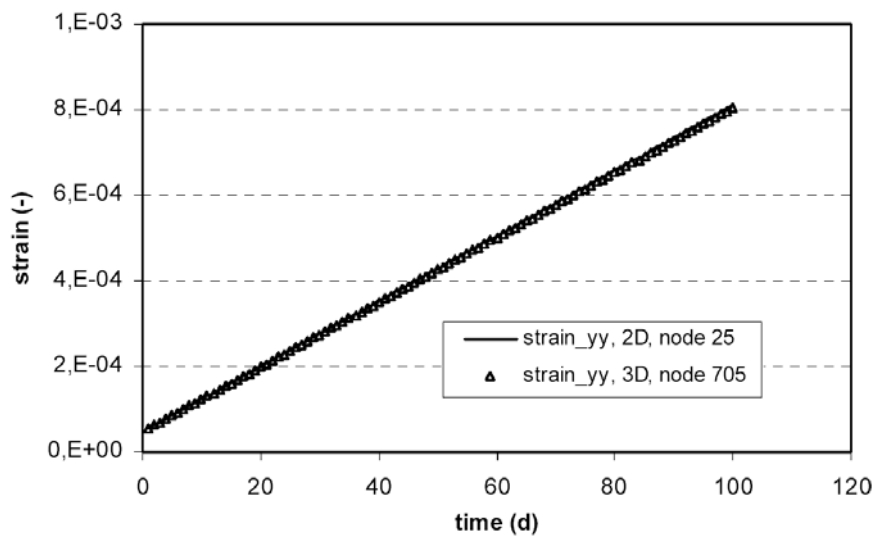


Figure 9.6.8: Comparison of 2D and 3D numerical results for strains (y-direction)

Results The effective stress σ_{eff} at node 25 and for the given time span is 5.03 MPa, which was calculated by the use of equation (9.6.11). The strain of time step 1 is $\varepsilon_{\text{eff}}(t_1) = 1.72 \times 10^{-3}$ and of time step 2: $\varepsilon_{\text{eff}}(t_2) = 1.73 \times 10^{-3}$, calculated by equation (9.6.11), is equal to $1.6 \times 10^{-5} d^{-1}$. After equation (9.6.9) the calculated parameter A is equal to 0.19, which corresponds approximately to the input A of 0.18. Therefore, it can be summarized that the BGRa creep model is implemented in GeoSys/RockFlow properly. The comparison between the 2D (node 25) and 3D results (node 705) are depicted in Fig. 9.6.7 and Fig. 9.6.8. The 2D and 3D results are identical to each other.

Benchmark deposit

PCS type	MSH type	Files	Version	Date	Author
M	axial-symmetry	uc_creep01	4.4.10(WW)	13.03.07	BGR
M	axial-symmetry	uc_creep3d	4.4.10(WW)	13.03.07	BGR

9.6.3 Lubby2: Transient and stationary creep model

Viscoplastic creep is mainly caused by diffusion and dislocations at the microscale, and results in hardening as well as recovery aspects. Hou and Lux propose an evolutional equation for the (viscoplastic) creep strain rate considering stationary as well as transient creep, damage impact, hardening and recovery (cf. [96, 97, 98]). Neglecting damage effects, this approach is known as Lubby2 model.

$$\dot{\varepsilon}^c = \frac{3}{2} \left[\frac{1}{\eta_k} \left(1 - \frac{\varepsilon^{tr}}{\max \varepsilon^{tr}} \right) + \frac{1}{\eta_m} \right] s \quad (9.6.11)$$

Here s denotes the deviatoric stress tensor

$$s = \sigma - \frac{1}{3}(\text{tr } \sigma) I \quad (9.6.12)$$

and ε^{tr} the equivalent transient creep strain

$$\varepsilon^{tr} = \sqrt{\frac{2}{3} \varepsilon^{tr} \cdot \varepsilon^{tr}} \quad (9.6.13)$$

with $\varepsilon^{tr} = \varepsilon^c - \varepsilon^{st}$ (ε^{st} – stationary creep fraction). In addition to the equivalent transient creep strain the generalized representation of the von Mises equivalent deviatoric stress s_v is defined.

$$s_v = \sqrt{\frac{3}{2} s \cdot s} \quad (9.6.14)$$

Furthermore, the following material functions are suggested, considering only hardening, and neglecting recovery effects:

$$\max \varepsilon^{tr} = \frac{s_v}{G_k} \quad (9.6.15)$$

$$G_k = \bar{G}_k^* \exp(k_1 s_v) \quad (\text{Kelvin shear modulus}) \quad (9.6.16)$$

$$\eta_k = \bar{\eta}_k^* \exp(k_2 s_v) \quad (\text{Kelvin viscosity modulus}) \quad (9.6.17)$$

$$\eta_m = \bar{\eta}_m^* \exp(m s_v) \exp(lT) \quad (\text{Maxwell viscosity modulus}) \quad (9.6.18)$$

As T denotes the absolute temperature, the following material parameters are necessary to model various constitutive effects:

- \bar{G}_k^* , k_1 hardening,
- $\bar{\eta}_k^*$, k_2 transient creep, and
- $\bar{\eta}_m^*$, m , l stationary creep.

Problem definition

Triaxial long-term compression under axisymmetric conditions is carried out to verify the Lubby2 creep model, and to study transient as well as stationary creep behavior assuming isothermal conditions and neglecting damage processes. As described in Sec. 9.2.7, for the calculation, the cross-section of a cylindrical sample with a radius of 30 mm and a height of 120 mm is studied. The loading in principal axes includes a radial pressure as well as an axial pressure, and is realized in two steps. It is resulting in a homogeneous stress-strain state. Details of the model (geometry, mesh, boundary conditions) according to K.-H. Lux and F. Werunsky (unpublished report, 2008) are presented in Fig. 9.6.9.

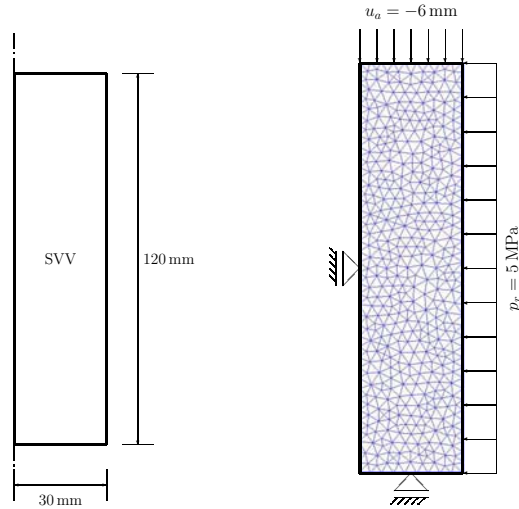


Figure 9.6.9: Triaxial compression of a cylindrical sample. Axisymmetric model. Left: Geometry. Right: Finite element grid and boundary conditions.

Initial and boundary conditions

Initial conditions do not have to be given for the problem under consideration. As the bottom edge is fixed in vertical direction, the left-hand edge is fixed in horizontal direction for symmetry reasons (axis of rotation). On the right-hand edge initially a radial casing pressure of 5 MPa is applied within 60 seconds with a constant stress rate. While keeping constant this radial pressure, a subsequent stress-driven axial compressive loading is applied within the following 1 440 seconds with a constant stress rate. The maximum axial pressure is 18 MPa. In the following, both the radial and the axial pressures are kept constant for 20 days (for the loading history cf. Fig. 9.6.10).

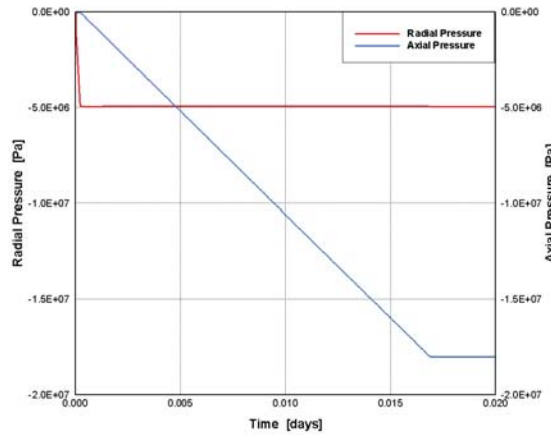


Figure 9.6.10: Triaxial compression of a cylindrical sample. Loading history for long-term creep experiments. Radial casing pressure (stress rate $\dot{p}_r = 0.083 \text{ MPa}\cdot\text{s}^{-1}$) with subsequent axial pressure (stress rate $\dot{p}_a = 0.0125 \text{ MPa}\cdot\text{s}^{-1}$). Each pressure loading with subsequent constant values over 20 days.

Material properties

The modified Lubby1 model was considered to generate the fourth-order elastic material matrix for the creep model under consideration. Within this context, the material parameters referring to the modified Lubby1 relation (9.2.11) are given in Tab. 9.6.4. The material parameters for the creep fraction (Lubby2 (9.6.11)) are given in Tab. 9.6.5. Within this context, the initial Young's modulus, the Poisson's ratio and all the creep parameters are close to values known for rock salt according to K.-H. Lux, M. Rutenberg and F. Werunsky (unpublished report, 2008).

Property	Value	Unit
Poisson's ratio ν	0.335	—
initial Young's modulus E_0	21 400	MPa
factor a in (9.2.11)	27 500	—
exponent n in (9.2.11)	1.0	—

Table 9.6.4: Material parameters for the elastic fraction of the material model (cf. Sec. 9.2.7)

Property	Value	Unit
Maxwell viscosity $\bar{\eta}_m^*$ in (9.6.18)	$1.09 \cdot 10^7$	MPa·day
factor m in (9.6.18)	-0.219	MPa $^{-1}$
factor l in (9.6.18)	0.0	K $^{-1}$
Kelvin viscosity $\bar{\eta}_k^*$ in (9.6.17)	$1.45 \cdot 10^5$	MPa·day
factor k_1 in (9.6.16)	-0.146	MPa $^{-1}$
factor k_2 in (9.6.17)	-0.121	MPa $^{-1}$
Kelvin shear modulus \bar{G}_k^* in (9.6.16)	$7.0 \cdot 10^4$	MPa

Table 9.6.5: Material parameters for the creep fraction of the material model

Results

The representation of the axial stress vs. the axial strain in Fig. 9.6.11 shows the complex creep behavior of the sample under consideration.

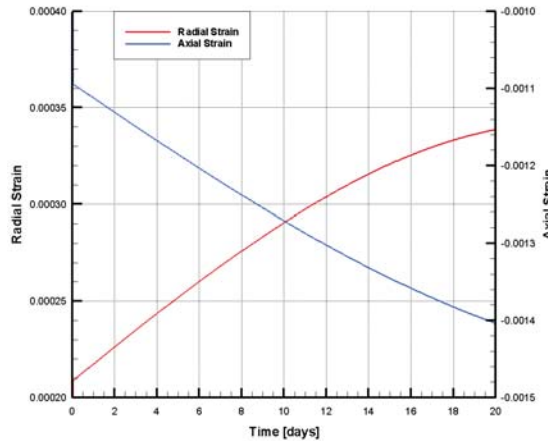


Figure 9.6.11: Triaxial compression of a cylindrical sample. Numerical simulation of the transient and stationary creep behavior using the Lubby2 model (9.6.11).

Benchmark deposit

Benchmark	Problem type	Path in benchmark deposit
<i>m_triax_lubby2</i>	M	benchmarks\М\creep

Chapter 10

Mass Transport – C-Processes

10.1 Theory

The mass transport in a homogeneous, saturated aquifer can be influenced by convection, diffusion, decay and biodegradation, sorption and chemical reactions. For a steady state 1-dimensional flow through a homogeneous isotropic medium with constant material parameters the following differential equation 10.1.1 is applied.

$$\frac{\partial C}{\partial t} + \frac{\rho_b}{R} \cdot \frac{\partial S}{\partial t} + \frac{q}{R} \cdot \frac{\partial C}{\partial x} = D_{xx} \cdot \frac{\partial^2 C}{\partial x^2} - \lambda \cdot C \quad (10.1.1)$$

with

- C – dissolved concentration ($\text{kg} \cdot \text{m}^{-3}$),
- S – sorbed concentration ($\text{kg} \cdot \text{kg}^{-1}$),
- t – time (s),
- ρ_b – bulk density ($\text{kg} \cdot \text{m}^{-3}$),
- R – retardation factor (-),
- q – flow rate ($\text{m} \cdot \text{s}^{-1}$),
- x – distance (m),
- D_{xx} – dispersion coefficient in x-direction ($\text{m}^2 \cdot \text{s}^{-1}$),
- λ – decay rate (s^{-1}).

This equation is used to calculate the concentration distribution under consideration of decay and sorption with the linear Henry-isotherm. The retardation coefficient R for the Henry isotherm is related to the Henry sorption coefficient K_D in the following way (equ. 10.1.2).

$$R = 1 + \frac{\rho_b}{\Phi} K_D = 1 + \frac{1 - \Theta}{\Phi} \rho_s K_D \quad (10.1.2)$$

with

$$\begin{aligned}\Phi &= \text{porosity } (-), \\ \rho_s &= \text{density } (\text{kg} \cdot \text{m}^{-3}),\end{aligned}$$

with the initial and boundary conditions

$$C(x, t = 0) = C_I \quad \forall x$$

with C_I - concentration at time I .

$$C(x = 0, t) = C_0 \quad \forall t, \quad \frac{\partial C}{\partial x}(x \rightarrow \infty, t) = C_I \quad \forall t > 0$$

with C_0 - initial concentration.

The following analytical solution is significant:

$$\begin{aligned}C = C_1 &+ (C_0 - C_1) \cdot \frac{1}{2} \left[\exp \left(\frac{v \cdot x(1 - \gamma)}{2 \cdot D_{xx}} \right) \cdot \operatorname{erfc} \left(\frac{x - v \cdot \gamma \cdot t/R}{2 \cdot \sqrt{D_{xx} \cdot t/R}} \right) \right. \\ &\left. + \exp \left(\frac{v \cdot x(1 + \gamma)}{2 \cdot D_{xx}} \right) \cdot \operatorname{erfc} \left(\frac{x + v \cdot \gamma \cdot t/R}{2 \cdot \sqrt{D_{xx} \cdot t/R}} \right) \right] \quad (10.1.3)\end{aligned}$$

with v - velocity

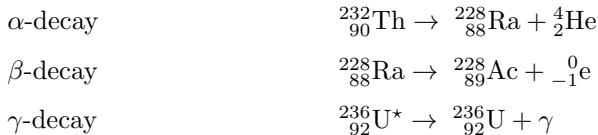
$$\gamma = \sqrt{1 + 4 \cdot \lambda \cdot R \cdot D_{xx}/v^2}. \quad (10.1.4)$$

Equation 10.1.3 is the basis for the verification of the RockFlow-simulation results for the 1-dimensional mass transport. All described equations and all analytical solutions of equation 10.1.3 are taken from [21].

10.2 Solute transport with decay

Theory

Radioactive decay is the change in the composition of a core by emitting particles and/or electro-magnetic radiation. Different kinds of radioactive decay are i.e. decay as a result of emission of negatrons or positrons and decay under emission of γ -rays.



The above given examples show that the radioactive decay is an irreversible process. The following differential equation describes the decay as first order reaction (without chain development):

$$\frac{\partial C}{\partial t} = -\lambda \cdot C \quad (10.2.1)$$

with λ - decay rate (s^{-1}).

The integration of this equation causes an exponential decay term in the following form.

$$C(t) = C_0 \cdot e^{-\lambda \cdot t} \quad (10.2.2)$$

with C_0 - initial concentration ($kg \cdot m^{-3}$).

The decay values are commonly expressed as the so-called half life ($t_{1/2}$). This is the point of time when half of the substance is degraded. The relation between the half-life T and the decay rate results from:

$$e^{-\lambda \cdot t} = \frac{1}{2} \Rightarrow \lambda = \frac{\ln(2)}{T} \cong \frac{0.693}{T} \quad (10.2.3)$$

Problem definition

The aim of this example is to simulate the mass transport with the influence of decay, but without any sorption. At the left side of the considered aquifer there is a volume source of $0.1 \text{ m}^3/\text{d}$, at the right side there is a constant water pressure of 20 kPa . The tracer substance in the source volume is distributed by a stationary flow in the homogeneous aquifer. The mass distribution after 100 days has to be calculated. Figure 10.2.1 shows a sketch of the calculation area.

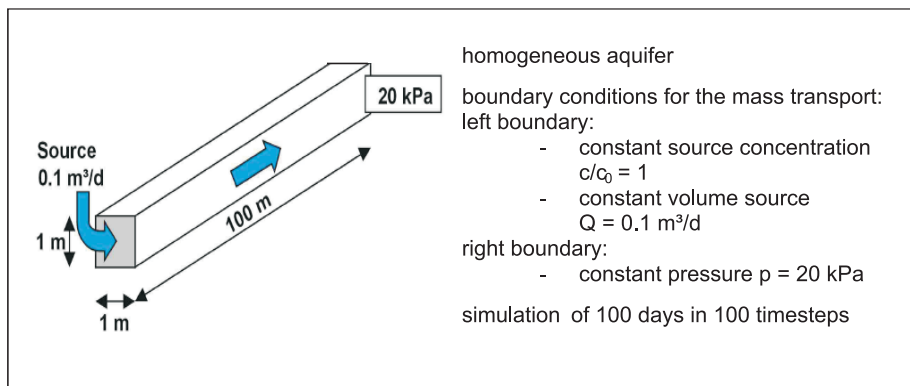


Figure 10.2.1: Calculation area: homogeneous aquifer

Assumptions

Component: no sorption, exclusively decay
 Aquifer: homogeneous, saturated, stationary flow

Model set-up of the 1 D numerical model

For the 1-dimensional calculation the calculation area is simplified as a line of a length of 100 m with 100 elements and 101 nodes. As boundary conditions the relative concentration amounts 1 and the source volume of the fluid phase with $0.1 \text{ m}^3/\text{d}$ is given at the left border of the calculation area and a constant pressure of 20 kPa at the right boundary. The used parameters of the soil are listed in table 10.2.1. The calculation is divided into 100 time steps with a constant time step length of 1 day. That means, the flow and transport processes in the aquifer within 100 days are simulated.

parameter	value	unit
porosity Φ	0.2	–
permeability K	$1.0 \cdot 10^{-12}$	m^2
density water ρ	1000	$\text{kg} \cdot \text{m}^3$
viscosity water η	0.001	$\text{Pa} \cdot \text{s}$
dispersion length α_l	5.0	m
decay in solved phase λ	$2.0 \cdot 10^{-7}$	s^{-2}

Table 10.2.1: Used parameters

Evaluation method

The concentration distribution at a special point in time and over a given distance is calculated by equation 10.1.3. Hereby the retardation coefficient is set equal to 1. The analytical solutions are depicted in figure 10.2.2 as single symbols.

Results

In figure 10.2.2 you can find the concentration distribution over the whole length of the 1 D model at the final simulation time of 100 days. Obviously, the numerical results meet well the analytical solutions.

Benchmark	Problem type	Path in benchmark deposit
hc_decay_1Du	HC	benchmarks \HC\decay

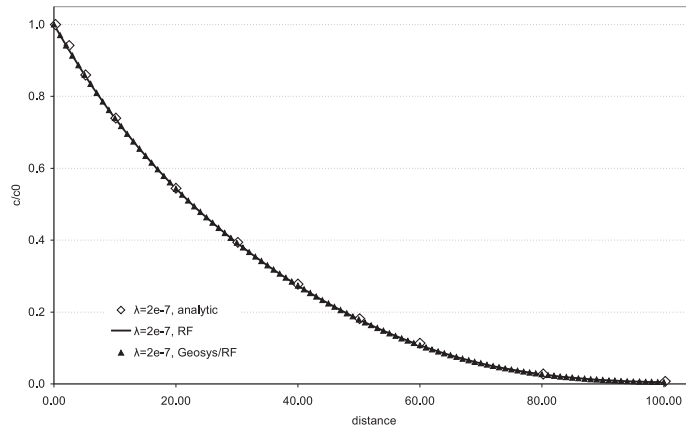


Figure 10.2.2: Concentration distribution after 100 d (decay)

10.3 Solute transport with sorption

Theory

Exchange processes, like sorption, between the solid and the liquid phase in the multiphase system of an aquifer can be caused by physical (Van-der-Waals-forces) or chemical bonds. Sorption processes can be reversible (adsorption-desorption) if the chemical environment is changing. When the transport in a multiphase system is simulated, the mass exchange between the liquid and the solid phase has to be included. The equations that describe the sorption processes are called sorption isotherms. Sorption isotherms describe the relation between the substance that is adsorbed on the solid matrix and the one which is dissolved in the fluid phase. Those equations are only valid under isothermal conditions. The isotherms that are listed below, base on the assumption that the adsorbed substance and the dissolved one are in the state of equilibrium.

$$\text{Henry : } S = K_D \cdot C \quad (10.3.1)$$

$$\text{Freundlich : } S = K_1 \cdot C^{K_2} \quad (10.3.2)$$

$$\text{Langmuir : } S = \frac{K_1 \cdot C}{1 + K_2 \cdot C} \quad (10.3.3)$$

with

K_D , K_1 , K_2 - distribution coefficients,

S - concentration of the adsorbed species (kg/kg),

C - concentration of the dissolved species (kg/m³).

The distribution coefficients are dependent on the substance and the specific soil properties like the pH. The linear Henry-isotherm is often used when there are low concentrations. Non-linear sorption processes are reproduced by the Freundlich or the Langmuir isotherm. Then the retardation is dependent on the solute concentration. In addition, the use of the Langmuir isotherm assumes a constant amount of sorption space at the solid surface. A maximum concentration for the adsorbed substance on the solid matrix is exclusively considered by the Langmuir isotherm (Habbar, 2001). This maximum concentration c_{\max} is included in the distribution coefficient K_1 ($K_1 = c_{\max} \cdot K_2$). The distribution coefficient K_2 of the Langmuir isotherm stands for the affinity between solid and sorbed solute. The distribution coefficients do not have comparable values: each sorption isotherm has to be considered separately with its specific constants.

10.3.1 Sorption with linear isotherm (Henry isotherm)

Problem definition

The aim of this example is to simulate the solute transport in an aquifer by convection with the influence of retardation as a result of sorption. The solute transport is influenced by linear sorption processes. That means, the Henry-isotherm is relevant to calculate the solute concentration. The calculation area and boundary conditions are the same as described for the precedent example.

Assumptions

Component: exclusively linear sorption (Henry isotherm), no decay

Aquifer: homogeneous, saturated, stationary flow

Model set-up of the 1 D numerical model

See chapter 10.2.

The soil parameters are the same as listed in table 10.2.1, but decay is not considered during these simulation runs. For the different simulation runs the Henry-sorption coefficients are varied as listed in table 10.3.1 in order to evaluate the influence of sorption on the mass transport. The retardation coefficients R are calculated by solving equation 10.1.2.

Evaluation method

The concentration distribution at a special point in time and over a given distance is calculated by equation 10.1.3. Hereby the decay term γ is set equal to 1. The analytical solutions are depicted in figure 10.3.1 as single symbols.

K_D -value [m^3/kg]	retardation coefficient [-]
0	1
$6.8 \cdot 10^{-6}$	1.05
$6.8 \cdot 10^{-5}$	1.54
$6.8 \cdot 10^{-4}$	6.44

Table 10.3.1: Variation of K_D -values and retardation coefficients as input variables

Results

In figure 10.3.1 you can find the concentration distribution over the whole length of the 1 D model at the final simulation time of 100 days. Obviously, the numerical results meet well the analytical solutions.

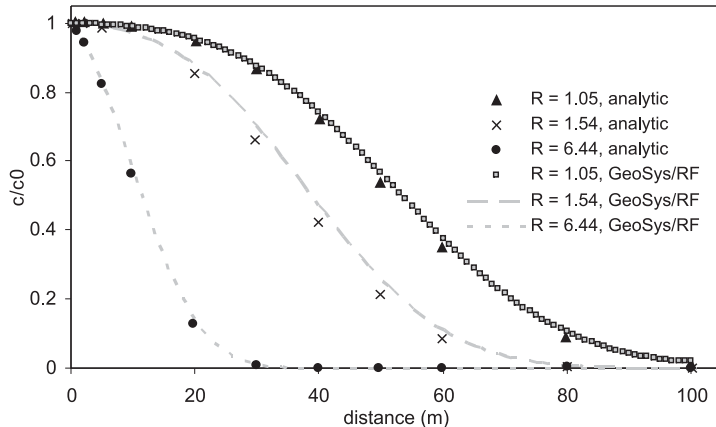


Figure 10.3.1: Concentration distribution after 100 d (Henry sorption)

Benchmark	Problem type	Path in benchmark deposit
hc_sorp_henry_1D	HC	benchmarks \HC\Sorption\Henry

10.3.2 Non-linear sorption with Freundlich isotherm

Problem definition

The non-linear Freundlich isotherm is often used to describe real sorption processes. Therefore, in this example, the transport process by including the Freundlich isotherm is calculated in the same way as in the precedent example (same model and boundary conditions). As there exists no opportunity to calculate analytically the solute transport with non-linear sorption, the results of

the simulation have to be compared with solutions of the transport equation with linear sorption in order to evaluate the simulation results.

Assumptions

Component: non-linear sorption (Freundlich isotherm), no decay
 Aquifer: homogeneous, saturated, stationary flow

Model set-up of the 1 D numerical model

See chapter 10.2

The soil parameters are the same as listed in table 10.2.1(except decay). For the different simulation runs the Freundlich-sorption coefficients (K_1) are varied in the same way as the K_D -values that are listed in table 10.4.1. The exponent K_2 was constant with a value of 1.

Evaluation method

The dependence of sorbed molecules on the amount of molecules in dilution is given by equation 10.3.3. The concentration distribution at a special point in time and over a given distance cannot be calculated analytically by equation 10.1.3 when a non-linear sorption process is assumed. A possibility to test the correctness of the simulation results for transport with Freundlich sorption is to choose values of distribution coefficients in order to create a concentration distribution which is approximately linear and must therefore almost be equal to the results of transport by use of the Henry isotherm.

Results

As the values for the Freundlich coefficients were chosen in that way, that the concentration distribution between sorbed and solute concentrations is almost linear, the results of the simulation runs have to be equal to the results that are obtained by using the linear Henry isotherm. In figure 10.3.2 the concentration distribution of the solute over the model length of 100 m is shown. As the concentrations of the transport simulation by using the Freundlich isotherm match those of the simulation runs with linear sorption, these results for non-linear sorption are reasonable. Additionally to this test, the values for the constant K_2 were changed to 0.8 in order to prove a difference between linear and non-linear sorption. The results of the comparison are shown in figure 10.3.3. These numerical results show the effect of the application of a non-linear sorption isotherm: the higher the influence of sorption (large value of sorption coefficient K_D resp. K_1) the higher the difference of solute concentration values between non-linear and linear sorption. However, the results for both isotherms were not evaluated quantitatively.

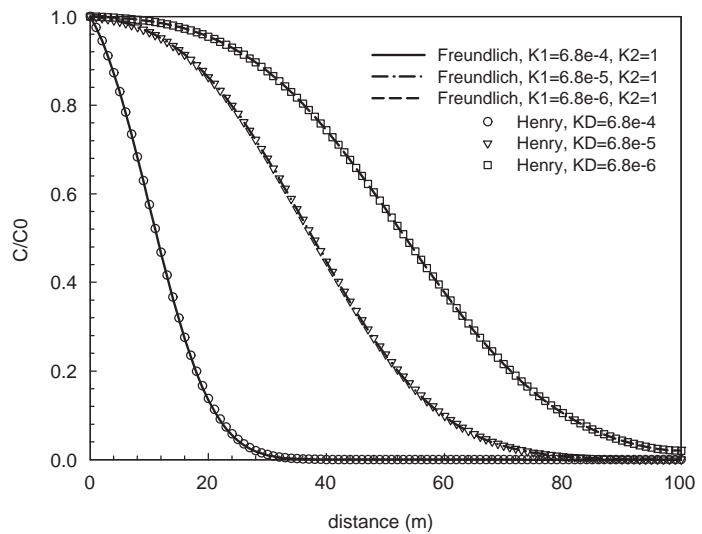


Figure 10.3.2: Concentration distribution after 100 d (Freundlich compared to Henry sorption)

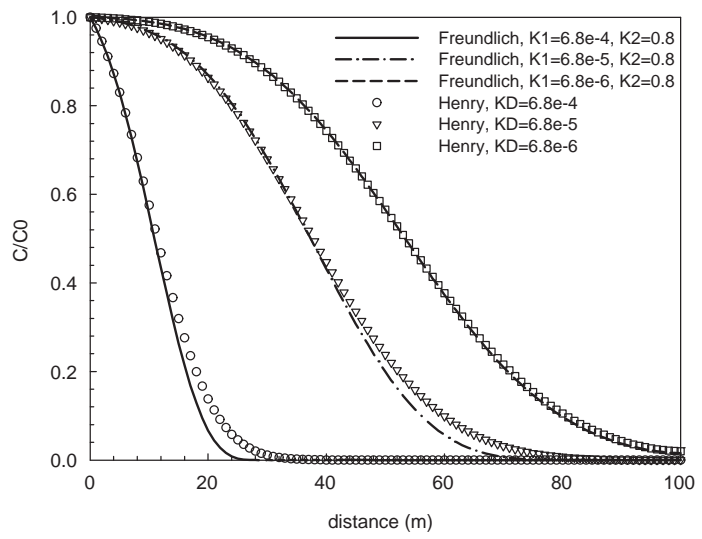


Figure 10.3.3: Different concentration distributions after 100 d (Freundlich compared to Henry sorption)

Benchmark	Problem type	Path in benchmark deposit
hc_sorp_Freundl_1D	HC	benchmarks \HC\Sorption\Freundlich

10.3.3 Non linear sorption with Langmuir isotherm

Problem definition

The non-linear Langmuir isotherm is used to describe sorption processes that are restricted by a maximum concentration of sorbed molecules. In this example, the transport process by including the Langmuir isotherm is calculated in the same way as in the precedent examples for mass transport. As there exists no opportunity to calculate analytically the solute transport with non-linear sorption, the results of the simulation have to be compared with solutions of the transport equation with linear sorption in order to evaluate the simulation results.

Assumptions

Component: non-linear sorption with maximum concentration (Langmuir isotherm)
no decay
Aquifer: homogeneous, saturated, stationary flow

Model set-up of the 1 D numerical model

See chapter 10.2

The soil parameters are the same as listed in table 10.2.1(except decay). In order to create a Langmuir equation which has almost the same linear characteristic as the Henry equation, the Langmuir sorption coefficients, K_1 , were varied in the same way as the Henry coefficients (K_D values in table 10.3.1) for the different simulation runs. The K_2 coefficients stand for the affinity between solid and sorbed solute. Thus, the K_2 value can not be set equal to 0, because this would cause a transport without any sorption. When K_2 equals 1, there is no effect on the binding affinity. Therefore, the coefficient K_2 was set constant with a value of 1 in order to approximate the linear characteristic of the Henry equation (10.3.2).

Evaluation method

The dependence of sorbed molecules on the amount of molecules in dilution is given by equation 10.3.3. The concentration distribution at a special point in time and over a given distance cannot be calculated analytically by equation 10.1.3 when a non-linear sorption process is assumed. Therefore, the simulation results are compared with the results for the mass transport by using the linear

Henry isotherm. The non-linear Langmuir isotherm was forced to be almost linear in the way as described above. Now the results of the transport by using the Langmuir isotherm can be compared with the results that were obtained by the transport simulation with the linear Henry isotherm.

Results

In figure 10.3.4 the concentration distributions over the whole model length by using the linear Henry isotherm and the non-linear Langmuir isotherm are depicted. Obviously, the results for each specified distribution constant are almost equal. This result is correct, because it was provoked by the choice of the sorption coefficients.

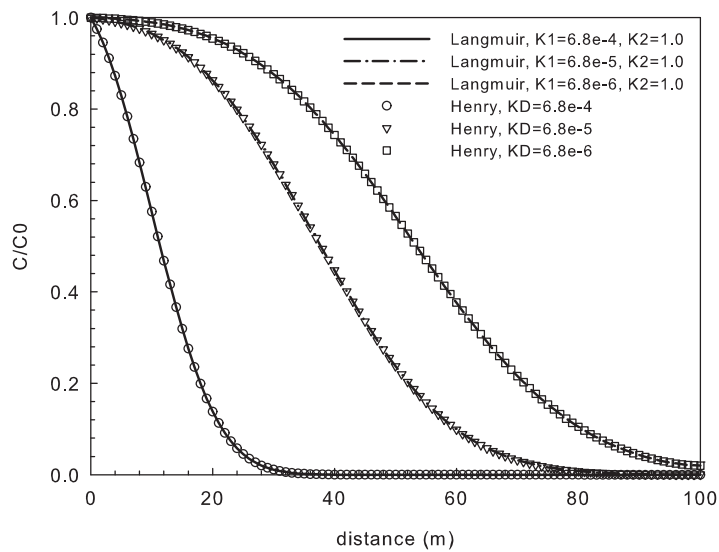


Figure 10.3.4: Concentration distribution after 100 d (Langmuir compared to Henry sorption)

In order to show that the results by the use of the Langmuir isotherm are actually different to those by using the Henry isotherm, the K_2 values were changed to a value of 0.8, so that the Langmuir isotherm got a real non-linear gradient. As the results show (fig. 10.3.5), the differences between the concentration distributions are evident.

Benchmark	Problem type	Path in benchmark deposit
hc_sorp_langmuir_1D	HC	benchmarks \HC\Sorption\Langmuir

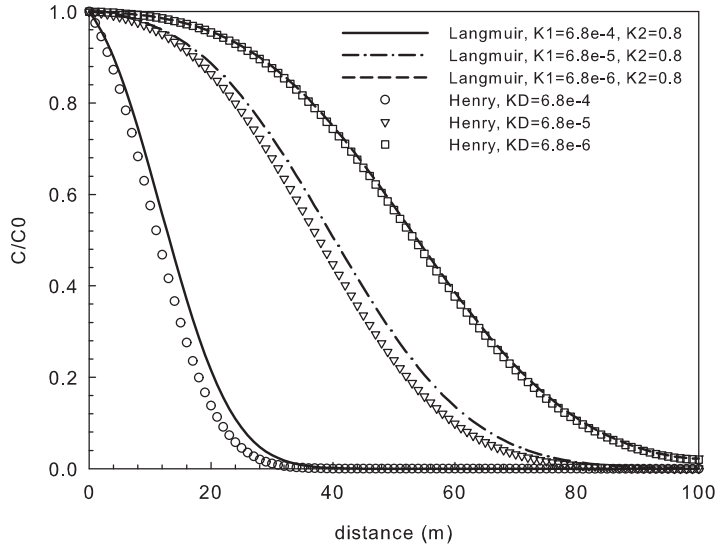


Figure 10.3.5: Different concentration distributions after 100 d (Langmuir compared to Henry sorption)

10.3.4 Solute transport with sorption and decay

Problem definition

The aim of this example is to simulate the solute transport in an aquifer by convection with the influence of retardation as a result of sorption. Additionally, the transported mass will be degraded. The calculation area and boundary conditions are the same as described in chapter 10.2.

Assumptions

Component: linear sorption, decay

Aquifer: homogeneous, saturated, stationary flow

Model set-up of the 1 D numerical model

See chapter 10.2

The soil parameters are the same as listed in table 10.2.1. The decay rate λ is $2 \cdot 10^{-7} \text{ s}^{-1}$. For the different simulation runs the Henry sorption coefficients are varied as listed in table 10.3.1 to evaluate again the influence of sorption on mass transport.

Evaluation method

The concentration distribution at a special point in time and over a given distance is calculated by equation 10.1.3. The analytical solutions are depicted in figure 10.3.6 as single symbols.

Results

The influence of radioactive decay on the transport process can be recognised at the typical declining exponential curves in figure 10.3.6. According to the different sorption coefficients the transport is retarded. Obviously, the numerical results (lines) meet well the analytical solutions. Therefore, it can be summarised that the transport under the combined consideration of both decay and sorption can be reproduced by the simulation with RockFlow.

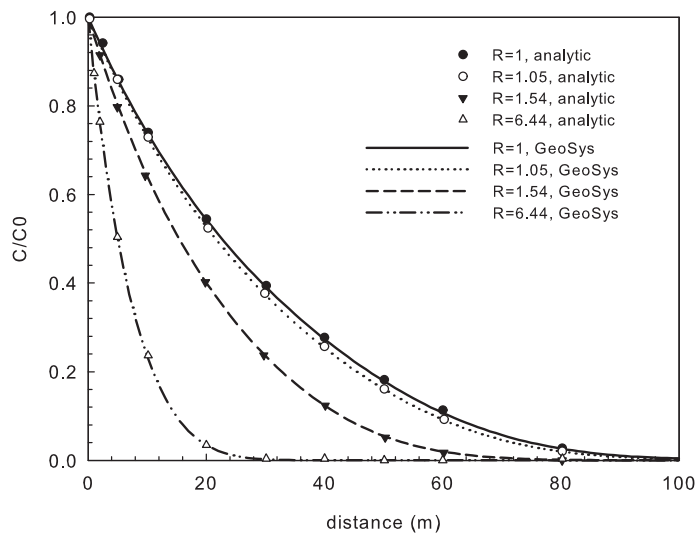


Figure 10.3.6: Concentration distributions after 100 d (sorption and decay)

Benchmark	Problem type	Path in benchmark deposit
hc_decay_sorp_henry_1Du	HC	benchmarks \HC\sorption_decay

10.4 Solute transport by diffusion

Theory

Diffusion is a process that equates concentration differences of gaseous or dissolved matter or energy. The particles move from higher to lower concentrations

by Brownian movement in dependence on the temperature. In an aquifer, diffusive transport appears when convective transport is not that relevant (small velocities).

The extent of diffusion is also dependent on the diffusing substance and the medium. In addition, diffusion in soils is influenced by other factors, e.g. tortuosity. The finer a soil the stronger are the interacting forces between the soil matrix and the diffusing molecules. The diffusion coefficient which has to be given in GeoSys/RockFlow is the so-called apparent diffusion coefficient (eq. 10.4.1).

$$D_a = \frac{D_e}{\Phi} \quad (10.4.1)$$

with D_e - effective diffusion coefficient.

10.4.1 Diffusion: axisymmetric model

Problem definition

This diffusion model is built to reproduce a field study in clay. This in situ test consists of a borehole where a solution is circulated that contains tracer substances like HTO. These tracers diffuse into the adjacent clay. The aim of the investigation is to simulate the HTO distribution after 300 d, the final test time, and to compare the simulation results of GeoSys/RockFlow to those that are calculated by HYDRUS 1 D (Simunek et al.) and PHAST (Parkhurst et al.).

Model set-up of the 1 D axisymmetric model

To build a proper model of the tracer test, a one-dimensional axisymmetric model with 3.8 cm of borehole radius and 21.2 cm horizontal distance in the clay soil is created. As initial condition a constant pressure of 0 was specified in the whole model and the concentration relation c/c_0 of 1 within the distance of the borehole radius and of 0 within the clay domain. The pressure boundary condition corresponds to the initial condition. The calculation model includes 310 elements and 311 nodes. Table 10.4.1 shows the used parameters for the clay and the apparent diffusion constant D_a of HTO. The calculation is performed for the test duration of 300 days with fitted time step lengths from 0.001 d to 1 d (Bahr, 2007). The porosity in the modelled borehole is assumed to be 1 in order to evoke the simulation of a tracer reservoir that supplies the tracer solution into the clay.

Evaluation method

The aim of the presented calculation example is the evaluation of the GeoSys/RockFlow-simulation results by comparing them with numerical results of two other simulation programmes. The comparison is made by the use of Hydrus 1 D, which is a

parameter	value	unit
density ρ	2.5	$t \cdot m^{-3}$
porosity Φ	0.15	-
permeability K	$1.0 \cdot 10^{-11}$	m^2
diffusion coefficient D_a	$3.6 \cdot 10^{-10}$	$m^2 \cdot s^{-1}$

Table 10.4.1: Parameters

one-dimensional transport model especially for the solute transport in soils. The second programme, PHAST, is linked to the chemical software PHREEQC. The simulation with both programmes was made under consideration of the same boundary conditions and parameters (Bahr, 2007).

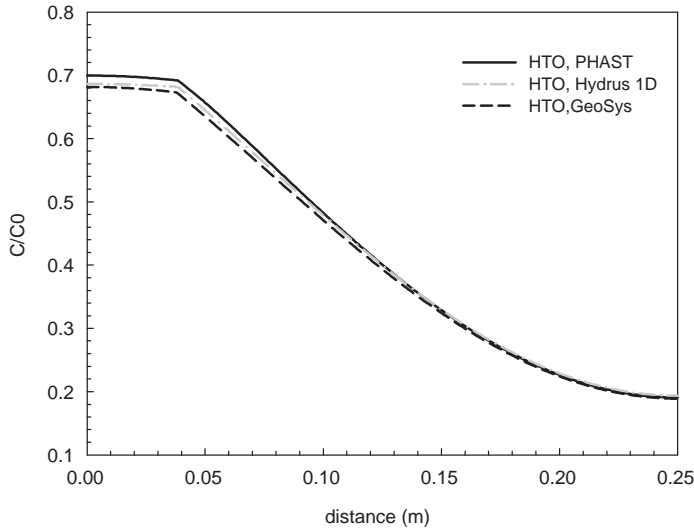


Figure 10.4.1: Concentration distributions after 300 d

Results

In figure 10.4.1 you can find the concentration distributions over the width of 0.25 m after a simulation time of 300 days that were calculated by means of GeoSys/RockFlow, PHAST and Hydrus 1D (Bahr, 2007). The numerical results accord well to each other. Thus, the comparison shows that the diffusion process can be well reproduced by the use of an axisymmetric GeoSys/RockFlow model.

Benchmark	Problem type	Path in benchmark deposit
Diff_HTO_test	HC	benchmarks\HC\Diffusion\

10.4.2 Diffusion in an anisotropic medium (2 D simulation)

Problem definition

The aim of this example is to simulate the transport of a tracer by molecular diffusion in an anisotropic porous medium. The side length of the square numerical model is 1 m. At the left corner at the bottom of the model a constant concentration is diffusing into the calculation area. Diffusion is the only process for tracer transport, there are no pressure differences in the whole area. Because of the anisotropy of the soil material the tracer has to diffuse much faster in x-direction than in vertical direction. This has to be evaluated by comparing the concentration distributions in both directions.

Model set-up of the 2 D numerical model

As initial condition the pressure and tracer concentration were set to 0 in the whole area. At the left corner at the bottom of the model a concentration relation c/c_0 of 1 is specified along two polylines of the length of 0.3 m. The boundary conditions correspond to the initial conditions. The calculation model includes 736 triangular elements and 409 nodes. Table 10.4.2 shows the used parameters for the simulation. As the porous medium is assumed to be anisotropic, which influences diffusion, the value for tortuosity is set equal to 1 in x-direction and 0.1 in y-direction.

parameter	value	unit
porosity Φ	0.4	–
permeability K	$1.0 \cdot 10^{-15}$	m^2
density water ρ	1000	kg/m^{-3}
viscosity water η	0.001	$\text{Pa} \cdot \text{s}$
dispersion length	10.0	m
diffusion coefficient D_a	$6.0 \cdot 10^{-10}$	m^2/s

Table 10.4.2: Used parameters

The calculation is made for 30 time steps with a length of $1 \cdot 10^7$ seconds. The calculation model is sketched in figure 10.4.2.

Evaluation method

As the process of diffusion is dependent on the actual concentration in the porous medium and on the point in time, an analytical solution for the present calculation model is not possible. Therefore, the results of the RockFlow simulation are solely evaluated in a qualitative way by comparing the concentration distributions in horizontal and vertical direction.

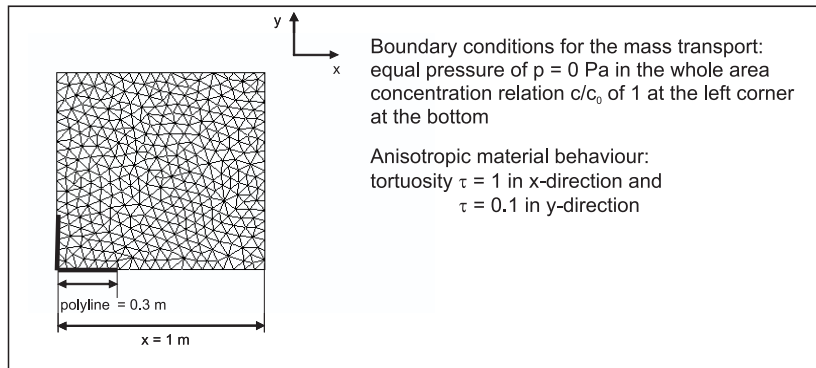


Figure 10.4.2: Calculation model (2D)

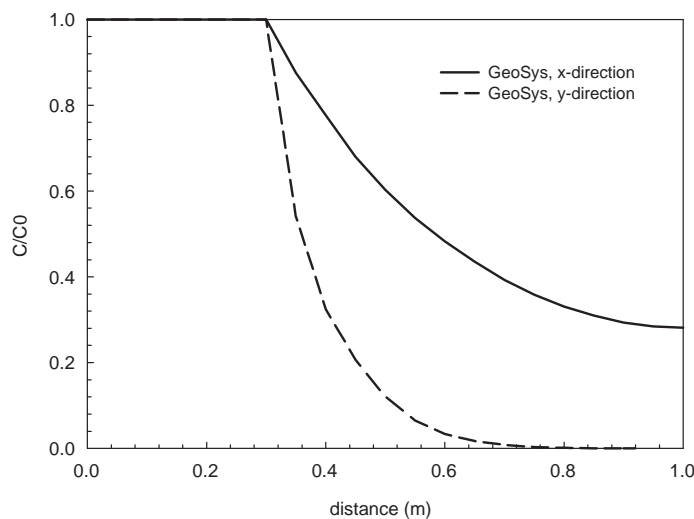


Figure 10.4.3: Concentration distributions in x- and y-direction

Results

In figure 10.4.3 you can find the concentration distributions over the model side length of 1 m in x- and y-direction, respectively, after a simulation time of $1 \cdot 10^8$ seconds. Assuming a small tortuosity of 0.1, the component is not yet transported over the whole transport length of 1 m in vertical direction, while in horizontal direction the concentration relation equals approximately 0.3 at the opposite border of the model. The shown trend in the change of diffusion velocity by assuming different tortuosities in x- and y-direction in order to specify anisotropic material behaviour for molecular diffusion has a comprehensible characteristic.

Benchmark	Problem type	Path in benchmark deposit
diff_aniso	HC	benchmarks \HC\Diffusion\

10.4.3 Solute transport with matrix diffusion

Problem definition

This benchmark is introduced to verify the matrix diffusion function developed by Chris McDermott and Georg Kosakowski. It simulates advective-dispersive transport of a solute in an one-dimensional fracture with constant aperture, with and without the effect of matrix-diffusion. The geometry and the material parameters are chosen to fit the parameters extracted from experiments conducted during the Colloid Radionuclide Retardation Experiment at Nagra's Grimsel test site ???. The result from GS/RF is compared with that from PIC-NIC, and they fit well.

Model set-up of the 1D domain

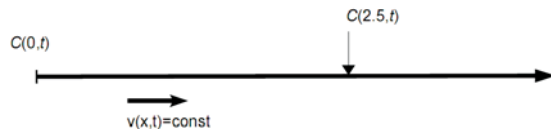


Figure 10.4.4: Conceptual setup of the 1D problem

The geometry and material parameters in PICNIC and GS/RF are summarized in Table 10.4.3 and the conceptual model is shown in Figure 10.4.4. PICNIC solves the one-dimensional problem, whereas in GS/RF a two-dimensional discretization was chosen. A rectangular domain of $5.2\text{m} \times 0.5\text{m}$ was discretized with 1155 nodes and 2080 triangular elements. One of the shorter domain edges was chosen as inflow boundary and fluid was injected at the boundary-nodes in such a way, that the resulting fluid velocity matches exactly the value from

10.4.3. The concentration is fixed at the inflow boundary. In 2.5m distance the breakthrough curve is recorded. The outflow boundary is assumed to be far away and should not influence the observed breakthrough curve. Picnic V2.2 and GS/RF Rev. 1535 from the subversion server were used for testing.

As defining exactly the same transport boundary conditions in GS/RF and PICNIC is not possible, the following procedure was used to get the inflow boundary condition as similar as possible:

- 1) The system was calculated for injecting a pulse of solute with a constant flux for a time length of 50s with PICNIC. The concentration vs. time was recorded for the inflow-leg.
- 2) The concentrations vs. time extracted from PICNIC's inflow-leg were applied (fixed) to the inflow boundary of the GS/RF system.

These procedures work, as long as advective fluxes are much higher than the dispersive-diffusive fluxes over the boundary.

The outflow boundary condition is set to infinity, i.e. a semi-infinite problem is calculated. In GS/RF the domain is set to 5m, double the distance between inflow boundary and observation point. This prevents the outflow boundary condition to influence the tracer breakthrough at the observation point.

Symbol	Unit	Description	Value
L	m	Distance between boundary and observation points	2.5
α_T	m	Trans. dispersion (GS/RF only)	—
ρ	kg/m^3	Bulk matrix density	2670
$2b$	m	Fracture aperture	0.55×10^{-3}
v	m/s	Fluid velocity	7.05×10^{-4}
α_L	m	Long. dispersion (GS/RF only)	0.1
Pe	—	Peclet number (PICNIC only)	25
ε_p	—	Matrix porosity	0.3
D_p	m^2/s	Diffusion constant in rock matrix	7.4×10^{-11}

Table 10.4.3: Geometry and material properties for the simulations

Results

For the investigated two cases, advection and dispersion(ADE) only and ADE plus matrix diffusion(MD), the PICNIC and GS/RF solutions are in general very similar (see Figure 10.4.5).

Benchmark	Problem type	Path in benchmark deposit
<i>matrix_diffusion</i>	C	benchmarks\c\matrix_diffusion\0gs_vs_picnic

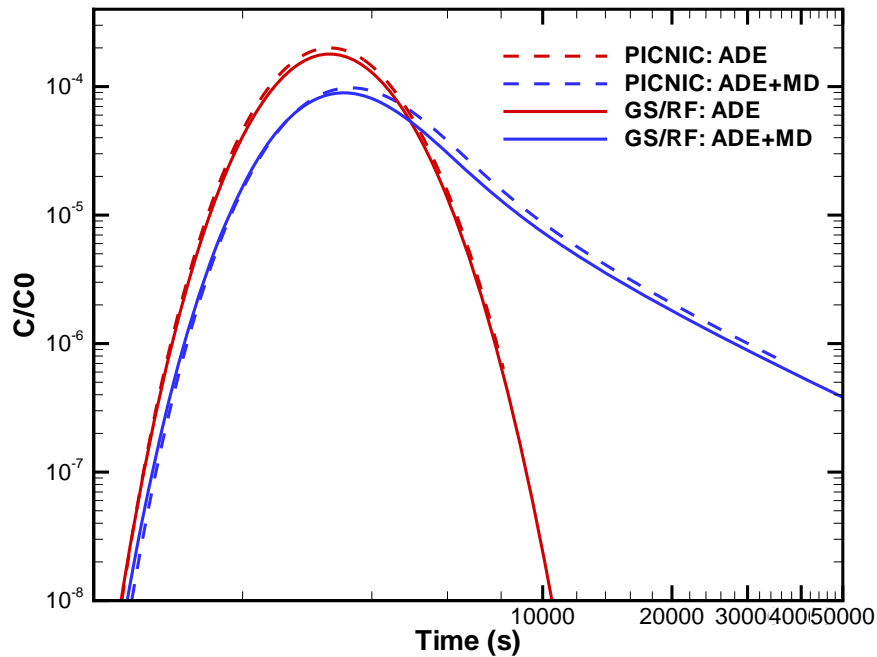


Figure 10.4.5: Breakthrough of the ADE and the ADE+MD solutions calculated with PICNIC and GS/RF

10.4.4 Solute transport with cation exchange

Theory

In contrast to sorption the ion exchange is the replacement of one chemical for another one at the solid surface, the so called ion exchanger. Ion exchange equations do explicitly account for all ions which compete for the exchange sites. The exchange of ions is limited by the exchange capacity, which is the sum of exchangeable ions in the soil and fluctuates with the change of pH in the soil solution. The ion exchanger can be unselective or can have binding preferences for certain ions or classes of ions, depending on their chemical structure (Appelo and Postma, 1996).

Problem definition

This test example is taken from the PHREEQC User's Guide (Parkhurst and Appelo, 1999), a manual for a computer program that is applicable for chemical reactions and transport processes. The simulation is made in order to reproduce the transport of solutes by saturated flow with the influence of cation exchange. The aim of the example is to check out the correctness of the coupling between GeoSys/RockFlow and PHREEQC by comparing the results of the simulations of both programs. With the calculation model the chemical composition of the effluent from a column containing a cation exchanger and a sodium-potassium-nitrate-solution is simulated. This column is flushed with 3 pore volumes of calcium chloride solution.

Assumptions

Components: calcium, potassium and sodium react to equilibrium with cation exchanger at all times

Aquifer: homogeneous, saturated, stationary flow

Model set-up of the 1 D numerical model

The 8.2 cm long column contains a sodium-potassium-nitrate solution that is in equilibrium with a cation exchanger. For the one-dimensional calculation the calculation area is simplified as a line of a length of 8.2 cm. The calculation model includes 82 elements and 83 nodes. As initial condition the water head in the whole domain is given with 2 m. The initial state of the solution is given in table 10.4.4.

parameter	value	unit
Ca	0	—
Cl	0	—
K	$2.0 \cdot 10^{-4}$	mol/kgw
Na	$1.0 \cdot 10^{-3}$	mol/kgw
N(5)	$1.2 \cdot 10^{-3}$	mol/kgw
pH	7	—
pe	12.5	—
Na-X	$5.493 \cdot 10^{-4}$	mol/kgw
K-X	$5.507 \cdot 10^{-4}$	mol/kgw
Ca-X ₂	0	—

Table 10.4.4: Used parameters

with

pe - redox potential
 X - ion exchanger

kgw – kilogram of water.

At the right border of the model the constant head is given with 2 m. At the left border a constant flux of $1.388 \cdot 10^{-6} \text{ m}^3/\text{s}$ is defined as source term. The concentrations of this infiltrating CaCl_2 -solution as well as the pH and pe are given in table 10.4.5.

parameter	value	unit
Ca	$6.0 \cdot 10^{-4}$	mol/kgw
Cl	$1.2 \cdot 10^{-3}$	mol/kgw
pH	7	–
pe	12.5	–

Table 10.4.5: State of the infiltration solution

The soil material is specified by the parameters in table 10.4.6. The dispersion of the transported solutes in this soil is set equal to $2 \cdot 10^{-3} \text{ m}$. The calculation is divided in 480 time steps with a constant time step length of 180 seconds. That means, the flow and transport processes in the aquifer within 1 day are simulated.

density ρ	2000	kg/m^{-3}
porosity Φ	0.5	–
permeability K	$1.157 \cdot 10^{-5}$	m^2

Table 10.4.6: Soil parameters

Evaluation method

As this test example has the aim to validate the coupling of GeoSys/RockFlow and PHREEQC, merely the comparison between the simulation results of both programs has to be accomplished.

Results

The numerical results are shown in figure 10.4.6. The time-dependent concentrations are the values of the compared GeoSys/RockFlow and PHREEQC models at the end node and end cell, respectively. Within the calculation time of one day the pore volume of the column model is exchanged three times. As chloride is a conservative tracer it arrives already after the exchange of about one pore volume in the effluent. As long as the exchanger contains sodium this component is eluted. Sodium is initially present in the column and exchanges with the incoming calcium. Potassium is released after sodium. When all of the potassium has been released, the concentration of calcium increases to a

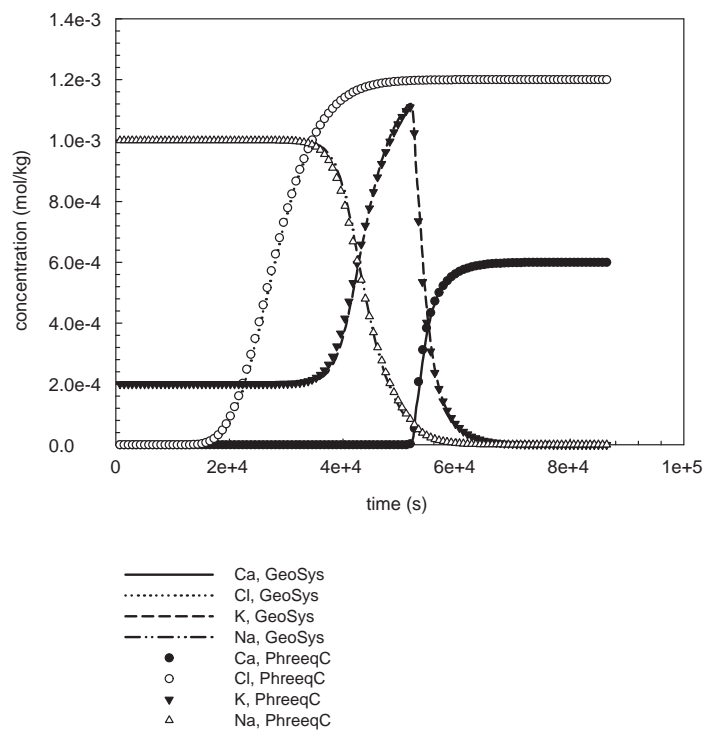


Figure 10.4.6: Effluent concentrations with time of the GeoSys/RockFlow and PHREEQC simulations

steady-state value. As depicted in figure 10.4.6, between the GeoSys/RockFlow and the PHREEQC simulation results there are no differences.

Benchmark	Problem type	Path in benchmark deposit
pqc1	HC	benchmarks \HC\ion_exchange

10.4.5 1-D Multi-component transport with dissolution and precipitation

Problem definition

In this example, a one-dimensional column that initially contains calcite is continuously flushed by water that contains magnesium chloride (Fig. 10.4.7). With the movement of water front, calcite starts to dissolve and dolomite is formed temporarily.

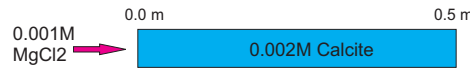


Figure 10.4.7: Model domain

Media Properties

The media properties of this model is listed in Table 10.4.7.

Property	Value	Unit
Column length	0.5	m
Effective porosity	0.32	–
Bulk density	1.8×10^3	kg/m ³
Longitudinal dispersivity	0.0067	m
Pore velocity	9.375×10^{-6}	m/sec
Flow rate	3×10^{-6}	m ³ /sec

Table 10.4.7: Material properties

Initial and Boundary conditions

For GS/RF-GEMIPM2K calculation, all the possible chemical species need to be explicitly set up for initial and boundary conditions. In this example, all concentration values are given in the unit of mol/kgwater. Detailed values can be get from the *.ic and *.bc files in the corresponding benchmark folder.

Results

This model can be simulated by GS/RF-PHREEQC, GS/RF-ChemApp, and GS/RF-GEMIPM2K. In these benchmarks, we use the Nagra/PSI database [99], which provides same thermodynamic data for all three calculations. Fig. 10.4.8 shows the three simulation results. Solid lines are for GS/RF-PHREEQC, symbols "+" are for GS/RF-GEMIPM2K, and triangles are for GS/RF-ChemApp.

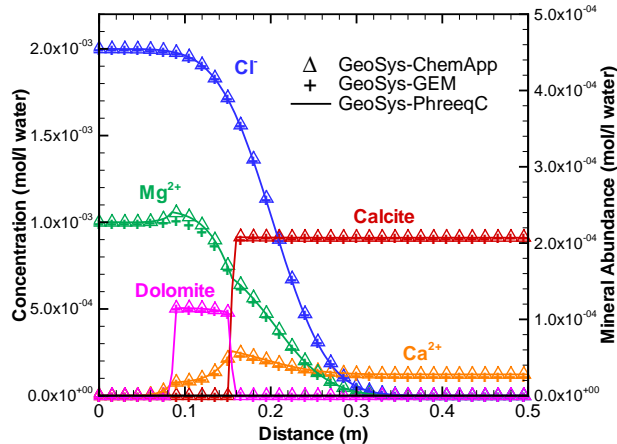


Figure 10.4.8: Benchmark results from GS/RF-ChemApp, GS/RF-PHREEQC, and GS/RF-GEMIPM2K

Benchmark deposit

Benchmark	Problem type	Path in benchmark deposit
<i>calcite_gems</i>	C	benchmarks\C\calcite_gems\
<i>calcite_pqc</i>	C	benchmarks\C\calcite_pqc\
<i>calcite_chemapp</i>	C	benchmarks\C\calcite_ChemApp\

10.5 1D and 2D conservative transport

10.5.1 1D reactive transport with comparison to analytical solution

This benchmark describes reactive and conservative mass transport in a one-dimensional aquifer and has two aims. Firstly, a conservative component, a linearly retarded component and a component decaying according to a first order decay are transported and profiles as well as breakthrough curves are compared with the corresponding analytical solution. This comparison is possible only

using these simplified reaction types. Secondly, the benchmark is set up in a way that allows to test all element types in this simplified "quasi" one-dimensional setup.

The model aquifer has a length of 100 m in x-direction and 1 m in both y and z direction. Discretization is in element sizes of 1 m in x direction, yielding 100 elements and 101 nodes for the line elements, 100 elements and 202 nodes for the quad elements, 200 elements and 202 nodes for the triangular elements, 100 elements and 404 nodes for the hexahedra elements, 200 elements and 404 nodes for the prism elements and 600 elements and 404 nodes for the tetrahedra elements. To make the boundary conditions consistent with all element types, surfaces in the y-z plane are used to define the boundary conditions at x=0 m and x=100 m.

The hydraulic conductivity is assumed to be isotropic and constant in the whole aquifer. Flow is from the left to the right (small to large x), induced by fixed head boundary conditions at x=0 and x=100 and a total head difference of 1 m. All components have initial conditions of 0 and a constant concentration boundary condition of 1 at x=0. For the purpose of this benchmark, the concentration units are arbitrary and are therefore normalized. Transport velocity corresponds to 1 m d^{-1} , thus time step length is chosen accordingly as 86400 s (corresponding to 1 d). Total simulation time is 100 d. Thus the Courant number $Co = 1.0$ and the grid Peclet number $Pe_g = 4$, keeping effects of numerical dispersion as well as oscillations sufficiently small. All parameters used in this simulation are given in table Tab. 10.5.2.

Three components are used in this benchmark: The component `ConsTracer` denotes the conservative tracer, for which the advection - dispersion equation is solved. Component `Decay` is transported according to the advection - dispersion equation with a first order decay rate λ . Component `SorbLin` is transported according to the advection - dispersion equation with a linear instantaneous sorption, which corresponds to a retardation of $R = 1 + \frac{1-n}{n} \rho_s K_d = 1 + \frac{0.5}{0.5} \cdot 2000 \cdot 0.001 = 3$. All components have the same aqueous phase diffusion coefficient.

Table 10.5.1: Parameters used for benchmark HC\1d_analyt

parameter	value	unit
porosity $\Phi = n$	0.5	–
hydraulic conductivity K	$5.787037 \cdot 10^{-4}$	ms^{-1}
storage coefficient S	0.0	s^{-1}
solid density ρ_s	2000	$\text{kg} \cdot \text{m}^{-3}$
density of water ρ_w	1000	$\text{kg} \cdot \text{m}^{-3}$
viscosity water η	0.001	$\text{Pa} \cdot \text{s}$
dispersion length α_l	0.25	m
component diffusion coefficient D	$1.0 \cdot 10^{-9}$	$\text{m}^2 \text{s}^{-1}$
first order decay rate in water λ	$1.0 \cdot 10^{-7}$	s^{-1}
distribution coefficient K_d	$1.0 \cdot 10^{-3}$	$\text{m}^3 \text{ kg}^{-1}$

Evaluation method

Model results are compared to the analytical solution for component profiles along x after a simulation time of 75 days, as well as for breakthrough curves at x=50 m for all components. To facilitate testing of all elements, a batch-file is provided (1D_all.bat) which reruns the benchmark for all element types by replacing the mesh file accordingly. Results can be viewed using the corresponding layout files by Tecplot. `companaProfile_*.lay` is used for displaying the profile results and `companaBTC_*.lay` is used for displaying the breakthrough curve results for element type *. The files `companalytBTC.1pk` and `companaProfile.1pk` save the simulation results for both types from an earlier GeoSys/RockFlow version for reference.

Results

Results of the simulation and the comparison with the analytical solution are shown in Fig. 10.5.1 for the profiles and in Fig. 10.5.2 for the breakthrough curves. Numerical results using GeoSys/RockFlow are denoted by symbols, the analytical solution is denoted by the full lines. Correspondence is very good in both cases.

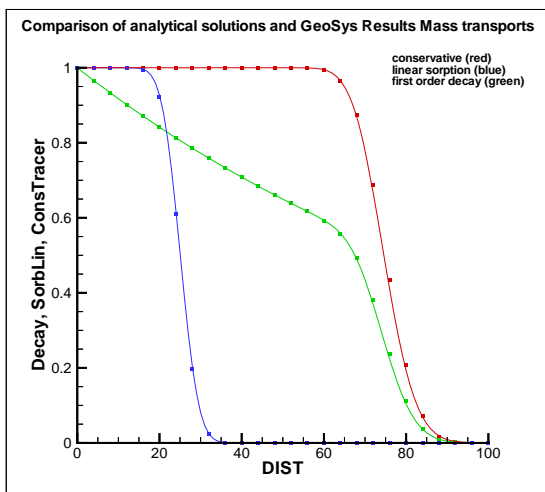


Figure 10.5.1: Concentration profiles after 100 d

Benchmark	Type	Path
1d_analyt	HC	benchmarks\C\1d_analyt

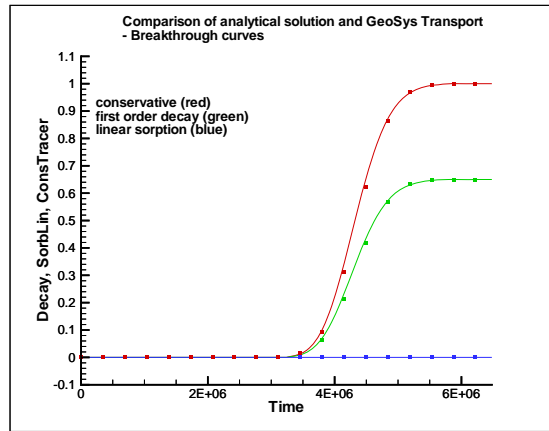


Figure 10.5.2: Concentration breakthrough curves at $x=50$ m

10.5.2 2D conservative transport with comparison to analytical solution

This benchmark describes the conservative mass transport in a two-dimensional homogeneous aquifer. The main purpose is to compare the numerical results of a conservative mass transport simulation without any reactions with the suitable analytical solution.

The model aquifer has a length of 100 m in the x-direction, 50 m in the y-direction and 1 m in the z direction. The whole domain is discretized into 10560 triangular elements with a constant x and y dimension of 1 m (this value guarantees a Peclet number = 4), except at the boundaries of the injection area where a finer grid is chosen.

The aquifer is assumed to have a homogeneous and isotropic hydraulic conductivity and the constant head boundary conditions on the left (piezometric surface of 2 m) and right side (piezometric surface of 1 m) produce a steady state flow in the right direction. As the material has a constant porosity of 0.5 the resulting flow velocity is $1.1574074 \cdot 10^{-3}$ m s $^{-1}$. Both longitudinal and transversal dispersivity have a value of 0.25, consequently the total simulation time of 80 days is divided into 160 time steps to insure a Courant number lower than 1. The constant tracer is injected with a relative concentration value of 1.0 from a source 8 m wide set on the left boundary of the aquifer, while the initial concentration of the tracer is zero all over the aquifer domain.

Evaluation method

Model results are compared to the Hewson analytical solution (Hewson, Thomas, 1976, Simulation of leachate movement in the areal plane-A finite element approach: Princeton University, B.S. thesis, 150 p.) for a x-y planar view of the

Table 10.5.2: Parameters used for benchmark HC\2d_analyt

parameter	value	unit
porosity $\Phi = n$	0.5	–
hydraulic conductivity K	$5.787037 \cdot 10^{-5}$	ms^{-1}
storage coefficient S	0.0	s^{-1}
solid density ρ_s	2000	$\text{kg} \cdot \text{m}^{-3}$
density of water ρ_w	1000	$\text{kg} \cdot \text{m}^{-3}$
viscosity water η	0.001	$\text{Pa} \cdot \text{s}$
longitudinal dispersivity α_l	0.25	m
transversal dispersivity α_t	0.25	m
component diffusion coefficient D	$1.0 \cdot 10^{-9}$	$\text{m}^2 \text{s}^{-1}$

model domain as well as for breakthrough curves at $x=60$ m and $x=80$ m after a simulation time of 80 days. The Hewson solution is more desirable for comparison of this benchmark than the Domenico (1978) solution, because it was developed for a finite width aquifer while the one of Domenico refers to an infinite width aquifer.

Results

Results of the simulation and the comparison with the analytical solution are shown in Fig. 10.5.3 for the profiles at 60 m and 80 m, and in Fig. 10.5.4 for the planar view. Numerical results using GeoSys/RockFlow are represented by the black line, while the Hewson analytical solution is denoted by the red line. Correspondence is very good in both cases and observing the x-y view we can also point out that the numerical simulation is able to properly reproduce lateral and transversal spreading of the constant tracer.

Benchmark	Type	Path
2d_analyt	HC	benchmarks\C\2d_analyt

10.5.3 2D conservative transport in heterogeneous media

In this benchmark conservative mass transport in a two-dimensional heterogeneous aquifer is tested. A secondary purpose of this benchmark is to test the functionality of assigning heterogeneous distributions of hydraulic conductivity and/or porosity. Furthermore, the functionality of reading in initial variable distributions from restart files is tested.

The 2D model aquifer has dimensions of 100 m by 100 m in x and y directions. The domain is uniformly discretized into 10000 quadrilateral elements with a constant x and y dimension of 1 m.

A randomly distributed but spatially correlated isotropic hydraulic conductivity field ($K_{eff} = 6.339 \cdot 10^{-4} \text{ ms}^{-1}$, $\sigma_{ln(K)}^2 = 1.0$) is provided, which is read in from

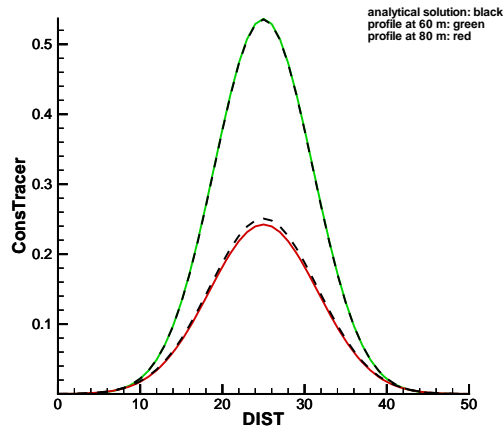


Figure 10.5.3: Profiles at 60 m and 80 m after 80 d. Comparison of analytical solution and GeoSys/RockFlow results.

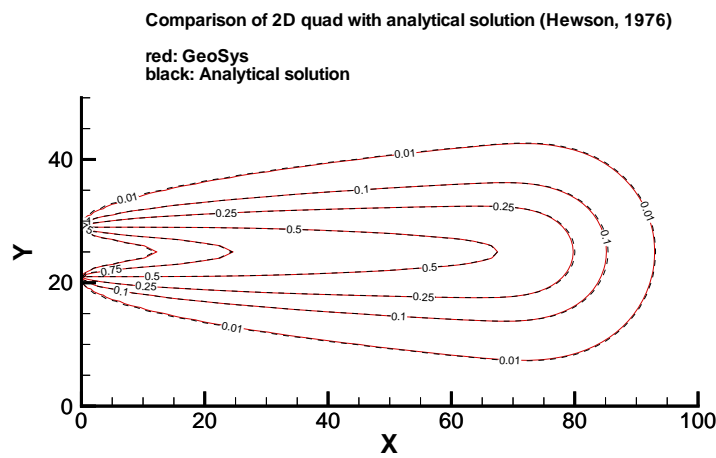


Figure 10.5.4: Planar x-y view after 80 d. Comparison of analytical solution and GeoSys/RockFlow results.

a text file. Also porosity n is not uniform. In the upper half of the aquifer (i.e. for $y > 50$ m) $n = 0.5$, while in the lower half (i.e. for $y \leq 50$ m) $n = 0.25$. A constant head boundary condition on the left hand side with a piezometric height of 10 m and a constant source term on the right hand side of the model with $q = -1.0 \text{ md}^{-1}$ produce a steady state flow field. The steady state head distribution is given as initial condition via a restart file. Longitudinal dispersivity has a value of 0.5, transversal dispersivity a value of 0.05 m. A conservative tracer is injected with a relative concentration value of 1.0 from two sources on the left hand side model boundary between $21.0 < y < 29.0\text{m}$ and $71.0 < y < 79.0\text{m}$, while the initial concentration of the tracer is zero all over the aquifer domain. The tracer diffusion coefficient is $1.0 \cdot 10^{-9} \text{ m}^2\text{s}^{-1}$. A total simulation time of 25 days divided into 100 time steps is regarded.

Evaluation method

Model results are compared to those of a previous GeoSys version.

Results

Fig. 10.5.5 shows results of the flow and transport simulation after 25 days. Due to the higher porosity in the upper half of the aquifer, the tracer plume here migrates slower than in the lower half of the aquifer. Accordingly, tracer breakthrough curves measured 20 m downgradient of each source show a later breakthrough of the tracer from the upper source (green curve). In the right hand side plots of Fig. 10.5.5, head distribution at the beginning and at the end of the simulation are plotted, demonstrating the correct reading in of data from a restart file.

Benchmark	Type	Path
2d_hetk+n+restart	HC	benchmarks\C\hetk+n+restart

10.6 Radial flow and conservative transport

10.6.1 Radial flow - Theiss problem

The Theiss problem is used to verify the transient flow behaviour of GeoSys. Theiss (1935) presented an analytical solution for the transient drawdown in an infinite, uniform, isotropic and confined aquifer of constant thickness (see Fig. 10.6.1). The pumping well is assumed to fully penetrate the aquifer, have a negligible diameter and no well effects and to pump at a constant extraction rate. The initial hydraulic head is constant throughout the aquifer. This analytical solution is:

$$h_0 - h(r, t) = \frac{Q}{4\pi T} W\left(\frac{r^2 S}{4Tt}\right) \quad (10.6.1)$$

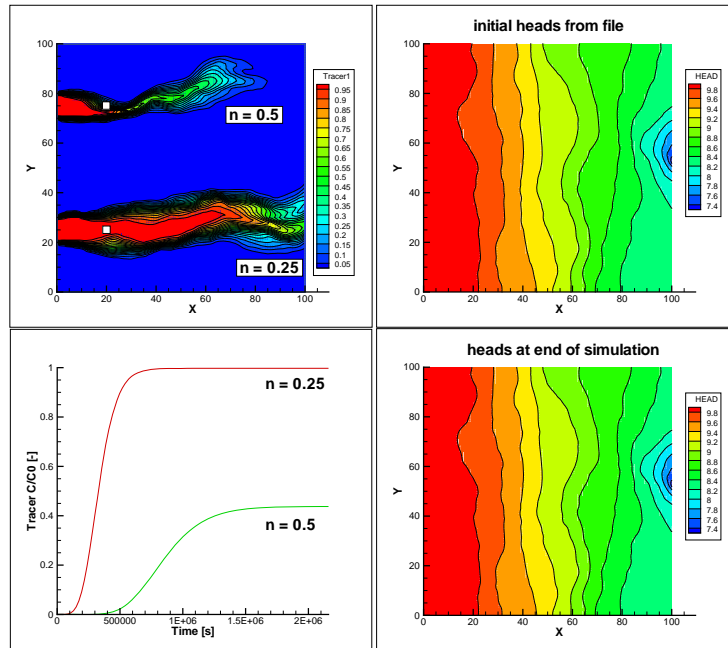


Figure 10.5.5: Tracer plumes and breakthrough curves 20 m downgradient from both sources (left upper and lower diagram); Initial and final head distribution (right upper and lower diagram).

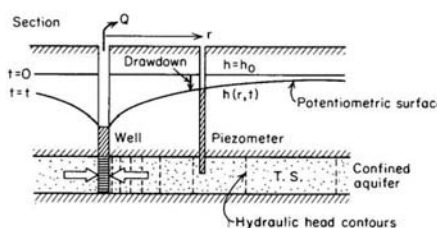


Figure 10.6.1: Radial flow to a well in a confined aquifer (from Freeze and Cherry, 1979).

where h_0 is the initial hydraulic head [m], $h(r, t)$ is the transient hydraulic head [m] at time t [s] at distance r [m] from the pumping well, Q is the constant extraction rate at the well [m^3s^{-1}], S is the storage coefficient [-] and T is aquifer transmissivity [m^2s^{-1}]. $W()$ is the Theiss well function.

The parameters used are: A model area of 1000 m times 1000 m with the well in the center, a constant thickness of 20 m, a hydraulic conductivity of 0.000578704 m/s and a storage coefficient S_0 of 1.000000e-005 (Caution: For the Theiss solution $S = MS_0$). This yields a transmissivity of 1000 m^2d^{-1} . Element sizes of 50 m are used, which are refined to 10 m and 2 m close to the pumping well. The pumping rate is -0.011574074 m^3s^{-1} , corresponding to 1000 m^3d^{-1} .

Results are shown in Figure 10.6.2 in top view, also showing the grid used, and in Figure 10.6.3, which depicts a comparison of the piezometric heads at observation points 30 m, 70 m and 100 m from the pumping well calculated by GeoSys and the analytical solution given by Theiss (1939). The correspondence is good, thus verifying radial transient flow.

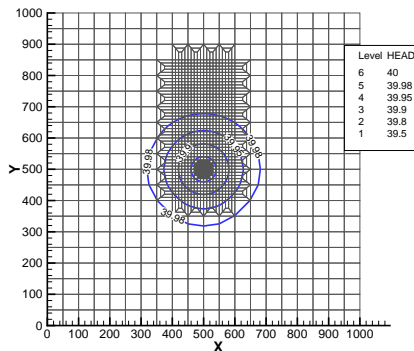


Figure 10.6.2: Radial flow to a well in a confined aquifer: Top view of the piezometric head.

Benchmark	Type	Path
radial_flow_Theiss	H	benchmarks\H\radial_flow_Theiss

10.6.2 Conservative Transport in radial flow

This benchmark describes the behaviour of a conservative tracer injected in a fully penetrating well in a two-dimensional homogeneous confined aquifer. The main purpose is to compare the numerical results of a conservative mass transport simulation without any reactions in a radial flow field, with the approximate analytical solution for this problem that is given by Moench and Ogata (1981)

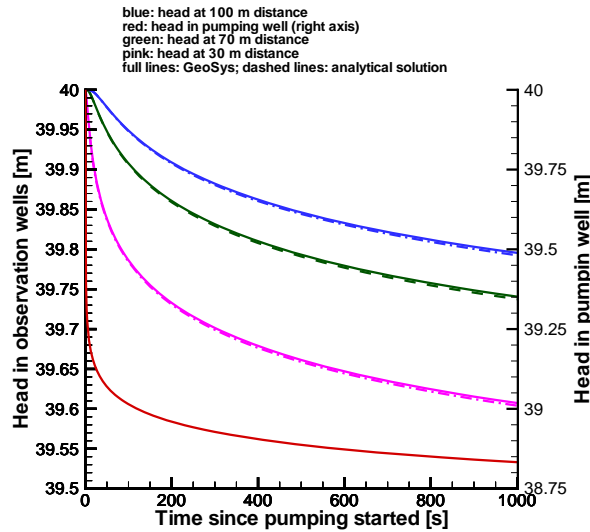


Figure 10.6.3: Radial flow to a well in a confined aquifer: drawdown in the observation well, comparison to the analytical solution.

and available in a computer program (LTIRD) provided by Javandel, Doughty, and Jsang (1984).

The aquifer is represented by a two-dimensional model of 300 m in both x and y direction with constant head boundary conditions at the four sides of the domain. The model is discretized in 30 rows and 30 columns with a constant width of 10 m. In order to obtain a better accuracy in the results, an area of 20 m around the injection well is further refined. The aquifer has an isotropic hydraulic conductivity K of $1.15741 \cdot 10^{-5} \text{ m s}^{-1}$, a porosity of 0.3 and injection rate Q $1.157407 \cdot 10^{-3} \text{ m}^3 \text{ s}^{-1}$. Both longitudinal and transverse dispersivity have the same value $\alpha_L = \alpha_T$ set to 10 m, while due to the model dimension and flow velocity, the diffusion coefficient is neglect. The physical aquifer parameters are summarized in Tab. 10.6.1. The transport simulation is run for a period of 2332800 s with a time step length of 243 s.

Evaluation method

Model results are compared to the approximate analytical solution from Moench and Ogata (1981).

Results

Results of the tracer distribution along a polyline after 27 days are shown in Fig. 10.6.5 and the correspondence between analytical solution and numerical

Table 10.6.1: Parameters used for benchmark HC\radial_flow_transport

parameter	value	unit
porosity $\Phi = n$	0.3	—
hydraulic conductivity K	$1.15741 \cdot 10^{-5}$	ms^{-1}
injection rate Q	$1.157407 \cdot 10^{-3}$	$\text{m}^3 \text{s}^{-1}$
storage coefficient S	0.0	s^{-1}
longitudinal dispersivity α_L	10	m
transverse dispersivity α_T	10	m
total simulation time	2332800	s
time step length	243	s

simulation is very good.

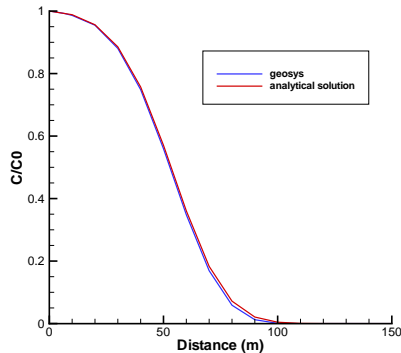


Figure 10.6.4: Tracer distribution for radial diverging flow along a profile. Comparison of analytical solution and GeoSys/RockFlow results after 27 days of injection.

Benchmark	Type	Path
radial_flow_transport	HC	benchmarks\C\radial_flow_transport

10.7 Reactive Transport

10.7.1 1D reactive transport: Xylene degradation with multiple monod kinetics, exchange kinetics and biomass growth

This benchmark describes the reactive transport of xylene in a homogeneous aquifer. The main purpose is to document the ongoing reactions, which are xylene degradation under aerobic, sulfate reducing and iron reducing conditions,

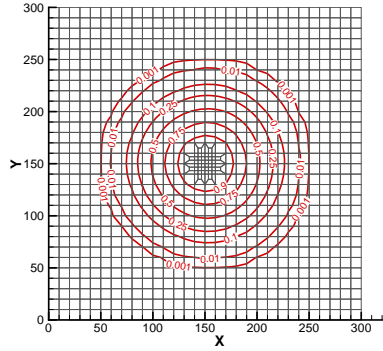


Figure 10.6.5: Tracer distribution for radial diverging flow in top view. Isolines of tracer concentration from GeoSys/RockFlow results after 27 days of injection.

considering growth of the respective biomasses. Also included is the rate limited exchange of iron goethite into bioavailable iron. The aquifer is represented by a one-dimensional model of 50 m length in the x-direction and 1 m in the y- and z directions, respectively. The model is discretized by 100 line elements of constant 0.5 m length in x direction. With an isotropic hydraulic conductivity K of $2.13 \cdot 10^{-3} \text{ m s}^{-1}$, a porosity of 0.24 and a hydraulic gradient I of $1.3 \cdot 10^{-4}$, the steady state transport velocity v_a is 0.1 m d^{-1} . Longitudinal dispersivity α_L is set to 0.25 m, the diffusion coefficient D_a is set to $1.0 \cdot 10^{-9} \text{ m}^2 \text{ s}^{-1}$. The physical aquifer parameters are summarized in Tab. 10.7.1. The transport simulation is run for a period of 1000 d with a time step length of 5 d.

The model aquifer has a length of 50 m in the x-direction, 1 m in the y-direction and 1 m in the z direction. The whole domain is discretized into 100 line elements with a constant x and y dimension of 1 m. The aquifer is assumed to have a homogeneous and isotropic hydraulic conductivity. Using a gradient of $1.23 \cdot 10^{-4}$ and a porosity of 0.24 produces a steady state transport velocity of 0.10 m d^{-1} .

Xylene degradation is simulated according to the typical redox sequence.

Evaluation method

Model results are compared an older version of GeoSys/RockFlow.

Results

Results of the simulation are shown in Fig. 10.7.1 for xylene, the electron acceptors oxygen and sulfate, as well as for the biomass of the aerobic microorganisms,

Table 10.7.1: Parameters used for benchmark HC\1d_xylene_degradation

parameter	value	unit
porosity $\Phi = n$	0.24	—
matrix volume fraction VOL_{MAT}	0.75	—
biomass volume fraction VOL_{BIO}	0.01	—
hydraulic conductivity K	$2.13 \cdot 10^{-3}$	ms^{-1}
storage coefficient S	0.0	s^{-1}
solid density ρ_s	2000	$\text{kg} \cdot \text{m}^{-3}$
density of water ρ_w	1000	$\text{kg} \cdot \text{m}^{-3}$
viscosity water η	0.001	$\text{Pa} \cdot \text{s}$
longitudinal dispersivity α_l	0.25	m
component diffusion coefficient D	$1.0 \cdot 10^{-9}$	$\text{m}^2 \text{s}^{-1}$

the sulfate reducers and the iron reducers simulation time steps of 100 days. For simulation time $t < 500$ d, one can see the advancing xylene front, a reduction of xylene concentrations is only visible for later times, when xylene concentrations reduce to about 90% of the inflow concentration. Also shown is the increasing consumption of oxygen with time, accompanied by the growth of the aerobic reducers at the inflow (left) end of the model area. After approximately 800 d, oxygen concentrations in the inflowing groundwater are reduced to almost zero within the first 20 m of the aquifer. Sulfate reducers initially decay from their initial amount, as growth is inhibited throughout the column by the still high concentrations of oxygen. Once oxygen is used up, however, sulfate reducers start to grow downstream of the oxygen reducers and sulfate concentrations in the groundwater reduce accordingly. The iron reducers decay from their initial values and start to grow only for late times $t > 80$ d and $x > 30$ m, as xylene degradation from iron reduction is inhibited by both, oxygen as well as sulfate, which is still present in concentrations larger than the inhibition concentration for iron reducers. Accordingly, the spatial distribution of bioavailable iron is still almost uniform throughout the aquifer.

Benchmark	Type	Path
1d_xylene_degradation	HC	benchmarks\C\1d_xylene_degradation

10.7.2 1D reactive transport: Competition of TCE- and cis-DCE-degradation for the zero valent iron surface

This example simulation demonstrates the use of GeoSys/RockFlow for simulation of multi-species kinetic reactions. The reaction system was set up by D. Schäfer and published in Schäfer et al. (2003) (Schäfer, D., R. Köber and A. Dahmke (2003): Competing TCE- and cis-DCE-degradation kinetics by zero-valent iron - experimental results and numerical simulation. Journal of Contaminant Hydrology, 65(3-4): 183-202). Further, it was used for model ver-

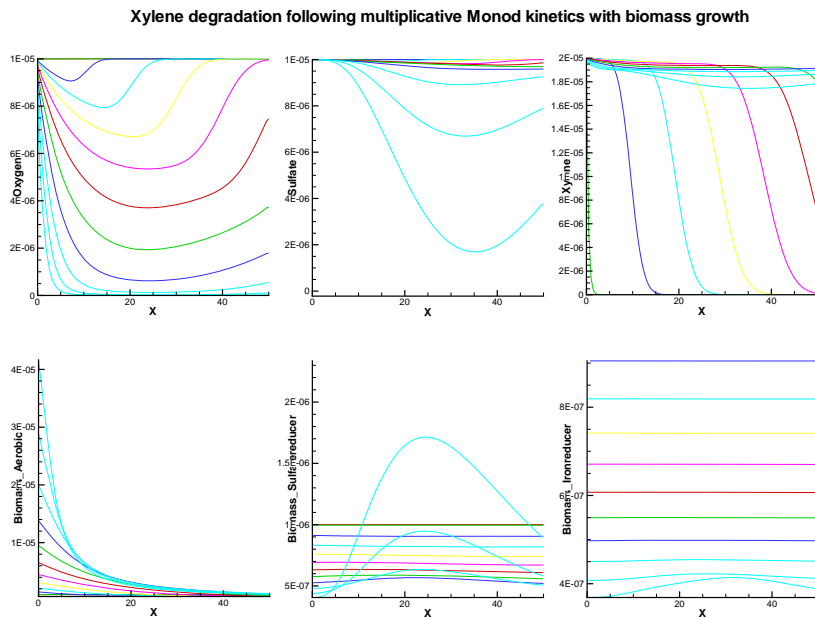


Figure 10.7.1: Profiles of oxygen, sulfate and xylene (top row, from left) and aerobic reducers, sulfate reducers and iron reducers at different times during the 1000 d simulation period.

ification of the newly implemented and developed kinetic reaction module in GeoSys/RockFlow. The example considers flow in a one-dimensional column of 1 m length, resembling the thickness of a reactive iron barrier perpendicular to the flow direction. It involves 19 species and 16 different geochemical reactions, both first-order degradation reactions of adsorbed substances and kinetic sorption reactions of the langmuir-type, considering competition for the available sorption sites.

The model set up consists of a 1d column with saturated ground water flow with a darcy velocity of $5.0 \cdot 10^{-4} \text{ m d}^{-1}$ from left to right. Geochemical species are added to the inflowing water, and their sorption and degradation behavior is modeled. For a complete description of input parameters see the paper by Schfer et al. (2003). Every degradation reaction follows a Langmuir-Hinshelwood-Hougen-Watson kinetics with a limited number of sites for the adsorption and desorption of chlorinated hydrocarbons on the reactive iron surface. Since all the reactive substances involved have to adsorb onto the reactive iron surface in order to be degraded, a competition for the surface sites occurs. This competition has been investigated in column studies and the observed concentration profiles were simulated with the numerical model TBC (Schfer et al., 2003).

Evaluation method

Model results are compared an older version of GeoSys/RockFlow, which was compared to the original TBC simulations.

Results

Results of the simulation are shown in Fig. 10.7.2, where profiles of the dissolved species are shown. TCE and cis-DCE are added to the inflowing water. They compete for the sorption sites, and when sorbed degrade according to a first order degradation reaction. The retardation of the reactive species compared to the conservative tracer `mobile` is clearly visible. Also, just downstream of the concentration decrease of TCE or cis-DCE, the degradation products ethane and C4-containing molecules increase. These species are again mobile and are transported with the water, so an instationary behaviour is observed in Fig. 10.7.2.

Benchmark	Type	Path
1d_TCEonIon	HC	benchmarks\1d_TCEonIon

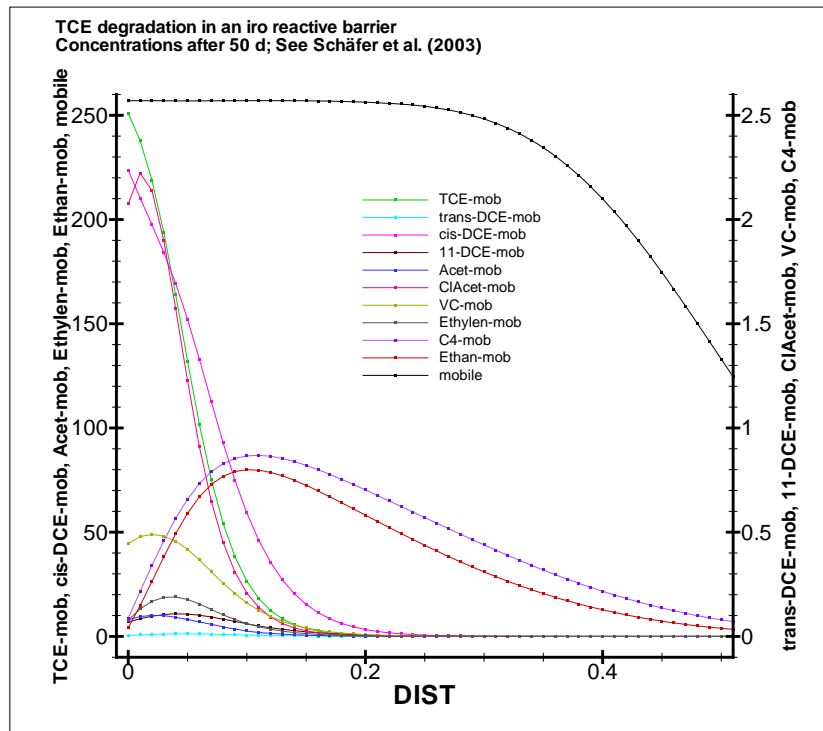


Figure 10.7.2: Concentration profiles of TCE, trans-DCE, cis-DCE, 1,1-DCE, Acetylene, chloroacetylene, C4, VC, ethene and ethane as well as the conservative tracer mobile after 50 d simulation time.

10.7.3 1D reactive transport: Sequential CHC degradation with isotope fractionation

Reaction model

When a substrate C is present in the form of light and heavy isotopes C^l and C^h and one of the isotopes is preferentially consumed by a microbial population X , a kinetic isotope fractionation effect can be observed, i.e. one of the isotopes will become enriched in the remaining fraction of electron donors relative to its isotope partner. At the same time, the preferentially consumed isotope will become enriched in the reaction product relative to the more recalcitrant isotope. The degree of isotope fractionation can be expressed by means of the fractionation factor α [-], which is a reaction specific constant and relates the isotopic ratio of the degradation reaction's product to the isotope ratio of the substrate. Often, the isotopic enrichment factor ε [-] is used to quantify the isotope effect of a reaction, which can be related to α for a one step process by

$$\varepsilon = (\alpha - 1) \cdot 1000 \quad (10.7.1)$$

According to [100], the degradation rate of the light carbon isotope substrate $d^{12}C_S/dt$ is given by the overall degradation rate dC_S/dt of substrate C_S corrected for the proportion of $^{12}C_S$ to total C_S

$$-\frac{d^{12}C_S}{dt} = \frac{d^{12}C_P}{dt} = -\frac{dC_S}{dt} \frac{^{12}C_S}{^{12}C_S + ^{13}C_S} \quad (10.7.2)$$

The degradation rate of the heavy isotope substrate $d^{13}C_S/dt$ then is given by

$$-\frac{d^{13}C_S}{dt} = \frac{d^{13}C_P}{dt} = -\frac{dC_S}{dt} \frac{^{13}C_S}{^{12}C_S + ^{13}C_S} (\varepsilon \cdot 10^{-3} + 1) \quad (10.7.3)$$

According to [100], dC_S/dt can be any rate expression, such as first order, Michaelis-Menten or Monod-kinetics. Based on this concept and using the general formulation of multiple Monod kinetics of first order growth of a microbial species X from consumption of the light isotope substrate $^{12}C_S$ can be expressed by

$$\left[\frac{\partial X}{\partial t} \right]_{^{12}C_S} = \mu_{max} X \left[\prod_{j=1}^{n_M-1} \left(\frac{C_j}{K_j^M + C_j} \right) \prod_{j=1}^{n_I} \left(\frac{K_j^I}{K_j^I + C_j} \right) \right] \frac{C_S^{tot}}{C_S^{tot} + K_{CS}^M} \frac{^{12}C_S}{C_S^{tot}} \quad (10.7.4)$$

where $C_S^{tot} = ^{12}C_S + ^{13}C_S$ and μ_{max} [T^{-1}] is the maximum growth rate of X with respect to substrate C . Growth of X from consumption of the heavy isotope substrate $^{13}C_S$ can be expressed accordingly by

$$\left[\frac{\partial X}{\partial t} \right]_{^{13}C_S} = \mu_{max}^* X \left[\prod_{j=1}^{n_M-1} \left(\frac{C_j}{K_j^M + C_j} \right) \prod_{j=1}^{n_I} \left(\frac{K_j^I}{K_j^I + C_j} \right) \right] \frac{C_S^{tot}}{C_S^{tot} + K_{C_S}^M} \frac{^{13}C_S}{C_S^{tot}} \quad (10.7.5)$$

where $\mu_{max}^* = \mu_{max}(\varepsilon/1000 - 1)$. The resulting degradation rates of $^{12}C_S$ and $^{13}C_S$ accordingly are given by

$$\frac{\partial^{12}C_S}{\partial t} = -\mu_{max} X \frac{St_{C_S}}{Y_{C_S}} \left[\prod_{j=1}^{n_M-1} \left(\frac{C_j}{K_j^M + C_j} \right) \prod_{j=1}^{n_I} \left(\frac{K_j^I}{K_j^I + C_j} \right) \right] \frac{C_S^{tot}}{C_S^{tot} + K_{C_S}^M} \frac{^{12}C_S}{C_S^{tot}} \quad (10.7.6)$$

$$\frac{\partial^{13}C_S}{\partial t} = -\mu_{max}^* X \frac{St_{C_S}}{Y_{C_S}} \left[\prod_{j=1}^{n_M-1} \left(\frac{C_j}{K_j^M + C_j} \right) \prod_{j=1}^{n_I} \left(\frac{K_j^I}{K_j^I + C_j} \right) \right] \frac{C_S^{tot}}{C_S^{tot} + K_{C_S}^M} \frac{^{13}C_S}{C_S^{tot}} \quad (10.7.7)$$

where St_{C_S} [-] and Y_{C_S} [-] are the stoichiometric and yield coefficients for substrate C_S . Degradation kinetics for the conceptually more simple Michaelis-Menten, first or zeroth order kinetics may be derived on basis of eqs. 10.7.4 - 10.7.7 assuming a constant microorganism mass and choosing appropriate values of μ_{max} , μ_{max}^* , $K_{C_S}^M$, St_{C_S} and Y_{C_S} .

For the simulation of biodegradation with isotope fractionation of a substrate species C_S by multiplicative Monod (or one of the more simplified) kinetics, heavy and light isotopes of the fractionating substrate, e.g. $^{12}C_S$ and $^{13}C_S$, must be defined as two individual species with corresponding transport processes. Also, two individual degradation reactions must be defined, requiring identical parameter values for μ_{max} , Y_{C_S} , and all K_i^M , K_i^I , and St_i . The isotopic enrichment factor ε then is used to calculate the modified maximum growth rate μ_{max}^* for the more recalcitrant isotope.

Problem definition

In this benchmark, which is based on a model of [100], sequential degradation of chlorinated hydrocarbons (CHC) from PCE to the end product ethylene (Eth), which is not further degraded, is simulated:



A contaminant source located at the upstream model boundary emits a constant concentration of PCE. All degradation reactions follow simple first order kinetics and involve an isotope fractionation effect. The one-dimensional transport model has a length of 876 m and is discretized by 120 finite line elements

of 7.3 m length, respectively. Basic flow and transport model parameters are summarized in Tab. 10.7.2, reaction parameters for the individual species in Tab. 10.7.3.

Table 10.7.2: Parameters used for benchmark HC\1d_isofrac

parameter	value	unit
porosity $\Phi = n$	0.25	–
matrix volume fraction VOL_MAT	0.74	–
biomass volume fraction VOL_BIO	0.01	–
hydraulic conductivity K	$1.1574 \cdot 10^{-4}$	ms^{-1}
flow velocity q	$1.1574 \cdot 10^{-6}$	ms^{-1}
longitudinal dispersivity α_l	1.0	m
component diffusion coefficient D	$3.0 \cdot 10^{-9}$	m^2s^{-1}

Table 10.7.3: Reaction parameters used for benchmark HC\1d_isofrac

CHC species	enrichment factor ε [-]	first order rate constant λ [s^{-1}]
PCE	-5.2	$6.366 \cdot 10^{-8}$
TCE	-8.5	$3.125 \cdot 10^{-8}$
DCE	-17.8	$2.199 \cdot 10^{-8}$
VC	-23.2	$1.273 \cdot 10^{-8}$
Eth	0.0	–

Each of the mobile hydrocarbon species is defined twice, once for the light isotopologue and once for the respective heavy isotopologue. Also, an immobile microorganism species X is defined, which has an initial unit concentration of 1.0 throughout the model domain. The microorganisms degrade each of the chlorinated species (i.e. PCE, TCE, DCE and VC). Thus, a total of eight monod-type growth reactions for X , one for each isotopologue species, must be defined. Growth of X , however, is inhibited by setting the growth parameter in the *.krc file to zero in each of the reactions and microorganism decay is not included in the simulation, i.e. X is constant in time and space. Each reaction contains only a single Monod term for the respective isotopologue species. To achieve degradation kinetics of first order in each case, the half saturation concentrations $K_i^M \gg C_i$ and are hence set to a value of $1.0 \cdot 10^{10}$. As the effective first order rate constant is given by $\lambda_i = \mu_{max,i}/K_i^M$, parameters $\mu_{max,i}$ are set to proportionally high values in the *.krc file, i.e. ten orders of magnitude larger than indicated in Tab. 10.7.3. Also, the yield coefficients Y_i for the individual reactions must be set to 1.0.

Initial concentrations of all species except the microorganisms are 0.0 mol L⁻¹ throughout the model domain. For ¹²PCE and ¹³PCE the upgradient boundary conditions are constant concentrations of $9.892 \cdot 10^{-4}$ and $1.078 \cdot 10^{-4}$ mol L⁻¹, respectively. The hydraulic gradient of 0.01 is induced by fixed head boundary conditions of 10.0 and 9.781 m at the up- and downgradient model boundaries. The reactive transport simulation is run for a period of 20 a with 200 time steps

of 3153600 s, respectively, and using an explicit-implicit time stepping scheme ($\theta = 0.5$).

Evaluation method

Model results are compared against the one-dimensional Domenico analytical solution including first order degradation kinetics as well as by comparison of an equivalent one dimensional simulation with PHREEQC, which was presented by Van Breukelen et al. (2005). The PHREEQC input file is available at http://pubs.acs.org/doi/suppl/10.1021/es048973c/suppl_file/es048973csi20050317_100816.pdf.

Results

Results at the end of the simulation are presented in Figs. 10.7.3 and 10.7.4. In Fig. 10.7.3, numerical simulation results for the PCE isotopologues in form of normalized concentrations C/C_0 are compared against results of the one-dimensional Domenico analytical solution including first order degradation, in which the first order degradation rate for the heavy PCE isotopologue $\lambda_{^{13}\text{PCE}} = \lambda_{^{12}\text{PCE}}(\varepsilon/1000 - 1)$. Note that for the comparison with the analytical solution kinetic reactions are suppressed on the first node of the FE mesh (i.e. on the upstream model boundary in order to correctly represent the concentration boundary condition of the analytical solution. Concentrations of the PCE isotopologues match the analytical solution over a concentration range of more than 10 orders of magnitude. Also the resulting $\delta^{13}\text{C}$ [permil] isotope signatures, which were computed by

$$\delta^{13}\text{C} = \left(\frac{R_{C_i}}{R_{Ref}} - 1 \right) 1000 \quad (10.7.8)$$

where R_{C_i} [-] is the isotope ratio $^{13}\text{C}_i/^{12}\text{C}_i$ of species C_i in the simulation, while R_{Ref} [-] is the isotope ratio of the international standard, i.e. in this case the Vienna Pee Dee Belemnite (V-PDB; $R_{Ref} = 0.011237$), match results of the analytical solution precisely, verifying the correctness of the implementation.

In Fig. 10.7.4 the upper left and right diagrams show simulated concentration profiles of the individual CHC species versus results obtained by PHREEQC. Note that for the comparison with the PHREEQC simulation, kinetic reactions are not suppressed on the upstream model boundary. The lower diagram shows $\delta^{13}\text{C}$ isotope signatures. While concentrations of ^{12}PCE and ^{13}PCE decrease exponentially with distance from the source at the left hand side model boundary, isotopologues of TCE, DCE and VC show concentration peaks in different distances from the source. Eth isotopologues finally accumulate as the end products of the degradation chain and reach the source concentrations of ^{12}PCE and ^{13}PCE , respectively. Also, while TCE, DCE and VC isotope signatures increase

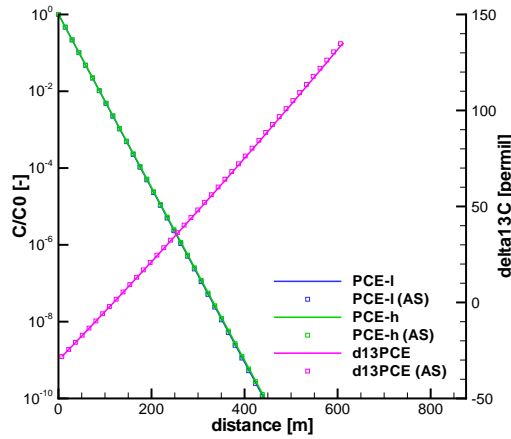


Figure 10.7.3: PCE isotopologue concentration profiles (left axis) and $\delta^{13}C$ isotope signature (right axis) versus transport distance along the 1D model. Lines represent GeoSys simulation results, symbols represent analytical solution results.

almost linearly with travel distance, demonstrating the increasing enrichment of the heavy isotopologues, the Eth signature approaches the $\delta^{13}C$ of the source, i.e. PCE. For all isotopologue species, concentration profiles and isotope signatures show an excellent agreement with the PHREEQC simulation, verifying the numerical implementation also for sequential degradation reactions.

Benchmark	Type	Path
1d_Isofrac	HC	benchmarks\C\1d.isofrac

10.7.4 1D reactive transport: degradation of organic contaminants in a sand column experiment by five bacterial groups forming a degradation network

The Biogeochemical Reaction Network Simulator (BRNS, [101, 102]) is coupled to GeoSys following a sequential non-iterative operator splitting scheme yielding the reactive transport model GeoSysBRNS. The technical coupling is sketched in Fig. 10.7.5.

The Model

An experimental study by [103] has been used to validate the reactive transport models TBC [104] and the stand-alone 1D version of BRNS [105]. Both models

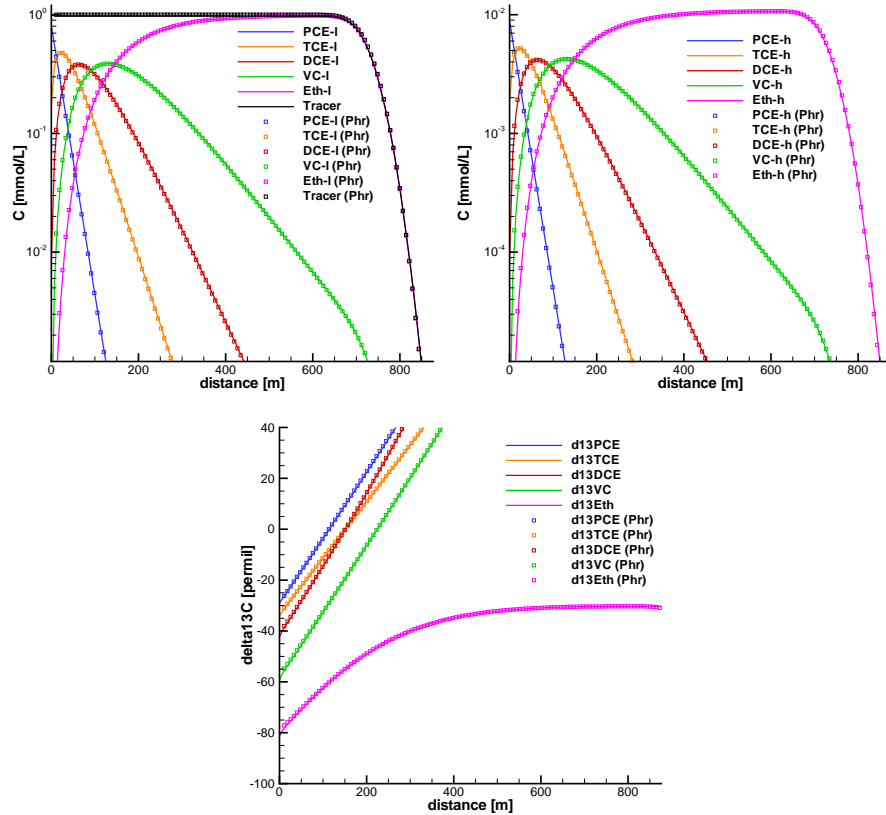


Figure 10.7.4: Light (upper left diagram), heavy (upper right diagram) isotopeologue chlorinated hydrocarbon species profiles and $\delta^{13}\text{C}$ isotope signatures (lower diagram) versus transport distance along the 1D model. Full lines represent GeoSys simulation results, symbols represent PHREEQC simulation results.

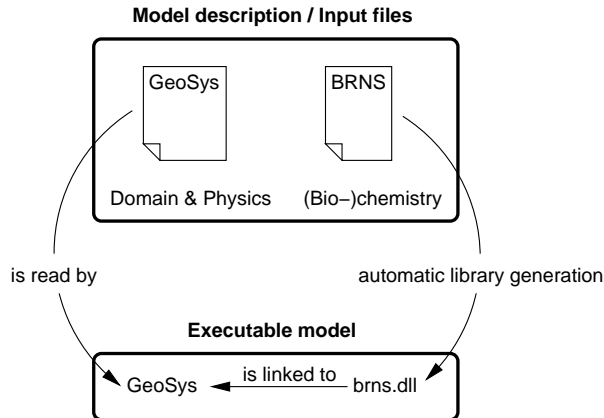


Figure 10.7.5: The setup of GeoSysBRNS. The model description is divided into two parts: the model domain definition, physical parameters, hydrogeological flow, and discretization parameters in GeoSys format, and the description of the coupled (bio-)chemical reaction processes in BRNS format. The latter is compiled into a problem specific library that is accessed by GeoSys at runtime.

could reproduce the experimental data set. Here, we use the same simulation scenario to validate GeoSysBRNS and compare simulation results to BRNS results.

In the example referred to as “Scenario 1” in [105], a sand column of 29 centimeters length is constantly flushed with water containing lactate as electron donor, and oxygen, nitrate, and sulfate as terminal electron acceptors (TEAs). Manganese and iron oxyhydroxides are bound to the sand matrix in solid phases and act as two additional TEAs. Five distinct microbial groups, which catalyze the reduction of each TEA to sustain their growth, are considered in the model. The experimental results suggest that lactate is concomitantly mineralized into dissolved inorganic carbon (DIC) and fermented to acetate and propionate, with the latter being further oxidized into DIC. In addition to these microbial degradation pathways, reactive species concentrations are influenced by a set of abiotic reactions (Fig. 10.7.6). The complete reaction network of the model consists of 21 mobile and 18 immobile reactive species. The dynamics of the system is determined by 24 kinetically controlled chemical reactions and nine equilibrium reactions describing acid base dissociations.

Evaluation method

The coupling of the BRNS to GeoSys is shown to be correct by comparing simulation results of GeoSysBRNS to BRNS results [106].

- phase exchange (matrix, biophase, pore water)
- oxidation of sulfide by Fe(III)
- precipitation and dissolution of calcite and Fe(II) minerals
- acid-base reactions for carbonates, sulfides, lactate, propionate, acetate

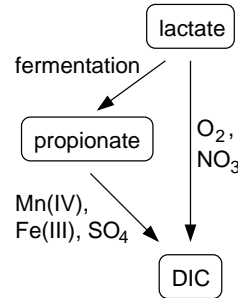


Figure 10.7.6: Modeling organic carbon degradation in a sand column experiment. Coupled abiotic processes considered in the model (left), and microbial degradation pathways with corresponding TAEs (right).

Results

We simulate the experiment with GeoSysBRNS using two spatial resolutions and three different temporal resolutions per spatial setting, ensuring Courant numbers smaller than 1.0 in all cases. As in previous studies [105, 104], we choose 48 days as the target time for comparing the results of the coupled model to those obtained with the BRNS model using the same set of spatio-temporal resolution settings. At this target time, the system is still in the transient phase.

The simulation results of GeoSysBRNS and BRNS agree very well for all 39 reactive species at the highest spatial and temporal resolution (see selected species in Figs. 10.7.7, 10.7.8). Decreasing the spatial resolution leads to slightly different results, with the coupled model generally staying closer to the high resolution result than the stand-alone version of BRNS (Figs. 10.7.7, 10.7.8).

When the time step size is increased, the numerical results of both models diverge from the high resolution result (Fig. 10.7.9). While increasing the time step from 4 s to 43.2 s does not lead to significant changes for both models and both spatial resolutions, a noticeable deviation is observed when the time step size is further increased to 108 s for the high, and to 216 s for the low spatial resolution. For these larger time step sizes, the results of GeoSysBRNS are again generally closer to the high resolution result than the BRNS solutions. The observed differences can be attributed to the different numerical schemes used by BRNS (finite differences) and GeoSysBRNS (finite elements). Further details of the GeoSysBRNS and its performance can be found in [106].

Benchmark	Type	Path
1d_degradation_network	C	benchmarks\C\1d_degradation_network

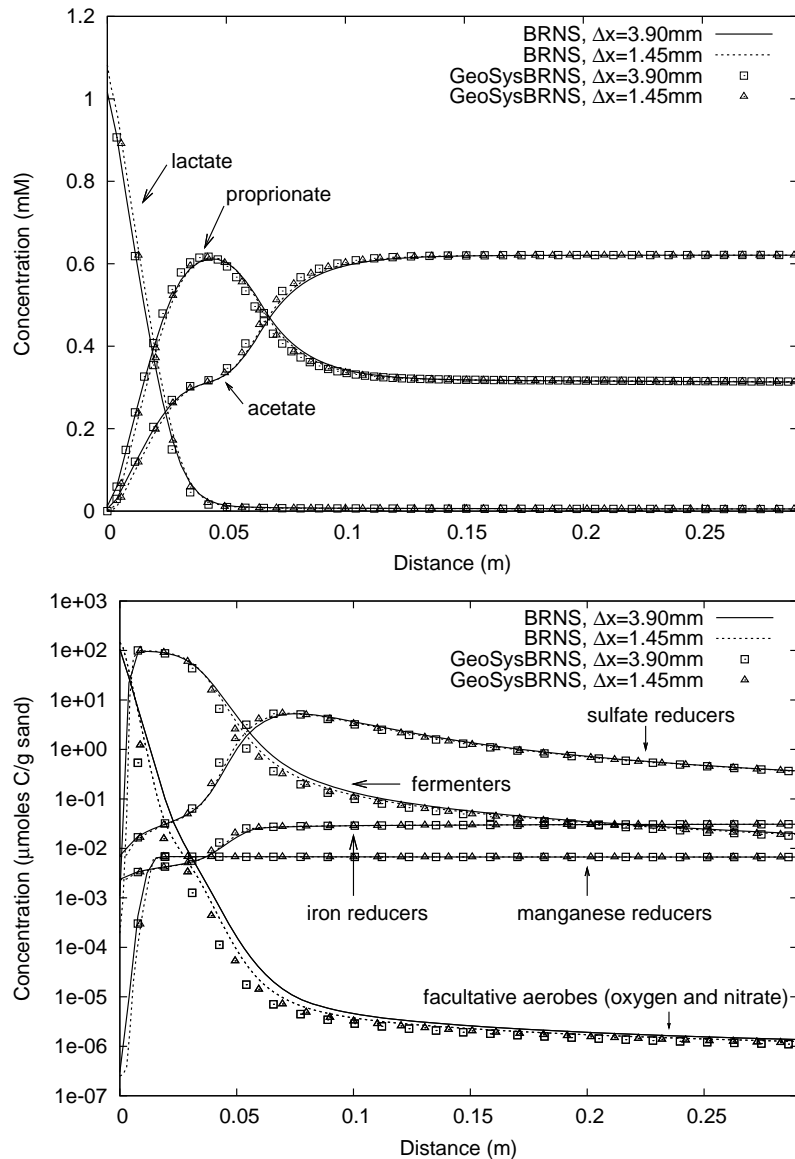


Figure 10.7.7: Comparison of simulation results obtained with BRNS (lines) and GeoSysBRNS (symbols): organic species (top) and all five bacterial groups (bottom) at day 48 using the highest temporal resolution ($\Delta t=4\text{ s}$) and two spatial resolutions.

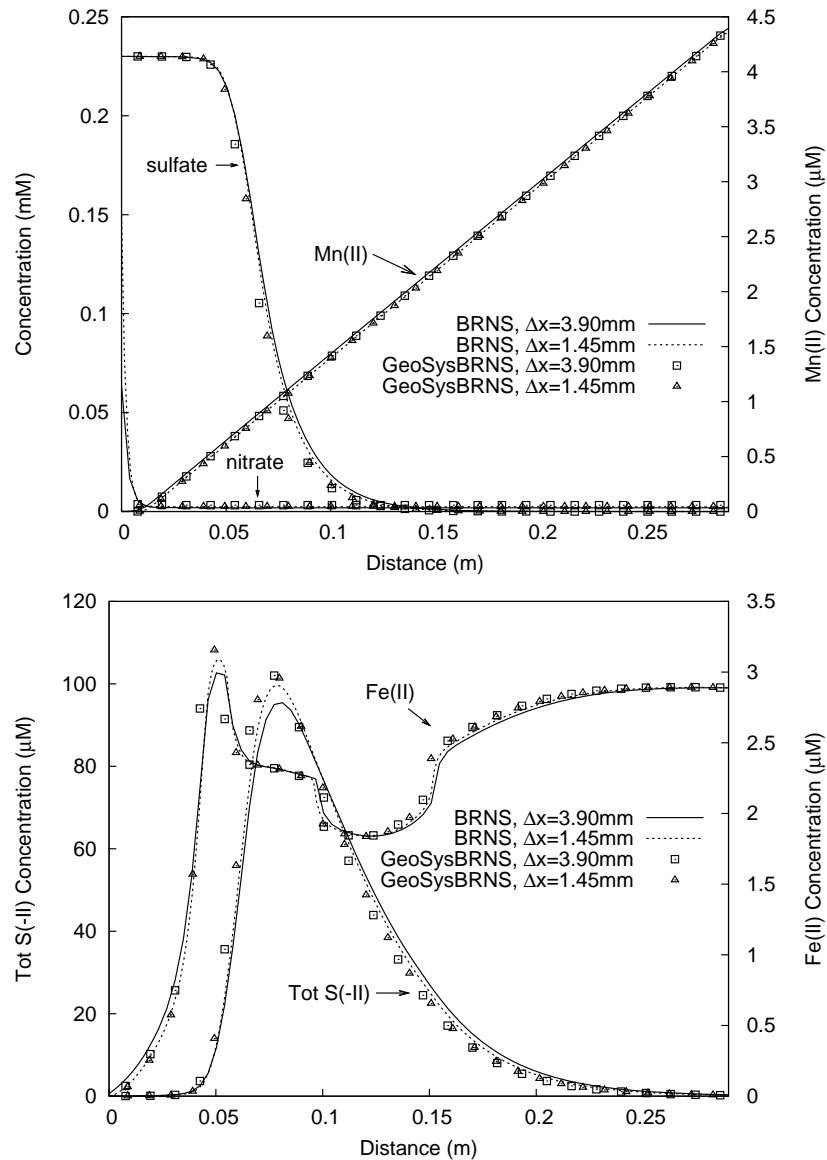


Figure 10.7.8: Comparison of simulation results obtained with BRNS (lines) and GeoSysBRNS (symbols): inorganic species at day 48 using the highest temporal resolution ($\Delta t=4\text{ s}$) and two spatial resolutions.

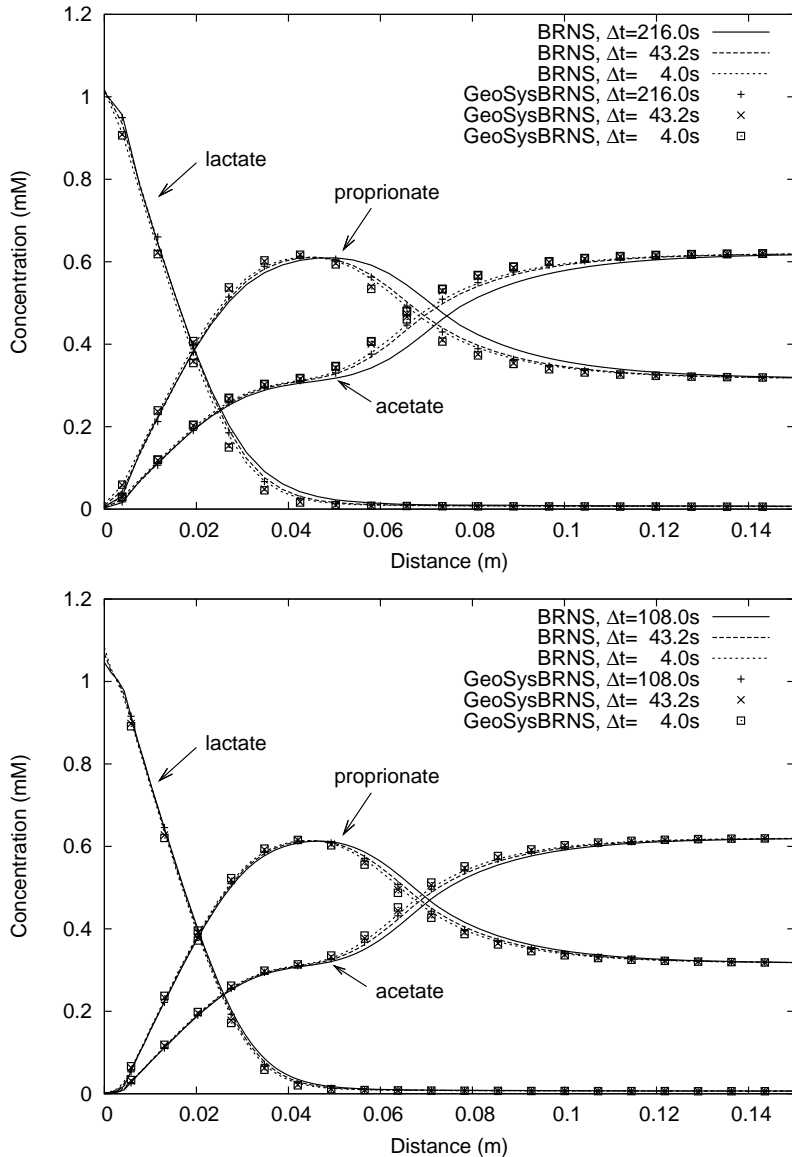


Figure 10.7.9: Comparison of simulation results obtained with BRNS (lines) and GeoSysBRNS (symbols) at day 48 using two spatial resolutions (top: $\Delta x=3.9\text{mm}$, bottom: $\Delta x=1.45\text{mm}$) and different time step sizes for lactate, propionate, and acetate.

10.7.5 Mixing Controlled Bioreactive Transport (2D)

Problem definition

For contaminated groundwater, the natural remediation process is usually limited by the availability of substrates acting as a carbon source for soil bacteria and the availability of electron acceptors. The transport of these chemical compounds is controlled by the dispersion length of the flow system. Recently, [107] presented an analytical solution (revised in [108]; see also [109]) for the steady state of a two-dimensional scenario dominated by transversal mixing. This example serves as a first multidimensional benchmark to validate GeoSysBRNS. [107] and [108] provide analytical solutions for double-monod kinetics with first-order biomass decay. GeoSysBRNS is also compared to the KinReact module of GeoSys (GeoSysKRC), which is able to solve the same problem.

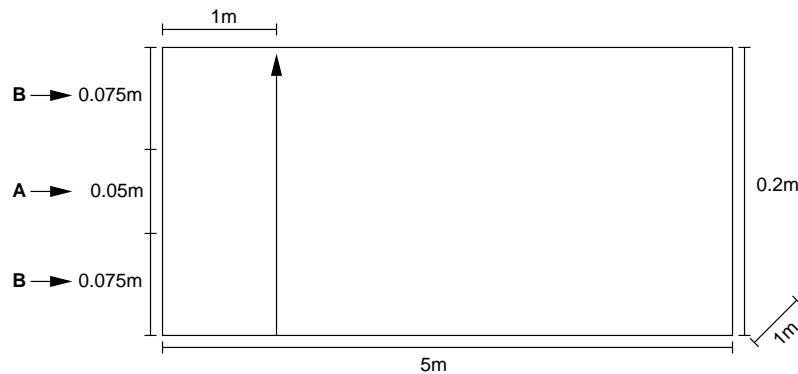


Figure 10.7.10: The simulation domain. Simulation results are compared using concentration profiles along a transect at a distance of one meter from the inflow boundary, indicated by the arrow.

Parameters

In this scenario, bacterial growth is modeled using double-monod terms for the substrates. Biomass decays with a constant decay rate d . The overall dynamics is described by four differential equations, with the dynamics of species A, B, and C directly linked to the biomass growth r via yield factor Y :

$$\frac{\partial C_{bio}}{\partial t} = \underbrace{\frac{C_A}{K_A + C_A} \cdot \frac{C_B}{K_B + C_B} \cdot \mu_{max} \cdot C_{bio}}_r - d \cdot C_{bio} \quad (10.7.9)$$

$$\frac{\partial C_A}{\partial t} = -\frac{1}{Y} \cdot r \quad (10.7.10)$$

$$\frac{\partial C_B}{\partial t} = -\frac{1}{Y} \cdot r \quad (10.7.11)$$

$$\frac{\partial C_C}{\partial t} = +\frac{1}{Y} \cdot r. \quad (10.7.12)$$

The chemical parameters and their values are listed in Table 10.7.4.

Table 10.7.4: Reaction parameters and values.

Symbol	Parameter	Value	Unit
K_A	monod constant substrate A	8.33×10^{-5}	mol/l
K_B	monod constant substrate B	3.13×10^{-5}	mol/l
μ_{max}	maximum growth rate	1.0	d^{-1}
d	biomass death rate	0.1	d^{-1}
Y	yield coefficient	1.0	g/mol

Using GeoSysBRNS, here we simulate the case as a transient state groundwater flow process coupled with biodegradation. The numerical solutions are compared to the analytical steady state solutions and against the GeoSysKRC simulation.

The model domain is five meters long and 20 centimeters wide (see Figure 10.7.10). Groundwater flows from left to right. Transport velocity is 1 m/d. The transport parameters are listed in Table 10.7.5. Two substrates are continuously emitted at the left inflow boundary throughout the simulation period. Substrate A is centrally injected over a width of five centimeters with a concentration of 3.3×10^{-4} mol/l, while substrate B is emitted at the remaining part of the boundary with a concentration of 2.5×10^{-4} mol/l. Initially, the concentration in the whole simulation domain is zero for substrate A, 2.5×10^{-4} mol/l for substrate B, and 1.0×10^{-6} g/l for biomass. Biomass is considered to be immobile.

In the presence of both species A and B, with A representing a generic organic contaminant acting as a carbon source and B representing a generic electron acceptor, the biomass grows, and a waste product C is formed.

For the numerical simulation, a grid spacing of 2.5 cm in flow, and 0.4 cm transversal to the flow direction is used. Temporal discretization of 2min is employed. The GeoSysKRC simulation additionally verifies the functionality of three routines, which were implemented to enhance computational efficiency of the numerical simulation:

Table 10.7.5: Transport parameters and values.

Parameter		Value	Unit
v_a	transport velocity	1.0	m/d
D_t	transversal dispersion coefficient	2.5	cm ² /d
D_l	longitudinal dispersion coefficient	0.0 ^a	cm ² /d

^aAs a zero value cannot be used in the numerical simulation, the value $2.5 \times 10^2 \text{ cm}^2/\text{d}$ was used instead. When the numerical simulation reaches steady state, this difference can be neglected.

- The steady state flow field is computed only once (i.e. for the first time step) during the simulation. For later time steps, the velocities calculated for the first time step are reused for all transport processes. This modus is invoked by the flow process keyword

```
$TIM_TYPE
STEADY.
```

- Mass matrices for all transported (i.e. mobile) species are computed only once (i.e. for the first time step), stored and reused for later time steps. This modus is invoked by mass transport process keyword

```
$MEMORY_TYPE
1
```

- Source terms are defined as volumetric fluxes [m^3s^{-1}]. The flux defined for a polyline is evenly distributed to all nodes of that polyline. This modus is invoked for a source term by the keyword

```
$DIS_TYPE
CONSTANT_GEO 2.31481E-06
```

where the number represents the volumetric flux assigned to a polyline.

In the GeoSysKRC simulation, the downgradient model boundary consists of two polylines with lengths of 0.15 and 0.05 m, respectively. In order to achieve a transport velocity (setting porosity $n = 0.5$) of 1 md^{-1} (or $1.15741 \cdot 10^{-6} \text{ ms}^{-1}$) with a given a total model cross section of 0.2 m^2 (i.e. assuming a unit width of the model), the volumetric fluxes assigned to the polylines are $-8.75130 \cdot 10^{-7}$ and $-2.822945 \cdot 10^{-7} [\text{m}^3\text{s}^{-1}]$, respectively.

Results

The concentrations of the conservative tracer (i.e. the mixing ratio X) fit well with the analytical solution, indicating that the flow field and conservative transport is properly simulated by both models, and all of the three routines tested

work correctly in the GeoSysKRC simulation, which allows a reduction of computation time by approximately 50 % for this test example. Also, both numerical simulations yield the same results for the reactive species. However, some small discrepancies are found between the numerical and the analytical solutions for the components A, B, C, and (most obvious) for the biomass concentration (see Figure 10.7.11). This is mainly due to the problem of exactly defining the transitions between boundary conditions of components A and B on the inflow boundary of the model: polylines defining inflow concentrations of A and B may not share nodes and hence the boundary condition polylines are separated by a distance of one element width (i.e. 0.005 m) which has to be overcome by transverse dispersion before A and B may react with each other, while in the analytical solution A and B are in direct contact right at the model boundary. This problem and hence differences between numerical and analytical solutions may be reduced by a local mesh refinement at the left hand side model boundary.

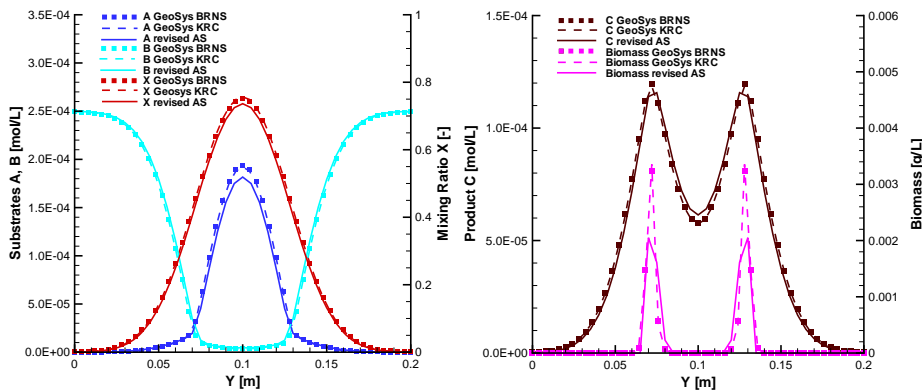


Figure 10.7.11: Simulation results for the transversal mixing model, using the kinetic approach and the finest temporal and spatial resolution. Analytical solution as solid lines, result of the numerical simulations with GeoSysBRNS as symbols and of GeoSysKRC as dashed lines.

Benchmark deposit

Benchmark	Problem type	Path in benchmark deposit
<i>monod2d</i>	C	benchmarks\C\monod2d\
<i>FG-monod</i>	C	benchmarks\C\monod2dKRC\

10.8 Conservative mass transport in unsaturated media

Problem definition

This case is a simulation of classical experiment of Warrick et al's(1971)[?]. The solution is Richards equation combining mass transport equation. For the hydraulic, it is define as section 5.2.1. For the mass transport, the tracer component goes into the soil column from top,

Initial and boundary conditions

Details of hydraulic are illustrated in Fig. 5.2.1. The initial concentration of each component is 0, and concentration at the top is in Fig. 10.8.1.

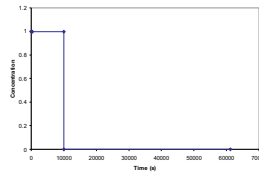


Figure 10.8.1: BC of component

Material properties

Homogenous material properties are assumed within the whole domain. Table 5.2.1 gives the parameters.

Component properties

Component properties are in Table 10.8.1.

Table 10.8.1: Parameters of component properties (mcp)

component	items	setting
tracer	mobile	1
	transport phase water	0
	diffusion coefficient	6.0e-10
adsorb	mobile	1
	transport phase water	0
	diffusion coefficient	6.0e-10
Sorption: $C_s = K_D C^e$	K_D	1e-3
	e	0.9

Results

The hydraulic features are in Fig.5.2.3. Fig. 10.8.2 shows the distribution of concentration. Points in the Fig.10.8.2 are observations.

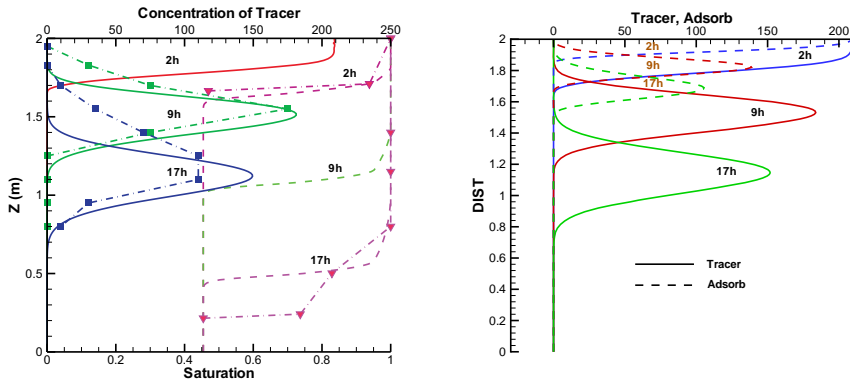


Figure 10.8.2: Distribution of saturation and concentrations

Benchmark deposit

Benchmark	Problem type	Path in benchmark deposit
<i>ust_line</i>	C	benchmarks\{C\}\1d_ust_line\

Chapter 11

Random Walk Particle Tracking – H- and Fluid Momentum- Process dependent

11.1 Theory

11.1.1 Governing Equation

The classical advection-dispersion equation of a conservative solute in porous media can be written as [110]

$$\frac{\partial C}{\partial t} = -\nabla(\mathbf{V}C) + \nabla(\mathbf{D}\nabla C) \quad (11.1.1)$$

where C is the concentration (ML^{-3}), \mathbf{V} is the pore velocity vector (ML^{-1}), and \mathbf{D} is the hydrodynamic dispersion tensor (L^2T^{-1}), t is time (T^2) and ∇ is the differential operator.

The modified velocity [111] and the dispersion tensor [110] are expressed as

$$V_i^* = V_i + \sum_{j=1}^3 \frac{\partial D_{ij}}{\partial x_j} \quad (11.1.2)$$

$$D_{ij} = \alpha_T |\mathbf{V}| \delta_{ij} + (\alpha_L - \alpha_T) \frac{V_i V_j}{|\mathbf{V}|} + D_{ii}^d \quad (11.1.3)$$

where δ_{ij} is the Kronecker symbol, α_L is the longitudinal dispersivity, α_T is the transverse dispersivity, D_{ij}^d is the tensor of molecular diffusion coefficient, and V_i is the component of the mean pore velocity in the i th direction.

The stochastic differential equation equivalent to (11.1.1) in three dimensional problems can be written as [112, 113, 114]

$$\begin{aligned} x_{t+\Delta t} &= x_t + \left(V_x(x_t, y_t, z_t, t) + \frac{\partial D_{xx}}{\partial x} + \frac{\partial D_{xy}}{\partial y} + \frac{\partial D_{xz}}{\partial z} \right) \Delta t \\ &\quad + \sqrt{2D_{xx}\Delta t} Z_1 + \sqrt{2D_{xy}\Delta t} Z_2 + \sqrt{2D_{xz}\Delta t} Z_3 \\ y_{t+\Delta t} &= y_t + \left(V_y(x_t, y_t, z_t, t) + \frac{\partial D_{yx}}{\partial x} + \frac{\partial D_{yy}}{\partial y} + \frac{\partial D_{yz}}{\partial z} \right) \Delta t \\ &\quad + \sqrt{2D_{yx}\Delta t} Z_1 + \sqrt{2D_{yy}\Delta t} Z_2 + \sqrt{2D_{yz}\Delta t} Z_3 \\ z_{t+\Delta t} &= z_t + \left(V_z(x_t, y_t, z_t, t) + \frac{\partial D_{zx}}{\partial x} + \frac{\partial D_{zy}}{\partial y} + \frac{\partial D_{zz}}{\partial z} \right) \Delta t \\ &\quad + \sqrt{2D_{zx}\Delta t} Z_1 + \sqrt{2D_{zy}\Delta t} Z_2 + \sqrt{2D_{zz}\Delta t} Z_3 \end{aligned} \quad (11.1.4)$$

where x , y , and z are the coordinates of the particle location, Δt is the time step, and Z_i is a random number whose mean is zero and variance is unit.

In equation (11.1.4), the spatial derivatives of the dispersion coefficients are introduced from the modified velocity [111]. Together with equation (11.1.3), the spatial derivatives of the dispersion coefficients can be expressed as a function of the derivatives of velocity. Note that to obtain the derivatives of velocity, velocity has to be continuous mathematically. For this end, we interpolate velocity at any location in an element from the known velocity at the element nodes. The velocity estimation and the interpolation method are provided in section 8.1.1.

Since the proposed RWPT method makes use of the FEM for velocity estimation, the derivative of velocity within each element is computed as in Figure 11.1.1 and written as

$$\begin{aligned} \frac{\partial V_x}{\partial x} &= \frac{V(x_R) - V(x_L)}{l_x}; \quad \frac{\partial V_y}{\partial y} = \frac{V(y_U) - V(y_D)}{l_y}; \quad \frac{\partial V_z}{\partial z} = \frac{V(z_N) - V(z_S)}{l_z} \\ \frac{\partial V_x}{\partial y} &= \frac{\partial V_x}{\partial z} = \frac{\partial V_y}{\partial z} = \frac{\partial V_y}{\partial x} = \frac{\partial V_z}{\partial x} = \frac{\partial V_z}{\partial y} \simeq 0 \end{aligned} \quad (11.1.5)$$

where x_L and x_R are the intersectional points of the element edges with an extension of a line parallel to the global x axis at which velocities are $V(x_L)$ and $V(x_R)$, y_D and y_U are the intersectional points of the element edge from down to up with extension of the line parallel to the global y axis at which velocities are $V(y_D)$ and $V(y_U)$, z_S and z_N are the intersectional points of the element edge from south to north with extension of the line parallel to the global z axis at which velocities are $V(z_S)$ and $V(z_N)$, and l_x , l_y , and l_z are the length of each intersectional line respectively.

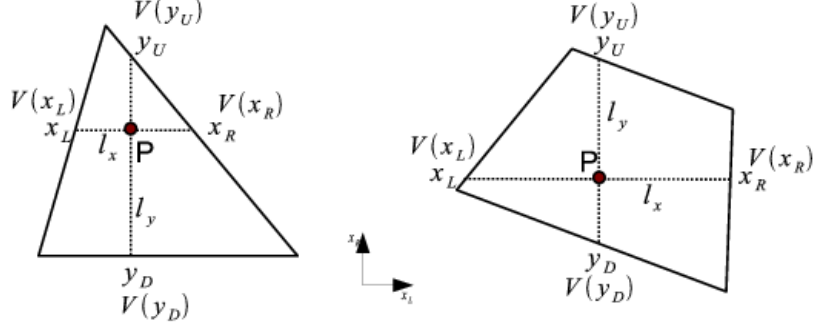


Figure 11.1.1: Spatial derivatives of velocity for a particle in triangular and quadrilateral elements: x_L and x_R are the intersectional points of the element edges with an extension of a line parallel to the global x axis at which velocities are $V(x_L)$ and $V(x_R)$, y_D and y_U are the intersectional points of the element edge from down to up with extension of the line parallel to the global y axis at which velocities are $V(y_D)$ and $V(y_U)$, z_S and z_N are the intersectional points of the element edge from south to north with extension of the line parallel to the global z axis at which velocities are $V(z_S)$ and $V(z_N)$, and l_x , l_y , and l_z are the length of each intersectional line respectively

Thus, the derivatives of the dispersion coefficients are as follows [115]

$$\begin{aligned}
 \frac{\partial D_{xx}}{\partial x} &= V_x \frac{\partial V_x}{\partial x} \left[\alpha_L \left(\frac{2}{V} - \frac{V_x^2}{V^3} \right) - \alpha_T \frac{V_y^2 + V_z^2}{V^3} \right] \\
 \frac{\partial D_{xy}}{\partial y} &= (\alpha_L - \alpha_T) \left[\frac{\partial V_y}{\partial y} \frac{V_x}{V} - \frac{V_x V_y^2}{V^3} \frac{\partial V_y}{\partial y} \right] \\
 \frac{\partial D_{xz}}{\partial z} &= (\alpha_L - \alpha_T) \left[\frac{\partial V_z}{\partial z} \frac{V_x}{V} - \frac{V_x V_z^2}{V^3} \frac{\partial V_z}{\partial z} \right] \\
 \frac{\partial D_{yy}}{\partial y} &= V_y \frac{\partial V_y}{\partial y} \left[\alpha_L \left(\frac{2}{V} - \frac{V_y^2}{V^3} \right) - \alpha_T \frac{V_x^2 + V_z^2}{V^3} \right] \\
 \frac{\partial D_{yx}}{\partial x} &= (\alpha_L - \alpha_T) \left[\frac{\partial V_x}{\partial x} \frac{V_y}{V} - \frac{V_y V_x^2}{V^3} \frac{\partial V_x}{\partial x} \right] \\
 \frac{\partial D_{yz}}{\partial z} &= (\alpha_L - \alpha_T) \left[\frac{\partial V_z}{\partial z} \frac{V_y}{V} - \frac{V_y V_z^2}{V^3} \frac{\partial V_z}{\partial z} \right] \\
 \frac{\partial D_{zz}}{\partial z} &= V_z \frac{\partial V_z}{\partial z} \left[\alpha_L \left(\frac{2}{V} - \frac{V_z^2}{V^3} \right) - \alpha_T \frac{V_x^2 + V_y^2}{V^3} \right] \\
 \frac{\partial D_{zx}}{\partial x} &= (\alpha_L - \alpha_T) \left[\frac{\partial V_x}{\partial x} \frac{V_z}{V} - \frac{V_z V_x^2}{V^3} \frac{\partial V_x}{\partial x} \right] \\
 \frac{\partial D_{zy}}{\partial y} &= (\alpha_L - \alpha_T) \left[\frac{\partial V_y}{\partial y} \frac{V_z}{V} - \frac{V_z V_y^2}{V^3} \frac{\partial V_y}{\partial y} \right]
 \end{aligned} \tag{11.1.6}$$

Because velocity is not derivable at the interface of two adjacent element in a nonuniform flow, computing dispersion coefficient derivatives by using a finite element approach would yield erroneous values [115]. To prevent the errors, a particle is coded to have information of an element index and the velocity estimation is continuous even at the elemental boundaries in this method. Thus, the derivatives of dispersion coefficients will be computed accordingly. This is an improved approach from the work by [115].

11.2 Transport: Advection and Dispersion

Purpose

To verify advective dispersive transport, a two-dimensional homogeneous aquifer is chosen to test the proposed RWPT method and the simulated particle distribution is converted to concentration contours.

Model description

The dimension of the model domain is 100 m by 60 m where the uniform velocity field is held constant at 0.5 $m d^{-1}$ in the x direction. The hydraulic conductivity is set as $10^{-5} m d^{-1}$ and the head gradient of one in the x direction is set by assigning two constant boundary conditions along both left and right sides. The longitudinal and transverse dispersivities are chosen to be isotropic with a length of 0.1 m. This converts to isotropic dispersion coefficients of $0.05 m^2 d^{-1}$. The initial source load is applied to an area with dimensions of 0.1 m by 0.1 m to have an initial concentration of $C_0 = 1 kg m^{-3}$. Figure 11.2.1 provides a schematic description of the test problem for the two-dimensional homogeneous aquifer. The domain is discretized with quadrilateral elements of 0.5 m by 0.5 m. The same grid density is also used for converting particle distributions to element concentrations.

The stated problem can be solved with an analytical solution provided by [116].

$$C(x, y, t) = \frac{C_0 A}{4\pi t \sqrt{D_{xx} + D_{yy}}} \exp \left[-\frac{(x - x_0)^2}{4D_{xx}t} - \frac{(y - y_0)^2}{4D_{yy}t} \right] \quad (11.2.1)$$

This allows to evaluate the computational accuracy of the proposed method.

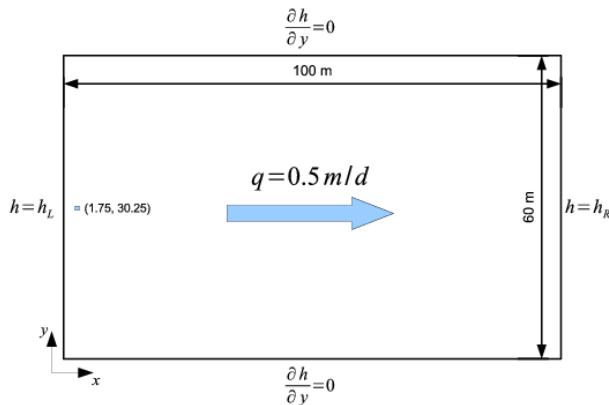


Figure 11.2.1: Schematic description of the two-dimensional aquifer and the boundary conditions of the flow system

Results

The comparison with the analytical solution is provided in Figure 11.2.2. As can be seen, the result of the RWPT method shows good agreement with the analytical solution. The number of particles used for this simulation is 50000. This is significantly less than the number of particles reported by [117], who reported that up to 2.5 million particles were necessary to achieve smoothness of the solution due to oscillations around the contours. As the oscillations observed here for the method proposed are smaller than reported by [117], the proposed method allows to dramatically reduce the number of particles required for a smooth solution by about two orders of magnitude. This shows that the proposed method is both accurate and efficient. In addition, the several numbers of particles used to solve the same problem produces particle clouds as in Fig. 11.2.3. However, the problem for only 1000 particles is used for the purpose of the benchmark test to reduce computation time.

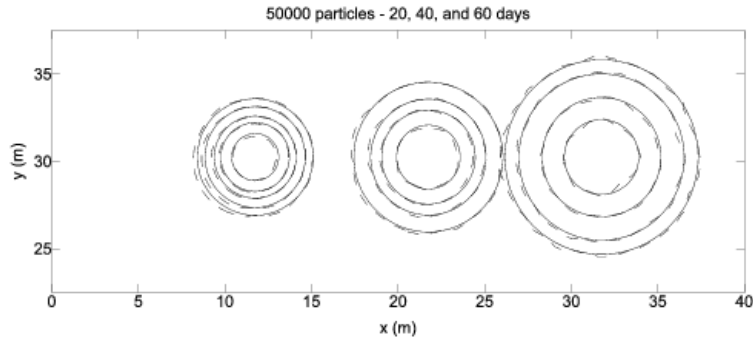


Figure 11.2.2: Transport results of the RWPT method compared with the analytical solution [116] for 50000 particles at 20, 40, and 60 days: The solid line is the analytical solution, the dotted line is the RWPT result. Contour lines are shown for $C = 2.6e^{-4}$, $1.6e^{-4}$, $1.0e^{-4}$, and $4e^{-5}$.

Benchmark	Problem type	Path in benchmark deposit
quad_homo	RWPT	benchmarks \RWPT\Veri1000

11.3 Transport: Sorption-desorption and Filtration

Problem definition

Harter et al.'s experiment [118] used a 10 cm long acrylic column filled with sand and fully saturated with water. A constant, uninterrupted flow rate was established with a peristaltic pump. The following sequence of solutions was

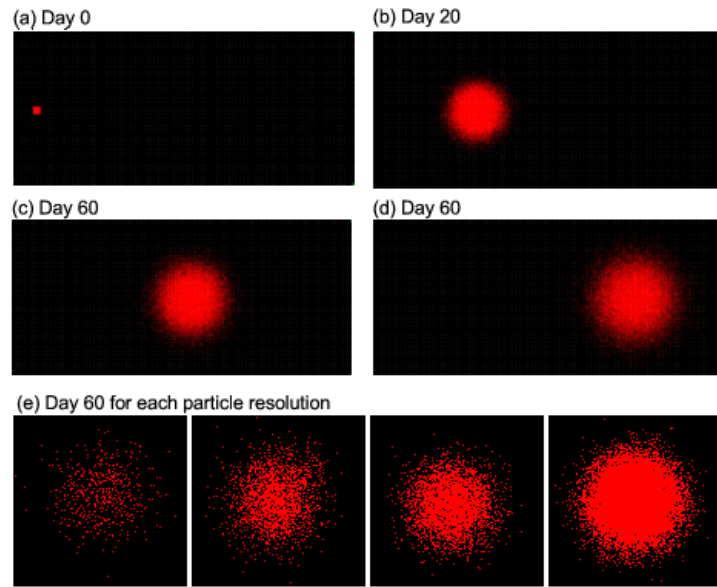


Figure 11.2.3: (a-d)Particle clouds of 50000 particles at 0, 20, 40, and 60 days,
(e) Particle clouds of 1000, 5000, 10000, and 50000 at 60 days

injected during the experiment: 10 pore volumes DTW (degassed tap water), 2.5 pore volumes NaCl - tap water solution, 10 pore volumes DTW, 2.5 pore volumes *Cryptosporidium parvum* solutions (1×10^5 oocysts per mL), 250 pore volumes DTW. The outflow was continuously collected for determination of concentration.

NaCl - tap water solution is used as tracer. The *Cryptosporidium parvum* can be classified as biological colloid. Colloids moving in porous media experience advection, dispersion, sorption-desorption, and filtration. A one-dimensional homogeneous aquifer is chosen to verify colloids transport in the experiment. Figure 11.3.1 shows the schematic discription of the experiment.

Governing equations and analytical solution

For the one-dimensional transport including sorption/desorption and filtration through a homogeneous medium the following differential equation 11.3.1 is applied.

$$\frac{\partial C}{\partial t} + \frac{\rho_b}{\theta} \frac{\partial S}{\partial t} = v\alpha_L \frac{\partial^2 C}{\partial x^2} - v\left(\frac{\partial C}{\partial x} + \lambda C\right) \quad (11.3.1)$$

with

C – dissolved concentration ($\text{kg}\cdot\text{m}^{-3}$),

S – sorbed concentration($\text{kg}\cdot\text{kg}^{-1}$),

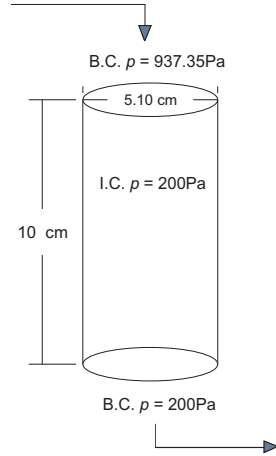


Figure 11.3.1: Schematic description of the Harter experiment

t – time (s),

ρ_b – bulk density ($\text{kg}\cdot\text{m}^{-3}$),

θ – porosity (-),

v – velocity ($\text{m}\cdot\text{s}^{-1}$),

α_L – longitudinal dispertivity (m),

x – distance (m),

λ – filtration coefficient (m^{-1}).

The instantaneous, linear sorption model assumes that

$$S = K_d C \quad (11.3.2)$$

where K_d is the partitioning coefficient ($\text{m}^3 \cdot \text{kg}^{-1}$). The retardation coefficient R is

$$R = 1 + \frac{\rho_b}{\theta} K_d \quad (11.3.3)$$

The dispersion coefficient in x -direction D_{xx} ($\text{m}^2 \cdot \text{s}^{-1}$) is

$$D_{xx} = v \alpha_L \quad (11.3.4)$$

The analytical solution for a pulse input (inject time from 0 to τ) is:

$$C = \frac{1}{2} C_0 \left[\exp \left(\frac{vx(1-\gamma)}{2D_{xx}} \right) \operatorname{erfc} \left(\frac{x - v\gamma t/R}{2\sqrt{D_{xx}t/R}} \right) + \exp \left(\frac{vx(1+\gamma)}{2D_{xx}} \right) \operatorname{erfc} \left(\frac{x + v\gamma t/R}{2\sqrt{D_{xx}t/R}} \right) \right] \quad (11.3.5)$$

for $t \in (0, \tau)$,

$$\begin{aligned}
C = & \frac{1}{2} C_0 \left[\exp \left(\frac{vx(1-\gamma)}{2D_{xx}} \right) \operatorname{erfc} \left(\frac{x-v\gamma t/R}{2\sqrt{D_{xx}t/R}} \right) \right. \\
& + \exp \left(\frac{vx(1+\gamma)}{2D_{xx}} \right) \operatorname{erfc} \left(\frac{x+v\gamma t/R}{2\sqrt{D_{xx}t/R}} \right) \\
& - \exp \left(\frac{vx(1-\gamma)}{2D_{xx}} \right) \operatorname{erfc} \left(\frac{x-v\gamma(t-\tau)/R}{2\sqrt{D_{xx}(t-\tau)/R}} \right) \\
& \left. - \exp \left(\frac{vx(1+\gamma)}{2D_{xx}} \right) \operatorname{erfc} \left(\frac{x+v\gamma(t-\tau)/R}{2\sqrt{D_{xx}(t-\tau)/R}} \right) \right] \quad (11.3.6)
\end{aligned}$$

for $t \in (\tau, \infty)$, where

$$\gamma = \sqrt{1 + 4v\lambda RD_{xx}/v^2} \quad (11.3.7)$$

Model description

The calculation area of the column is simplified to a line with the length of 0.1m. For the numerical model 100 elements and 101 nodes are included. Head gradient is set by giving two constant pressures at both left and right boundaries to establish a uniform velocity field. Particles are loaded near the left boundary for several time steps. The longitudinal dispersivity is chosen to be isotropic with a length of 0.005m. The sorption-desorption process is described by the two-rate model from Johnson et al.[119]. Filtration is described by using the filtration coefficient.

The two-rate model provides for a large number of particles to be released initially, followed by a slow release of attached particles. It is given by

$$N/N_0 = Ae^{-k_1 t} + (1-A)e^{-k_2 t} \quad (11.3.8)$$

where N is the number of particles remaining on the medium at time t , N_0 is the initial number of particles on the medium at the time of initial sorption, A is a weighting factor, k_1 and k_2 are the fast and slow sorption rate coefficient, respectively. Relative parameters are listed in Tab. 11.3.1.

Results

The number of pore volume(x -axis) is calculated by

$$P_V = \frac{vt}{L} \quad (11.3.9)$$

Parameter	Value
<i>Advection-dispersion parameters</i>	
permeability k	$1.114476^{-11} \text{ m}^2$
longitudinal dispersivity α_L	0.005 m
porosity(colloid) θ	0.42
porosity(tracer) θ	0.5
<i>Sorption-desorption parameters</i>	
A	0.9
k_1	0.1
k_2	0.001
<i>Filtration parameter</i>	
filtration coefficient λ	5.2 m^{-1}

Table 11.3.1: Model parameters for the column experiment.

The time step size is set by assigning P_V to 0.01. The chloride in the column experiences only advection and dispersion, which means in the Equation 11.3.1, $S = 0$, $\lambda = 0$. The comparison with the measurements from the experiment by Harter, the analytical solution, and the OGS simulation with mass transport method are shown in Figure 11.3.2.

100 particles per time steps are injected for 250 time steps. The leaving particles from the right boundary are counted to obtain the corresponding breakthrough curves. The comparison with the measurements from the experiment by Harter are shown in Figure 11.3.3.

Benchmark	Problem type	Path in benchmark deposit
colloid.t	RWPT	benchmarks \RWPT\Harter

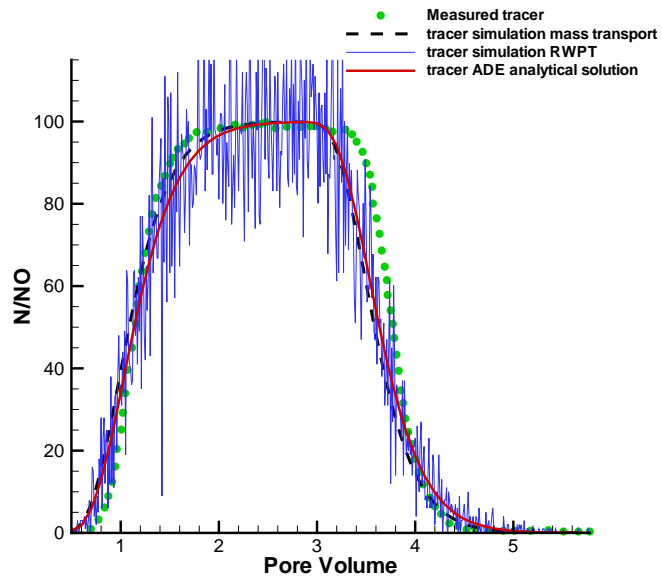


Figure 11.3.2: Tracer transport with advection and dispersion

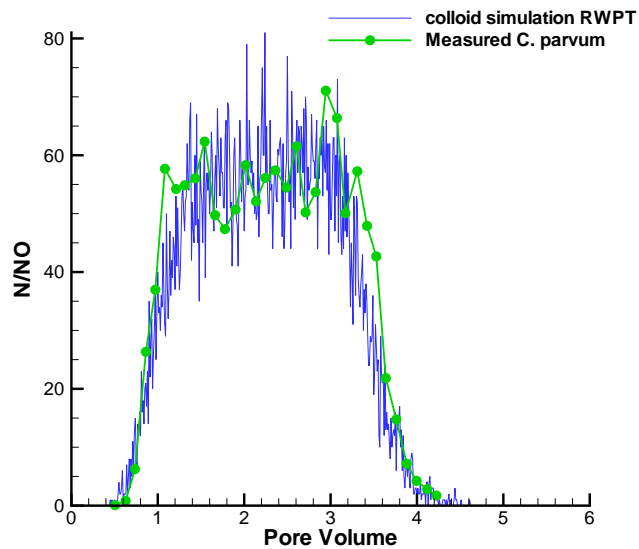


Figure 11.3.3: Colloid transport with advection, dispersion, sorption-desorption and decay

Chapter 12

Anisotropy – H or C or HC

12.1 Theory

There are situations where the coordinate directions do not align easily with the directions of anisotropy of the medium. In that case, the governing equation of the flow should be written in the more general form.

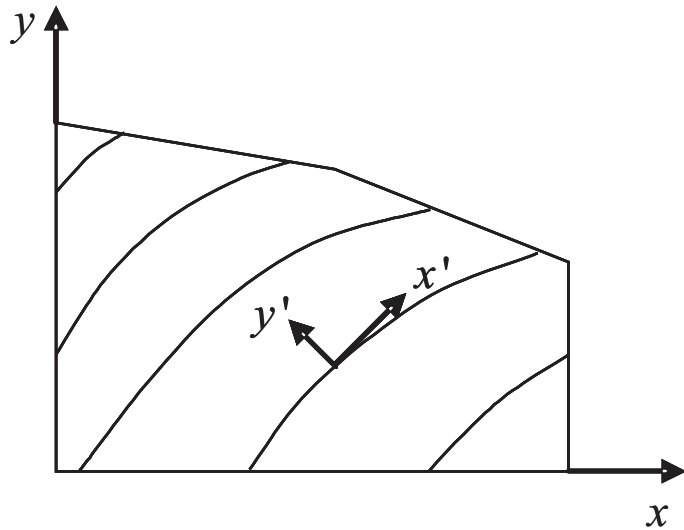


Figure 12.1.1: General anisotropy system

Assumption:

1. The material is isotropic
or

2. The coordinate axes coincide with the principal directions of anisotropy.

For the general case that the coordinate axes do not coincide with the principal directions, the continuity equation is of the form:

$$\frac{\partial}{\partial x_i} \left(K_{ij} \frac{\partial u}{\partial x_j} \right) = S \frac{\partial u}{\partial t} \quad (12.1.1)$$

where S is the hydraulic conductivity tensor. Equation 12.1.1 can be expanded as to:

$$\begin{aligned} \frac{\partial}{\partial x} \left(K_{xx} \frac{\partial u}{\partial x} \right) + \frac{\partial}{\partial x} \left(K_{xy} \frac{\partial u}{\partial y} \right) + \frac{\partial}{\partial y} \left(K_{yx} \frac{\partial u}{\partial x} \right) + \frac{\partial}{\partial y} \left(K_{yy} \frac{\partial u}{\partial x} \right) \\ = S \frac{\partial u}{\partial t} \end{aligned} \quad (12.1.2)$$

For a valid solution of the general case, these terms must be included in the numerical procedure, and in finite differences this would be the only available option. In finite elements, we have a second option, which is to rotate the local coordinate axes into the principal directions of hydraulic conductivity. The second option is computationally more efficient, since the terms in the finite element equation are kept to a minimum. This option is preferred where the principal directions are invariant in time, and where the rotation is easily accomplished, as for example in 2D flow problems. Note that the principal directions can be different for each element. This feature is particularly useful for cross-sectional systems with complex stratification.

The rotation is performed for each element individually. The nodal coordinates on the element are rotated (Figure 12.1.2) according to:

$$\begin{Bmatrix} x' \\ y' \end{Bmatrix} = \begin{bmatrix} \cos \beta & \sin \beta \\ -\sin \beta & \cos \beta \end{bmatrix} \begin{Bmatrix} x \\ y \end{Bmatrix} \quad (12.1.3)$$

where x' , y' are the coordinates of the point x , y in the principal direction coordinate system, and β is the angle between the Cartesian axes and the principal axes. The angle can be different for each element.

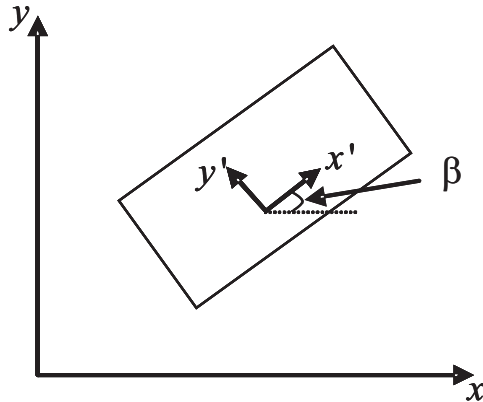


Figure 12.1.2: Rotation of axes

The same theory for anisotropy can be applied to any tensor material properties such as molecular diffusion coefficients.

12.2 Anisotropic permeability for pressure or hydraulic head

Knowing the theoretical background in 9.1, we formulate a simple flow problem to show the difference of three results obtained from isotropic, orthotropic, and anisotropic flow conditions.

Problem definition:

A unit square of the porous medium is created and discretized with triangle elements as in Figure 12.2.1. To generate flow in the model domain, two constant pressure boundary conditions are applied to the top left corner and the bottom right corner. The pressure difference between these two points is set to be unity.

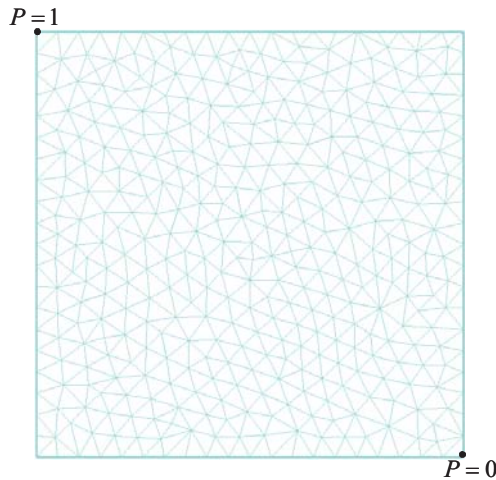


Figure 12.2.1: Boundary conditions and grid

As for material properties for flow system, permeability is set to have isotropic, orthotropic, and anisotropic over the whole model domain and provided in Table ??.

Material Types	Permeability(m^2)
Isotropic	$k_{xx} = k_{yy} = 10^{-14}$ and $k_{xy} = k_{yx} = 0$
Orthotropic	$k_{xx} = 10^{-14}$, $k_{yy} = 10^{-15}$, and $k_{xy} = k_{yx} = 0$
Anisotropic	$k_{xx} = 5.5 \times 10^{-15}$, $k_{xy} = 4.5 \times 10^{-15}$, $k_{yx} = 4.5 \times 10^{-15}$, $k_{yy} = 5.5 \times 10^{-15}$

Table 12.2.1: Various flow types set by material properties

Anisotropic ratio is set to be 10 to 1 for the x and y axes respectively for the orthotropic case while the anisotropic case uses the same ratio for the x' and y' axes rotated 45° counter-clock-wise from the x and y axes.

The resulting pressure distributions for the three different flow system are provided in Figure 12.2.2.

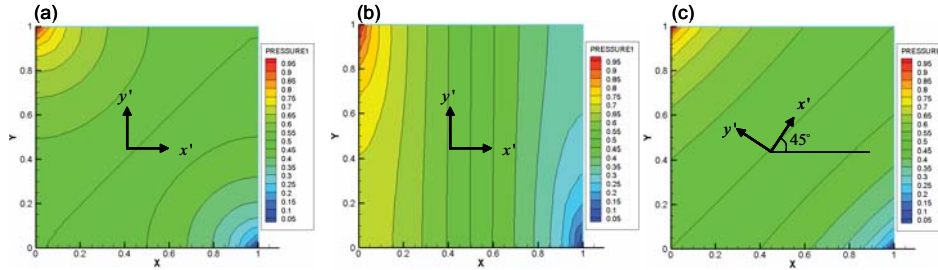


Figure 12.2.2: Pressure distributions for (a) isotropic, (b) orthotropic, and (c) anisotropic permeability

Note that there is no technical difference between the orthotropic and anisotropic cases when full values of permeability tensor are given and set into GeoSys/Rock Flow. However, users have two options for orthotropic cases in setting up .mmp files using different keywords such as ORTHOTROPIC and ANISOTROPIC. In the case that diffusion coefficients are treated as tensor via tortuosity, ORTHOTROPIC keyword is no longer valid. Therefore, ANISOTROPIC keyword should be used for Case (b) in anisotropic diffusion via tortuosity.

Benchmark deposit

Benchmark	Problem type	Path in benchmark deposit
<i>soil_layer</i>	Anisotropy	benchmarks\Anisotropy\permeability

12.3 Anisotropic tortuosity for molecular diffusion coefficients

As mentioned previously, the theory is exactly same with permeability. One thing to note before introducing another benchmark problem for anisotropic diffusion is that there is clear distinction between hydrodynamic dispersion and molecular diffusion. Since the hydrodynamic dispersion for mass transport in porous media is mainly a function of velocity and dispersivity, the hydrodynamic dispersion may be influenced more significantly by anisotropic hydraulic conductivity as well as pressure distributions than molecular diffusion. However, the hydrodynamic dispersion has also the molecular diffusion term. In this section, this molecular diffusion is treated as tensor via tortuosity that is a material property for instance clay.

The dispersion tensor can be written as (Bear, 1979)

$$\hat{D} = \tau D_m \hat{\delta} + \alpha_T |v| \hat{\delta} + (\alpha_L - \alpha_T) \frac{\vec{v}_i \vec{v}_j}{|v|} \quad (12.3.1)$$

where τ is the tortuosity tensor ($-$), D_m is the coefficient of molecular diffusion (L^2T), δ is the Kronecker-delta (unit tensor) ($-$), α_T is the transverse dispersivity (L), v is the characteristic value of macroscopic velocity (LT^{-1}), α_L is the longitudinal dispersivity (L), and, \vec{v}_i and \vec{v}_j are the velocities in i and j directions respectively (LT^{-1}).

Problem definition:

On the unit square of the porous medium created for the previous flow system, as well as one constant concentration boundary condition is applied, a constant line source is introduced to study the difference of component diffusive transport in various types of media. The transport boundary and source condition are depicted in Figure 12.3.1.

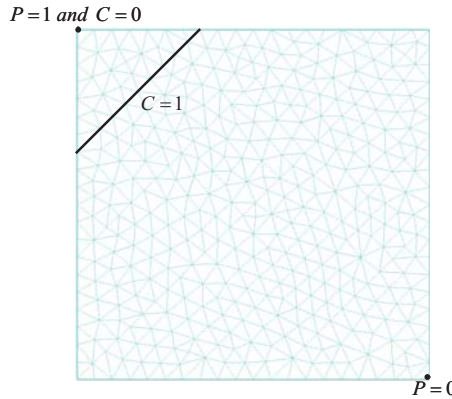


Figure 12.3.1: Boundary conditions and a line source for transport model

As for material properties for molecular diffusive transport, tortuosity is set to have isotropic and anisotropic over the whole model domain and provided in Table ??.

Material Types	Tortuosity
Isotropic	$\tau_{xx} = \tau_{yy} = 1$ and $\tau_{xy} = \tau_{yx} = 0$
Anisotropic	$\tau_{xx} = 0.55$, $\tau_{xy} = 0.45$, $\tau_{yx} = 0.45$, $\tau_{yy} = 0.55 : 45^\circ$ CCW $\tau_{xx} = 0.55$, $\tau_{xy} = -0.45$, $\tau_{yx} = -0.45$, $\tau_{yy} = 0.55 : 135^\circ$ CCW

Table 12.3.1: Isotropic and anisotropic tortuosity set for the componential molecular diffusive transport

An anisotropic ratio is set to be 10 to 1 for the x' and y' axes rotated 45° counter-clock-wise from the general directions. The equivalent tortuosity expression in

the principal directions of anisotropic tortuosity in general coordinate system can be given as

$$\tau' (x', y') = \begin{bmatrix} 1 & 0 \\ 0 & 1.0 \end{bmatrix} \rightarrow \tau (x, y) = \begin{bmatrix} 0.55 & 0.45 \\ 0.45 & 0.55 \end{bmatrix} \quad (12.3.2)$$

The resulting concentration contours for the three different material systems are provided in Figure 12.3.2.

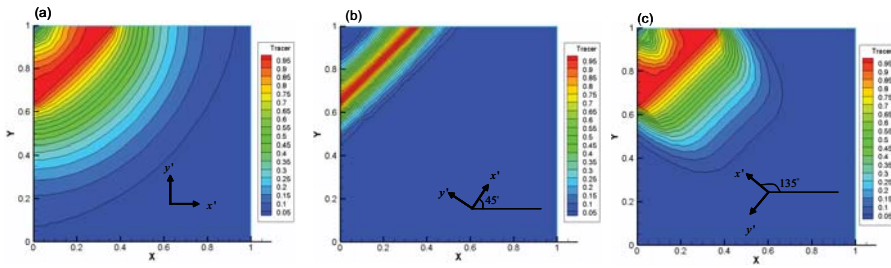


Figure 12.3.2: Concentration contours at $t = 1.0 \times 10^8$ seconds for (a) the isotropic, (b) anisotropic media (45 degrees rotated CCW), and (c) (135 degrees rotated CCW)

Finally, the medium is configured to have one bedding subject to anisotropic diffusive transport and all the rest model domain isotropic as depicted in Figure 12.3.3. The resulting concentration contours for this bedding problem is also provided in Figure 12.3.3.

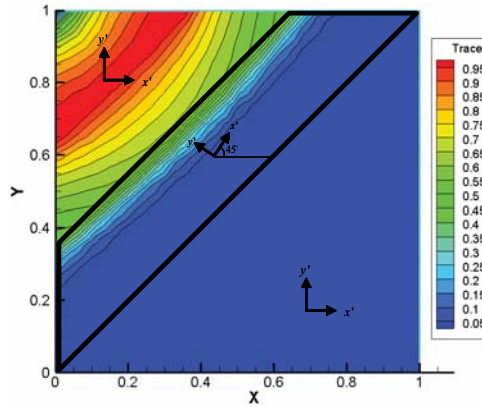


Figure 12.3.3: Concentration contours at $t = 1.0 \times 10^8$ seconds for the porous medium with an anisotropic bedding

Benchmark deposit

Benchmark	Problem type	Path in benchmark deposit
<i>soil_layer</i>	Anisotropy	benchmarks\Anisotropy\moleculardiffusion

12.4 Converting an angle of orientation to tensor

Currently, a universal function for converting an arbitrary angle to tensor is not written yet. In obtaining full tensor values from orthotropic tensor in the global coordinates, the direction of rotation and the magnitude of the angle should be handled carefully. The direction of rotation is counter-clock-wise and the reference tensor should be an identity matrix. Then, the converting function can be written such that

$$K = T^t K' T \quad (12.4.1)$$

Note that one anisotropic material rotated 180 degrees CCW becomes exactly same anisotropic material. This is obvious from Equation 12.4.1, because 180 degrees produce exactly same matrix K . To clarify the conversion, one example is prepared and explained in Figure 12.4.1. Suppose that an anisotropic medium has the ratio of 10 (i.e., $10x' = y'$, to satisfy this ratio, we can make countless tensors. Thus, we set $\begin{bmatrix} 1 & 0 \\ 0 & 0.1 \end{bmatrix}$ for conversion). Note that we talk about anisotropy in principle coordinates thus the coordinate system is single quotation marked. Now we can arbitrarily select rotation angles. Figure 12.4.1 shows some geometrically meaningful angles together with transformed matrix of Equation 12.4.1.

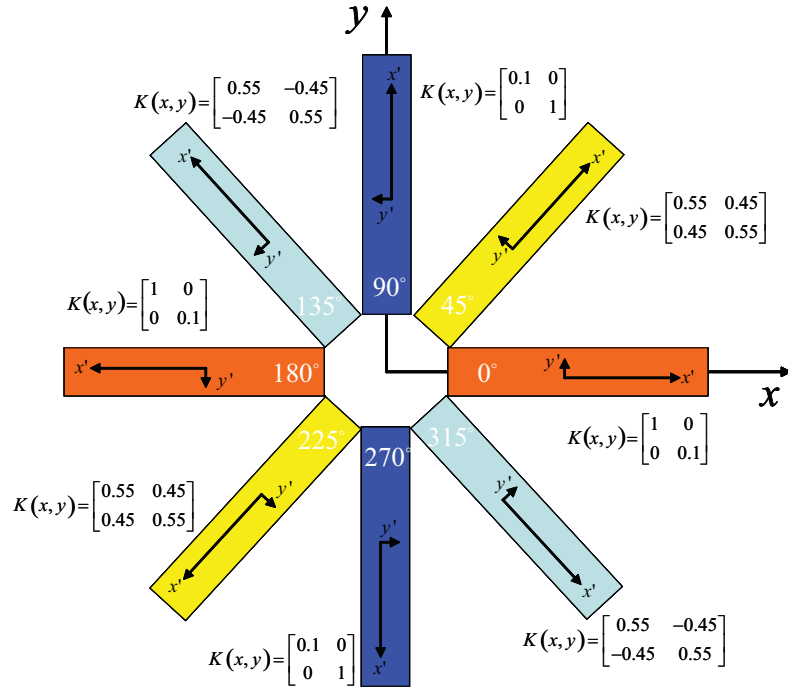


Figure 12.4.1: Transformed tensors referenced from $[1, 0][0, 0.1]$ in the principle coordinates

In extension to the second rank tensors in other words three dimensions, this direction of the rotation, the magnitude of the two angles, and the rotating axes should carefully be defined when the angles are used to compute the corresponding tensors internally. The transform matrix for three dimensions rotated along the y axis with α degrees CCW and the x axis with β degrees CCW can be written as

$$T = \begin{bmatrix} \cos \alpha & \sin \alpha \sin \beta & -\cos \alpha \sin \beta \\ 0 & \cos \beta & \sin \beta \\ \sin \alpha & -\cos \alpha \sin \beta & \cos \alpha \cos \beta \end{bmatrix} \quad (12.4.2)$$

Since the determinant of T is unity, we can use Equation 12.4.1 to compute full tensor values. This universal converting function will be provided in the future. Until then, full values of tensor should be used in GeoSys/RockFlow for simulating anisotropic problems.

Coupled Processes

Chapter 13

Surface/Subsurface flow coupling – H-Processe

This chapter deals with the coupling of rivers and overland flow with the variably saturated zone and aquifers.

13.1 Theory

For the coupling of flow processes on separate but adjacent domains exchange fluxes are calculated at common interfaces. The exchange fluxes between overland and variably saturated flow read

$$q_{of}^{sf} = k_{a'} \Lambda (h^{of} - h^{sf}), \quad \Lambda = \frac{K^c}{a'}, \quad q_{sf}^{of} = -q_{of}^{sf} \quad (13.1.1)$$

where h^{of} is the overland flow water head, h^{sf} the matric head in the variably saturated zone, Λ is the leakance, a' the interface thickness, and the scaling factor $0 \leq k_{a'} \leq 1$, given by

$$k_{a'} = S^{2(1-S)} \quad (13.1.2)$$

$$S = \min \left(\max \left(\frac{H}{a'}, 0 \right), 1 \right), \quad (13.1.3)$$

where H is the surface flow water depth, ensures that infiltration does not exceed the available water on the surface. For the coupling conductivity K^c the saturated soil hydraulic conductivity is taken.

The exchange fluxes between overland and groundwater flow read

$$q_{of}^{gf} = \Lambda (h^{of} - h^{gf}), \quad q_{gf}^{of} = -q_{of}^{gf} \quad (13.1.4)$$

where h^{gf} is the groundwater flow head. The exchange fluxes between river and groundwater flow read

$$q_{of}^{gf} = \frac{P}{B} \Lambda (h^{of} - h^{sf}), \quad q_{gf}^{of} = -q_{of}^{gf} \quad (13.1.5)$$

where P is the wetted perimeter and B the channel width. For a channel with rectangular cross section $P = 2H_a + B$. Is the groundwater level below the river bed the exchange fluxes become

$$q_{of}^{gf} = \Lambda H, \quad q_{gf}^{of} = -q_{of}^{gf}. \quad (13.1.6)$$

Figure 13.1.1: Exchange fluxes between (a) overland and variably saturated flow q_{of}^{sf} , (b) river and aquifer flow q_{of}^{gf} , calculated with an interface (conductivity K^c) between the surface flow compartment (friction coefficient C_r) and variably zone/aquifer compartment (conductivity K).

13.2 Benchmarks examples

13.2.1 Horton flow

Problem definition

This example is based on the experiments by Smith and Woolhiser, 1971 [67] for initially drained conditions. Infiltration excess overland (Hortonian) flow was generated by 15 minutes of artificial precipitation at a rate of 4.2 mm min^{-1} on a soil flume with a length of 12.2 m, a width of 5.1 cm, and a slope of 0.01. The experimental setup is shown in Figure 13.2.1 with the discretization meshes used in the simulations. Both overland and variably saturated flow are simulated one dimensionally with line elements.

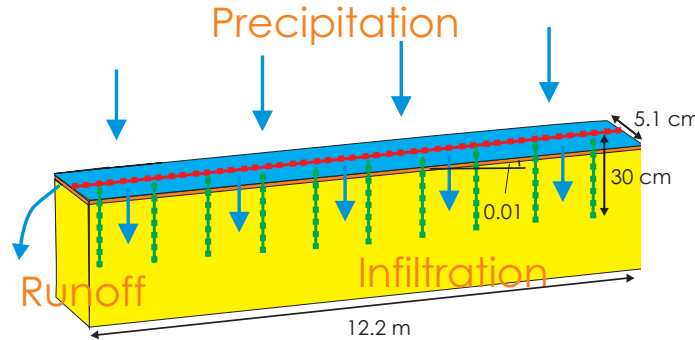


Figure 13.2.1: Setup and discretization meshes in the Smith and Woolhiser, 1971 [67] benchmark example.

Items	Symbol	Setting	Unit
Fluid			
Kinematic viscosity	ν	177	$\text{mm}^2 \text{ min}^{-1}$
Density	ρ	0.756	g mm^{-3}
Overland flow			
Surface friction	C	80000	$\text{mm}^{-1} \text{min}^{-1}$
	j	1	—
	l	2	—
Unsaturated flow			
Porosity	ϕ	0.42	—
Residual saturation	S_r	0.05	—
Hydraulic conductivity	K	1.7	mm min^{-1}
Pore size	α	0.006	mm^{-1}
Grain size distribution	m	0.75	—
Interface			
Conductivity	K^c	1.7	mm min^{-1}
Thickness	a'	1	mm
Immobile depth	a	1	mm

Table 13.2.1: Hydraulic parameters in the simulations of the laboratory experiment by Smith and Woolhiser, 1971 [67].

Initial and boundary conditions

The overland flow compartment is initially dry ($H = 1 \times 10^{-6} \text{ m}$) and initial soil saturation is 0.2 uniformly. A critical depth boundary condition assigned at the overland flow outlet. At the residual boundaries no-flow is assigned

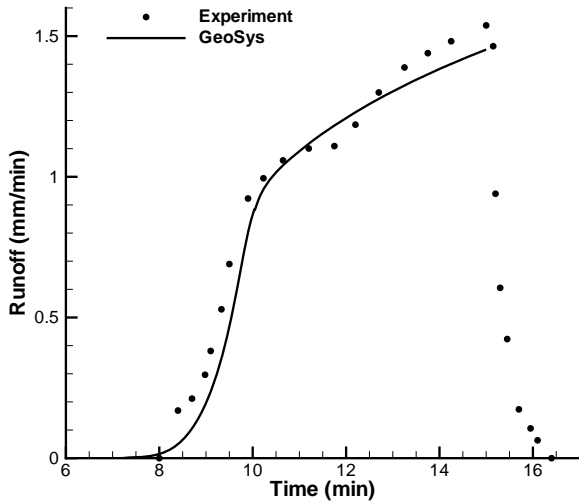


Figure 13.2.2: Simulated and measured outflow hydrographs in the Smith and Woolhiser, 1971 [67] benchmark example.

Material properties

A uniform soil representation is chosen. Light oil was used as a fluid. Surface friction is described by the laminar Chézy resistance to flow relationship. The soil-water-characteristic curves by VanGenuchten are used. Parameters are given in Table 13.2.2. Wool_little_lines_coup describes overland flow and soil flow one-dimensionally with line elements. Wool_little_hex_coup uses quadrants for overland flow which continue to three-dimensional soil flow hexahedra. Time steps are 2s. The material and fluid properties used for the simulations are given in Tab. 13.2.2. Soil heterogeneity is neglected and the fluid parameters correspond to light oil. Surface friction is described by the laminar Chézy resistance to flow relationship. The soil-water-characteristic curves by VanGenuchten are used for the Richards soil flow description.

Results

Runoff at the free-fall outlet is taken for comparison of experimental and simulation data (Figure 13.2.2). Time steps are 1 second. Line element sized for overland flow are $\Delta x = 12.2$ cm and for flow in the variably saturated zone $\Delta x = 1$ mm.

Benchmark deposit

Benchmark	Problem type	Path in benchmark deposit
<i>Wool_lines_coup</i>	H	benchmarks\COUPLED_FLOW\

13.2.2 Dunne flow

Problem definition

This example is based on the experiments by Abdul and Gilham, 1984 [120] which were designed to examine the role of capillary fringe on runoff generation processes. Precipitation was applied for 20 min on a soil flume with a length of 1.4 m, a width of 8 cm, and a slope of 0.12 (Figure 13.2.3). The initial groundwater level is set at the height of the outlet such that immediately overland flow occurs. In the simulations the flume part above the initial groundwater level is simulated with Richards equation and below with Darcy groundwater equation.

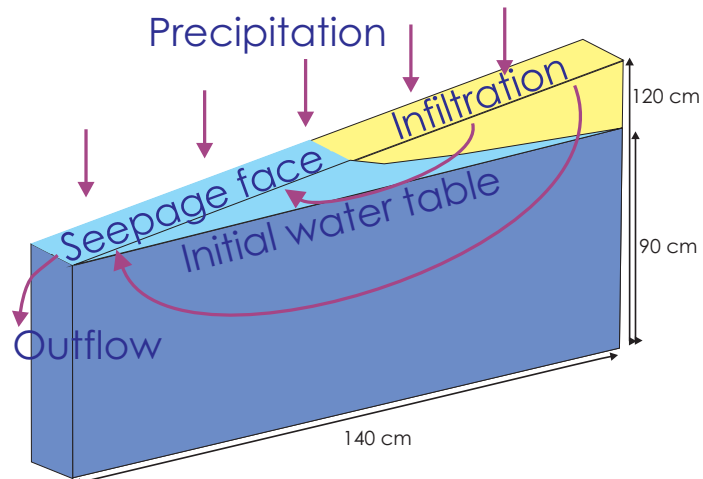


Figure 13.2.3: Setup of the Abdul and Gilham, 1984 [120] benchmark example.

Items	Symbol	Setting	Unit
Overland flow			
Surface friction	C	5.39	$\text{m}^{1/3}\text{s}^{-1}$
Immobile depth	a	0.5	mm
Variably saturated flow			
Porosity	ϕ	0.34	–
Residual saturation	S_r	0.0	–
Hydraulic conductivity	K	5×10^{-5}	m s^{-1}
Pore size	α	2.4	m^{-1}
Grain size distribution	m	0.8	–
Groundwater flow			
Porosity	ϕ	0.34	–
Specific storage	S	0.0	–
Overland/soil Interface			
Conductivity	K^c	5×10^{-5}	m s^{-1}
Thickness	a'	0.5	mm
Soil/aquifer Interface			
Leakance	Λ	5×10^{-4}	s^{-1}

Table 13.2.2: Hydraulic parameters in the simulations of the laboratory experiment by Abdul and Gilham, 1984 [120].

Initial and boundary conditions

Material properties

Results

Measured and simulated outflow are compared in Fig. 13.2.4.

Benchmark deposit

Benchmark	Problem type	Path in benchmark deposit
<i>abduLab</i>	H	benchmarks\COUPLED_FLOW\

13.2.3 Aquifer recharge from channel

Problem definition

This example deals with a confined aquifer with inflow by a rectangular channel (Figure 13.2.5). An analytical solution is given by Glover, 1978 [46].

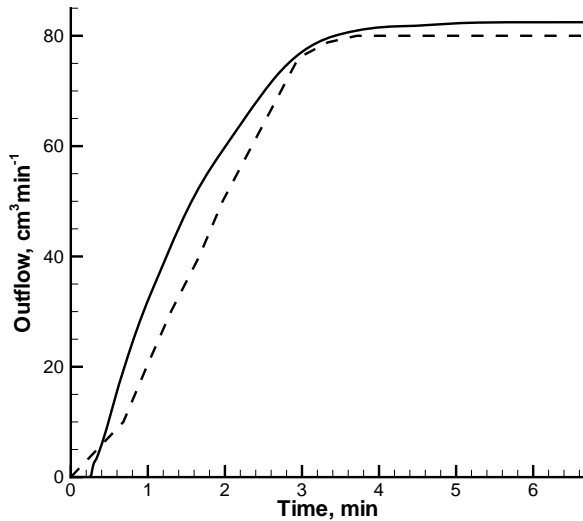


Figure 13.2.4: Simulated and measured outflow hydrographs in the Abdul and Gilham, 1984 [120] benchmark example.

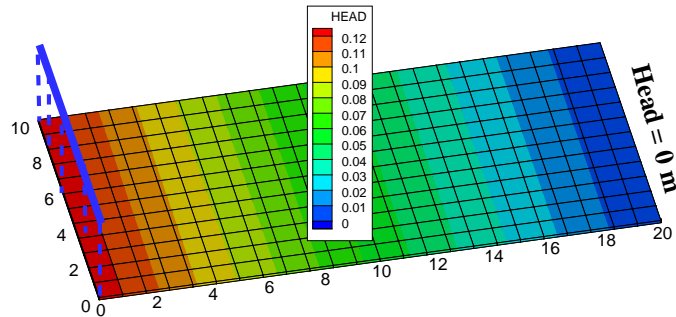


Figure 13.2.5: Setup of the Glover, 1978 [46] benchmark example.

Initial and boundary conditions

Channel initial and boundary conditions are 3m for water depth. Initial ground-water head is 0m. The head at the boundary opposite of the channel is 0. At

the remaining boundaries no-flow is imposed.

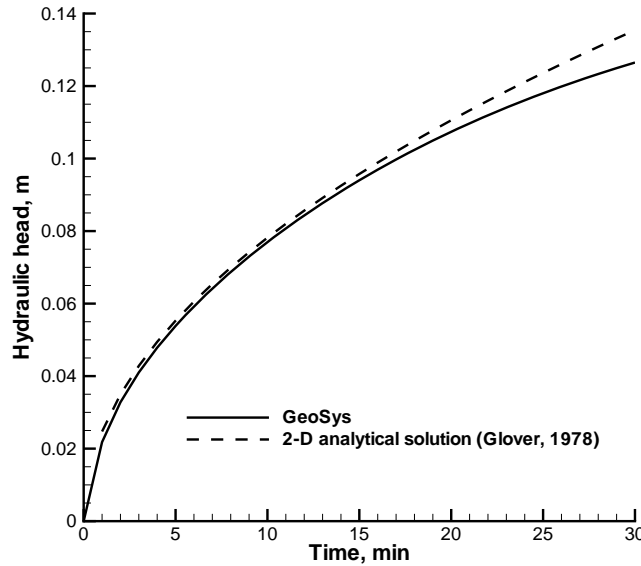


Figure 13.2.6: Comparison of Simulated groundwater depths below the river bed with the analytical solution by Glover, 1978 [46].

Material properties

The domain is discretized with 24×12 quadrants and the time step size is 60s. Simulation parameters are given in Tab. 13.2.4.

Table 13.2.3: Parameters for aquifer recharge example

Parameter	Symbol	Setting	Unit
Friction coefficient	C	333	ms
Corresponding Manning coefficient	n	3×10^{-3}	$1/ms$
Channel width	B	14	m
Leakance		3.33×10^{-6}	$1/s$
Rill depth/ Interface layer thickness	a	0	m
Surface structure parameter	ϵ	0	m
Specific yield	S_y	0.2	$1/m$
Permeability	k	1×10^{-3}	m^2
Aquifer thickness	L	25	m

Results

Comparison of simulation results and analytical solution is shown in Fig. 13.2.6.

Benchmark deposit

Benchmark	Problem type	Path in benchmark deposit
<i>riv1-quad_coup</i>	H	benchmarks\COUPLED_FLOW\

13.2.4 Flood at channel junction

Problem definition

Two uniform rectangular channels confluence symmetrically and form a larger rectangular channel which continues uniformly. The aquifer is unconfined, flat, homogeneous, and has a size of $10000m \times 4000m$ (Figure 13.2.7). A flood waves starts propagating at both upstream inlets and merge at the junction. Manning's roughness coefficient is constant throughout as well as the slope of about 0.0001. The total time is 5 days and comprises a part of the rising limb of the flood. Two scenarios are considered by varying the aquifer initial conditions such that flow occurs from the channels to the aquifer or vice versa. The total time is 30 days and comprises the rising and falling limb of the flood. These examples were proposed by [121]. Benchmarking is based on code comparison.

Initial and boundary conditions

Initial water depth in the rivers is $4.5m$ and the aquifer is set at $z = 0$. The initial head for the aquifer is $h = 32$ m for scenario I and $h = 35$ m for scenario II. At the aquifer boundaries constant head and no-flow conditions are imposed (Figure 13.2.7). At the river inlets the inflow rises linearly from $100m^3/s$ to $350m^3/s$ between $t = 3$ and $t = 10$ days and declines again linearly to the initial value between $t = 11$ and $t = 17$ days. At the channel outlet a normal depth boundary condition is assigned.

Material properties

The simulation parameters for the channels and aquifer are given in Tab. 13.2.4.

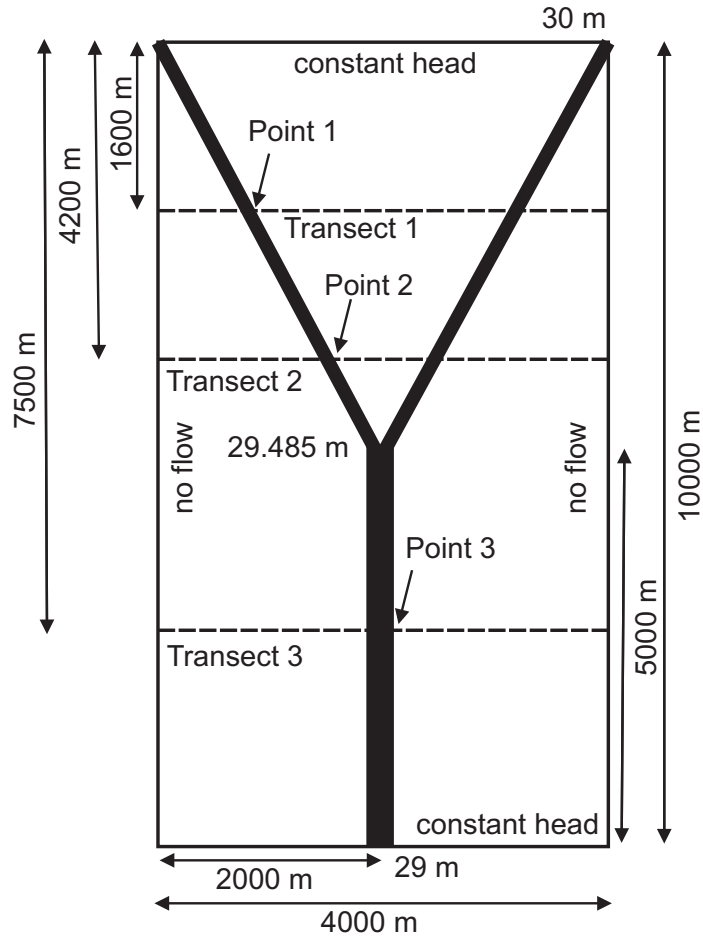


Figure 13.2.7: Setup of the Gunduz and Aral, 2005 [121] benchmark example.

Table 13.2.4: Parameters for channel junction examples

Items	Symbol	Setting	Unit
Friction coefficient	C	40	ms
Corresponding Manning coefficient	n	0.025	$1/ms$
Width of upstream channels	B	30	m
Width of downstream channel	B	45	m
Leakance	Λ	3.33×10^{-6}	$1/s$
Rill depth/ Interface layer thickness	a	0	m
Surface structure parameter	ϵ	0	m
Specific yield	S_y	0.2	$1/m$
Permeability	k	1×10^{-9}	m^2

Results

Figs. 13.2.8-13.2.11 show groundwater heads and river stages at Points 1-3 and groundwater heads at transect I for both scenario I and II.

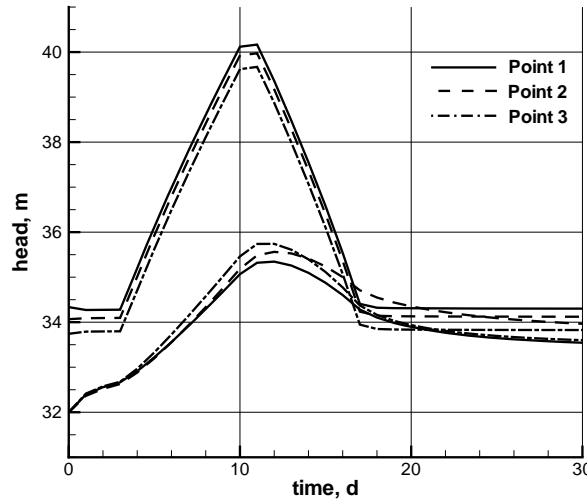


Figure 13.2.8: Groundwater heads and river stages of the Gunduz and Aral, 2005 [121] benchmark example for scenario I.

Benchmark deposit

Benchmark	Problem type	Path in benchmark deposit
<i>biFork1_coup</i>	H	benchmarks\COUPLED_FLOW\
<i>biFork2_coup</i>	H	benchmarks\COUPLED_FLOW\

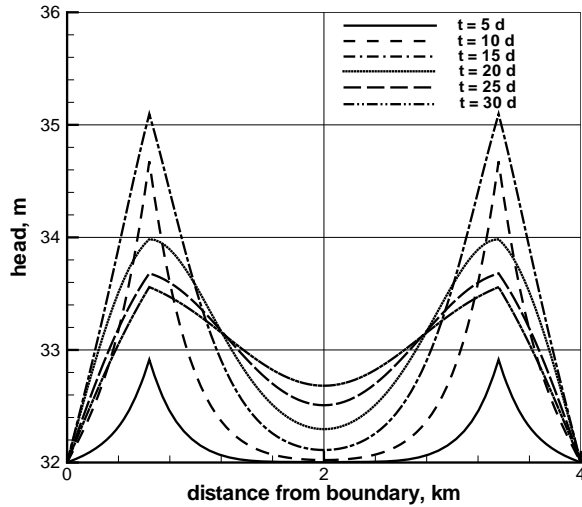


Figure 13.2.9: Groundwater heads at transect I of the Gunduz and Aral, 2005 [121] benchmark example for scenario I.

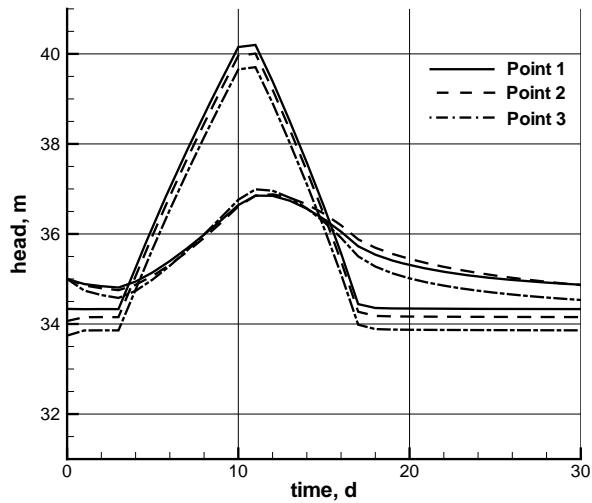


Figure 13.2.10: Groundwater heads and river stages of the Gunduz and Aral, 2005 [121] benchmark example for scenario II.

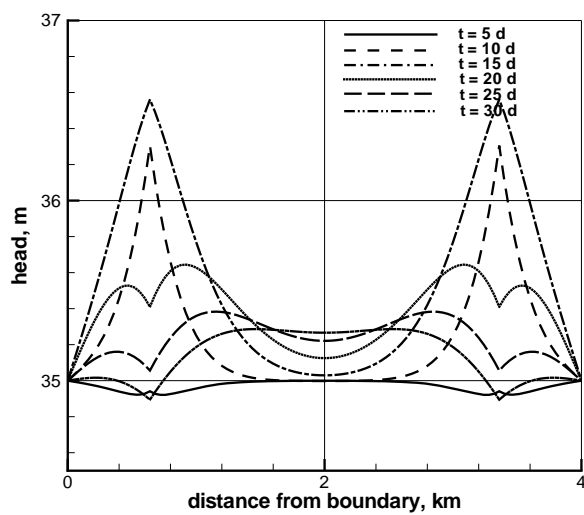


Figure 13.2.11: Groundwater heads at transect I of the Gunduz and Aral, 2005 [121] benchmark example for scenario II.

Chapter 14

Consolidation – H^nM -Processes

14.1 Theory

We consider flow of an incompressible fluid (liquid) in a deforming porous medium. The system consists of two phases (liquid and solid phase). The unknown field functions are liquid pressure p and solid displacement \mathbf{u} . For the determination of the unknown field functions we combine the mass balance equations and the momentum balance equation of fluid and solid phases ([122], [123]).

The deformation process is modelled by the system

$$\nabla \cdot (\boldsymbol{\sigma} - p\mathbf{I}) + \rho\mathbf{g} = \mathbf{0} \text{ in } \Omega , \quad (14.1.1)$$

$$\boldsymbol{\sigma} - \mathbf{C}\boldsymbol{\varepsilon}(\mathbf{u}) = \mathbf{0} \text{ in } \Omega , \quad (14.1.2)$$

where $\boldsymbol{\sigma}$ denotes the effective stress, and the momentum balance equation is modified such that it incorporates stresses and forces connected to the fluid pressure. Here, \mathbf{I} denotes the identity, \mathbf{g} denotes the gravity vector and \mathbf{C} is the elasticity tensor representing the dependence of strain and stress for a linear elastic material law.

Fluid flow in deformable porous media is described by the following mass and momentum balance equations,

$$\nabla \cdot \mathbf{w} + \nabla \cdot \frac{\partial \mathbf{u}}{\partial t} = 0 \text{ in } \Omega , \quad (14.1.3)$$

$$\mathbf{w} + \frac{\mathbf{k}}{\mu} (\nabla p - \rho\mathbf{g}) = \mathbf{0} \text{ in } \Omega . \quad (14.1.4)$$

In consolidation theory, the fluid mass balance equation (14.1.3) has an extra term due to the deformation process. The second equation (14.1.4) is denoted as

the Darcy law. Here, \mathbf{w} denotes the volumetric flux of the fluid and p the liquid phase pressure. \mathbf{k} denotes the permeability tensor, μ is the liquid viscosity, and ρ is the density of the porous medium. Hereby we assume solid grains itself are incompressible, i.e. $d^s\rho/d^st = 0$

After applying Galerkin finite element approach to eqns . (14.1.1) and (14.1.3) build a set of coupled linear equations to be solved for the primary variables liquid pressure p and solid deformation \mathbf{u} of the p/\mathbf{u} formulation of the consolidation problem. The resulting equation system can be compactly written in following form

$$\begin{bmatrix} \mathbf{K}_{pp}^* & \frac{1}{\Delta t} \mathbf{C}_u^* \\ \mathbf{K}_{up}^* & \mathbf{K}_{uu}^* \end{bmatrix} \begin{bmatrix} \hat{\mathbf{p}}^{i+1} \\ \hat{\mathbf{u}}^{i+1} \end{bmatrix} = \begin{bmatrix} \mathbf{f}_p^* + \frac{1}{\Delta t} \mathbf{C}_u^* \hat{\mathbf{u}}^i \\ \mathbf{f}_u^* \end{bmatrix} \quad (14.1.5)$$

The above algebraic equation system (14.1.5) for determination of the primary variables of the p/\mathbf{u} formulation, i.e. nodal pressures and displacements.

14.2 Saturated consolidation

Equation system (14.1.5) is solved with a one-step monolithic algorithm. Moreover, the Newton-Raphson method is adopted to deal with the nonlinearity.

14.2.1 Poro-elastic column (1D)

Problem definition

The example is a simple one dimensional problem for which an analytical formula for its solution is known. We consider a porous column bounded by rigid and impermeable walls, except on its top where a mechanical pressure load σ_0 is prescribed and which is free to drain. Suppose that the length of the column is H . The boundary and initial conditions for the problem are depicted in Figure 14.2.1: The analytical solution for this problem can be found in [124] as

$$\begin{aligned} \sigma_D &= -1 + \sum_{n=0}^{\infty} \frac{2}{M} \sin(Mx_D) e^{-M^2 t_D} \\ u_D &= 1 - x_D - \sum_{n=0}^{\infty} \frac{2}{M} \cos(Mx_D) e^{-M^2 t_D} \\ p_D &= \sum_{n=0}^{\infty} \frac{2}{M} \sin(Mx_D) e^{-M^2 t_D} \end{aligned} \quad (14.2.1)$$

where $x_D = x/H$, $t_D = (\lambda + 2\mu)kt/\eta H^2$, $M = 1/2\pi(2n+1)$ are non-dimensional quantities and $\sigma_D = \sigma/p_0$, $u_D = u(\lambda + 2\mu)/p_0H$, $p_D = p/p_0$ are dimensionless effective stress, displacement and pore pressure, respectively.

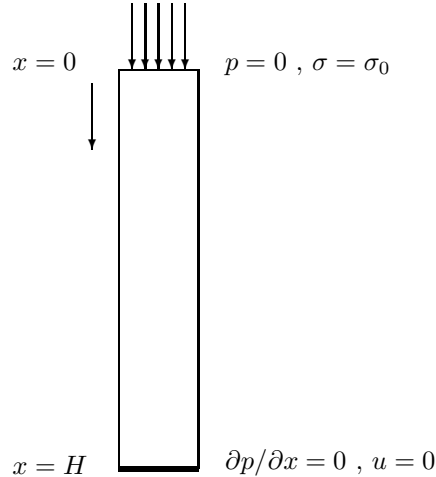


Figure 14.2.1: Column test problem

Material properties

The material parameters used in the computation are given in Table 14.2.1. The load put on the strip is -10^3 Pa , time step size is $\Delta t = 1.0 \text{ s}$ and the total simulation time is $t = 10 \text{ s}$.

Parameter	Unit	Value
Young's modulus	3×10^4	N/m^2
Poisson's ratio	0.2	–
Permeability	10^{-10}	m^2
Fluid viscosity	10^{-3}	Pa s

Table 14.2.1: Material parameters

Results

Time step size is proposed as 1s. Comparison of the results for fluid pressure and effective stress obtained by the LS-MFEM, GFEM and the analytical solution are shown in Figure 14.2.2

Benchmark deposit

Benchmark	Problem type	Path in benchmark deposit
<i>hm-tri</i>	HM	benchmarks\HM\

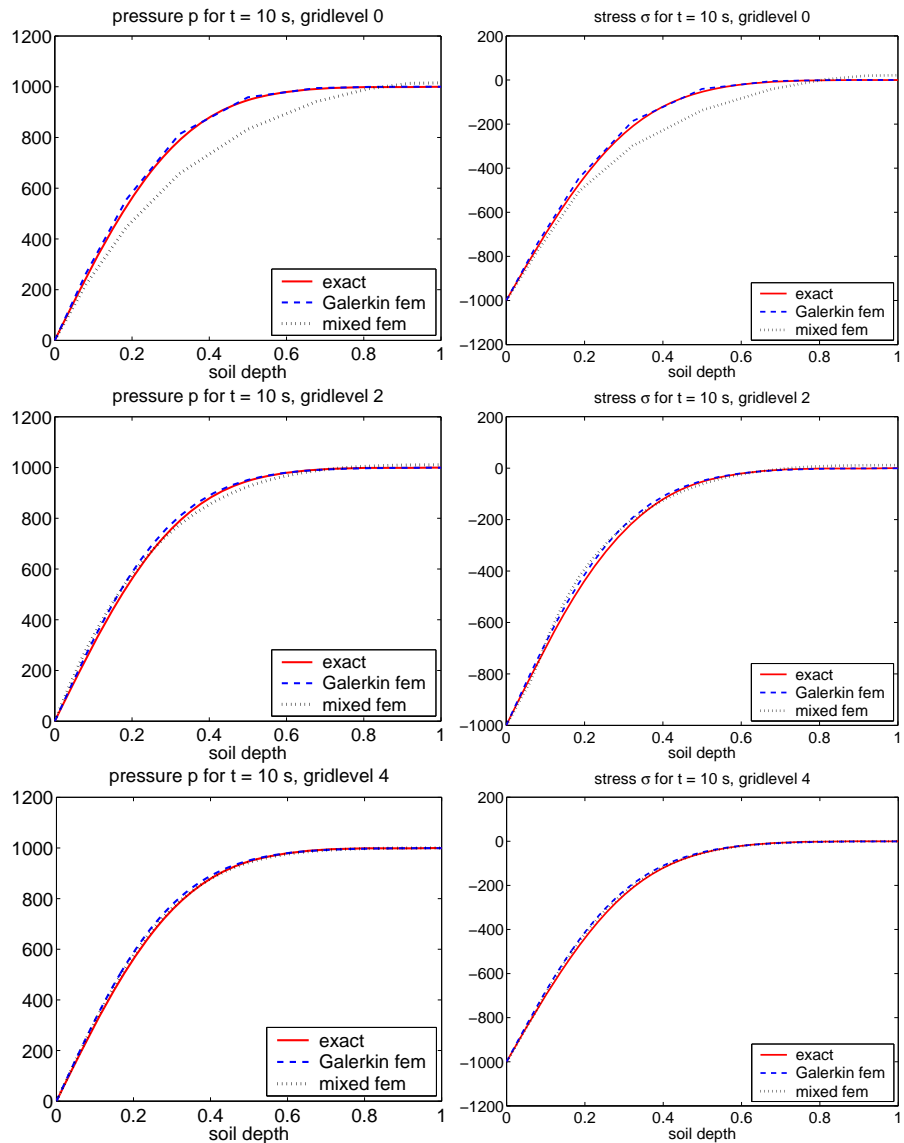


Figure 14.2.2: Simulated fluid pressures (left) and effective stress (right) at time $t=10\text{ s}$ by grids from the coarsest to finest one

14.2.2 Poro-elastic cube (3D)

Problem definition

We consider a vertical cross-section through a homogeneous soil. Due to symmetry we can limit the investigation to half of the domain. The model domain is then extending 8 meters in length and 5 meters in height. The problem is solved in 2D and 3D space, respectively.

Initial and Boundary conditions

Boundary conditions are: strip loading ($\sigma_{yy} = \sigma_0$ in $x \in [0, 1]$), zero stresses ($\sigma_{yy} = \sigma_{xy} = 0$ in $x \in (1, 8]$) and zero pressure at the top; no horizontal flux, no horizontal displacements and zero shear stresses at left and right hand sides; no vertical flux and no displacements at bottom (Figure 14.2.3).

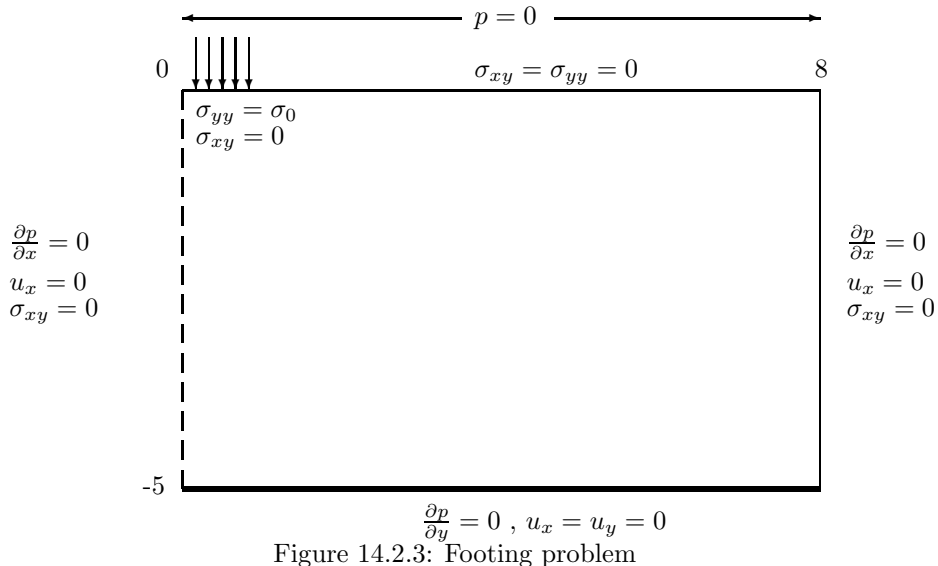


Figure 14.2.3: Footing problem

Material properties

The material properties of the porous medium for this case are given in Table 14.2.2.

Results

The geometry is to expand the 2D domain by extruding the 2D shape of 1m in off-plane direction (14.2.4). Results at the critical step, i.e., the first step, are

Table 14.2.2: Material properties

Property	Value	Unit
Young's modulus	3×10^4	N/m^2
Poisson's ratio	0.2, 0.4	—
Permeability	10^{-10}	m^2
Fluid viscosity	10^{-3}	Pas

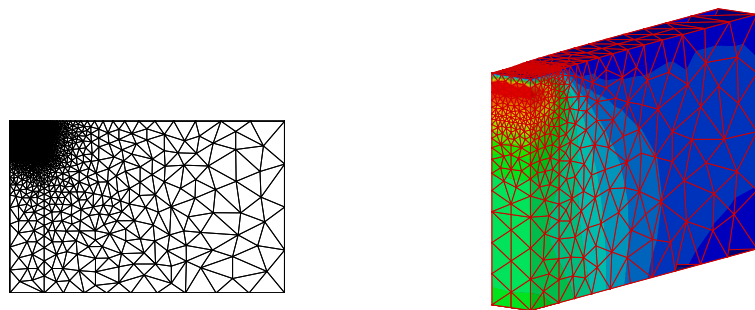


Figure 14.2.4: Analyzed models

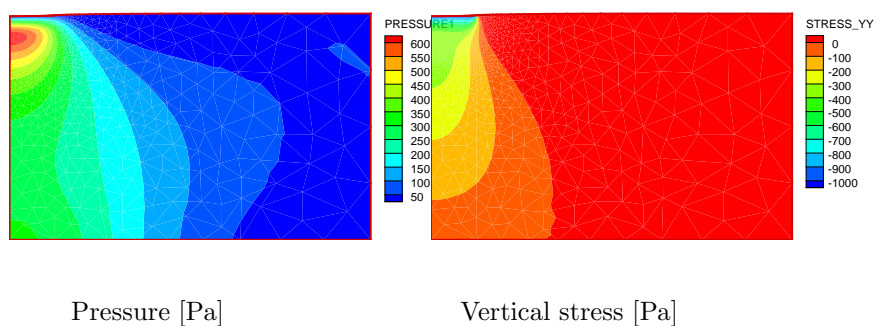


Figure 14.2.5: 2D: distribution

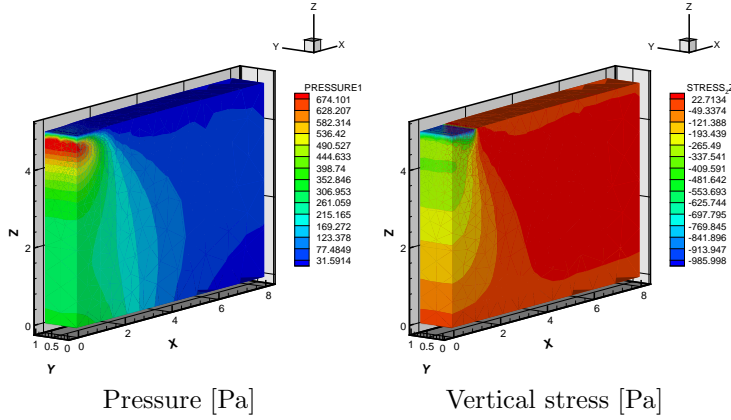


Figure 14.2.6: 3D: distribution

shown in Fig. 14.2.5, 14.2.7 and 14.2.6

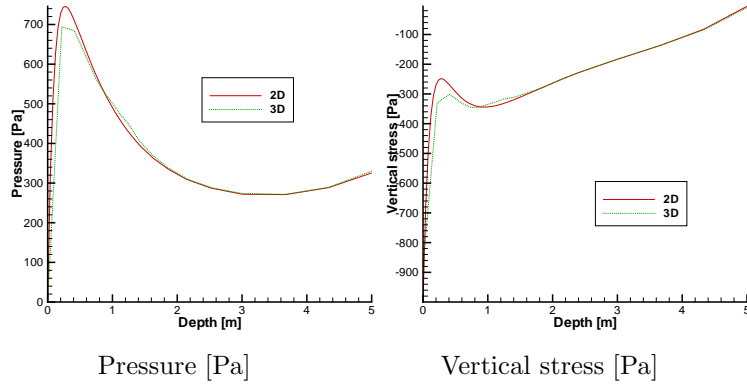


Figure 14.2.7: Comparison along symmetrical axis

The results produced by 2D model with triangle element and 3D model with tetrahedral element matches each other. This shows that all objects presented in this study work fine for TH coupling problem.

Benchmark deposit

Benchmark	Problem type	Path in benchmark deposit
<i>hm-foot_tri& hm-foot_tet</i>	HM	benchmarks\HM\

14.2.3 Plastic consolidation

Problem definition

A quarter of the cylindrical sample of 5cm in diameter and 10cm in length under constant pressure. We assume that the plastic behavior the sample material can be represented by the Cam-Clay model and the problem is axisymmetrical.

Initial and Boundary conditions

The initial void ratio $e_0 = 1.5$ at such initial stress state

$$\sigma_r^0 = \sigma_\theta^0 = \sigma_z^0 = 50\text{kPa}$$

The top of sample is compressed down to 5cm. While the radial stress kept constant of 50kPa, i.e., the traction boundary condition at cylindrical surface must be zero. Both uncoupled and coupled cases are analyzed. For the coupled case, drainage is assigned on the bottom of the sample. The two case should give the same results. The displacement load is applied in 50 increments.

Material properties

Table ?? shows the material parameters.

Property	Value	Unit
Poisson's ratio	0.3	—
Slope of the critical line, M	1.2	—
Virgin compression index, λ	0.2	—
Swelling/recompression index κ	0.02	—
Initial pre-consolidation pressure	60	kPa
Permeability	10^{-11}	m^2
Fluid viscosity	10^{-3}	Pa s

Table 14.2.3: Material properties

Results

The evolution of the deviatoric stress along with the axial strain are demonstrated in Fig. 14.2.8. Both uncoupled (see Section 9.5.3) and coupled cases give the same result as expected[95].

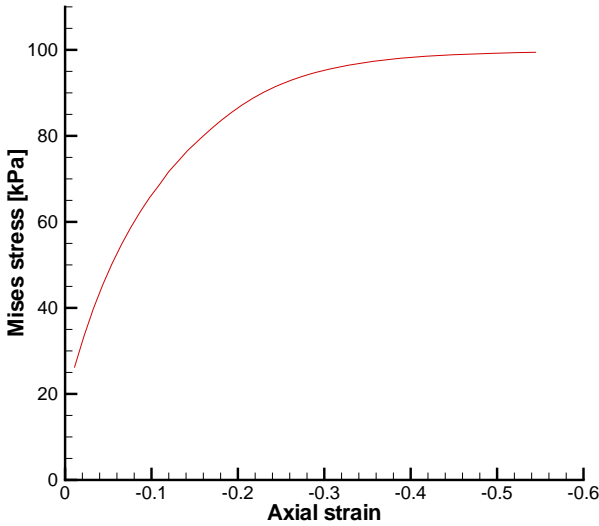


Figure 14.2.8: Mises stress vs axial strain: Cam-Clay consolidation

Benchmark deposit

Benchmark	Problem type	Path in benchmark deposit
<i>hm_cc_tri_s</i>	HM	benchmarks\HM\

14.2.4 Dynamic consolidation

Problem definition

This example is used just to demonstrate that the global assembly of matrices and vectors, the time stepping of dynamic problems are dealt with correctly. The example described below is modified from the footing example given in Section 14.2.2.

Initial and Boundary conditions

All stresses and pressure are zero at the beginning of deformation. Strip loading ($\sigma_{yy} = \sigma_0$ in $x \in [0, 1]$), zero stresses ($\sigma_{yy} = \sigma_{xy} = 0$ in $x \in (1, 8]$) and zero pressure at the top; no horizontal flux, no horizontal displacements and zero shear stresses at left and right hand sides; no vertical flux and no displacements at bottom (Figure 14.2.3).

Material properties

Material parameters are given in Table ??.

Property	Value	Unit
Young's modulus	3×10^4	N/m ²
Poisson's ratio	0.2, 0.4	—
Permeability	10^{-10}	m ²
Fluid viscosity	10^{-3}	Pa s

Table 14.2.4: Material properties of dynamic consolidation problem

Results

Constant time step size of 10s with time damping parameters:

$$\beta_1 = 0.51, \beta_2 = 0.515, \bar{\beta} = 0.51$$

Time duration is ten time steps.

The following figures, Fig. 14.2.9–14.2.12 show the distribution of state variables within the domain after 10 time steps. Such distribution is similar to the static case illustrated in Fig. 14.2.5.

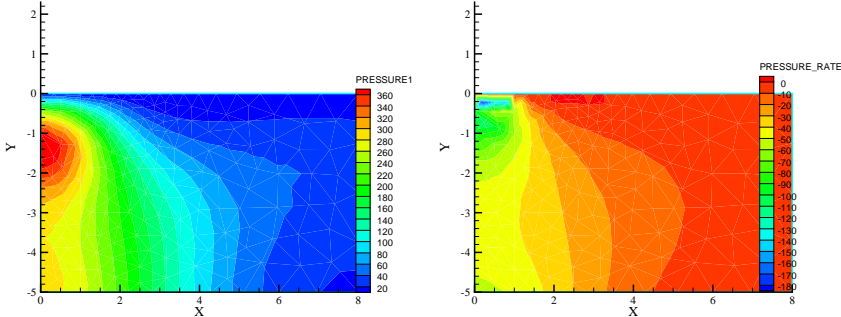


Figure 14.2.9: Fluid pressures p and rate of fluid pressure \dot{p}

Benchmark deposit

Benchmark	Problem type	Path in benchmark deposit
<i>hm_dyn_tri</i>	HM	benchmarks\HM\

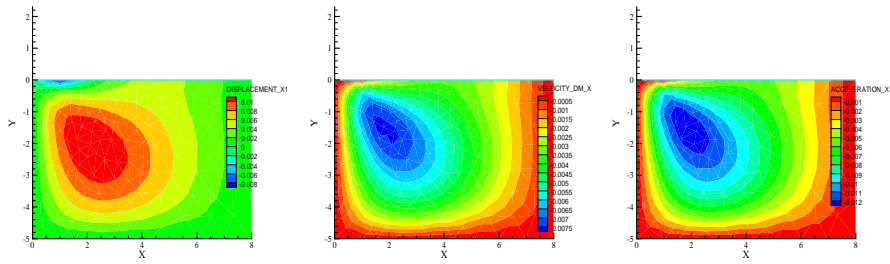


Figure 14.2.10: Displacement, its rate and acceleration: horizontal component

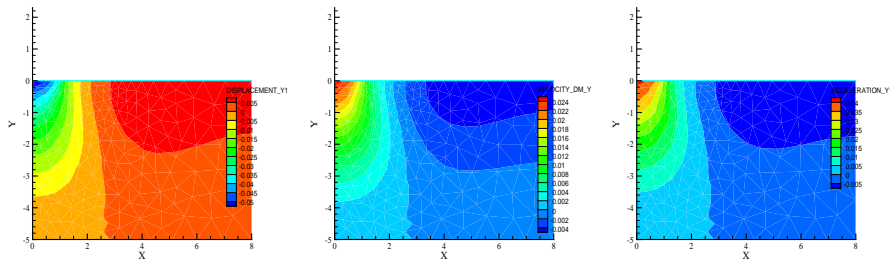


Figure 14.2.11: Displacement, its rate and acceleration: vertical component

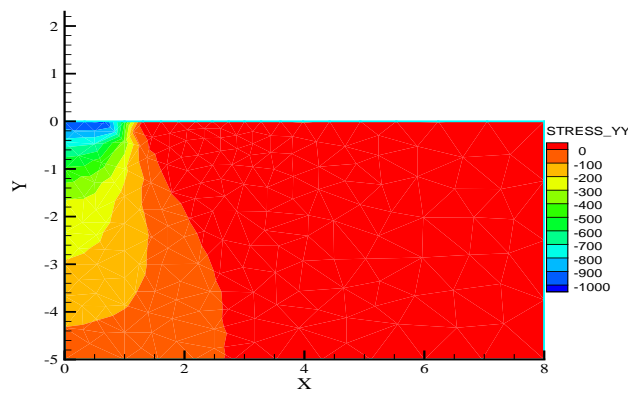


Figure 14.2.12: Vertical stress

14.3 Unsaturated consolidation

14.3.1 Theory

Fluid mass balance

The general fluid mass balance equation for unsaturated flow in a deformable porous medium is

$$\begin{aligned} nS^l \dot{\rho}^l + n\rho^l \dot{S}^l + nS^l \rho^l \mathbf{v}^{ls} + S^l \rho^l \nabla \cdot \mathbf{v}^s + S^l \rho^l \frac{1-n}{\rho^s} \dot{\rho}^s = \\ Q_\rho^l + S^l \frac{\rho^l}{\rho^s} Q_\rho^s \end{aligned} \quad (14.3.1)$$

Hereby, the basic assumption of Richards type models is that the gaseous phase is immobile, i.e. $\mathbf{v}^g = 0$. Assuming grain incompressibility for isothermal conditions (i.e. $\dot{\rho}^s = 0$) and no solid sources (e.g. resulting from chemical reactions) as well as applying the constitutive equations for fluid compressibility, capillary pressure, and Darcy flux, we obtain the following Richards equation for an unsaturated deformable porous medium.

$$nS^l \rho_0^l \beta_p p^l - n\rho^l \frac{dS^l}{dp_c} p^l - \nabla \left(\frac{k_{rel}^l \mathbf{k}}{\mu^l} (\nabla p^l - \rho \mathbf{g}) \right) + S^l \rho^l \nabla \cdot \dot{\mathbf{u}}^s = Q_\rho^l \quad (14.3.2)$$

Rearrangement with respect to the primary variables p^l, \mathbf{u}^s yields

$$\begin{aligned} \left(-n\rho^l \frac{dS^l}{dp_c} + nS^l \rho_0^l \beta_p \right) \dot{p}^l - \nabla \left(\frac{k_{rel}^l \mathbf{k}}{\mu^l} \nabla p^l \right) + S^l \rho^l \nabla \cdot \dot{\mathbf{u}}^s = \\ Q_\rho^l + \nabla \left(\frac{k_{rel}^l \mathbf{k}}{\mu^l} \rho \mathbf{g} \right) \end{aligned} \quad (14.3.3)$$

A constitutive equation, the water content function obtained by experiments, characterizes the relationship between p^l and S^l and therefore the derivative dS^l/dp_c .

Momentum balance

The deformation process is described by the momentum balance equation for the unsaturated porous medium in terms of stresses.

$$\nabla \cdot (\boldsymbol{\sigma} - \alpha_b S^l p^l \mathbf{I}) + \rho \mathbf{g} = \mathbf{0} \quad (14.3.4)$$

All symbols are denoted in chapter ??.

Numerical scheme

The standard Galerkin finite element approach is applied for the numerical solution of the PDEs (14.3.3) and (14.3.4) resulting into the following system of algebraic equations.

$$\underbrace{\begin{bmatrix} \mathbf{C}_{pp} & \mathbf{C}_{pu} \\ \mathbf{C}_{up} & \mathbf{C}_{uu} \end{bmatrix}}_{\mathbf{C}} \frac{d}{dt} \underbrace{\begin{Bmatrix} \hat{\mathbf{p}}^l \\ \hat{\mathbf{u}}^s \end{Bmatrix}}_{\mathbf{x}} + \underbrace{\begin{bmatrix} \mathbf{K}_{pp} & \mathbf{K}_{pu} \\ \mathbf{K}_{up} & \mathbf{K}_{uu} \end{bmatrix}}_{\mathbf{K}} \begin{Bmatrix} \hat{\mathbf{p}}^l \\ \hat{\mathbf{u}}^s \end{Bmatrix} = \underbrace{\begin{Bmatrix} \mathbf{r}_p \\ \mathbf{r}_u \end{Bmatrix}}_{\mathbf{r}} \quad (14.3.5)$$

where $\mathbf{C}_{up}, \mathbf{C}_{uu}, \mathbf{K}_{pu}$ are zero.

$$\begin{bmatrix} \mathbf{C}_{pp} & \mathbf{C}_{pu} \\ \mathbf{0} & \mathbf{0} \end{bmatrix} \frac{d}{dt} \begin{Bmatrix} \hat{\mathbf{p}}^l \\ \hat{\mathbf{u}}^s \end{Bmatrix} + \begin{bmatrix} \mathbf{K}_{pp} & \mathbf{0} \\ \mathbf{K}_{up} & \mathbf{K}_{uu} \end{bmatrix} \begin{Bmatrix} \hat{\mathbf{p}}^l \\ \hat{\mathbf{u}}^s \end{Bmatrix} = \begin{Bmatrix} \mathbf{r}_p \\ \mathbf{r}_u \end{Bmatrix} \quad (14.3.6)$$

Time discretization with explicit finite differences yields

$$\begin{aligned} & \left(\frac{1}{\Delta t} \mathbf{C}_{pp} + \theta \mathbf{K}_{pp} \right) \hat{\partial}_{n+1}^l + \frac{1}{\Delta t} \mathbf{C}_{pu} \hat{\mathbf{u}}_{n+1}^s \\ &= \left(\frac{1}{\Delta t} \mathbf{C}_{pp} + (1 - \theta) \mathbf{K}_{pp} \right) \hat{\partial}_n^l + \frac{1}{\Delta t} \mathbf{C}_{pu} \hat{\mathbf{u}}_n^s + \mathbf{r}_p \end{aligned} \quad (14.3.7)$$

$$\begin{aligned} & \theta \mathbf{K}_{up} \hat{\partial}_{n+1}^l + \theta \mathbf{K}_{uu} \hat{\mathbf{u}}_{n+1}^s \\ &= (1 - \theta) \mathbf{K}_{up} \hat{\partial}_{n+1}^l + (1 - \theta) \mathbf{K}_{pp} \hat{\mathbf{u}}_{n+1}^s + \mathbf{r}_u \end{aligned} \quad (14.3.8)$$

with following finite element matrices

$$\begin{aligned} \mathbf{C}_{pp}^e &= \int_{\Omega^e} \mathbf{N}_p^T \left[-n\rho^l \frac{dS^l}{dp_c} + nS^l \rho_0^l \beta_p \right] \mathbf{N}_p d\Omega^e \\ \mathbf{K}_{pp}^e &= \int_{\Omega^e} \nabla \mathbf{N}_p^T \left[-\frac{k_{rel}^l \mathbf{k}}{\mu^l} \right] \nabla \mathbf{N}_p d\Omega^e \\ \mathbf{C}_{pu}^e &= \int_{\Omega^e} \mathbf{N}_p^T [S^l \rho^l] \nabla \mathbf{N}_u d\Omega^e \\ \mathbf{r}_p^e &= \int_{\Omega^e} [Q_\rho^l] \mathbf{N}_p d\Omega^e + \int_{\Omega^e} \mathbf{N}_p^T \left[\frac{k_{rel}^l \mathbf{k}}{\mu^l} \rho^l \mathbf{g} \right] \nabla \mathbf{N}_p d\Omega^e \end{aligned} \quad (14.3.9)$$

$$\begin{aligned}
 \mathbf{K}_{up}^e &= \int_{\Omega^e} \mathbb{B}^T [\alpha_b S^l] \mathbf{m} \mathbf{N}_p d\Omega^e \\
 \mathbf{K}_{uu}^e &= \int_{\Omega^e} \mathbb{B}^T [\mathbb{C}] \mathbb{B} d\Omega^e \\
 \mathbf{r}_u^e &= \int_{\Omega^e} \mathbf{N}_u [\rho \mathbf{g}] d\Omega^e
 \end{aligned} \tag{14.3.10}$$

where \mathbf{m} is a mapping vector as

$$\mathbf{m} = [1 \ 1 \ 1 \ 0]^T$$

for plane strain problems and

$$\mathbf{m} = [1 \ 1 \ 1 \ 0 \ 0 \ 0]^T$$

for 3D problems

14.3.2 Liakopoulos Experiment

Problem definition

The first example is a drainage test based on an experiment by Liakopoulos (1965). Desaturation takes place due to gravitational effects. This example was studied previously by several authors, e.g. Liakopoulos (1965), Narasimhan & Witherspoon (1978), Zienkiewicz et al. (1990), Schrefler & Zhan (1993). Therefore, this example is well suited as benchmark, moreover, because of the lack of any analytical solutions for this type of coupled, non-linear problems. In this test example, multiphase flow in a deforming porous medium is studied. At first we employ the Richards approximation, i.e. air remains at atmospheric pressure.

The physical experiment of Liakopoulos was conducted in a column packed with so-called Del Monte sand. Moisture content and tension at several points along the column were measured with tensiometers (Fig. 14.3.1, Fig. 14.3.2).

In the simulation, the column is assumed has size of $0.1m \times 1m$ and discretized into 20 quadrilateral elements (Fig. 14.3.3).

Initial and boundary conditions

Based on the experiment, we assume that the initial pressure is zero everywhere in the domain. Boundary conditions for both fluid and displacement fields is depicted in Fig. 14.3.3. Such initial boundary conditions imply that the sample is fully saturated at the beginning, the water is allowed to flow out from the bottom boundary.

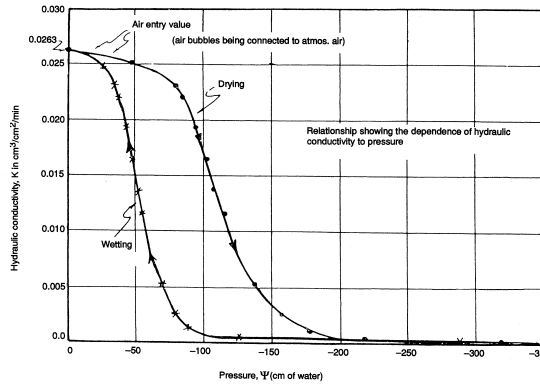


Figure 14.3.1: Hydraulic conductivity vs pressure, with $K = k\rho g/\mu$ and $\Psi = p/\rho g$ (Liakopoulos 1965)

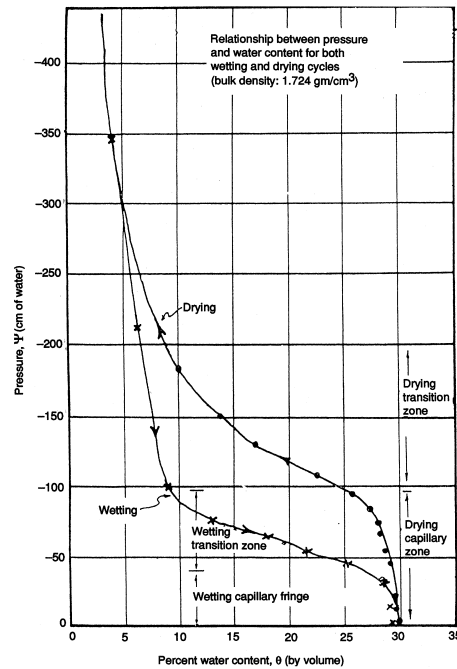


Figure 14.3.2: Hydraulic head vs water content, with $\Psi = p/\rho g$ and $\theta = nS$ (Liakopoulos 1965)

Material properties

The capillary pressure $p_c(S)$

$$p_c = \left(\frac{1-S}{1.9722} \times 10^{11} \right)^{\frac{1}{2.4276}} \quad (14.3.11)$$

$$\partial p / \partial \mathbf{n} = 0, \sigma_{yy} = 0, \sigma_{xy} = 0$$

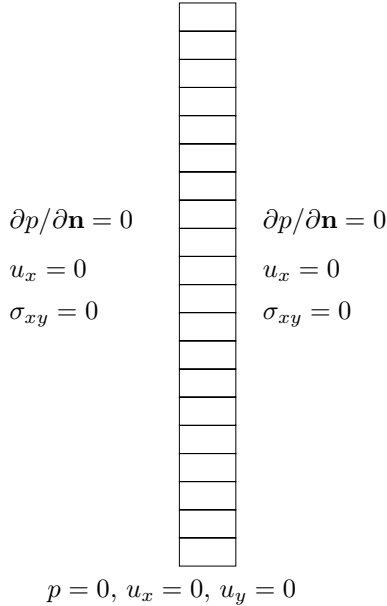


Figure 14.3.3: Boundary conditions

as well as the relative permeability relationships $k_{\text{rel}}(S)$

$$k_{\text{rel}} = 1 - 2.207(1 - S)^{1.0121} \quad (14.3.12)$$

fit the measured data for saturations larger than 0.84. The physical parameter are given in the table below.

Property	Value	Unit
Young's modulus, E	MPa	1.3
Poisson's ratio, ν	—	0.4
Solid grain density, ρ^s	kgm^{-3}	2000
Liquid density, ρ^l	kgm^{-3}	kgm^{-3}
Porosity, n	—	0.2975
Permeability, k	m^2	4.5×10^{-13}
Water viscosity, μ	Pas	10^{-3}
Gravity, g	ms^{-2}	9.806
capillary pressure $p_c(S)$	Pa	eqn. (14.3.11)
Relative permeability, $k_{\text{rel}}(S)$	—	eqn. (14.3.12)

Table 14.3.1: Material parameters

Results

We conduct two kinds of simulation such as: one is taking account of the gravity force as a load for displacement field, while the other ignore the the gravity force.

For the case of non-gravity force, Fig. 14.3.4 shows history profile of water pressure p , water saturation S , vertical solid displacement u_y and vertical stress σ_{yy} . Results of p , water saturation S , vertical solid displacement u_y agree with

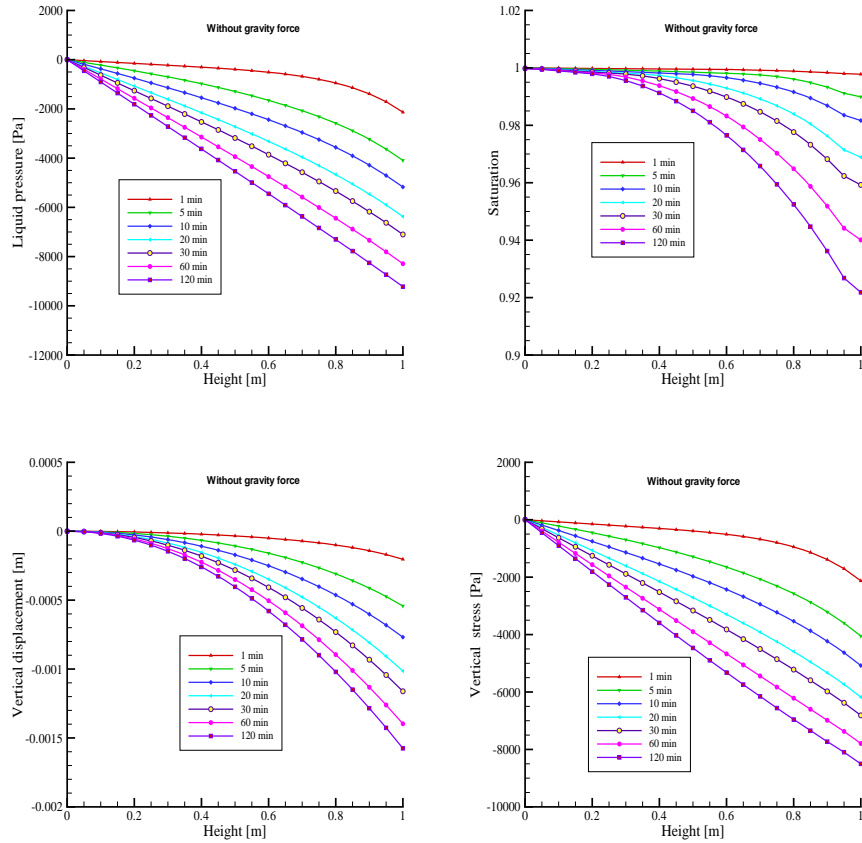


Figure 14.3.4: Simulated results (without gravity force), p , S , u_y , σ_{yy}

what given in [125] (see pages 167-172).

The vertical profile of results obtained by taking account of the gravity force are shown in Fig. 14.3.5. If compare the saturation result with that obtained by ignoring the gravity fore, one can easily find the desaturated procedure is enhanced apparently. This highlights the impact of displacement to water pressure

and the coupling effects.

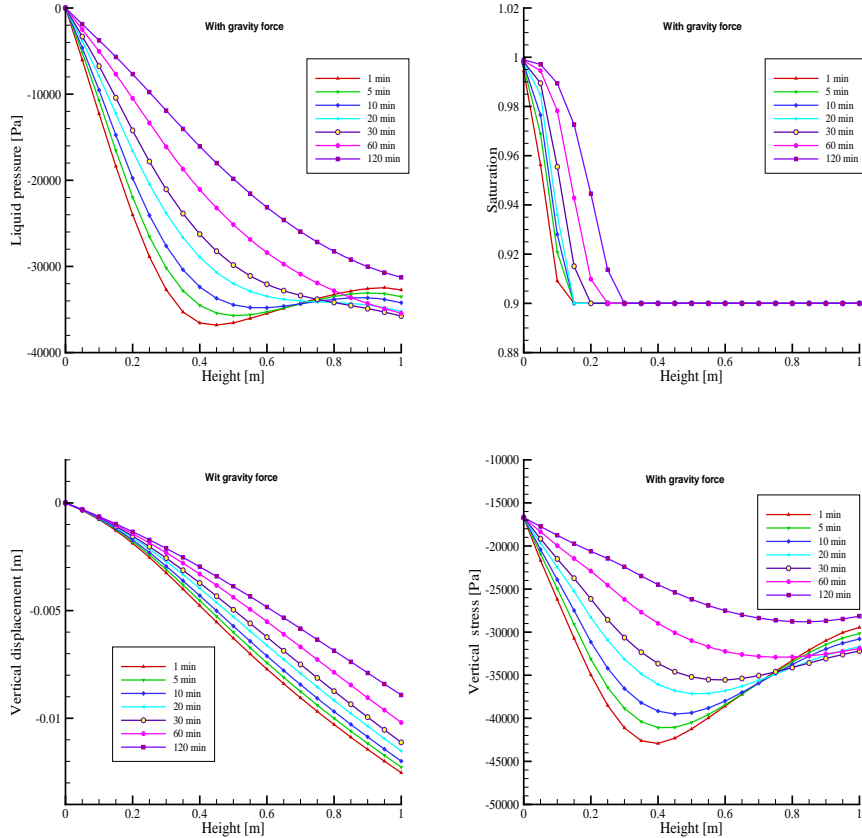


Figure 14.3.5: Simulated results (with gravity force), p , S , u_y , σ_{yy}

Benchmark deposit

Benchmark	Problem type	Path in benchmark deposit
<i>hm_unsat</i>	HM	benchmarksHM

14.3.3 DECOVALEX HM test case

DECOVALEX is an international code comparison project for the verification of thermo-hydro-mechanical (THM) and thermo-hydro-chemical (THC) numerical simulators [126] (see also sec. 18.2).

Definition

The original DECOVALEX-THM benchmark definition is a 2-D problem [126] (Fig. 14.3.6). For the comparison of different HM swelling models, we consider a simplified case representing a horizontal cross-section through the 2-D domain (Fig. 14.3.6, BME1H).

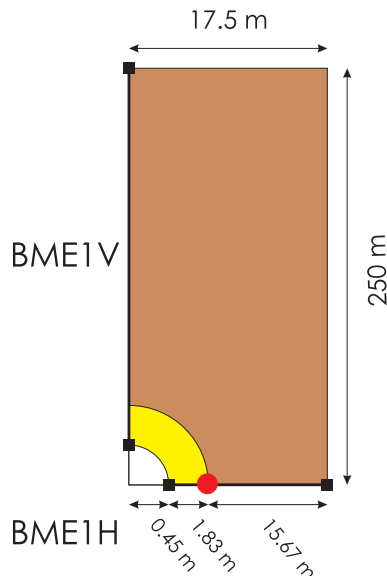


Figure 14.3.6: 2-D DECOVALEX THM definition and simplification for the benchmark exercise BME1H

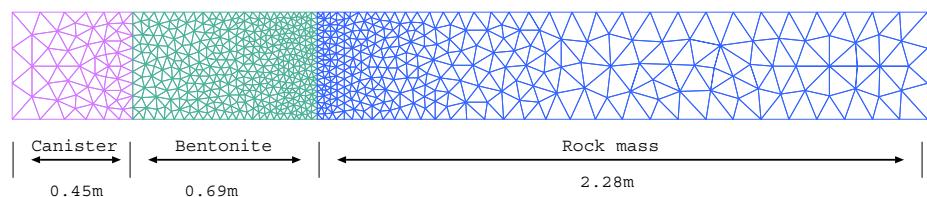


Figure 14.3.7: Mesh of the simplified BME1H model including canister, bentonite, and rock mass sections

The simplified model takes a rectangle shape. The mesh of the domain together with material types are shown in Fig. 14.3.7.

Fig. 14.3.8 illustrates the definition of initial and boundary conditions for the horizontal cross-section BME1H. Observation points are set at $x = 0.45\text{ m}$, $x = 1.10\text{ m}$ to record temporal breakthrough curves.

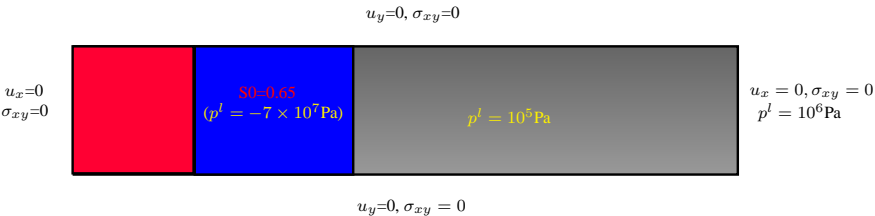


Figure 14.3.8: Simplified horizontal cross-section model

The material parameters for rock mass and bentonite are given in Table 14.3.2 and 14.3.3, respectively.

Parameter	Unit	Value
Density	kg/m^3	2700
Young's modulus	GPa	35
Poisson ratio	-	0.3
Porosity	-	0.01
Saturated permeability	m^2	1.0×10^{-17}

Table 14.3.2: Rock Mass

Density	kg/m^3	1600
Young's modulus	MPa	317
Poisson ratio	-	0.35
Saturated permeability	m^2	2.0×10^{-21}

Table 14.3.3: Bentonite

The dependency of capillary pressure as well as relative permeability on liquid saturation for both of rock and bentonite are depicted in Fig. 14.3.9.

Results

Fig. 14.3.10 displays a contour plot of saturation and vertical swelling stress in the domain. Apparently, the swelling stress in the bentonite is induced by change of water saturation.

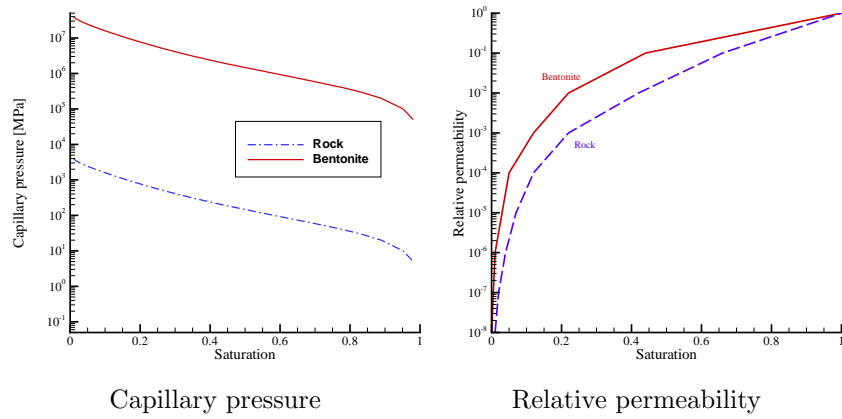


Figure 14.3.9: Capillary pressure - relative permeability - functions

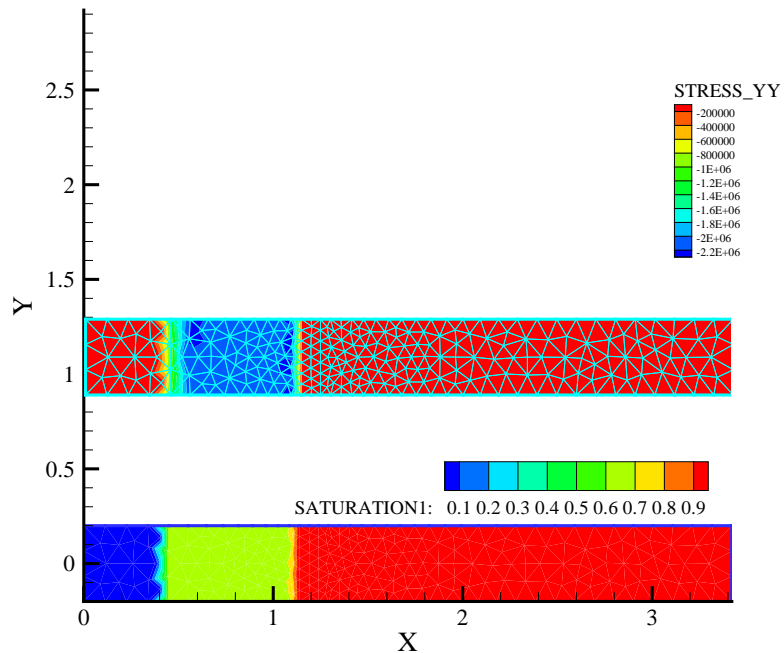


Figure 14.3.10: Distribution of saturation and vertical swelling stress

Fig. 14.3.11 shows the simulated horizontal profiles (top) and temporal evolutions at observation point (bottom) of water saturation and swelling stress based on the linear swelling model (14.4.5) proposed by Rutqvist (2005) [127].

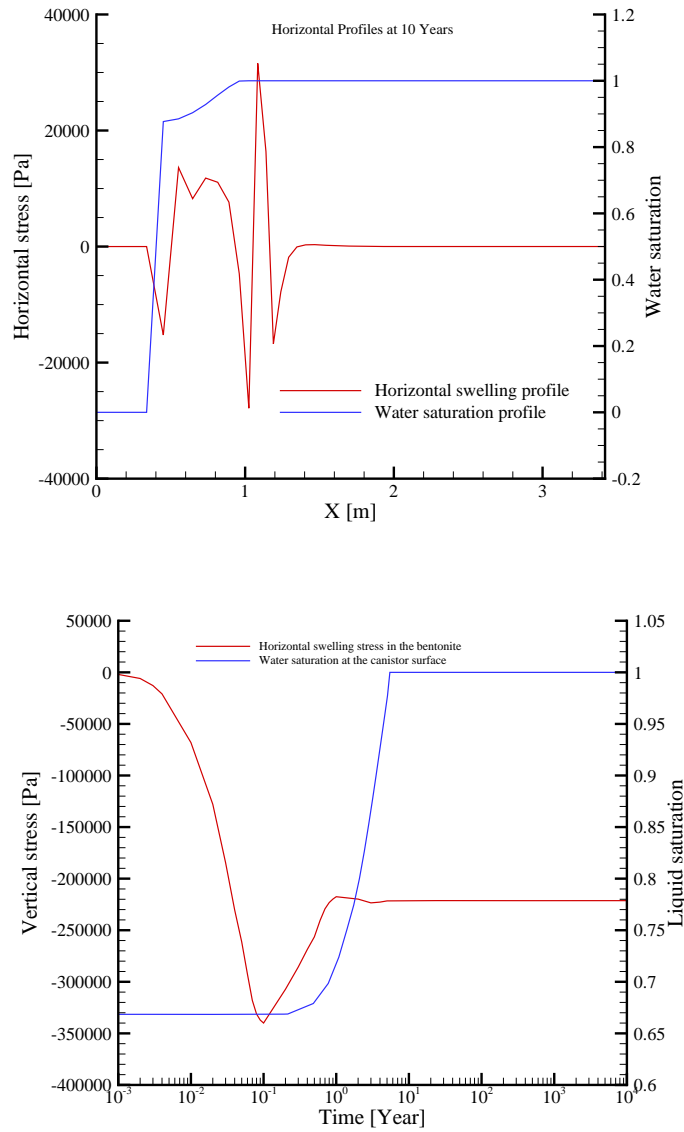


Figure 14.3.11: Horizontal profile (top) and temporal evolution at observation point (bottom) of water saturation and swelling stress

Benchmark deposit

Benchmark	Problem type	Path in benchmark deposit
<i>hm-swelling</i>	HM	HM/LinearSwelling

14.4 Two-phase flow consolidation - H²M Process

14.4.1 Theory

Balance equations

The fluid mass balance equations for two-phase flow in a deformable porous medium (H²M process) using capillary pressure p_c and gas pressure p^g as primary variables (pp model) is

$$n\rho^l \frac{\partial S^l}{\partial p_c} \dot{p}_c + \rho^l S^l \nabla \cdot \dot{\mathbf{u}} + \nabla \cdot \left[\rho^l \frac{\mathbf{k} k_{rel}^l}{\mu^l} (-\nabla p^g + \nabla p_c + \rho^l \mathbf{g}) \right] = Q^l \quad (14.4.1)$$

$$\begin{aligned} -n\rho^g \frac{\partial S^l}{\partial p_c} \dot{p}_c + n(1 - S^l) \left(\frac{\partial \rho^g}{\partial p^g} \dot{p}^g + \frac{\partial \rho^g}{\partial p_c} \dot{p}_c \right) + [\rho^l S^l + \rho^g (1 - S^l)] \nabla \cdot \dot{\mathbf{u}} \\ + \nabla \cdot \left[\rho^g \frac{\mathbf{k} k_{rel}^g}{\mu^g} (-\nabla p^g + \rho^g \mathbf{g}) \right] = Q^g \end{aligned} \quad (14.4.2)$$

momentum balance in terms of stress equilibrium

$$\nabla \cdot (\sigma - \alpha_b (S^g p^g + S^l p^l) + \rho \mathbf{g}) \quad (14.4.3)$$

Swelling models

A simple model was proposed by Rutqvist (2005) [127], which defines the increment of swelling stress being proportional to the liquid (water) saturation increment

$$\Delta \sigma^{sw} = \alpha \Delta S^l \quad (14.4.4)$$

$$\Delta \sigma^{sw} = n \alpha (\Delta S^l)^2 \quad (14.4.5)$$

example in sec. 16

TEP model, for more details see [128], example in sec. 14.4.2

14.4.2 TEP test case

Definition

Fig. 14.4.1 shows the axi-symmetric model domain for the confined swelling test as well as the initial and boundary conditions for the two-phase flow consolidation problem.

$$\partial p^c / \partial y = 0, p^g = 0.1 \text{ MPa}, u_y = 0, \sigma_{xy} = 0$$

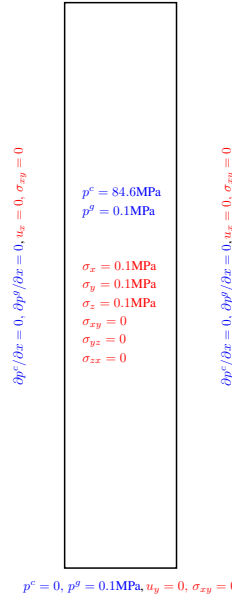


Figure 14.4.1: Model set-up with initial and boundary conditions

The hydraulic and fluid properties are given in Table 14.4.1.

Meaning	Value	Unit
Liquid density, ρ^l	1000	kg/m^3
Liquid viscosity, μ^l	10^{-3}	Pa s
Gas density, ρ^g	Clapeyron equation (D7)	kg/m^3
Gas viscosity, , μ^g	1.8×10^{-5}	Pa s
Intrinsic permeability	0.6×10^{-20}	m^2
Porosity	0.4	m^3/m^3
Media properties for liquid:		
Relative permeability:	Power law $k_{rel}^l = S_e^3$	
Residual saturation	0	—
Maximum saturation	1	—
Water retention:	van Genuchten	
Exponential index, m	0.42	—
Air entry pressure, p_0	62	MPa
Relative permeability of gas, k_{rel}^g	$5.103 \times 10^{-12} [e(1 - S^l)]^{4.3}$	e , void ratio

Table 14.4.1: Hydraulic properties

The parameters of the thermo-elasto-plastic swelling model are given in Table 14.4.2. Cam-Clay plasticity.

Meaning	Value	Unit
Slope of the critical state line, M	1.5	—
Virgin compression index, λ_p	1.5	—
Swelling/recompression index, κ	0.1	—
Initial preconsolidation pressure, p_c	8.0	MPa
Initial void ratio, e	0.7	--
Poisson ratio	0.4	—
Initial ($s = 0$) elastic slope for $1 + e - p$, κ_{i0}	0.01	—
Initial ($\sigma = 0$) elastic slope for $1 + e - s$, κ_{s0}	0.25	—
Minimum bulk modulus, K_{min}	10	MPa
First parameter for κ_s , α_{ss}	-0.03	MPa ⁻¹
Second parameter for κ_s , α_{sp}	-0.1609	—
Parameter for κ_i , α_i	-0.003	MPa ⁻¹
Reference mean stress, p_{ref}	0.1	MPa

Table 14.4.2: Plasticity parameters

Results

Fig. 14.4.2 shows the temporal evolution of water saturation on the bottom of the sample.

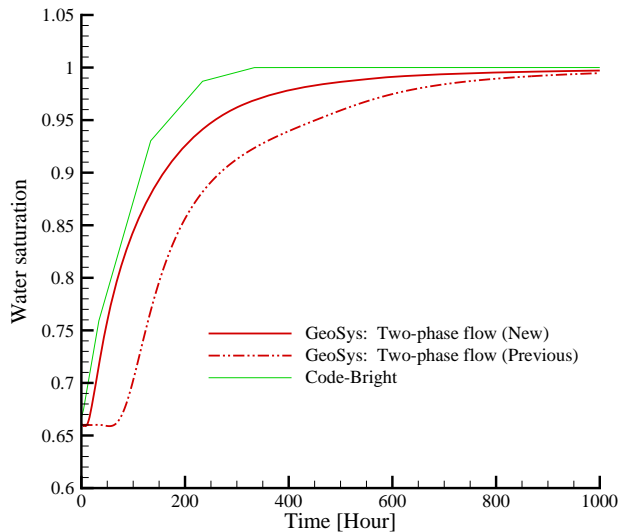


Figure 14.4.2: Vertical stress evolution at the sample bottom

Fig. 14.4.3 shows the temporal evolution of the vertical effective stress on the

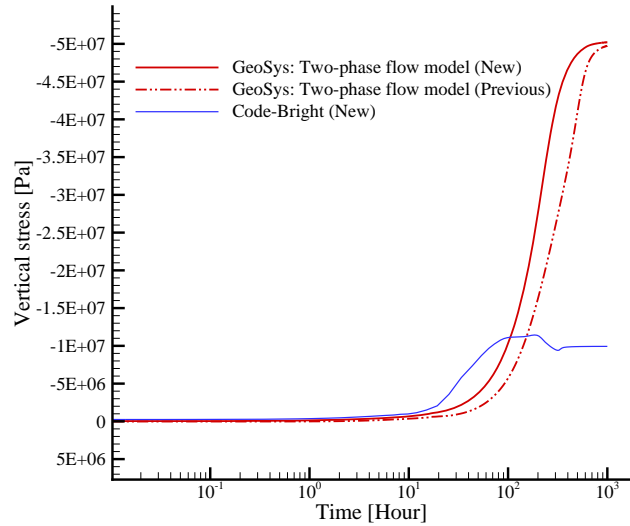


Figure 14.4.3: Water saturation evolution at the sample bottom

bottom of the sample.

Benchmark deposit

Benchmark	Problem type	Path in benchmark deposit
<i>h2m-tap</i>	H2M	H2M/TEP

Chapter 15

Thermo-Mechanics – TM-Processes

15.1 Theory

Heat transport in solids or porous media

For heat transport problem in any medium, the governing equation is given by

$$\rho C_p T' = -\nabla \mathbf{q}_T + Q_T(\mathbf{x}, t), \mathbf{x} \in \mathbb{R}^3 \quad (15.1.1)$$

where ρ is medium density, $C_p(T)$ is the specific heat capacity, Q_T is heat source and \mathbf{q}_T is the heat flux, which takes the forms

$$\mathbf{q}_T = -K_e \nabla T \quad (15.1.2)$$

for solid and

$$\mathbf{q}_T = -K_e \nabla T + n \sum_{\gamma}^{phase} (\rho^\gamma C_p^\gamma) T \mathbf{v}, \gamma = \text{liquid, gaseous} \quad (15.1.3)$$

for porous media considering of advective and diffusive fluxes with K_e the heat conductivity. For porous media, the specific heat capacity consists of portions of solid, liquid and gaseous phase as

$$\rho C_p = \sum_{\gamma}^{phase} (\rho^\gamma C_p^\gamma) \quad (15.1.4)$$

where γ specifies solid, liquid or gaseous phase. The boundary conditions are given by

$$\mathbf{q}_T \cdot \mathbf{n} = q_T^T, \text{ or } T = T_\Gamma, \forall \mathbf{x} \in \partial\Omega \quad (15.1.5)$$

and the initial condition reads

$$T(\mathbf{x}, t) = T_0(\mathbf{x}), \forall \mathbf{x} \in \Omega \quad (15.1.6)$$

with \mathbf{n} , the normal direction at $\mathbf{x} \in \partial\Omega$

Thermal stress

We consider the total strain rate $\Delta\epsilon$ can be admissible decomposed into components such as reversible (elastic), temperature deduced as

$$\Delta\epsilon = \mathbb{C}(\Delta\epsilon^e - \alpha \Delta T) \quad (15.1.7)$$

where α is the thermal expansion. With the generalized Hook's law, the total stress with the thermal effect can be expressed as

$$\Delta\sigma = \mathbb{C}(\Delta\epsilon - \alpha \Delta T) \quad (15.1.8)$$

with \mathbb{C} the constitutive tensor.

The volume of a solid is increasing or decreasing with temperature changes. Homogeneous bodies expand evenly in each direction by increasing temperatures. In this case no variation of the stresses occurs. If the deformation of the solid is prevented, the stresses are increasing or decreasing with temperature changes (Beitz et al., 1987). This phenomenon can be easily calculated by analytical solutions of the Hooke's linear elastic model. The equations of the mechanical behaviour base on the Hooke's law for linear elastic materials:

$$\varepsilon_x = \frac{1}{E} \cdot (\sigma_x - \nu \cdot (\sigma_y + \sigma_z)) + \alpha \cdot \Delta T \quad (15.1.9)$$

$$\varepsilon_y = \frac{1}{E} \cdot (\sigma_y - \nu \cdot (\sigma_x + \sigma_z)) + \alpha \cdot \Delta T \quad (15.1.10)$$

$$\varepsilon_z = \frac{1}{E} \cdot (\sigma_z - \nu \cdot (\sigma_x + \sigma_y)) + \alpha \cdot \Delta T \quad (15.1.11)$$

with

ε_i – strains

σ_i – stresses in Pa

E – Young's modulus in Pa

ν – Poisson's ratio

α – thermal expansion in K^{-1}

ΔT – temperature change in K

indices:

x, y, z - x, y, z -direction.

15.2 Thermo-Elasticity

15.2.1 Thermo-elastic plate (2D)

We first solve a plane strain TM coupling problem, then solve this problem again with 3D model.

All parameters are dimensionless. Time step size is 0.1 and the simulation runs 100 steps.

Benchmark name: *tm2D*.

Geometry and mesh : A rectangle domain with size of 10×10 . The domain is discretized into quadrilateral elements (Fig. 15.2.1).

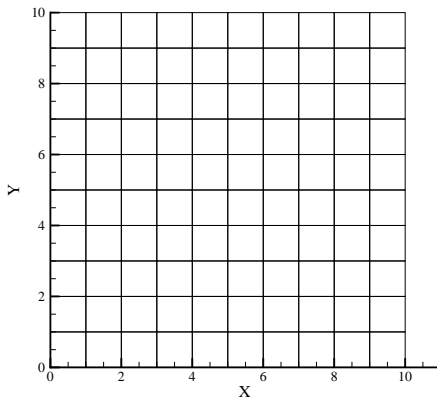


Figure 15.2.1: Mesh for TM coupling plane strain problem

Material: Table 15.2.1.

Table 15.2.1: Material properties for TM coupling plane strain problem

Property	Value	Unit
Young's modulus	3×10^3	---
Poisson's ratio	0.3	---
Density	1.0	---
Thermal expansion	1	---
Thermal capacity	1	---
Thermal conductivity	1	---

Initial and boundary conditions : Initial condition is given by

$$\sigma_0 = \mathbf{0}, T_0 = 198.15$$

Boundary condition is depicted in Fig. 15.2.2.

$$u_y = 0, \nabla T \cdot \mathbf{n} = 0$$

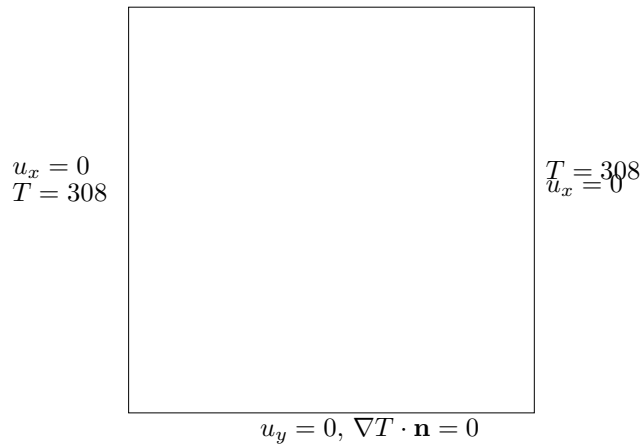


Figure 15.2.2: Boundary conditions for TM coupling plane strain problem

Results: Fig. 15.2.3 provides the distribution of temperature and vertical stress after 100 time steps. The vertical stress distribution shows the effect of gravity force.

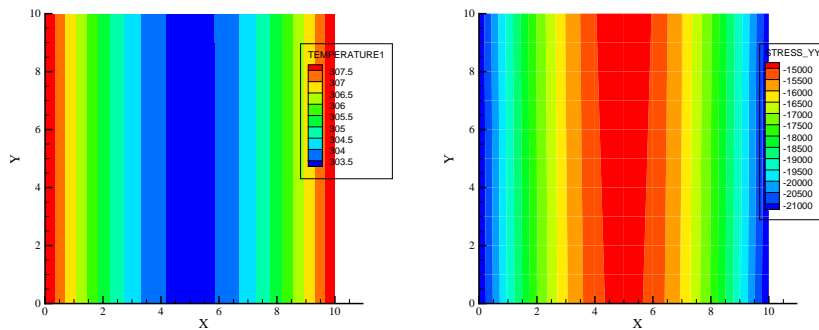


Figure 15.2.3: Distribution of temperature and vertical stress

15.2.2 Thermo-elastic cube (3D)

3D simulation of the problem given in Section 15.2.1.

Benchmark name: *tm3D*.

Geometry and mesh : Extrude the 2D model in off-plane direction for 1 unit. The domain is discretized into hexahedra (Fig. 15.2.4).

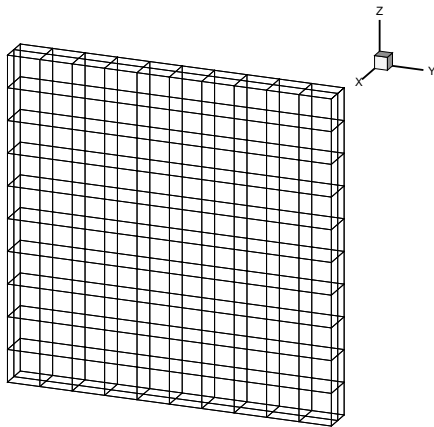


Figure 15.2.4: Mesh for TM coupling 3D problem

Material: Table 15.2.1.

Initial and boundary conditions : Similar to that described in Section 15.2.1 for plane strain problem.

Results: Fig. 15.2.5 provides the distribution of temperature and vertical stress after 100 time steps. The distribution is identical to that given in Fig. 15.2.3 for plane strain problem.

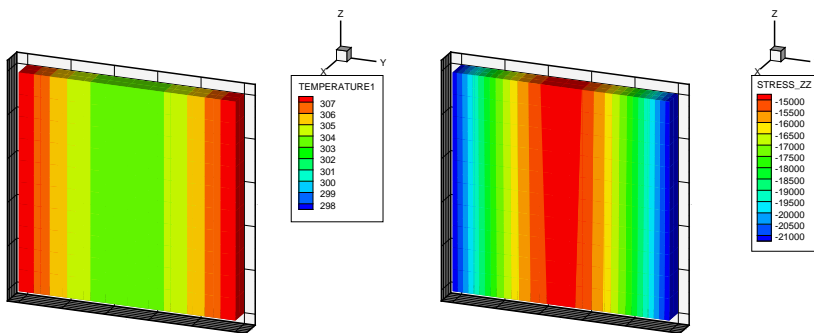


Figure 15.2.5: Distribution of temperature and vertical stress

Fig. 15.2.6 gives a comparison about the variation of state variables at the gravity center of 2D and 3D model. The results agree well with each other.

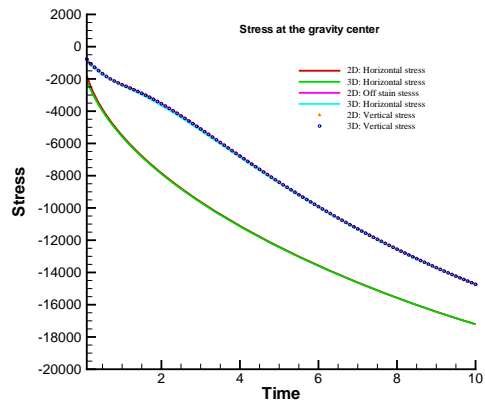


Figure 15.2.6: Comparison of 2D, 3D results

15.2.3 Homogeneous material (3 D)

Problem definition

The top and the bottom of a solid body that consists of one homogeneous material are heated. The xy -plane is the horizontal plane. The height of the body is in z -direction. The dimensions of this 3 D-model are 10 m in all directions. As deformations in x - and y -direction are suppressed, the increasing temperature evokes stresses within the solid. The aim of the calculation is to find out the isotropic state of stress that is reached after the whole solid is heated. Fig. 15.2.7 shows a sketch of the calculation area.

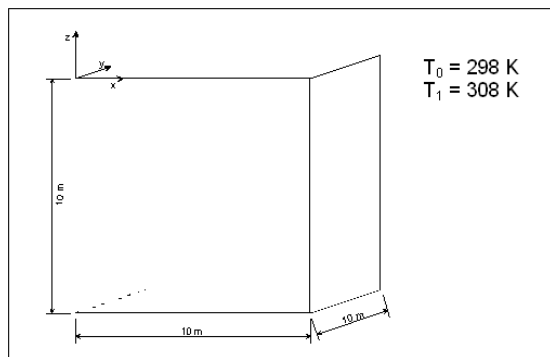


Figure 15.2.7: Calculation area with one material

Assumptions

- Temperature: constant temperature in the whole body at the beginning, heating of the body about 10 K
- Solid: homogeneous, anisotropic, finite dimensions, no deformation at the boundaries, linear elastic material behaviour, isotropic thermal expansion, different thermal expansion for the materials

Model set-up of the 3 D numerical model

The dimensions of this 3 D-model are 10 m in all directions. Deformations perpendicular to the outer surfaces are suppressed. The initial temperature in the whole area is 298 K. At the top and at the bottom of the model thermal boundary conditions are set with a temperature of 308 K. Thereby the heating of the solid about 10 K is simulated. The used parameters of the solid represent the material behaviour of concrete (Tab. 15.2.2). 1000 elements and 1331 nodes are used. The calculation is divided in 384 time steps with a constant time step length of 900 seconds. That means the heating of the solid within 4 days is simulated. The calculation model is sketched in Fig. 15.2.8.

symbol	quantity	value
T_0	Initial temperature (before heating)	298 K
T_1	Temperature after heating	308 K
ρ	Density of the solid	2.2 t·m ⁻³
E	Young's modulus of the solid	25 GPa
ν	Poisson ratio	0.27
α	Thermal expansion	6.0 · 10 ⁻⁶ K ⁻¹
c	Thermal capacity	1.0 J·kg ⁻¹ ·K ⁻¹
κ	Thermal conductivity	1.0 W·m ⁻¹ ·K ⁻¹

Table 15.2.2: Used parameters

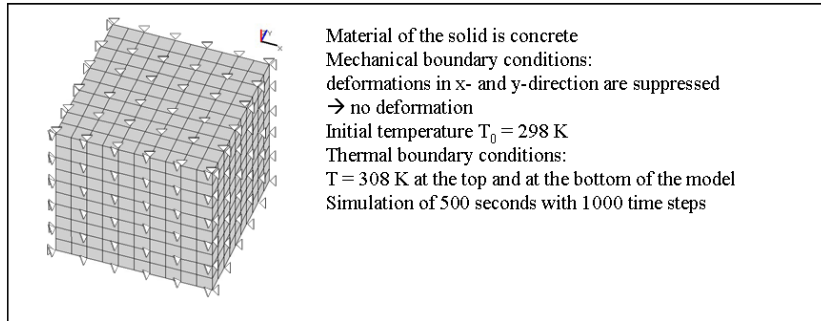


Figure 15.2.8: Calculation model (3 D)

Evaluation method

The analytical solution can be derived from the time independent Eqns. 15.1.9 to 15.1.11 with the assumptions of no deformation and an isotropic thermal expansion:

$$\varepsilon_i \equiv 0$$

$$\sigma_x = \sigma_y = \sigma_z = -\frac{\alpha \cdot \Delta T \cdot E}{1 - 2 \cdot \nu} \quad (15.2.1)$$

Eqn. 15.2.1 provides the stresses after heating the solid and shows an isotropic state of stress.

Results

With the analytical solution in Eqn. 15.2.1 and the used parameters the stress values in the solid amount. This isotropic state of stress is reached after the whole solid is heated. The temporal development of the stresses in the centre of the model (at node 665) calculated is presented in Fig. 15.2.9. The results of the 3 D simulation show an exact agreement with the analytical solutions.

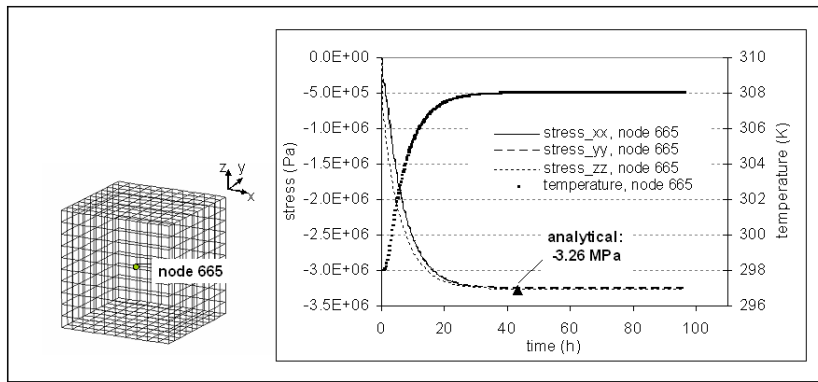


Figure 15.2.9: Temporal stress development in the centre of the calculation model (node 665)

Path in the benchmark deposit	Used code	Used version	Date of simulation run
TM\heating\cube\ tm_01_3Du	GeoSys/RockFlow	RockFlow 4, rf4 4.05.07	Dec. 2007

15.2.4 Composite materials (3 D)

Problem definition

If there are 2 materials with different thermal expansions the volume changes of the materials will be uncommon. The material with the higher thermal expansion expands more than the material with the low thermal expansion. If deformations at the outer boundaries are prevented, different states of stress will occur in these two materials. But the stresses perpendicular to the parting plane must be equal. The values of the stresses as a result of temperature changes can also easily be calculated by the HOOKE's linear elastic model. The aim of this simulation is to specify the stresses at several areas in the solid. Fig. 15.2.10 shows a sketch of the calculation area.

Model set-up of the 3 D numerical model

The calculation was done with a 3 D model. The xy -plane is the horizontal plane. The height of the body is in z -direction. The dimensions of this 3 D model are 10 m in all directions. The model includes 1000 elements and 1331 nodes. Deformations perpendicular to the outer surfaces are suppressed. Deformations in x - and z -direction are suppressed. The initial temperature in the whole area is 298 K. At the top and at the bottom of the model thermal boundary conditions are set with a temperature of 308 K. Thereby the heating of the body about 10 K is simulated. The used parameters of the solids represent the material

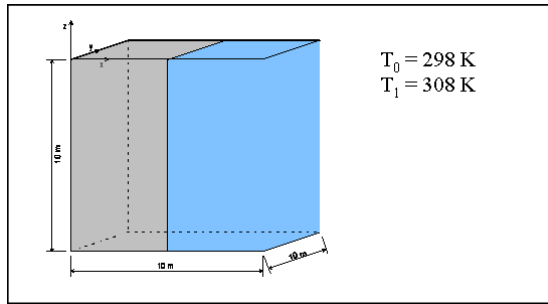


Figure 15.2.10: Calculation area with two different materials

behaviour of concrete. The calculation is divided in 1000 time steps with a constant time step length of 0.5 seconds. A sketch of the calculation model is shown in Fig. 15.2.11.

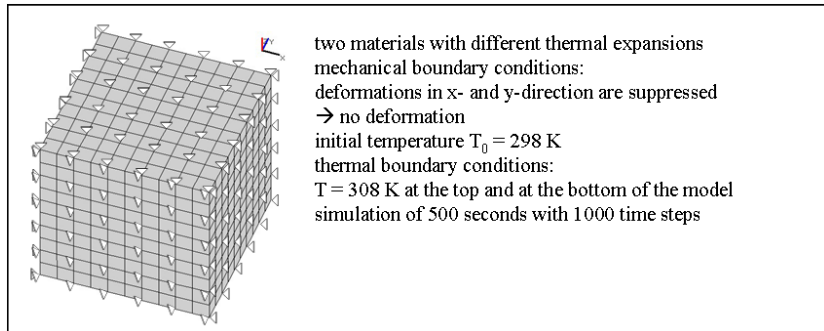


Figure 15.2.11: Calculation model (3D) with 2 materials

Evaluation method

The equations of the mechanical behaviour base on the Hooke's law for linear elastic materials (see Eqns. 15.1.9 to 15.1.11). The analytical solution can be derived from these time independent equations with the assumptions of suppressed deformations in y - and z -direction and an isotropic thermal expansion:

$$\varepsilon_x = \varepsilon_z \equiv 0$$

Additionally the stresses in x -direction (perpendicular to the parting plane between the two materials) must be equal:

$$\sigma_{x1} = \sigma_{x2}$$

Further the expansion of the one material leads to a compression of the other material with the same value in x -direction:

$$\varepsilon_{x1} = -\varepsilon_{x2}$$

symbol	quantity	value
T_0	Initial temperature (before heating)	298 K
T_1	Temperature after heating	308 K
ρ	Density of the solid	$2.2 \text{ t} \cdot \text{m}^{-3}$
E	Young's modulus of the solid	25 GPa
ν	Poisson ratio	0.27
α_1	Thermal expansion of material 1	$6.0 \cdot 10^{-6} \text{ K}^{-1}$
α_2	Thermal expansion of material 2	$1.2 \cdot 10^{-5} \text{ K}^{-1}$
c	Thermal capacity	$1.0 \text{ J} \cdot \text{kg}^{-1} \cdot \text{K}^{-1}$
κ	Thermal conductivity	$1.0 \text{ W} \cdot \text{m}^{-1} \cdot \text{K}^{-1}$

Table 15.2.3: Used parameters

With these limiting conditions the analytical solutions are:

$$\varepsilon_{x1} = \frac{\Delta T}{2} \cdot (\alpha_1 - \alpha_2) \cdot \left(\frac{1 + \nu}{1 - \nu} \right) \quad (15.2.2)$$

$$\varepsilon_{x2} = -\varepsilon_{x1} = -\frac{\Delta T}{2} \cdot (\alpha_1 - \alpha_2) \cdot \left(\frac{1 + \nu}{1 - \nu} \right) \quad (15.2.3)$$

$$\sigma_{x1} = \sigma_{x2} = E \cdot \frac{\varepsilon_{x2} \cdot (1 - \nu) - \alpha_2 \cdot \Delta T \cdot (1 + \nu)}{1 - \nu - 2\nu^2} \quad (15.2.4)$$

$$\sigma_{y1} = \sigma_{z1} = \frac{\nu \cdot \sigma_{x1} - \alpha_1 \cdot \Delta T \cdot E}{1 - \nu} \quad (15.2.5)$$

$$\sigma_{y2} = \sigma_{z2} = \frac{\nu \cdot \sigma_{x2} - \alpha_2 \cdot \Delta T \cdot E}{1 - \nu} \quad (15.2.6)$$

indices:

1 – material 1

2 – material 2

Eqns. 15.2.2 to 15.2.6 provide the strains and stresses after heating the body of two materials. The state of stress is anisotropic.

Results

With the analytical solution in Eqns. 15.2.2 to 15.2.6 and the used parameters the values of the strains in x -direction at the parting plane amount

$$\varepsilon_{x1} = -5.219178 \cdot 10^{-5}$$

$$\varepsilon_{x2} = 5.219178 \cdot 10^{-5}$$

The values of the stresses are

$$\sigma_{x1} = \sigma_{x2} = -4891304.34 \text{ Pa} = -4.8913 \text{ MPa}$$

$$\sigma_{y1} = \sigma_{z1} = -3863907.08 \text{ Pa} = -3.8639 \text{ MPa}$$

$$\sigma_{y2} = \sigma_{z2} = -5918701.60 \text{ Pa} = -5.9187 \text{ MPa}$$

This anisotropic state of stress is reached after the whole body is heated. The temporal stress developments in several nodes calculated with both RockFlow and

GeoSys/RockFlow are presented in Fig. 15.2.12 and Fig. 15.2.13.

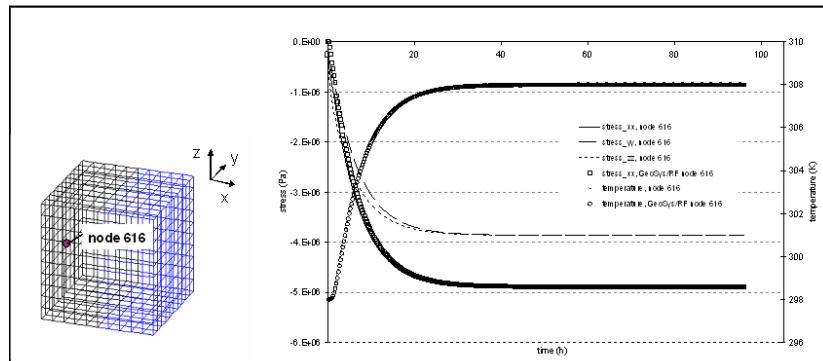


Figure 15.2.12: Temporal stress development in node 616

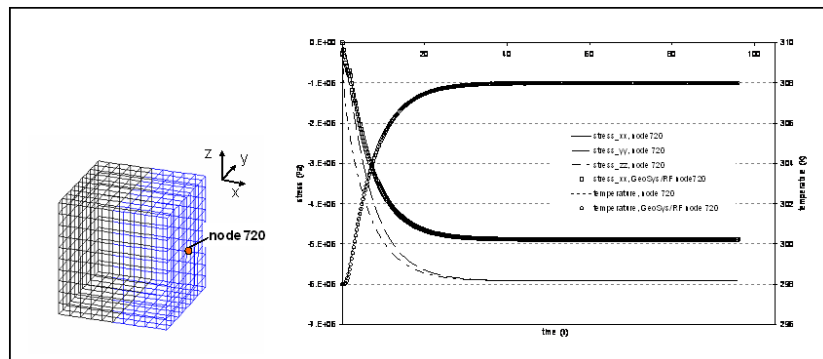


Figure 15.2.13: Temporal stress development in node 720

The results of the 3 D simulation show an exact agreement with the analytical solutions.

Path in the benchmark deposit	Used code	Used version	Date of simulation run
TM\heating\cube\2.mat\GeoSys/RockFlow\tm_02_3Du	GeoSys/RockFlow	RockFlow 4, rf4-507	Dec. 2007

15.2.5 Temperature increase in a hollow cylinder

Problem definition

A hollow cylinder which consists of a solid of a constant temperature is exposed to a higher temperature at the surface of its hole. As a result of the increased temperature the cylinder is expanding. The aim of this calculation is to get out the radial displacement as well as the temperature distribution that are caused by the thermal expansion process by the use of an axisymmetric model. Fig. 15.2.14 shows a sketch of the calculation area.

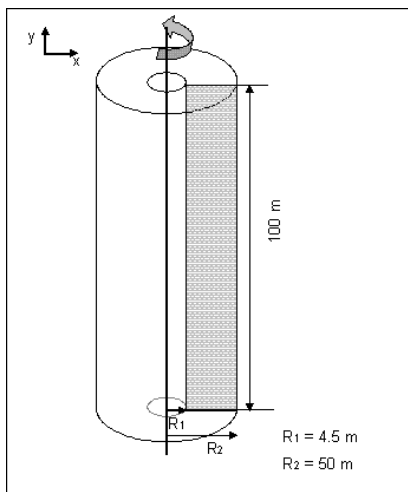


Figure 15.2.14: Calculation area (grey area)

Assumptions

Temperature: constant temperature in the whole body at the beginning, heating of the cylinder at the inner surface

Solid: homogeneous, finite dimensions, no deformation in y -direction at the bottom and the top, no deformation in x -direction at the right border, linear elastic material behaviour, isotropic thermal expansion

Model set-up of the 2 D numerical model

The axisymmetric model is in the xy -plane. The inner radius $R1$ of the cylindrical model is 4.5 m and the outer radius $R2$ 50 m. The cylinder is 100 m high. The initial temperature in the whole area is 25°C. As boundary condition deformations in y -direction at the bottom and the top are suppressed, as well as deformations in x -direction at the right border. At the right boundary of the model a thermal boundary condition is set with a constant value of 25°C. At the left boundary a source term for heat flux of $q = 30 \text{ W/m}^2$ is defined. Thereby the continuous heating of the solid is simulated. The used parameters of the solid are listed in Tab. 15.2.4. The simulation of only one time step is done. The numerical model consists of 766 elements and 426 nodes. It is sketched in Fig. 15.2.15.

symbol	quantity	value
T_0	Initial temperature (before heating)	25°C
q	Heat source	30 W/m ²
ρ	Density of the solid	2.0 t·m ⁻³
E	Young's modulus of the solid	2.5 GPa
ν	Poisson ratio	0.25
α	Thermal expansion	$4.2 \cdot 10^{-5} \text{ K}^{-1}$
κ	Thermal conductivity	$5.5 \text{ W} \cdot \text{m}^{-1} \cdot \text{K}^{-1}$

Table 15.2.4: Used parameters

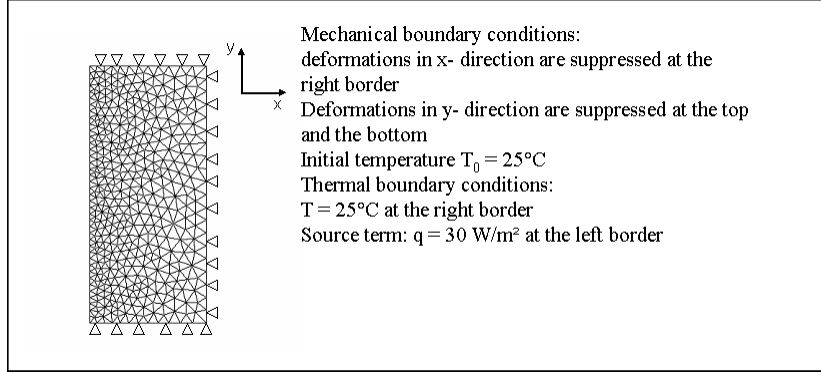


Figure 15.2.15: Calculation model (2 D, axisymmetric) of the hollow cylinder

Evaluation method

For the hollow cylinder with the inner radius $R1$ and the outer radius $R2$ the following analytical solution for radial displacement u_r , stress σ_r and temperature

in dependency on the radius was used (Wang II, 2007).

$$u_r = \frac{q R_1 \beta}{2 \psi \kappa} \cdot r \cdot \left(\ln r - \frac{1}{2} \right) + \frac{A_0}{2} r + \frac{A_1}{r} \quad (15.2.7)$$

$$\begin{aligned} \sigma_r &= \psi \left[-\frac{q R_1 \beta}{2 \psi \kappa} \cdot r \cdot \left(\ln r + \frac{1}{2} \right) + \frac{A_0}{2} - \frac{A_1}{r^2} \right] \\ &\quad + \lambda \left[-\frac{q R_1 \beta}{2 \psi \kappa} \cdot r \cdot \left(\ln r - \frac{1}{2} \right) + \frac{A_0}{2} + \frac{A_1}{r^2} \right] \\ &\quad - \beta \left[\frac{R_1 q}{\kappa} \ln \left(\frac{R_2}{r} \right) + T_0 \right] \end{aligned} \quad (15.2.8)$$

$$T(r) = \frac{R_1 q}{\kappa} \ln \left(\frac{R_2}{r} \right) + T_0 \quad (15.2.9)$$

where

$$\psi = \lambda + 2G \quad \text{and} \quad \beta = \alpha(3\lambda + 2G)$$

with

- λ – Lamé elastic constant
- G – shear modulus
- α – thermal expansion coefficient
- κ – thermal conductivity
- A_0, A_1 – integration constants

At the outer surface of the hollow cylinder (where $r = R_2$) there is no deformation, that means the displacement u_{R2} is zero. Therefore Eqn. 15.2.7 is set equal to zero for this boundary and adapted to A_0 .

$$A_0 = -\frac{2 A_1}{R_2^2} - 2 \cdot B \cdot \left(\ln R_2 - \frac{1}{2} \right) \quad (15.2.10)$$

where

$$B = \frac{q R_1 \beta}{2 \psi \kappa}$$

At the inner surface of the hollow cylinder (where $r = R_1$) no stress is effected by the expansion because this boundary is phreatic. Therefore Eqn. 15.2.8 is set equal to zero and A_1 is calculated by using Eqn. 15.2.11.

$$A_1 = \frac{\beta \left(\frac{R_1 q}{\kappa} \ln \left(\frac{R_2}{r} \right) + T_0 \right) + \lambda B \left(\ln R_1 - \frac{1}{2} \right) + \psi B \left(\ln R_1 + \frac{1}{2} \right) - \left(\frac{\lambda + \psi}{2} \right) 2B \left(\ln R_2 - \frac{1}{2} \right)}{\frac{\lambda - \psi}{R_1^2} - \frac{\lambda + \psi}{2} \cdot \frac{2}{R_1^2}} \quad (15.2.11)$$

After having solved this equation, A_1 is used to calculate A_0 . The results are:

$$A_0 = 5.96 \cdot 10^{-3}$$

$$A_1 = -1.19 \cdot 10^{-1}$$

Results

The results of the analytical equations for stresses, displacements and temperatures are compared to those of the numerical simulation by GeoSys/RockFlow. Fig. 15.2.16 shows the temperature distribution over the radius of the hollow cylinder. In Fig. 15.2.17 displacements in radial direction that are caused by the thermal expansion are depicted. In addition you can find the induced stresses in Fig. 15.2.18. Obviously, with the axisymmetric model a GeoSys/RockFlow simulation generates comprehensible results that meet well the analytic solution.

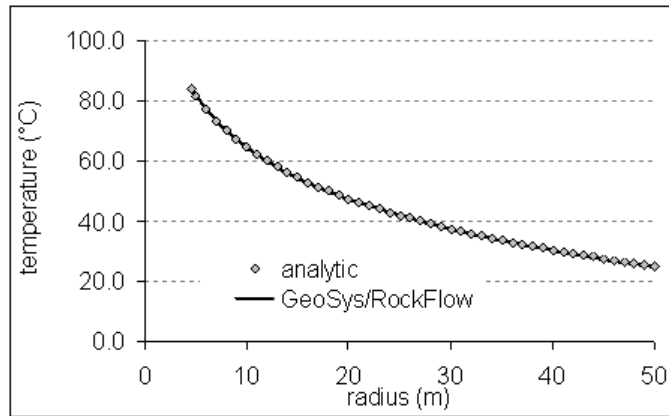


Figure 15.2.16: Temperature distribution over the radius

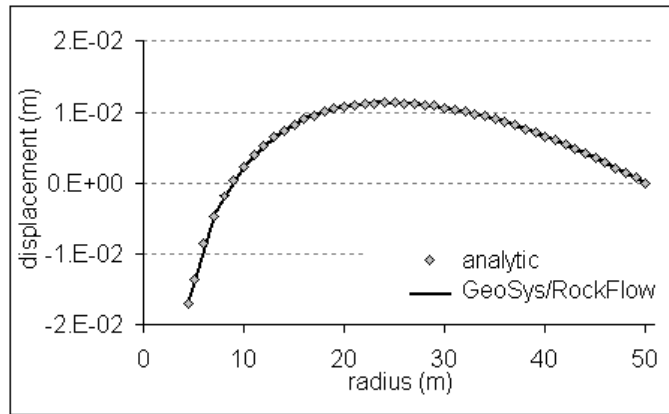


Figure 15.2.17: Displacements in radial direction

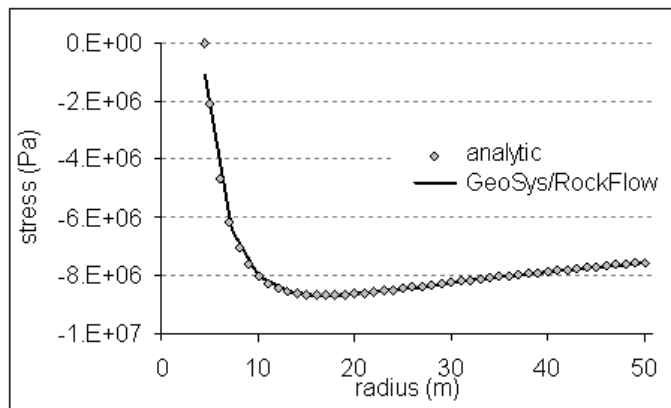


Figure 15.2.18: Stresses in radial direction

Path in the benchmark deposit	Used code	Used version	Date of simulation run
\TM\heating\hollowcylinder\TM_axi	GeoSys/RockFlow	RockFlow 4, rf4-502.exe	July 2007

Chapter 16

Thermo-mechanical consolidation – THM-Processes

16.1 Theory

For thermo-mechanical consolidation, the vapor diffusion is considered. The governing equations, which are essential for the analysis, are detailed hereafter.

16.1.1 Non isothermal flow in porous media

Consider a general case of a flow problem in deformable porous media under the Richard's approximation. With the classical Darcy's law, the large scale water flow \mathbf{q}_w is defined as

$$\mathbf{q}_w = -nS \left(\rho_w \frac{k_{rel}\mathbf{k}}{\mu} (\nabla p - \rho\mathbf{g}) \right) \quad (16.1.1)$$

where S is water saturation, p is the water pressure, ρ is density, n is effective porosity of the media, μ is viscosity of flow, k_{rel} is the relative permeability tensor, \mathbf{g} is the gravity force by density and \mathbf{k} denotes permeability. Meanwhile, we consider vapor flow filled pores due to molecular diffusion, which is coupled with temperature. Similar to what is defined in [127], the vapor flow is given by

$$\mathbf{q}_v = -D_{pv}\nabla P - f_{Tv}D_{Tv}\nabla T \quad (16.1.2)$$

where f_{TV} is a thermal diffusion enhancement factor takes value of 1.0 in the present simulation, D_{pv} and D_{Tv} are diffusion coefficients takes form as

$$\begin{aligned} D_{pv} &= \frac{D_v \rho_v}{\rho_w R T_{abs}} \\ D_{Tv} &= D_v \left(h \frac{\partial \rho_{vs}}{\partial T} - \frac{\rho_v P}{\rho_w R T_{abs}^2} \right) \end{aligned} \quad (16.1.3)$$

with h , the relative humidity according to

$$h = e^{P/\rho_w R T_{abs}} \quad (16.1.4)$$

$R = 461.6 \text{ J/kgK}$, the specific gas constant for water vapour, ρ_{vs} , the saturated vapour density given by

$$\rho_{vs} = 10^{-3} e^{19.891 - 4975/T_{abs}} \quad (16.1.5)$$

and vapour density $\rho_v = h \rho_{vs}$.

The expressions of flow defined in (16.1.1) and (16.1.2) lead the governing equation of flow field in the terms of mass balance equation given by

$$\begin{aligned} n \left[\frac{\rho_w - \rho_v}{\rho_w} \frac{\partial S}{\partial p} + S \beta_p + (1 - S) \frac{\rho_v}{\rho_w^2 R T_{abs}} \right] \frac{\partial p}{\partial t} \\ + \nabla \cdot (\mathbf{q}_w + \mathbf{q}_v) / \rho_w + S \frac{\partial}{\partial t} (\nabla \cdot \mathbf{u}) \\ n \frac{1 - S}{\rho_w} \left(h \frac{\partial \rho_{vs}}{\partial T} + \frac{\rho_v p}{R T_{abs}^2} \right) \frac{\partial T}{\partial t} = 0 \end{aligned} \quad (16.1.6)$$

for any point $\mathbf{x} \in \Omega \in \mathbb{R}^n$ with n the dimension of the real space. In eqn. 16.1.6, β_p is the storitivity. The unknown of eqn. (16.1.6) to be solved are saturation of the phase S , fluid pressure p and the coupling term, i.e. temperature and displacement \mathbf{u} , deduced by solid deformation. The boundary conditions for this problem can be simplified for this Richard's flow model

$$\mathbf{q}_w \cdot \mathbf{n} = q_\Gamma, \forall \mathbf{x} \in \partial\Omega \quad (16.1.7)$$

or Dirchlet type as

$$p = p_\Gamma, \quad S = S_\Gamma, \forall \mathbf{x} \in \partial\Omega \quad (16.1.8)$$

This initial-boundary-value-problem can be solved with the corresponding initial condition of unknowns.

16.1.2 Deformation

Assuming solid grains itself are incompressible, i.e. $d^s \mathbf{u} / d^s t = 0$, deformations in porous media can be described by the momentum balance equation in the terms of stress as

$$\nabla \cdot (\boldsymbol{\sigma} - Sp \mathbf{I} - \alpha \mathbf{I} \Delta T) + \rho \mathbf{g} = 0 \quad (16.1.9)$$

and for bentonite material

$$\nabla \cdot (\boldsymbol{\sigma} - \alpha \mathbf{I} \Delta T) + \rho \mathbf{g} = 0 \quad (16.1.10)$$

and for rock, where $\boldsymbol{\sigma}$ is the effective stress of the porous medium, α is the thermal expansion coefficient, \mathbf{I} is the identity. Density of porous media consists of the portion contributed by liquid l and by the portion contributed of solid as $\rho = n\rho^l + (1 - n)\rho^s$.

The swelling pressure in bentonite is calculated by

$$\boldsymbol{\sigma}_{sw} = S^2 \sigma_{sw}^{max} \mathbf{I}$$

16.1.3 Heat transport

For heat transport problem, we consider the convective transport, i.e. the transport of heat by flow. There are two basic kinds of convection recognized such as *forced convection* and *free convection*. In the former, the velocity of convective motion does not have any impact on the temperature on the fluids and the heat energy transport is forced by the flow movement. In the latter, flow velocities are driven solely by buoyancy effects in the fluid, and these are related to temperature change through the coefficient of thermal expansion. In real ground water systems, there is a mixture of both types of convection. The simple expression of heat flux in forced convection is given by

$$\mathbf{q}_T = -K_e \nabla T + n \sum_{\gamma}^{phase} (\rho^{\gamma} C_p^{\gamma}) T \mathbf{v} \quad (16.1.11)$$

where K_e is the heat conductivity, $\sum_{\gamma}^{phase} (\rho^{\gamma} C_p^{\gamma}) T \mathbf{v}$ is the flux of heat transported by velocity \mathbf{v} per unit area, and across the entire rock face this flux is reduced by the effective porosity, n . With the definition of heat flux (16.1.11), the governing equation of the convective heat transport can be derived for any point $\mathbf{x} \in \Omega \subset \mathbb{R}^n$ as

$$\sum_{\gamma}^{phase} (\rho^{\gamma} C_p^{\gamma}) \frac{\partial T}{\partial t} - \nabla \cdot \mathbf{q}_T + Q_T = 0 \quad (16.1.12)$$

with boundary condition

$$\mathbf{q}_T \cdot \mathbf{n} = q_T|_{\Gamma}, \text{ or } T = T_{\Gamma}, \forall \mathbf{x} \in \partial\Omega \quad (16.1.13)$$

and initial condition

$$T(\mathbf{x}) = T_0(\mathbf{x}), \forall \mathbf{x} \in \Omega \quad (16.1.14)$$

16.1.4 Repository in crystalline rock with unsaturated bentonite buffer: DECOVALEX Task IV - THM1

Problem definition

This example is dealing with fully coupled thermo-hydraulic-mechanical (THM) processes in geotechnical applications. This model is developed in the framework of Task D of DECOVALEX III project (www.decovalex.com). This DECOVALEX test case was designed by [129] for modeling THM coupling processed in FEBEX type nuclear waste repository. Fig. 16.1.1 illustrates the set-up of the model, in which, V_1, \dots, V_6 indicate the observation points.

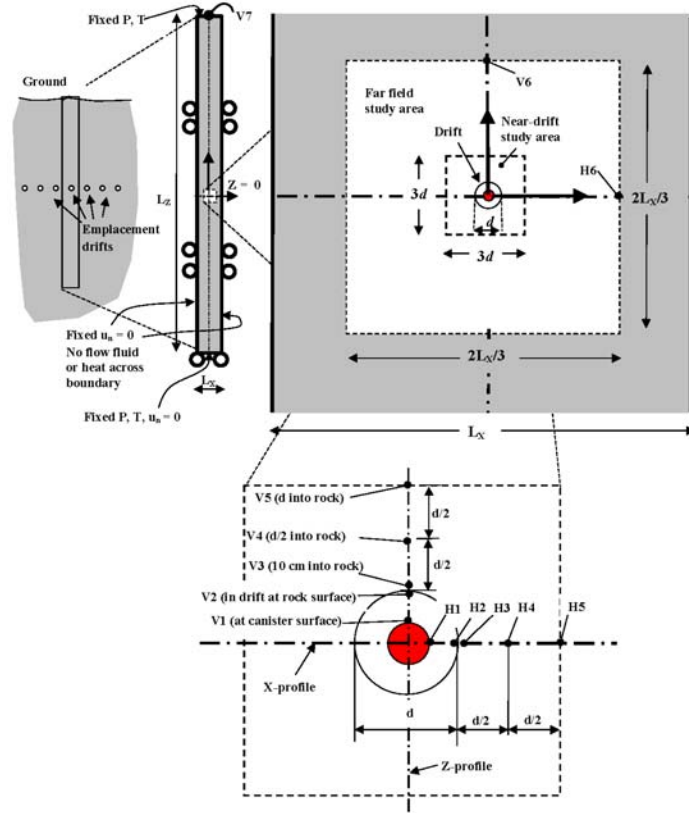


Figure 16.1.1: Model step-up ([129])

A full scale simulation of this problem is given in [130]. The results are compared with that obtained by other research teams[131]. In order to save benchmark running time and keep the original physics of the problem, this benchmark takes a patch cut from the full domain and the results of the full scale simulation at the edge of the patch as boundary condition. The initial stress is obtained by

excavation simulation. The simulation gives results of THM processes till 1000 years. The domain contains that occupied by the waste canister, bentonite buffer and surrounding rock. A triangular mesh of the domain is shown in Fig. 16.1.2.

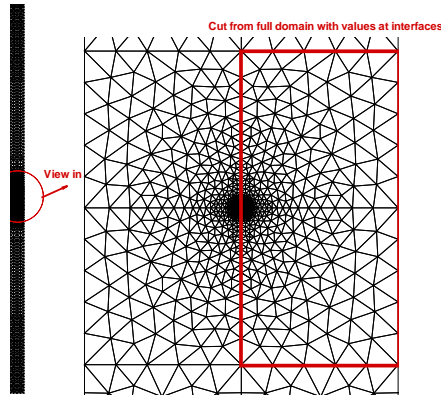


Figure 16.1.2: Near field of DECOVALEX THM1 model

The simulation is split in two phases. In the first phase, an initial state of stress, water pressure and temperature are established by excavation simulation. The operation simulation, that means the THM simulation after having installed the canister and bentonite, is done in a second phase.

The simulation of the excavation phase was done within 4 steps (Wang et al., 2007). At first the initial stress of the whole domain was calculated. Then the released force on the surface of the excavation tunnel was obtained. In a third step the domain with the excavation was analysed with the released force as unique boundary condition. The last step is the combination of step 1 and 3: the stress after excavation. After this the initial conditions of water pressure and temperature were calculated by simulating one time step of the TH coupled process. In the second phase the THM coupled processes in the bentonite and the near field rock mass on the base of the described initial condition set-up are modelled for a period of 1 million years under the assumption that the permeability of the rock mass and bentonite is constant. The initial and boundary conditions that are indicated in Fig. ?? are relevant for the simulation run. To avoid flow within the canister domain the method of activating and deactivating elements was applied. Thus during the flow process the elements of the canister are devoid with a zero Neumann boundary condition on the surface of the canister. The heat power function which represents the source term of heat (due to radioactive decay, Fig. ??) in the canister was given in a graphical form to the simulation teams (Birkholzer et al., 2007).

Initial and Boundary conditions

Values of variables at the cut interfaces of the full scale domain are taken as boundary condition directly (see Fig. 16.1.2 and cf. [130] and [131]).

Material properties

The material parameters for rock mass and bentonite are given in Table 16.1.1 and 16.1.2, respectively.

Parameter	Unit	Value
Density	kg/m^3	2700
Young's modulus	GPa	35
Poisson ratio	-	0.3
Biot's constant	-	1
Thermal expansion coefficient	-	1.0×10^{-5}
Thermal conductivity	W/mK	3
Thermal capacity	J/kgK	900
Porosity	-	0.01
Saturated permeability	m^2	1.0×10^{-17}

Table 16.1.1: Rock Mass

Density	kg/m^3	1600
Young's modulus	MPa	317
Poisson ratio	-	0.35
Biot's constant	-	1
Tortuosity	-	0.8
Porosity	-	0.41
Thermal expansion coefficient	-	1.0×10^{-5}
Thermal conductivity	W/mK	$c_s = 1.38T + 732.5$
Thermal capacity	J/kgK	$\kappa_m = 1.28 - \frac{0.71}{1+e^{10(S_w-0.65)}}$
Saturated permeability	m^2	2.0×10^{-21}

Table 16.1.2: Bentonite

A time-depending heat power function is given in order to describe the heat source condition of the containment. Measured soil-water-characteristic curves are used in order to describe the thermo-hydraulic behaviour. The dependency of capillary pressure as well as relative permeability on liquid saturation for both of rock and bentonite are depicted in Fig. 16.1.3.

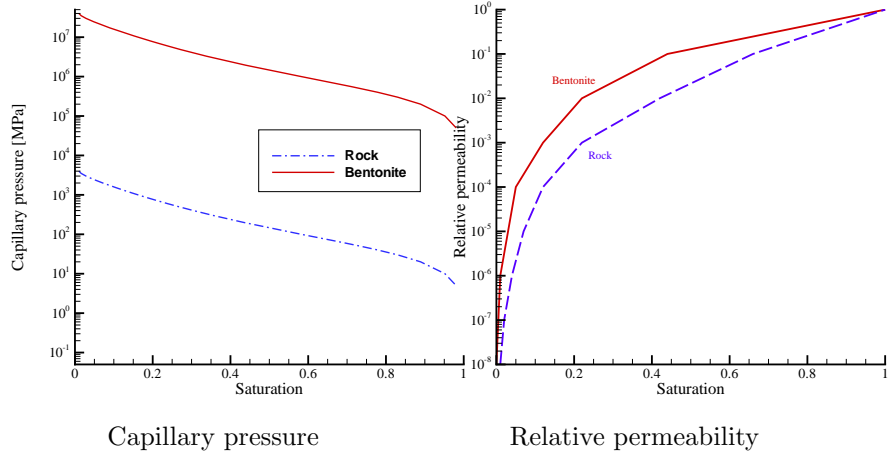


Figure 16.1.3: Capillary pressure - relative permeability - functions

Results

Evaluation method: The numerical results are compared to those of the simulation programmes TOUGH-FLAC (TH processes coupled in TOUGH; M-processes with FLAC) and ROCMAS (THM processes coupled) (Birkholzer et al., 2007).

Fig. 16.1.4 provides the distribution of temperature and saturation after 1 year.

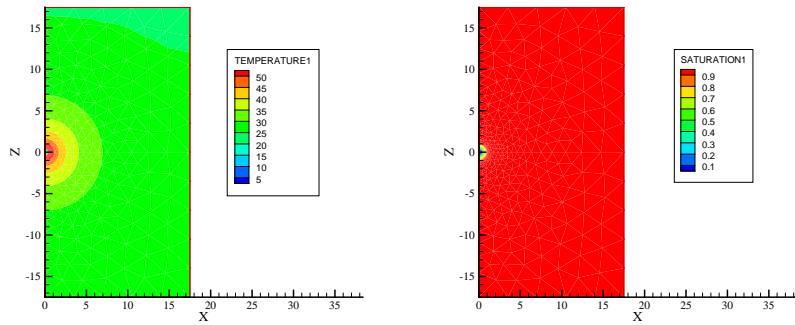


Figure 16.1.4: Distribution of temperature and saturation

Fig. 16.1.5 provides the distribution of vertical stress and fluid velocity after 1 year.

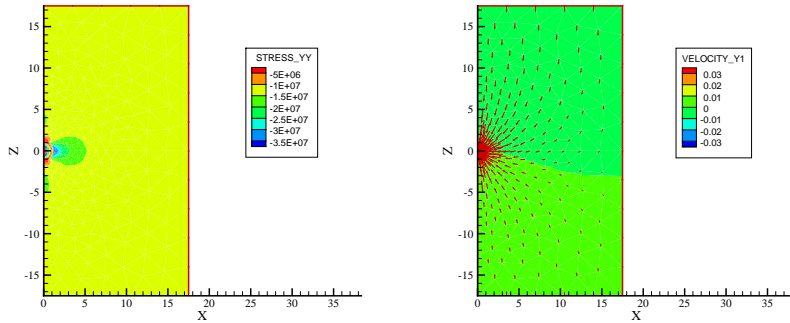


Figure 16.1.5: Distribution of vertical stress and fluid velocity

Fig. 16.1.6 shows the evolution of temperature and saturation at observation points.

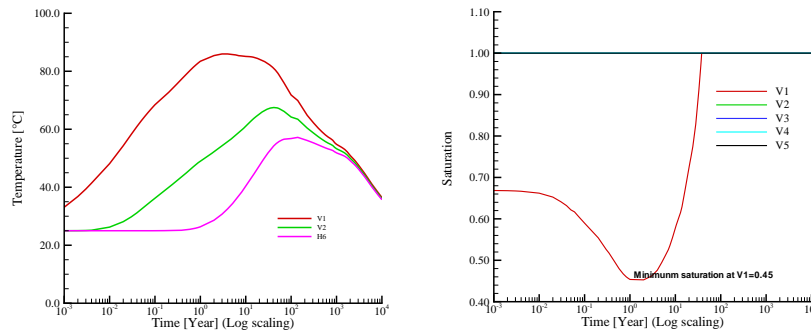


Figure 16.1.6: Evolution of temperature and saturation

Fig. 16.1.7 shows the evolution of horizontal stress and vertical displacement at observation points.

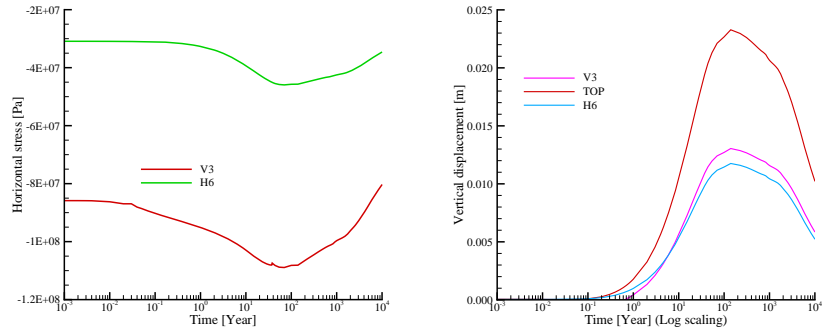


Figure 16.1.7: Evolution of horizontal stress and vertical displacement

Fig. 16.1.8 gives vertical velocity profile along horizontal line cross the canister center.

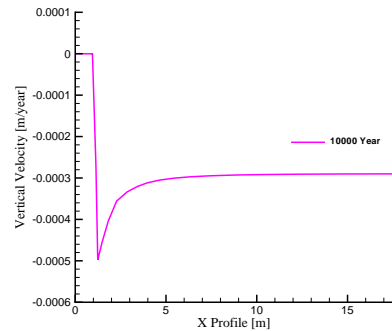


Figure 16.1.8: Vertical velocity profile

The above results agree with that obtain by using a full domain.

Benchmark deposit

Benchmark	Problem type	Path in benchmark deposit
<i>thm-decov</i>	THM	benchmarks\THM\

Chapter 17

Non-isothermal two-phase flow consolidation

17.1 Balance equations

In section 16 we considered non-isothermal flow in an unsaturated deformable porous medium using the Richards model. In this section we treat the partially saturated porous media as multi-phase system composed of constituents with the voids of the solid skeleton filled with water and gas. Similar to what presented in [132], we assume that capillary pressure p_c , gas pressure p^g , temperature T , and solid displacement \mathbf{u} are primary variables to describe the state of the porous media. The general notation for the multi-phase, multi-componental formulation is

$$\rho_k^\gamma \quad (17.1.1)$$

where k is component and γ is phase identification. The governing equations are given hereafter.

17.1.1 Non-isothermal two-phase flow

For liquid water ρ^l , vapor ρ_w^g and the solid skeleton ρ^s , the mass balance is governed by the following equation:

$$\begin{aligned} n(\rho^l - \rho_w^g)(\frac{\partial S^l}{\partial T}\dot{T} + \frac{\partial S^l}{\partial p_c}\dot{p}_c) + n(1 - S^l)(\frac{\partial \rho_w^g}{\partial T}\dot{T} + \frac{\partial \rho_w^g}{\partial p_c}\dot{p}_c) \\ + [\rho^l S^l + (1 - S^l)\rho_w^g]\nabla \dot{\mathbf{u}} - \nabla \left[\rho^g \frac{M_a M_w}{M_g^2} \mathbb{D}_w^g \nabla \left(\frac{p_w^g}{p^g} \right) \right] \\ + \nabla \left[\rho^l \frac{\mathbf{k} k_{rel}^l}{\mu^l} (-\nabla p^g + \nabla p_c + \rho^l \mathbf{g}) \right] \\ + \nabla \left[\rho_w^g \frac{\mathbf{k} k_{rel}^g}{\mu^l} (-\nabla p^g + \rho^g \mathbf{g}) \right] - \beta_T \dot{T} = 0 \end{aligned} \quad (17.1.2)$$

While, for dry air and the solid skeleton, the mass balance equation is given by

$$\begin{aligned} -n\rho_a^g(\frac{\partial S^l}{\partial T}\dot{T} + \frac{\partial S^l}{\partial p_c}\dot{p}_c) + (1 - n)(1 - S^l)\beta^s \rho_a^g \dot{T} \\ n(1 - S^l)(\frac{\partial \rho_a^g}{\partial T}\dot{T} + \frac{\partial \rho_a^g}{\partial p_c}\dot{p}_c + \frac{\partial \rho_a^g}{\partial p^g}\dot{p}^g) \\ + [\rho^l S^l + (1 - S^l)\rho_a^g]\nabla \dot{\mathbf{u}} \\ - \nabla \left[\rho^g \frac{M_a M_w}{M_g^2} \mathbb{D}_a^g \nabla \left(\frac{\partial p_a^g}{\partial p^g} \right) \right] \\ + \nabla \left[\rho_a^g \frac{\mathbf{k} k_{rel}^g}{\mu^l} (-\nabla p^g + \rho^g \mathbf{g}) \right] = 0 \end{aligned} \quad (17.1.3)$$

where ρ^l , ρ_w^g , ρ_a^g are liquid, vapor, air density, respectively; μ^l , μ^g are liquid and gas viscosities, respectively; $S^l = 1 - S^g$ is liquid saturation; M_w , M_a , M_g are water, air, and gas molar masses, respectively; \mathbb{D}_w^g is vapor diffusion coefficient; \mathbf{k} , k_{rel}^l , k_{rel}^g are saturated and relative permeabilities for liquid and gas phases, respectively; \mathbf{g} is gravity acceleration vector and $\beta_T = nS^l\beta^l + nS^g\beta^g + (1-n)\beta^s$ is thermal expansion coefficient of the porous medium.

17.1.2 Deformation

The thermo-poro-elastic deformation process in the porous medium is described by the momentum balance in terms of stress equilibrium:

$$\nabla \cdot (\sigma - \alpha_b \max(p^g - S^l p_c, 0) - \beta_T(T - T_0) \mathbf{I}) + \rho \mathbf{g} = 0 \quad (17.1.4)$$

where σ is effective stress; α_b is Biot coefficient; T_0 is reference temperature and \mathbf{I} is identity tensor.

17.1.3 Heat transport

Heat transport in two-phase flow including storage, advection, diffusion processes in porous medium consisting of liquid, gas, and solid phases is described by following equation

$$c\rho \frac{\partial T}{\partial t} + (c\rho\mathbf{v})^f \cdot \nabla T - \nabla(\kappa \nabla T) = Q_T \quad (17.1.5)$$

where

$$\begin{aligned} c\rho &= nS^l c^l \rho^l + nS^g c^g \rho^g + (1-n)c^s \rho^s \\ (c\rho\mathbf{v})^f &= nS^l c^l \rho^l \mathbf{v}^l + nS^g c^g \rho^g \mathbf{v}^g \\ \kappa &= nS^l \kappa^l + nS^g \kappa^g + (1-n)\kappa^s \end{aligned} \quad (17.1.6)$$

are heat capacity, fluid phase part for heat advection, and thermal heat conductivity of the porous medium, respectively

17.2 Constitutive equations

17.2.1 Density

Liquid density is affected by thermal expansion effects

$$\rho^l(T) = \rho_0^l (1 - \beta_T^l (T - T_0)) \quad (17.2.1)$$

For the gaseous mixture, the ideal gas law is adopted for dry air and water vapour. Applying the Clapeyron equation and Dalton's law to describe the state of dry air, water vapour and moist air yields

$$p^g = p_a^g + p_w^g, \quad \rho^g = \rho_a^g + \rho_w^g, \quad (17.2.2)$$

with

$$\rho_a^g = \frac{M_a p_a^g}{RT}, \quad \rho_w^g = \frac{M_w p_w^g}{RT} \quad (17.2.3)$$

with R , the specific gas constant. The water vapour pressure p_w^g is given by the Kelvin-Laplace equation

$$p_w^g = p^{gws}(T) \exp \left(\frac{p^c M_w}{\rho^l R T} \right) \quad (17.2.4)$$

where p^{gws} is the water vapour saturation pressure. In the current version of GeoSys/Rockflow, we use an empiric formula for p^{gws}

$$p^{gws}(T) = \frac{RT}{M_w} [10^{-3} \exp(19.89 - 4975.9/T)] \quad (17.2.5)$$

17.2.2 Flux of gaseous mixture

Based on the Fick's law, the relative flux of the gaseous mixture can be obtained as

$$\mathbf{v}_a^g = -\frac{M_a M_w}{M_g^2} \mathbb{D}_a^g \nabla \left(\frac{p_a^g}{p^g} \right) \quad (17.2.6)$$

$$= \frac{M_a M_w}{M_g^2} \mathbb{D}_a^g \nabla \left(\frac{p_w^g}{p^g} \right) = -\mathbf{v}_w^g \quad (17.2.7)$$

where molar mass of the gaseous mixture is given by

$$\frac{1}{M_g} = \frac{\rho_a^g}{\rho^g} \frac{1}{M_a} + \frac{\rho_w^g}{\rho^g} \frac{1}{M_w} \quad (17.2.8)$$

17.2.3 Latent heat effects

The amount of latent heat required to vaporize the liquid pore water is given by

$$\Delta(\rho c) = \frac{n \rho^l S^l h_v}{\Delta T} \quad (17.2.9)$$

17.3 Test example

Problem definition

Hereby, we use a simple plane strain biaxial test to verify the implemented scheme. The sample of the test is homogeneous soil with size of 34cm height and 10 cm width. The set-up of the biaxial compression problem as proposed by [132] is shown in Fig. 17.3.1.

Boundary conditions

The bottom of the specimen is placed in a solid foundation. While the top of it is prescribed a vertical displacement 0.12cm. All boundaries are impervious for fluid flow and heat. The simulation starts with initial conditions of $p^c = 10^5$ Pa and $T = 30^\circ\text{C}$ in the whole domain.

Material properties

We assume that the deformation is plastic and the Drucker-Prager model is adopted. All material parameters are given in Table (17.3.1)

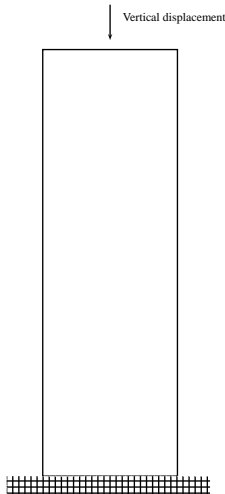


Figure 17.3.1: Plane strain biaxial test

Parameter	Unit	Value
Young's modulus	kPa	3×10^4
Poisson ratio	-	0.4
Parameter α	-	0.326599 (30° friction angle)
Parameter β	-	0.210128 (20° dilatancy angle)
Initial stress σ_0	kPa	29.69 (20 of initial cohesion)
Hardening modulus H	kPa	1000
Permeability	m^2	5×10^{-14}
Solid density	kg/m^3	2000

Table 17.3.1: Material parameters of the plane strain biaxial test

The water content curve, or the capillary-saturation function is depicted in Fig.17.3.2. The relative permeability of water and gas is shown in Fig. 17.3.3.

Results

Fig. 17.3.4 and Fig. 17.3.5 show the distribution of several state variables in the domain after 12 time steps, when the top displacement reaches 0.12cm. Since there is not any other boundary conditions for flow process, the changes of gas/water pressure and water saturation are induced by the mechanical load solely.

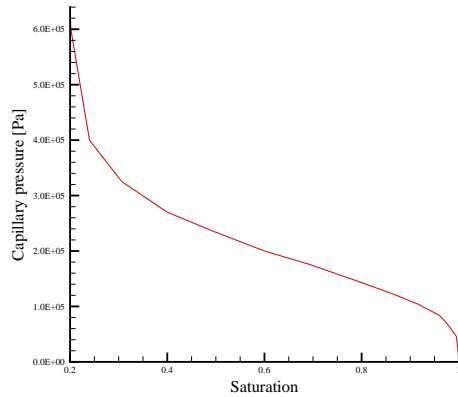


Figure 17.3.2: Capillary saturation function

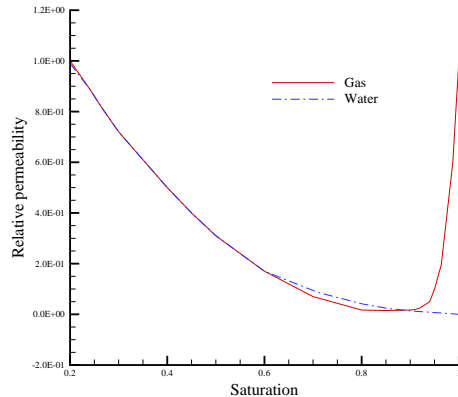


Figure 17.3.3: Vertical reaction of the top

Benchmark deposit

Benchmark	Problem type	Path in benchmark deposit
<i>th2m_quad</i>	TH2M	benchmarks\TH2M\

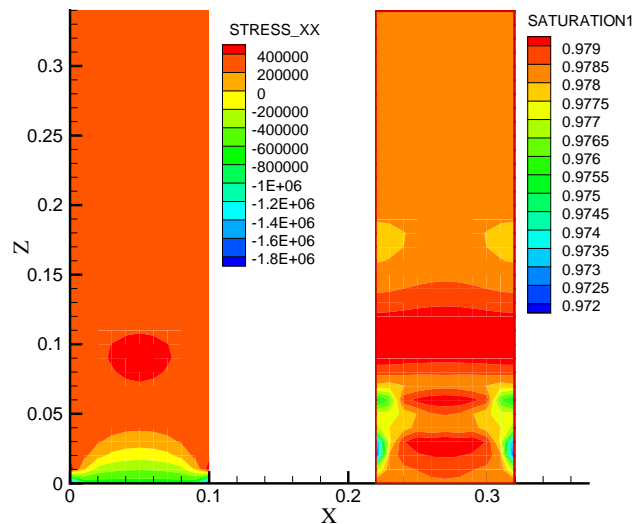


Figure 17.3.4: Distribution of horizontal stress and water saturation.

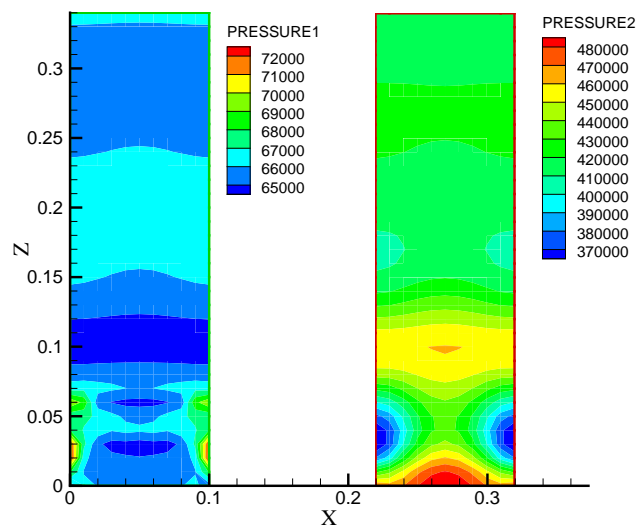


Figure 17.3.5: Distribution of capillary and gas pressure.

Chapter 18

THC-Process

18.1 Theory

The coupling between the simulation of mass transport by GeoSys/RockFlow and the calculation of chemical reactions under equilibrium conditions works by a coupling to the external equilibrium chemical solver PHREEQC. Once the hydraulic and thermal transport has been calculated, the mass transport is solved, the velocity vector being taken from the solution of the hydraulic equations. The concentrations of the species transported and the minerals present are given by the solution of the mass transport equations. The temperature is known from the solution of the heat transport equations. Temperature and concentration of the individual species are passed to PHREEQC (Parkhurst and Appelo 1999). PHREEQC calculates the equilibrium conditions and returns the concentrations of the various phases after reaction (McDermott et al., 2007).

18.2 Repository in crystalline rock with unsaturated bentonite buffer (THC1)

Problem definition

This calculation example, called Task D-THC 1, is done in the framework of the international DECOVALEX project. The model, which is described in the following, is a simplified 1 D benchmark test, which reproduces the processes in a generic repository in saturated crystalline rock where horizontal emplacement tunnels are backfilled with bentonite buffer material (Fig. ??, see chapter 8.1). The horizontal model begins at the left end with the heat source and includes bentonite and granite to the right of this source (Fig. 18.2.1). The model includes simulation of unsaturated flow, heat and mass transport coupled with a consideration of the reactions occurring (McDermott et al., 2007).

Model set-up of the 2 D numerical model

The material parameters for granite and bentonite buffer are given in Tab. ??, but the thermal conductivity of bentonite is set constant with a value of 1.3 W/(m·K) and the heat capacity of bentonite is defined by the following function:

$$c = (1600 \cdot (1.38 \cdot T + 732.5) + 1000 \cdot \Phi \cdot S \cdot 4162) / p.$$

The relationship between capillary pressure and saturation for both of granite and bentonite are depicted in Fig. ???. The relationship between relative permeability and saturation is described in Fig. ???. The model set-up including initial and boundary conditions is given in Fig. 18.2.1. The 1 D model begins from left end ($x = 0.45$ m) to right end ($x = 17.5$ m). It includes bentonite and granite and is discretised into 46 elements. The total simulation time is $1 \cdot 10^6$ years.

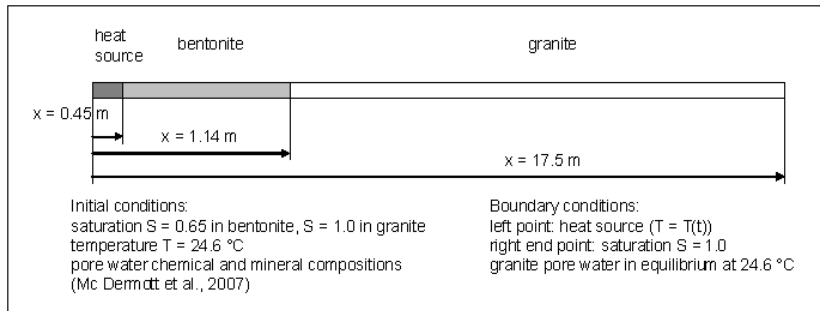


Figure 18.2.1: Calculation model (1 D)

The mineral compositions of granite, bentonite and the related initial as well as equilibrated aqueous chemical compositions of porewater in granite and bentonite are given in McDermott et al. (2007). In granite the minerals Quartz, K-Feldspat, Plagioclase, Annite and Phlogopite are present. In bentonite also Quartz and K-Feldspat can be found, but also the minerals Na-Montmorillonite, Calcite, Dolomite and Pyrite. For mass transport, mass diffusion is included and the coefficients of mass diffusion for all ions and anions are assumed to be the same $1 \cdot 10^{-9}$ m²/s. The minerals are immobile. The geochemically balanced fluid and element concentrations (C, Ca, K, Na, Mg, Cl, Si, Al, S, Fe) are given in McDermott et al. (2007). The geochemical reactions considered in the simulation are aqueous and mineral-solution interactions. The chemical reactions in porewater are taken from the PHREEQC database. The temperature dependence of the reactions was regarded.

Evaluation method

The numerical results of the THC benchmark investigation are compared to those of TOUGH-REACT.

Results

The comparison of the results is presented in Fig. 18.2.2 and Fig. 18.2.3 for the 1000 year simulation case. Significant dissolution and precipitation is predicted at the contact between the different material groups of bentonite and granite. Both models predicted similar mineralogical alterations at the same location and to the same degree (McDermott et al., 2007)

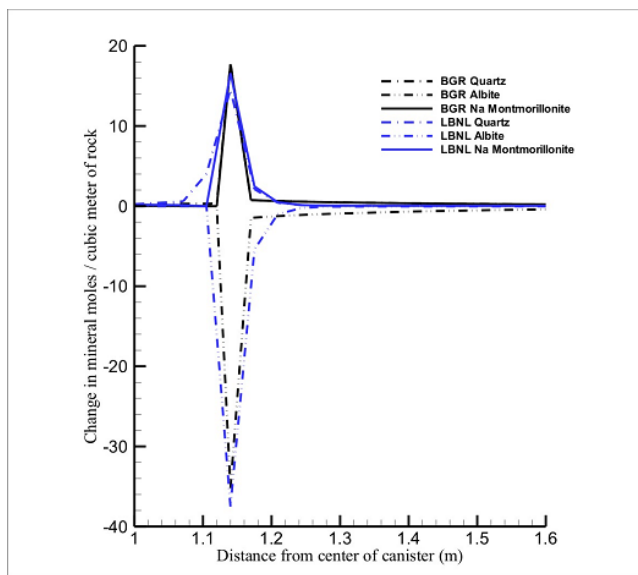


Figure 18.2.2: Deposition of Quartz, Albite and Na-Montmorillonite after 1000 years of emplacement

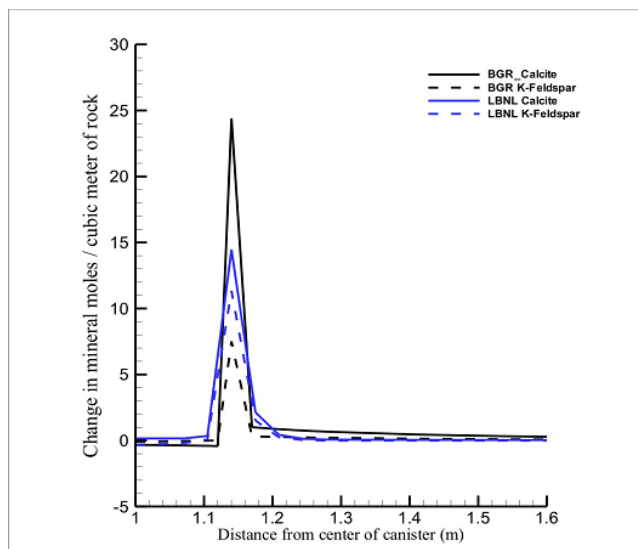


Figure 18.2.3: Deposition of Calcite and K-Feldspat after 1000 years of emplacement

Chapter 19

Density-dependent Flow – HC or THC

19.1 Theory

19.1.1 Governing Equation

The governing equations used for variable density flow consist of three fundamental conservation equations: (i) continuity equation of flow, (ii) momentum equation, and (iii) contaminant transport equation. In addition, these three equations are linked to the equations of the bulk fluid density and the hydrodynamic dispersion equations.

Equation of the Bulk Fluid Density

The linearized equation of the bulk fluid density under an isothermal state was formulated in terms of hydraulic head as,

$$\rho = \rho_0 (1 + \lambda_h (h - h_0) + \lambda_c C) \quad (19.1.1)$$

where h is the hydraulic head, λ is the reference hydraulic head, ρ is the density of fluid, ρ_0 is the reference density of the fluid, λ_h represents the coefficient of compressibility of the fluid associated with the change of the hydraulic head at constant mass fraction of the solute, λ_c is the coefficient of expansivity resulting from the change of the mass concentration of the solute at constant hydraulic head, and C is the relative concentration.

The relationship between density and concentration can also be approximated using other representations such as an exponential function as given by Kolditz et al. [1998]. The equations describing the relationship between density and

other relevant parameters are formulated based on experiments and are approximate relationships.

Another equation for describing the relationship between density and concentration (or mass fraction) is provided by Herbert et al. [1988] and used by Oldenburg and Pruess [1995]. This equation was derived from the assumption that when two liquids are well mixed, the masses or the volumes of respective components are additive. In this study, among these equations which describe the relationship between density and concentration, the linear equation obtained from the experiments is chosen to describe the relation between the bulk fluid density and concentration.

Continuity Equation of Flow

The macroscopic mass balance equation of the fluid averaged over a representative elementary volume (REV) in a porous medium is

$$\frac{\partial(S\phi\rho)}{\partial t} + \nabla \cdot (\phi\rho\vec{v}) = \rho Q_\rho \quad (19.1.2)$$

where S is the saturation ratio, ϕ is the porosity, t is the time, \vec{v} is the fluid velocity vector, and ρQ_ρ is the source term of the fluid mass in an aquifer. Based on Equation 19.1.2, the flow equation for a variably saturated porous medium can be written in terms of hydraulic head and mass concentration,

$$\phi \frac{\partial S}{\partial t} + SS_0^h \frac{\partial h}{\partial t} + S\phi\lambda_C \frac{\partial C}{\partial t} + \nabla \cdot \vec{q} + \lambda_c \vec{q} \cdot \nabla C = Q_\rho \quad (19.1.3)$$

where S_0^h is the specific storativity of a porous medium with respect to hydraulic head change and \vec{q} is the Darcy velocity vector. The head-based flow equation, Equation 19.1.3, has the advantage over pressure-based flow equations because numerically large static pressures may dominate the dynamic pressure differences that cause motion. The resulting pressure-based numerical scheme may therefore operate at less than optimum numerical efficiency. A more efficient way is to write the flow equation in terms of a quantity that can be directly related to the driving forces. Such a quantity is the equivalent freshwater hydraulic head, defined as $h = \frac{p}{\rho_0 g} + z$ [Frind, 1982].

Momentum Equation of Flow (the Darcy Equation) and Dispersive Flux

The momentum balance equation for variable-density fluid flow in a porous medium in terms of hydraulic head can be given as

$$\vec{q} = \phi\vec{v} = -\frac{\hat{k}\rho_0\vec{g}}{\mu} \left(\nabla h + \left(\frac{\rho - \rho_0}{\rho_0} \right) \vec{e} \right) \quad (19.1.4)$$

where \hat{k} is the tensor of permeability of a porous medium and \vec{e} is the unit vector in the gravitational direction. The dispersion tensor can be written as Bear [1979]

$$\hat{D} = \gamma D_m \delta + \alpha_T |v| \delta + (\alpha_L - \alpha_T) \frac{\vec{v}_i \vec{v}_j}{|v|} \quad (19.1.5)$$

where γ is the tortuosity, D_m is the coefficient of molecular diffusion, δ is the Kronecker-delta (unit tensor), α_T is the transverse dispersivity, v is the characteristic value of macroscopic velocity, α_L is the longitudinal dispersivity, and i and j are the velocities in and directions respectively.

Contaminant Transport Equation

The solute transport with a source is governed by the following advection-dispersion equation

$$\frac{\partial(\phi C)}{\partial t} + \nabla \cdot (\phi \vec{v} C) - \nabla \cdot (\phi \hat{D} \cdot \nabla C) = Q_C \quad (19.1.6)$$

where Q_C is the source term of the solute in terms of mass concentration. Ignoring the expansivity resulting from the change of mass concentration λ_C , Equation 19.1.6 can be written as follows

$$\phi \frac{\partial C}{\partial t} + (1 - \phi) \lambda_h C \frac{\partial h}{\partial t} + \phi \vec{v} \cdot \nabla C - \nabla \cdot (\phi \hat{D} \cdot \nabla C) + C Q_\rho = Q_C \quad (19.1.7)$$

Kolditz et al. [1998] defined approximation level of density variations in the mass equations when Equation 19.1.2 and 19.1.6 are expanded.

19.2 The Elder Problem

Benchmark name: *elder*.

Purpose: To verify density-dependent flow such as free convection, seawater intrusion, and possibly enhanced gas recovery with CO₂.

Model description: The elder problem is a good example of free convection phenomena, where the fluid flow is driven purely by the density differences of the fluids. Figure 19.2.1 illustrates the boundary conditions of the Elder problem. Table 19.2.1 presents the specific parameters for the Elder problem used in this application.

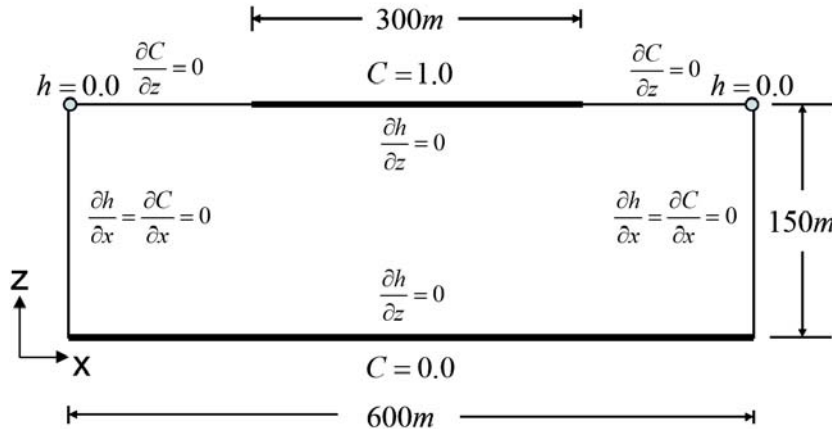


Figure 19.2.1: Boundary conditions of the Elder problem

Symbol	Quantity	Value	Unit
D_m	Molecular diffusion coefficient	3.565e-6	$m^2 s^{-1}$
k	Permeability	4.845e-13	m^2
μ	Dynamic viscosity	10e-6	$kg m^{-1} s^{-1}$
g	Gravitational coefficient	9.81	ms^{-2}
α_L, α_T	Longitudinal and transverse dispersivity	0, 0	m
ϕ	porosity	0.1	—
ρ_0, ρ_s	Density of water and saltwater	(1,1.2)e3	$kg m^{-3}$

Table 19.2.1: Parameters for the Elder problem

Results: The mesh was created with hexahedral elements for further expansion to 3D applications. The grid density level is defined as the l th level that consists of 2^{2l+1} identical square elements. Based on the definition of the grid density, the number of the hexahedral elements is 8192. The isochlor is defined as a ratio of a density difference to the maximum density difference. Figure 19.2.2 shows the numerical results obtained from GeoSys/RockFlow as the solution of the Elder problem

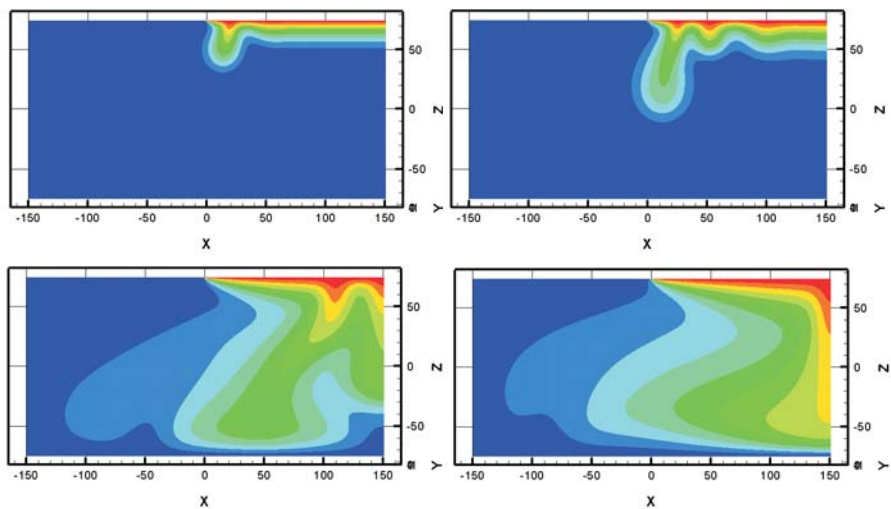


Figure 19.2.2: Isochlors of the Elder problem for 1, 2, 10, and 20 year at regular grid of level 6

Chapter 20

Isothermal two-phase flow – HH-Process

We consider isothermal two-phase flow processes in (sec.20.1). There are several formulations for simulating isothermal two-phase flow systems for instance isothermal two-phase flow system with respect to primary variables: (1) pressure-pressure, (2) pressure-saturation, and (3) saturation-saturation formulation.

20.1 Isothermal two-phase flow

Here we just ignored temperature effect and treated partially saturated sample as isothermal two-phase system composed of constituents with the voids of the solid skeleton filled with two immiscible fluid of two different phase, compressible gas with single component as air and incompressible liquid with single component as water. In the pressure-pressure formulation primary variables are gas pressure p^g , and capillary pressure p^c , whereas in pressure-saturation formulation primary variables are non-wetting phase saturation S_{nw} , and wetting phase pressure p_w .

20.1.1 Mass balance equation

Consider two-phase flow in porous media, e.g liquid (denoted by l) and gas (denoted by g). For each phase in two-phase fluid flow, the mass conservation is given by the following equation:

$$\frac{\partial}{\partial t} (nS^g \rho_k^g + nS^l \rho_k^l) + \nabla \cdot (\mathbf{J}_k^g + \mathbf{J}_k^l) = Q_k \quad (20.1.1)$$

where S is saturation, ρ stands for phase density, n is the porosity, \mathbf{J} is total flux. The subscript k in equation (20.1.1) denotes the components of phase, e.g

air ($k = a$) and water ($k = w$). For any phase $\gamma = (g, l)$, an advection vector $\mathbf{J}_{A_k}^\gamma$ and a diffusion vector $\mathbf{J}_{D_k}^\gamma$ makes up a total flux, i.e

$$\mathbf{J}_k^\gamma = \mathbf{J}_{A_k}^\gamma + \mathbf{J}_{D_k}^\gamma \quad (20.1.2)$$

According to the Darcy's equation, the advective part of the total flux be written as

$$\mathbf{J}_{A_k}^\gamma = -\rho_k^\gamma \frac{\mathbf{k} k_{rel}^\gamma}{\mu^\gamma} (\nabla p^\gamma - \rho^\gamma \mathbf{g}) \quad (20.1.3)$$

where \mathbf{k} is the intrinsic permeability, k_{rel}^γ is the relative permeability of the phase, and μ^γ is the viscosity.

The diffusion part of the total flux is given by Fick's law as

$$\mathbf{J}_{D_k}^\gamma = -n S^\gamma \rho^\gamma \mathbb{D}_k^\gamma \nabla \left(\frac{\rho_w^\gamma}{\rho^\gamma} \right) \quad (20.1.4)$$

where \mathbb{D} is a diffusion parameters in the terms of tensor. Since $\rho^\gamma = \rho_a^\gamma + \rho_w^\gamma$, we have

$$\mathbf{J}_{D_w}^\gamma + \mathbf{J}_{D_a}^\gamma = \mathbf{0} \quad (20.1.5)$$

under the assumption of $\mathbb{D}_a^\gamma = \mathbb{D}_w^\gamma$

Consider water-air mixture. We expand the mass balance equation (20.1.1) with the flux defined in equations (20.1.2) based upon the above equations (20.1.2, 20.1.3, 20.1.4). For water component, the diffusion part of the total flux take the form

$$\mathbf{J}_{D_w}^l = -n S^l \rho^l \mathbb{D}_w^l \nabla \left(\frac{\rho_w^l}{\rho^l} \right), \quad \mathbf{J}_{D_w}^g = -n S^g \rho^g \mathbb{D}_w^g \nabla \left(\frac{\rho_w^g}{\rho^g} \right) \quad (20.1.6)$$

Obviously, $\mathbb{D}_w^l = \mathbf{0}$. Therefore, the mass balance equation for water component can be written as follows

$$\begin{aligned} & \frac{\partial}{\partial t} (n S^g \rho_w^g + n S^l \rho_w^l) - \nabla \cdot \left[\rho_w^l \frac{\mathbf{k} k_{rel}^l}{\mu^l} (\nabla p^l - \rho^l \mathbf{g}) \right] \\ & - \nabla \cdot \left[\rho_w^g \frac{\mathbf{k} k_{rel}^g}{\mu^g} (\nabla p^g - \rho^g \mathbf{g}) \right] - \nabla \cdot \left[n S^g \rho^g \mathbb{D}_w^g \nabla \left(\frac{\rho_w^g}{\rho^g} \right) \right] = Q_w \end{aligned} \quad (20.1.7)$$

Since the capillary pressure p^c is chosen as one of the two unknowns of equation (20.1.1) and $S^g = 1 - S^l$, equation (20.1.7) becomes

$$\begin{aligned} & n(\rho_w^l - \rho_w^g) \frac{\partial S^l}{\partial t} + (1 - S^l)n \frac{\partial \rho_w^g}{\partial t} - \nabla \cdot \left[\rho_w^l \frac{\mathbf{k} k_{rel}^l}{\mu^l} (\nabla(p^g - p^c) - \rho^l \mathbf{g}) \right] \\ & - \nabla \cdot \left[\rho_w^g \frac{\mathbf{k} k_{rel}^g}{\mu^g} (\nabla p^g - \rho^g \mathbf{g}) \right] - \nabla \cdot \left[n S^g \rho^g \mathbb{D}_w^g \nabla \left(\frac{\rho_w^g}{\rho^g} \right) \right] = Q_w \end{aligned} \quad (20.1.8)$$

Similar to the previous procedure, the diffusion part of the total flux of air component can be written as

$$\mathbf{J}_{D_a}^l = -nS^l \rho^l \mathbb{D}_a^l \nabla \left(\frac{\rho_a^l}{\rho^l} \right), \quad \mathbf{J}_{D_a}^a = -nS^g \rho^g \mathbb{D}_a^g \nabla \left(\frac{\rho_a^g}{\rho^g} \right) \quad (20.1.9)$$

The density shift from air component to liquid ρ_a^l is very small and can be omitted. Therefore, we can assume $\mathbf{J}_{D_a}^l \approx 0$. As a consequence, the mass balance equation for air component is derived as:

$$\begin{aligned} & \frac{\partial}{\partial t} (nS^g \rho_a^g) - \\ & \nabla \cdot \left[\rho_a^g \frac{\mathbf{k} k_{rel}^g}{\mu^g} (\nabla p^g - \rho^g \mathbf{g}) \right] - \nabla \cdot \left[nS^g \rho^g \mathbb{D}_a^g \nabla \left(\frac{\rho_a^g}{\rho^g} \right) \right] = Q_a \end{aligned} \quad (20.1.10)$$

Expanding the temporary derivative term of equation (20.1.10) yields

$$\begin{aligned} & -n\rho_a^g \frac{\partial S^l}{\partial t} + (1 - S^l)n \frac{\partial \rho_a^g}{\partial t} - \\ & \nabla \cdot \left[\rho_a^g \frac{\mathbf{k} k_{rel}^g}{\mu^g} (\nabla p^g - \rho^g \mathbf{g}) \right] - \nabla \cdot \left[nS^g \rho^g \mathbb{D}_a^g \nabla \left(\frac{\rho_a^g}{\rho^g} \right) \right] = Q_a \end{aligned} \quad (20.1.11)$$

Mass balance equations (20.1.8) and (20.1.11) are exactly the same as that described in [132].

20.1.2 Pressure-pressure (pp) scheme

Based on the description of the isothermal two-phase flow in (sec.20.1); (20.1.8) and (20.1.11) can be modified in order to get governing equation for isothermal two-phase flow in a porous medium. In this formulation primary variables are gas pressure p^g , and capillary pressure p^c .

Basic equations of the isothermal two-phase flow system:

$$n\rho_w \frac{\partial S_w}{\partial p_c} \dot{p}_c + \nabla \cdot \left[\rho_w \frac{\mathbf{k} k_{relw}}{\mu_w} (-\nabla p^g + \nabla p^c + \rho_w \mathbf{g}) \right] = Q_w \quad (20.1.12)$$

$$\begin{aligned} & -n\rho_a \frac{\partial S_w}{\partial p_c} \dot{p}_c + n(1 - S_w) \left(\frac{\partial \rho_a}{\partial p^g} \dot{p}^g + \frac{\partial \rho_a}{\partial p_c} \dot{p}_c \right) + \\ & \nabla \cdot \left[\rho_a \frac{\mathbf{k} k_{rela}}{\mu_a} (-\nabla p^g + \rho_a \mathbf{g}) \right] = Q_a \end{aligned} \quad (20.1.13)$$

20.1.3 Pressure-saturation (pS) scheme

Based on the description of the isothermal two-phase flow in (sec.20.1); (20.1.8) and (20.1.11) can be modified in order to get governing equation for isothermal two-phase system. This formulation is based on total pressur. Primary variables of this formulation are wetting phase pressure p_w , and non-wetting phase saturation S_{nw} .

In addition, governing equations of the isothermal two-phase system is also based on following assumptions:

- Assumption: Immiscible (fractional) flow
- Macroscopic mass balance equation
 1. Pressure: p_w
 2. Saturation: S_{nw}
- Darcy law: Momentum equation
 1. Mobility by the relation between saturation and relative permeability
- Equation of the state
 1. Density is same for both wetting and non-wetting phase with a constant value

20.1.4 Liakopoulos experiment

Problem definition

This benchmark is based on an experiment by Liakopoulos [133] and is proposed by Lewis and Schrefler [125](pp 167–174). The Liakopoulos test case is already described and used for unsaturated consolidation in section 14.3.2. There you can find the complete problem definition.

The benchmark is simulated with different element types using the pressure-pressure scheme. The grids used in such simulations are illustrated in Fig. 20.1.1.

Results

The temporal evolution of vertical profiles of primary variables capillary and gas pressures are given in Fig. 20.1.2. Fig. 20.1.3 shows the vertical profiles for water saturation as a secondary variale. The results agree well with the findings by Lewis and Schrefler [125].

The results of the element test are depicted in Fig. 20.1.4 for capillary pressure. A comparison if the results between the two-phase flow model and the Richards model used in section 14.3.2 can be seen in Fig. 14.3.4.

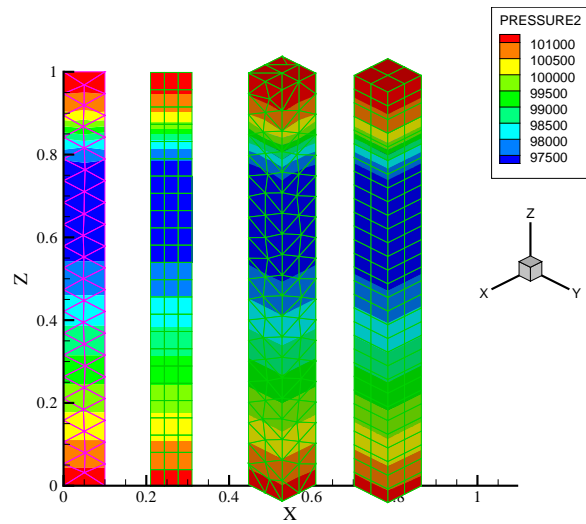


Figure 20.1.1: Grids with different element types for the Liakopoulos benchmark

Property	Symbol	Value	Unit
Porosity	n	—	2.975×10^{-1}
Permeability	κ	m^2	4.5000×10^{-13}
Liquid dynamic viscosity	μ_w	$Pa.s$	1.0000×10^{-3}
Gas dynamic viscosity	μ_a	$Pa.s$	1.8×10^{-5}
Liquid density	ρ_w	$kg.m^{-3}$	1.0000×10^3
Gas density	ρ_a	$kg.m^{-3}$	Ideal Gas Law's
Capillary pressure	p^c	Pa	Experimental Curve
Relative permeability	κ_{relw}	—	Experimental Curve
Relative permeability	κ_{rela}	—	Brook-Corey functions

Table 20.1.1: Material parameters for the Liakopoulos problem.

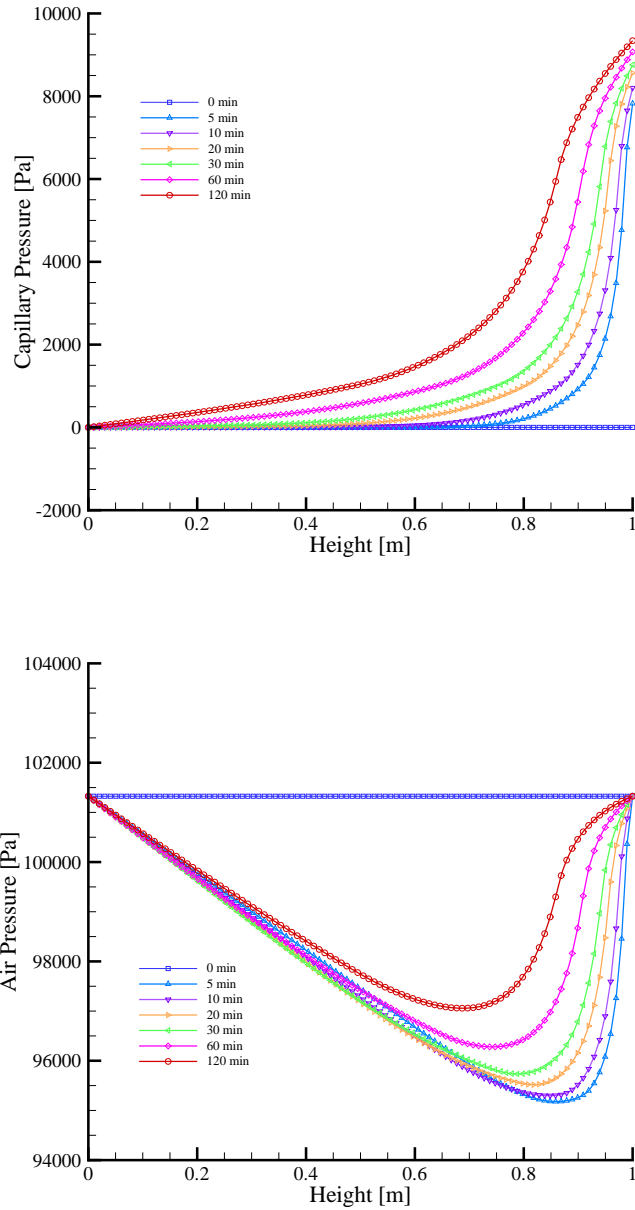


Figure 20.1.2: Vertical profiles of capillary (top) and gas pressures (bottom)

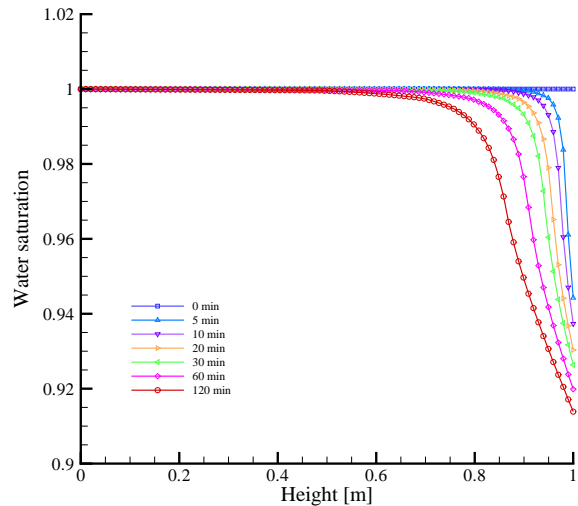


Figure 20.1.3: Water profile of water saturation

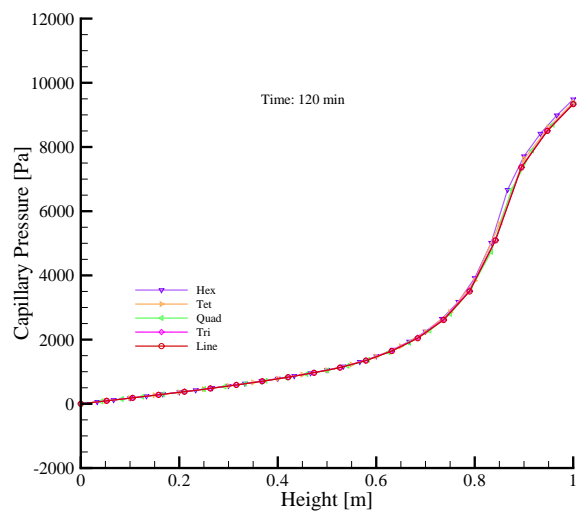


Figure 20.1.4: Results of element test

20.1.5 Buckley-Leverett problem

Theory

Buckley and Leverett [93] developed semi-analytical solution for the displacement of two immiscible fluids in porous media. Assuming constant fluid density (i.e. liquid flow), porosity, and no source/sink terms the fluid mass balance equation can be simplified.

$$n \frac{\partial S^\gamma}{\partial t} = -\nabla \cdot \mathbf{q}^\gamma \quad (20.1.14)$$

Buckley and Leverett derived the following expression

$$\frac{\partial S^l}{\partial f^l} = \frac{q_{tot}}{n} \frac{\Delta t}{\Delta x} \quad (20.1.15)$$

with the fractional flow function $f^\gamma = q^\gamma / q_{tot}$

$$f^1 = \left(1 + \frac{\mu_1}{k_1} \frac{k_2}{\mu_2} \right)^{-1} \quad (20.1.16)$$

1 and 2 are the fluid phase numbers. The position of the shock front separating the two fluid phases can be calculated from the following expression.

$$\Delta x = -\frac{q_{tot}}{n} \frac{\partial f^l}{\partial S^l} \quad (20.1.17)$$

Buckley and Leverett suggested that the capillary pressure is a function of the saturation only. Note that the original Buckley-Leverett considered the water and oil phase flow. Moreover, they assumed that the condition that the derivative of the capillary pressure with respect to the saturation is zero ($dp_{cwo}/dp_{cwo} = 0$) is a sufficient approximation that both gradients of water and oil are equal each other.

$$\frac{\partial p_w}{\partial x} = \frac{\partial p_o}{\partial x} + \frac{\partial p_{cwo}}{\partial x} = \frac{\partial p_o}{\partial x} + \frac{dp_{cwo}}{dS^w} \frac{\partial S^w}{\partial x} = \frac{\partial p_o}{\partial x} \quad (20.1.18)$$

Problem definition

The Buckley Leverett problem is frequently used to test numerical models for the functional relation between relative permeability and saturation. In comparison to the analytical solution, the problem is simplified to describe one fluid displacing the other residing fluid in aquifers or reservoirs. In the derivation of the analytical solution, the effect caused by capillary forces between two fluids is not considered.

A non-wetting phase displaces a wetting phase from left to right. The initial total velocity of the two-phase system is $1.0m/s$. The ratio of the dynamic viscosities is one, residual saturations are zero and the Brooks-Corey function ($\lambda = 2$) is used for the relative permeabilities. A space-time discretization of delta $x = 0.025$ m and delta $t = 0.005$. The total simulation time is $0.4s$.

PS-Global

Saturation equation, the mass conservation equation is converted to the volumetric one by dividing with fluids density.

$$n \frac{\partial S_w}{\partial t} - \nabla \cdot \left(\frac{\mathbf{k} k_{relw}}{\mu_w} (\nabla p_w - \rho_w \mathbf{g}) \right) = q_w \quad (20.1.19)$$

$$n \frac{\partial S_{nw}}{\partial t} - \nabla \cdot \left(\frac{\mathbf{k} k_{relnw}}{\mu_{nw}} (\nabla p_{nw} - \rho_{nw} \mathbf{g}) \right) = q_{nw} \quad (20.1.20)$$

A new BL result is obtained by GeoSys multiphase module that solves in a global-implicit scheme. As shown in the figure, the global-implicit scheme produces more accurate result compared to that obtained by the sequential-coupling scheme. The result has little oscillation and is closer to the analytical solution particularly in the location of the sharp front of the intruding fluid.

One thing important to note is that the global scheme is sensitive to matrix solvers. LIS solver (BiCG with Jacobi preconditioned) works on Windows. However, this iterative solver for this benchmark takes much more time than the PARDISO (a parallel direct solver) that works only on Unix with GeoSys.

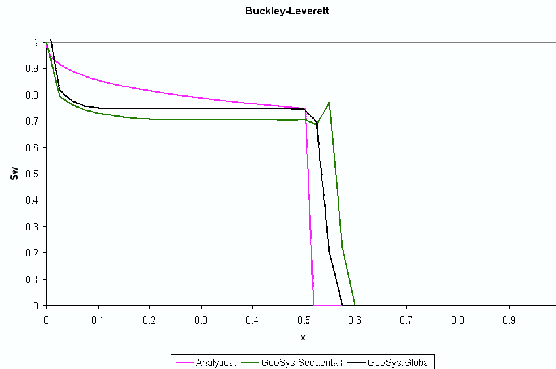


Figure 20.1.5

PS-Sequential

Adding (20.1.19) and (20.1.20) with using the relation $S_{nw} + S_w = 1$ and $p^c(S_w) = p_{nw} - p_w$, we get equation for wetting phase pressure, p_w and non-wetting phase saturation, S_{nw} .

$$-n \frac{\partial S_{nw}}{\partial t} - \nabla \cdot \left(\frac{\mathbf{k} k_{relw}}{\mu_w} (\nabla p_w - \rho_w \mathbf{g}) \right) = q_w \quad (20.1.21)$$

$$\nabla \cdot \left(\frac{\mathbf{k} k_{relw}}{\mu_w} (\nabla p_w - \rho_w \mathbf{g}) \right) + \nabla \cdot \left(\frac{\mathbf{k} k_{relnw}}{\mu_{nw}} (\nabla p_w + p_c - \rho_{nw} \mathbf{g}) \right) + q_w + q_{nw} = 0 \quad (20.1.22)$$

In (20.1.21), non-wetting phase saturation, S_{nw} can be easily solved explicitly with the known pressure obtained from (20.1.22).

The analytical solution for the frontal location of the infiltrating fluid is derived and found there is the discrepancy with previous results (Helming and Huber 1998, Figure 9). In contrast to the previous results, the standard Galerkin-type method does tend to produce overestimated frontal infiltrating locations compared against the analytical solution. This can be explained by the diffusion term of the saturation originally omitted in the BL equation that makes purely advective transport. Handling this purely advective transport in general by the numerical models does introduce the numerical dispersion term naturally, and this added numerical dispersion can be interpreted by the saturation diffusion term.

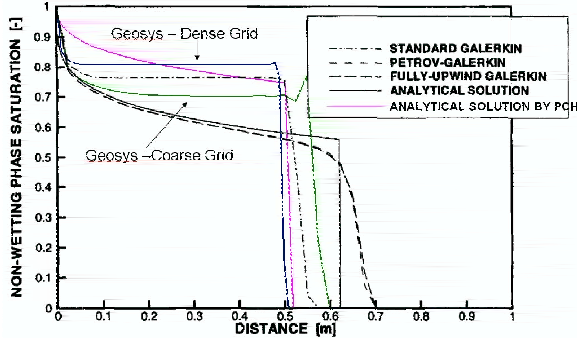


Figure 20.1.6

Problem definition

Buckley and Leverett developed semi-analytical solution for the displacement of two immiscible fluid in porous media. Assume saturated CO_2 displacing H_2O with constant fluid properties.

Results

Here, we show the saturation profile, S_w in Fig. 18.1.7 along 1 m column calculated with line element with space-time discretization of $\delta x = 0.025$ m and $\delta t = 0.005$ s. The total simulation time is 0.4 s; using the total-pressure-based pS-GLOBAL. Based on linear relation between saturation and relative permeability, saturation profile, S_w is shown in Fig. 18.1.8.

Property	Symbol	Value	Unit
Column length	L	m	1.0
Porosity	n	—	2.0×10^{-1}
Permeability	κ	m^2	1.0×10^{-10}
Water dynamic viscosity	μ_w	$Pa.s$	1.0×10^{-3}
Gas dynamic viscosity	μ_{nw}	$Pa.s$	7.0343×10^{-4}
Water density	ρ_w	$kg.m^{-3}$	1.0×10^3
Gas density	ρ_{nw}	$kg.m^{-3}$	7.73×10^2
Capillary pressure	$p^c(S)$	Pa	0
Relative permeability	$\kappa_{rel}(S)$	—	Brook-Corey functions

Table 20.1.2: Material parameters for the BL problem.

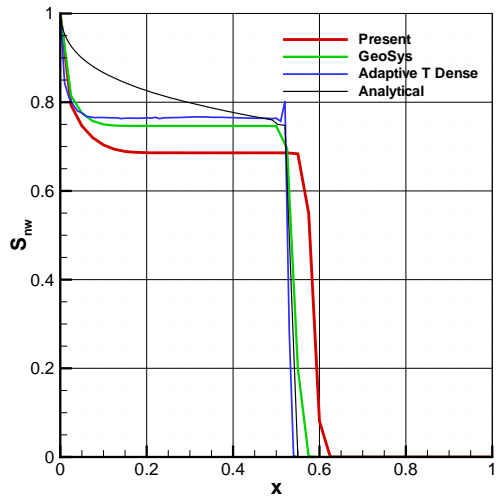


Figure 20.1.7: Saturation profile obtained with present analysis along with others.

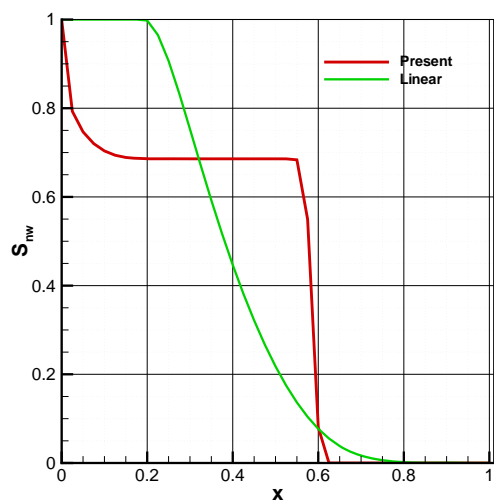


Figure 20.1.8: Saturation profile obtained with present analysis along with linear permeability and saturation relation.

Benchmark deposit

Benchmark	Problem type	Path in benchmark deposit
<i>hm_unsat</i>	HH	MULTIPHASE

20.1.6 McWhorter problem

Theory

It is assumed that the flow of both wetting and non-wetting phases can be adequately described by the Darcy's law if the phases are immiscible and incompressible.

$$n \frac{\partial S^\gamma}{\partial t} + \nabla \cdot \mathbf{q}^\gamma = 0, \gamma = w, nw \quad (20.1.23)$$

$$\mathbf{q}^\gamma = -\mathbf{K} \lambda^\gamma \nabla p^\gamma \quad (20.1.24)$$

where λ_w and λ_{nw} are mobility of wetting and non-wetting fluid. Both phase are linked by the state equation $S_w + S_{nw} = 1$ and $p_c = p_g - p_w$. Here total flux, $\mathbf{q}_t = \mathbf{q}_w + \mathbf{q}_{nw}$ once p_c is function of the S_w .

A formulation that is often used for two phase flow problem is so called fractional flow model. One of the attractive of this formulation is that the model become more accessible to analysis. Subtracting equation (18.1.24) for both phases we have.

$$\mathbf{q}_w = f \mathbf{q}_t - D \frac{\partial S_w}{\partial x} \quad (20.1.25)$$

where

$$f = \frac{1}{1 + \frac{\lambda_{nw}}{\lambda_w}}, \quad D = -\lambda_{nw} f \frac{\partial p_c}{\partial S_w}$$

First term on the right of equation (20.1.25) is dictated by rate at which flux is injected on the boundary and second term represent the addition impelling force due to gradient of capillary pressure. Put equation (20.1.25) in equation (18.1.23) for wetting phase and assume that total flux, \mathbf{q}_t is space invariant.

$$\frac{\partial}{\partial x} \left(D \frac{\partial S_w}{\partial x} \right) - \mathbf{q}_t \frac{\partial f}{\partial S_w} \frac{\partial S_w}{\partial x} = n \frac{\partial S_w}{\partial t} \quad (20.1.26)$$

In the last benchmark (Buckley and Leveret) it is assume that force due to gradient of capillary pressure is very small as consequence of total flux, \mathbf{q}_t is large hence suppressed the second order term in the equation.

Knowing the capillarity effect, model verification need a comparison with an analytical solution based on one by McWhorter and Sunada (1990). They developed an exact quasi-analytical solution of equation (20.1.26) for unidirectional displacement where non-wetting phase by wetting phase using the concept of a fractional flow function.

The fractional flow function is defined as ratio of wetting phase flux, \mathbf{q}_w to the total flux, \mathbf{q}_t . It has shown that this ratio is function of S_w only, when \mathbf{q}_t is inversely related to square root of the time.

Problem definition

The test benchmark problem for capillary effects is formulated as if the instantaneous displacement occurs in one-dimensional horizontal reservoir initially occupied by oil. Solution has been obtained through solving the governing equations (18.1.12) and (18.1.13) by pressure-pressure scheme described in sec (sec.20.1.2). Different from the Buckley-Leverett problem, here flow is governed by capillary force when water saturation at the left end of the horizontal column is kept to be one, while the right end is kept to be no flux at all. So for no source term is accounted.

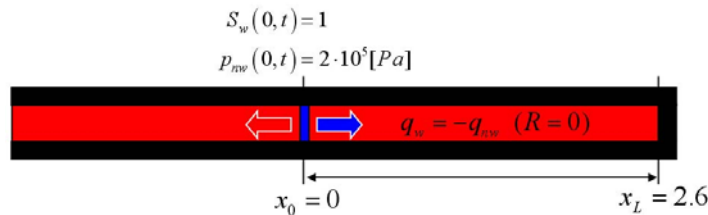


Figure 20.1.9: Schematic of the benchmark formulated to test McWhorter and Sunada's analytical solution.

Results

Based on the above discussion GeoSys produces agreeable solution. Fig. 18.1.10 shows water saturation profile, S_w with a fine grid along with 2.6m long horizontal column for different time steps. Line elements have been used with time and space discretization $\delta t = 0.5s$ and $\delta x = 0.05m$ respectively.

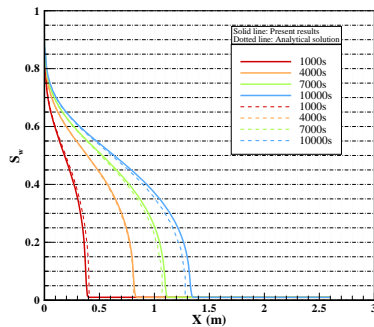


Figure 20.1.10: Water saturation, S_w profile of the present result along with analytical solution based on one by McWhorter.

Here, we have solved exactly same problem using the total-pressure-based saturation model in sequential iterative coupling scheme.

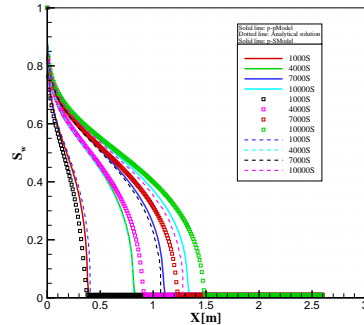


Figure 20.1.11: Water saturation, S_w profile in sequential iterative coupling scheme.

Unlike the pressure-pressure model, one downside for the total-pressure-based saturation model is less accurate for the problems dominated by capillarity (see Fig. 18.1.11). Since the pressure-pressure model directly solves for capillary pressure as a primary variable, the model has an advantage for the capillary related problems. On the other hand, the total-pressure-based saturation model is limited to the problems when dP_c/dS_w is close to zero. The condition for dP_c/dS_w close to zero caused physically in the cases of fractures, shear zones and transitions between heterogeneities.

Property	Symbol	Value	Unit
Column length	L	m	2.6
wetting dynamic viscosity	μ_w	$Pa.s$	1.0×10^{-3}
non-wetting dynamic viscosity	μ_{nw}	$Pa.s$	1.0×10^{-3}
wetting phase density	ρ_w	$kg.m^{-3}$	1.0×10^3
Non-wetting phase density	ρ_{nw}	$kg.m^{-3}$	1.0×10^3
Permeability	K	m^2	1.0×10^{-10}
Porosity	n	--	3.0×10^{-1}
Residual saturation of water	S_{rw}	--	0
Residual saturation of oil	S_{nrw}	--	0
Entry pressure	p_d	Pa	5.0×10^3
Soil distribution index	λ	--	2.0
Capillary pressure	$p^c(S_{eff})$	Pa	Brooks-Corey model
Relative permeability	$\kappa_{rel}(S_{eff})$	--	Brooks-Corey model

Table 20.1.3: Material parameters for the McWhorter problem.

Benchmark deposit

Benchmark	Problem type	Path in benchmark deposit
<i>mcwt</i>	H2	McWhorter

20.1.7 Kueper problem

Theory

The former two benchmarks (Buckley-Leverett and McWorter) used for verification, both schemes are further tested for model validation with the benchmark chosen to test two-phase flow in heterogeneous media. Kueper and Frind (1991) developed the model to simulate their experiment for DNAPL penetration (Kueper et al., 1989). The simultaneous movement of a dense non-wetting phase (DNAPL) through an initially wetting phase (water) saturated heterogeneous porous media may be represented mathematically as a case of two-phase flow. A distinctive feature of the solution is that the primary variables solved for, wetting phase pressure and wetting phase saturation, are both existent throughout the solution domain regardless of whether the non-wetting phase is present.

The continuity equation of each phase (γ) can be defined by

$$\frac{\partial(n\rho^\gamma S^\gamma)}{\partial t} + \nabla \cdot (\rho^\gamma \mathbf{q}^\gamma) = \mathbf{Q}^\gamma, \gamma = w, nw \quad (20.1.27)$$

where n is porosity, S^γ is saturation, ρ^γ is density, \mathbf{Q}^γ is a source or sink term, and \mathbf{q}^γ is the Darcy velocity for phase γ defined by

$$\mathbf{q}^\gamma = -\mathbf{K} \frac{\kappa_r^\gamma}{\mu^\gamma} (\nabla p^\gamma - \rho^\gamma \mathbf{g}), \gamma = w, nw \quad (20.1.28)$$

where κ_r^γ is relative permeability, μ^γ is viscosity, p^γ is pressure for phase γ , \mathbf{K} is intrinsic permeability tensor and \mathbf{g} is the gravitational vector.

Inherently for saturation, the sum of all saturation in pore space is

$$\sum S^\gamma = 1 \quad (20.1.29)$$

Assuming relative preference (i.e., wettability) of the fluid to media exists and it is not negligible, the capillary pressures relation for a two-phase system is defined over representative elementary volume (REV) by

$$p_c = p_{nw} - p_w \quad (20.1.30)$$

where p_c is capillary pressure, p_{nw} is pressure for the non-wetting phase fluid and p_w is the wetting phase fluid.

Problem definition

A $60cm \times 80cm \times 0.6cm$ parallel-plate glass-lined cell was packed with four types of sands and initially fully saturated with water. The configuration of the assembled sand lenses and the two sets of the boundary conditions for the $p_w - S_{nw}$ and $p_c - p_{nw}$ schemes are illustrated in Figure 18.1.12. Concerning to the constitutive relation between relative permeability and saturation and capillary pressure and saturation, they have used the Brooks-Corey model.

Properties of Sands for the Brooks-Corey model are measured experimentally and summarized in table. The numerical solutions obtained from the $p_w - S_{nw}$ scheme and the $p_c - p_{nw}$ scheme for the benchmark Kueper and Frind (1991) are compared against each other in Figure 18.1.13.

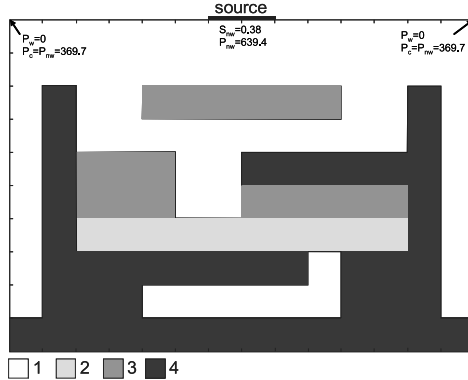


Figure 20.1.12: Configuration of heterogeneous media in parallel-plate cell.

Fluid and medium properties with numerical space and time discretization.

Fluid properties	Unit	Wetting fluid	Non-wetting fluid
Density	$kg \cdot m^{-3}$	1.0×10^3	1.0×10^3
Viscosity	$Pa \cdot s$	1.0×10^{-3}	1.0×10^{-3}
Residual saturation	-	0.0	0.0
Maximum saturation	-	1.0	1.0

Medium properties	Unit	Medium
Δx	m	0.01
Δt	s	100
Porosity	-	0.3
Intrinsic permeability	m^2	1×10^{-10}
Brook-Corey's index	-	2
Entry pressure	Pa	5×10^3

Hydraulic properties of sands for the Brooks-Corey model.

Property	$P_d(\text{Pa})$	$\lambda(-)$	$S_{wr}(-)$	$k(m^2)$	$n(-)$
1	369.73	3.86	0.078	5.04×10^{-10}	0.40
2	434.45	3.51	0.069	2.05×10^{-10}	0.39
3	1323.95	2.49	0.098	5.26×10^{-11}	0.39
4	3246.15	3.30	0.189	8.19×10^{-12}	0.41

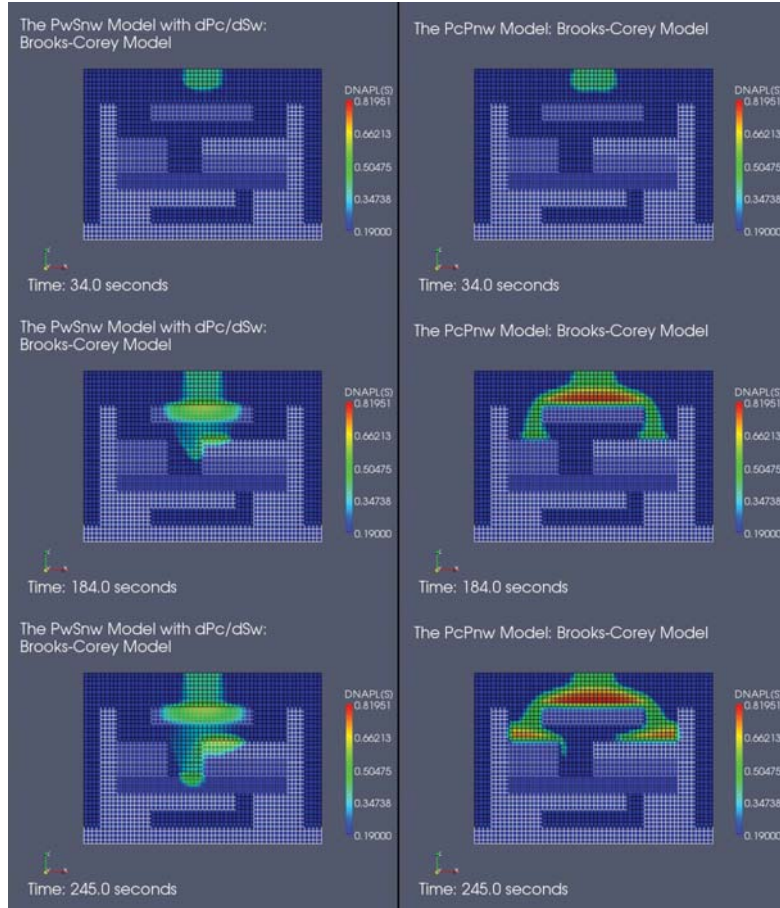


Figure 20.1.13: Comparison of the results obtained from the $p_w - S_{nw}$ and $p_c - p_{nw}$ schemes. The second column shows good agreement with observed distribution of DNAPL of the experiment (Kueper and Frind 1991).

Both schemes produce DNAPL plume propagation physically until the plume reaches to the less previous media under the top medium in the model domain. The striking difference occurs at the interface between these two media. While the $p_w - S_{nw}$ scheme simulates the plume to infiltrate into the less previous medium, the $p_c - p_{nw}$ scheme does the plume to bypass the less previous medium. A similar experiment and simulation comparison against experimental observation are also conducted by Helming and Huber (1998). They have reported unphysical fluid behavior captured by the $p_w - S_{nw}$ scheme, and this phenomenon can be avoided with fully upwind technique (Helming and Huber, 1998).

Benchmark deposit

Benchmark	Problem type	Path in benchmark deposit
<i>Kueper</i>	H2	MULTIPHASE

Appendix A

Fluid property equations

A.1 Viscosity

A.1.1 Carbon dioxide [1]

Equation (4.1.18)

$$\eta(\rho, T) = \eta_0(T) + \Delta\eta(\rho, T) + \Delta\eta_c(\rho, T) \quad (\text{A.1.1})$$

in section 4.1.5 will be explained in the following. The influence of the term $\Delta\eta_c(\rho, T)$ is very low so that it can be neglected ($\Delta\eta_c(\rho, T) = 0$). For the zero-density viscosity $\eta_0(T)$ it can be written

$$\eta_0(T) = \frac{1.00697 T^{\frac{1}{2}}}{\mathfrak{S}_\eta^*(T^*)} \quad (\text{A.1.2})$$

For $\theta_\eta^*(T^*)$ can be set

$$\ln \mathfrak{S}_\eta^*(T^*) = \sum_{i=0}^4 a_i (\ln T^*)^i \quad (\text{A.1.3})$$

and for the reduced temperature T^*

$$T^* = \frac{kT}{\varepsilon} \quad (\text{A.1.4})$$

with $\varepsilon/k = 251.196 \text{ K}$. Values for the coefficient a_i of (A.1.3) are listed in Tab. A.1.1.

Table A.1.1: Values for the coefficient a_i in (A.1.3).

i	a_i
0	0.235 156
1	−0.491 266
2	$5.211 155 \cdot 10^{-2}$
3	$5.347 906 \cdot 10^{-2}$
4	$-1.537 102 \cdot 10^{-2}$

Instead of $\Delta\eta(\rho, T)$ it can be written

$$\Delta\eta(\rho, T) = \sum_{i=1}^n b_i(T) \rho^i, \quad (\text{A.1.5})$$

with

$$b_i = \sum_{j=1}^m \frac{d_{ij}}{T^{*(j-1)}}. \quad (\text{A.1.6})$$

For the coefficient d_{ij} the values are given in Tab. A.1.2.

Table A.1.2: Values for the coefficient d_{ij} in (A.1.6).

d_{ij}	value
d_{11}	$0.407 111 9 \cdot 10^{-2}$
d_{21}	$0.719 803 7 \cdot 10^{-4}$
d_{64}	$0.241 169 7 \cdot 10^{-16}$
d_{81}	$0.297 107 2 \cdot 10^{-22}$
d_{82}	$-0.162 788 8 \cdot 10^{-22}$

A.1.2 Nitrogen [2]

For nitrogen exists the equation

$$\eta(\rho, T) = \eta_0(T) + \eta_{ex}(\rho) \quad (\text{A.1.7})$$

which can be separated in two terms. It can be written for

$$\eta_0(T) = \frac{5}{16} \left[\frac{MkT}{\pi N_A} \right]^{0.5} (\sigma^2 \Omega(T^*))^{-1} \quad (\text{A.1.8})$$

with

$$\ln \Omega(T^*) = \sum_{i=0}^4 A_i (\ln T^*)^i \quad (\text{A.1.9})$$

and

$$T^* = \frac{T k}{\epsilon}. \quad (\text{A.1.10})$$

The adjustable parameters ϵ/k and σ have energy-scaling and length-scaling functions with the weighted least-square fitted values of $\epsilon/k = 100.016\,54\,\text{K}$ and $\sigma = 0.365\,024\,96\,\text{nm}$. In (A.1.8) k represents the Boltzmann's constant, N_A the Avogadro's number and M the molecular weight. For values for A_i in (A.1.9) see Tab. A.1.3.

The term $\eta_{ex}(\rho)$ will be described as

$$\frac{\Delta\eta_{ex}(\rho)}{\eta_c} = \frac{C_1}{\chi - C_2} + \frac{C_1}{C_2} + \sum_{i=3}^5 C_i \chi^{i-2} \quad (\text{A.1.11})$$

where η_c represents the critical viscosity factor and χ is the reduced density with $\chi = \rho/\rho_c$. The values for parameter C_i are listed in Tab. A.1.3.

Table A.1.3: Values for the parameters A_i in (A.1.9) and C_i in (A.1.11).

i	A_i	C_i
0	0.466 49	
1	-0.572 15	-20.099 970
2	0.191 64	3.437 641 6
3	-0.037 08	-14.447 005 1
4	0.002 41	-0.027 766 561
5		-0.216 623 62

A.1.3 Methane [3] and Ethane [4]

For the viscosity of methane and ethane the following equation is given:

$$\eta(\rho, T) = \eta_0(T) + \eta_{ex}(\rho, T). \quad (\text{A.1.12})$$

Instead of $\eta_0(T)$ it can be written:

for methane

$$\eta_0(T) = \frac{5\sqrt{\pi u M_r k T}}{16\pi\sigma^2\Omega^{(2.2)*}(t)} = 10.50 \frac{\sqrt{t}}{\Omega^{(2.2)*}(t)}(t) \text{ } \mu\text{Pa s}, \quad (\text{A.1.13})$$

and for ethane

$$\eta_0(T) = \frac{5\sqrt{\pi u M_r k T}}{16\pi\sigma^2\Omega^{(2.2)*}(t)} = 12.0085 \frac{\sqrt{t}}{\Omega^{(2.2)*}(t)}(t) \text{ } \mu\text{Pa s}. \quad (\text{A.1.14})$$

M_r stands for the molecular mass with $M_{r,Methane} = 16.043\,\text{g/mol}$ and $M_{r,Ethane} = 30.070\,\text{g/mol}$, u for the unified atomic mass unit with $u = 1.660\,540\,2 \cdot 10^{-27}\,\text{kg}$

and k for the Boltzmann constant with $k = 1.380\,658 \cdot 10^{-23} \text{ JK}^{-1}$. The term $\Omega^{(2.2)^*}$ is a function of the reduced temperature $t = kT/\epsilon$ with $\epsilon/k = 174 \text{ K}$. It can be given as

$$\Omega^{(2.2)^*} = \left[\sum_{i=1}^9 C_i t^{[(i-1)/3-1]} \right]^{-1}. \quad (\text{A.1.15})$$

The values for the coefficient C_i in (A.1.15) are shown in Tab. A.1.4.

Table A.1.4: Values for the coefficient C_i in (A.1.15) for both methane and ethane.

i	C_i
1	-3.032 813 828 1
2	16.918 880 086
3	-37.189 364 917
4	41.288 861 858
5	-24.615 921 14
6	8.948 843 096
7	-1.873 924 504 2
8	0.209 661 013 90
9	-9.657 043 7074 $\cdot 10^{-3}$

The term $\eta_{ex}(\rho, T)$ can be expressed

for methane as

$$\begin{aligned} \eta_{ex}(\rho, T) &= \frac{P_c^{\frac{2}{3}} (M_r u)^{\frac{1}{2}}}{(T_c k)^{\frac{1}{6}}} \left[\sum_{i=1}^9 g_i \delta^{r_i} \tau^{s_i} \right] \left[1 + \sum_{i=10}^{11} g_i \delta^{r_i} \tau^{s_i} \right]^{-1} \\ &= 12.149 \left[\sum_{i=1}^9 g_i \delta^{r_i} \tau^{s_i} \right] \left[1 + \sum_{i=10}^{11} g_i \delta^{r_i} \tau^{s_i} \right]^{-1} \mu\text{Pas}, \end{aligned} \quad (\text{A.1.16})$$

and for ethane as

$$\begin{aligned} \eta_{ex}(\rho, T) &= \frac{P_c^{\frac{2}{3}} (M_r u)^{\frac{1}{2}}}{(T_c k)^{\frac{1}{6}}} \left[\sum_{i=1}^9 g_i \delta^{r_i} \tau^{s_i} \right] \left[1 + \sum_{i=10}^{11} g_i \delta^{r_i} \tau^{s_i} \right]^{-1} \\ &= 15.977 \left[\sum_{i=1}^9 g_i \delta^{r_i} \tau^{s_i} \right] \left[1 + \sum_{i=10}^{11} g_i \delta^{r_i} \tau^{s_i} \right]^{-1} \mu\text{Pas}. \end{aligned} \quad (\text{A.1.17})$$

In this context δ is the reduced density with $\delta = \rho/\rho_c$ and τ is the temperature reduced by the critical temperature with $\tau = T_c/T$. The exponents r_i , s_i and the dimensionless fitted coefficient g_i from (A.1.16) and (A.1.17) are given in Tab. A.1.5

Table A.1.5: Values for the exponents r_i , s_i and the coefficient g_i in (A.1.16) and (A.1.17) for excess transport property function.

i	r_i	s_i	methane (A.1.16)	ethane (A.1.17)
			g_i	g_i
1	1	0	0.412 501 37	0.471 770 03
2	1	1	-0.143 909 12	-0.239 503 11
3	2	0	0.103 669 93	0.398 083 01
4	2	1	0.402 874 64	-0.273 433 35
5	2	1.5	-0.249 035 24	0.351 922 60
6	3	0	-0.129 531 31	-0.211 013 08
7	3	2	0.065 757 76	-0.004 785 79
8	4	0	0.025 666 28	0.073 781 29
9	4	1	-0.037 165 26	-0.030 425 255
10	1	0	-0.387 983 41	-0.304 352 86
11	1	1	0.035 338 15	0.001 215 675

A.1.4 Water[5]

The viscosity for water is given in equation

$$\bar{\eta} = \bar{\eta}_0(\bar{T}) \cdot \bar{\eta}_1(\bar{T}, \bar{\rho}) \cdot \bar{\eta}_2(\bar{T}, \bar{\rho}). \quad (\text{A.1.18})$$

In this connection it is used the dimensionless term for temperature T , pressure p , density ρ and viscosity η defined by the overline. They are given in the following:

$$\bar{T} = T/T^*, \quad (\text{A.1.19})$$

$$\bar{p} = p/p^*, \quad (\text{A.1.20})$$

$$\bar{\rho} = \rho/\rho^*, \quad (\text{A.1.21})$$

$$\bar{\eta} = \eta/\eta^*. \quad (\text{A.1.22})$$

In this case the $*$ stands for reference values which agree with the values for the critical point of T , p and ρ . For η the reference constant has no physical significance. The reference values are given in Tab. A.1.6. For pressure p and temperature T are the following ranges given:

$0 < p < p_t$	<i>and</i>	$273.16 \text{ K} \leq T \leq 1173.15 \text{ K}$
$p_t \leq p \leq 300 \text{ MPa}$	<i>and</i>	$T_m(p) \leq T \leq 1173.15 \text{ K}$
$300 \text{ MPa} < p \leq 350 \text{ MPa}$	<i>and</i>	$T_m(p) \leq T \leq 873.15 \text{ K}$
$350 \text{ MPa} < p \leq 500 \text{ MPa}$	<i>and</i>	$T_m(p) \leq T \leq 433.15 \text{ K}$
$500 \text{ MPa} < p \leq 1000 \text{ MPa}$	<i>and</i>	$T_m(p) \leq T \leq 373.15 \text{ K}$

Table A.1.6: Reference values for the variables T , p , ρ and η for (A.1.19) - (A.1.22).

variable	reference value
T^*	647.096 K
p^*	22.064 MPa
ρ^*	$322 \text{ kg} \cdot \text{m}^{-3}$
η^*	$1.00 \cdot 10^{-6} \text{ Pa} \cdot \text{s}$

where p_t is the triple-point pressure and $T_m(p)$ is the pressure-dependent melting temperature.

Based on (A.1.18) it can be written for the viscosity in the dilute-gas limit $\bar{\eta}_0(\bar{T})$

$$\bar{\eta}_0(\bar{T}) = \frac{100\sqrt{\bar{T}}}{\sum_{i=0}^3 \frac{H_i}{\bar{T}^i}} \quad (\text{A.1.23})$$

with the coefficient H_i , whose values are shown in Tab. A.1.7.

Table A.1.7: Values for the coefficient H_i in (A.1.23).

i	H_i
0	1.677 52
1	2.204 62
2	0.636 656 4
3	-0.241 605

The term $\bar{\eta}_1(\bar{T}, \bar{\rho})$ in (A.1.18) represents the contribution to viscosity due to finite density and is given by

$$\bar{\eta}_1(\bar{T}, \bar{\rho}) = \exp \left[\bar{\rho} \sum_{i=0}^5 \left(\frac{1}{\bar{T}} - 1 \right) \sum_{j=0}^6 H_{ij} (\bar{\rho} - 1)^j \right]. \quad (\text{A.1.24})$$

The values for the coefficient H_{ij} are shown in Tab. A.1.8. The coefficients H_{ij} which were omitted from Tab. A.1.8 are identically equal to zero.

The third factor $\bar{\eta}_2(\bar{T}, \bar{\rho})$ in (A.1.18) represents the critical enhancement of the viscosity. It is only significant in a very small region in density and temperature around the critical point. Exactly at the critical point the viscosity is infinite, but the enhancement term contributes an amount greater than 2 % of the full viscosity only within the following boundaries:

$$645.91 \text{ K} < T < 650.77 \text{ K}, \quad 245.8 \text{ kgm}^{-3} < \rho < 405.3 \text{ kgm}^{-3}. \quad (\text{A.1.25})$$

Table A.1.8: Values for coefficients H_{ij} in (A.1.24).

i	j	H_{ij}
0	0	$5.200\,94 \cdot 10^{-1}$
1	0	$8.508\,95 \cdot 10^{-2}$
2	0	$-1.083\,74$
3	0	$-2.895\,55 \cdot 10^{-1}$
0	1	$2.225\,31 \cdot 10^{-1}$
1	1	$9.991\,15 \cdot 10^{-1}$
2	1	$1.887\,97$
3	1	$1.266\,13$
5	1	$1.205\,73 \cdot 10^{-1}$
0	2	$-2.813\,78 \cdot 10^{-1}$
1	2	$-9.068\,51 \cdot 10^{-1}$
2	2	$-7.724\,79 \cdot 10^{-1}$
3	2	$-4.898\,37 \cdot 10^{-1}$
4	2	$-2.570\,40 \cdot 10^{-1}$
0	3	$1.619\,13 \cdot 10^{-1}$
1	3	$2.573\,99 \cdot 10^{-1}$
0	4	$-3.253\,72 \cdot 10^{-2}$
3	4	$6.984\,52 \cdot 10^{-2}$
4	5	$8.721\,02 \cdot 10^{-3}$
3	6	$-4.356\,73 \cdot 10^{-3}$
5	6	$-5.932\,64 \cdot 10^{-4}$

Only within the boundaries of (A.1.25) the critical enhancement is significant. Outside the region given in (A.1.25) the enhancement is less than the uncertainty in the formulation and allows a simplification to reduce complexity and computing time:

$$\bar{\eta}_2 = 1. \quad (\text{A.1.26})$$

For the function $\bar{\eta}_2$ defined for the entire ranges of states it can be referred to [5].

A.1.5 Propane

[?]

For the viscosity of propane exists the equation

$$\eta(\rho, T) = \eta_0(T) + \eta_1(T)\rho + \Delta\eta_h(\rho, T) + \Delta\eta_c(\rho, T). \quad (\text{A.1.27})$$

For the viscosity in the zero-density limit it can be written

$$\eta_0(T) = \frac{0.021\,357(MT)^{\frac{1}{2}}}{\sigma^2 \mathfrak{S}_\eta^*(T^*)}, \quad (\text{A.1.28})$$

whereas M represents the molar mass and σ is a scaling parameter with $\sigma = 0.497\,48 \text{ nm}$. The expression $\ln \mathfrak{S}_\eta^*(T^*)$ can be replaced by

$$\ln \mathfrak{S}_\eta^*(T^*) = \sum_{i=0}^4 a_i (\ln T^*)^i, \quad (\text{A.1.29})$$

and T^* by

$$T^* = \frac{k_B T}{\varepsilon}. \quad (\text{A.1.30})$$

Here ε/k_B is a scaling parameter with $\varepsilon/k_B = 263.88 \text{ K}$. Furthermore the values for the coefficient a_i are shown in Tab. A.1.9.

Table A.1.9: Values for the coefficient b_i in (A.1.35).

i	b_i	a_i
0	-19.572 881	0.251 045 74
1	219.739 99	-0.472 712 38
2	-1015.322 6	
3	2471.012 51	0.060 836 515
4	-3375.171 7	
5	2491.659 7	
6	-787.260 86	
7	14.085 455	
8	-0.346 641 58	

The term $\eta_1(T)\rho$ should be calculated by the following equations:

$$B_\eta^*(T^*) = \sum_{i=0}^6 b_i (T^*)^{-0.25i} + b_i (T^*)^{-2.5} + b_8 (T^*)^{-5.5}, \quad (\text{A.1.31})$$

$$B_\eta^*(T^*) = \frac{B_\eta(T)}{N_A \sigma^3} \quad \longrightarrow \quad B_\eta(T) = B_\eta^*(T^*) N_A \sigma^3, \quad (\text{A.1.32})$$

$$B_\eta(T) = \frac{\eta_1(T)}{\eta_0(T)} \quad \longrightarrow \quad \eta_1(T) = B_\eta(T) \eta_0(T) \quad (\text{A.1.33})$$

whereas B_η represents the viscosity virial coefficient and N_A is the Avogadro's number with $N_A = 6.022\,141\,79 \cdot 10^{23} \text{ mol}^{-1}$. For values of b_i see Tab. A.1.9.

For the third term in (A.1.27) $\Delta\eta_h(\rho, T)$ there exists the following expression, but this is related to the reduced terms of density and temperature $\delta = \rho/\rho_c$ and $\tau = T/T_c$

$$\Delta\eta_h(\delta, \tau) = \sum_{i=2}^5 \sum_{j=0}^2 e_{ij} \frac{\delta^i}{\tau^j} - f_k \left(\frac{\delta}{\delta_0(\tau) - \delta} - \frac{\delta}{\delta_0(\tau)} \right). \quad (\text{A.1.34})$$

with $f_k = 1616.884\,053\,74$ and

$$\delta_0(\tau) = g_1(1 + g_2\tau^{\frac{1}{2}}). \quad (\text{A.1.35})$$

with $g_1 = 2.500\,539\,388\,63$ and $g_2 = 0.860\,516\,059\,264$. For f_k in (A.1.34) there are values given in Tab. A.1.10.

Table A.1.10: Values for the coefficient e_{ij} in (A.1.34).

i	j	e_{ij}
2	0	35.987 303 019 5
2	1	-180.512 188 564
2	2	87.712 488 822 3
3	0	-105.773 052 525
3	1	205.319 740 877
3	2	-129.210 932 610
4	0	58.949 158 775 9
4	1	-129.740 033 100
4	2	76.628 041 997 1
5	0	-9.594 078 684 75
5	1	21.072 698 659 8
5	2	-14.397 196 818 7

The term $\Delta\eta_c(\rho, T)$ is neglectible and is set to zero.

A.2 Thermal conductivity

A.2.1 Carbon Dioxide [6]

For carbon dioxide the following equation exists:

$$\lambda(\rho, T) = \lambda^0(T) + \Delta\lambda(\rho, T) + \Delta_c\lambda(\rho, T). \quad (\text{A.2.1})$$

The term $\Delta_c\lambda(\rho, T)$ is neglectible because of the validity only in a very small region around the critical point. For $\lambda^0(T)$ it can be written

$$\lambda^0(T) = \frac{0.475589(T)^{\frac{1}{2}}(1 + r^2)}{\Omega_\lambda^*(T^*)}. \quad (\text{A.2.2})$$

The term $\Omega_\lambda^*(T^*)$ can be replaced by

$$\Omega_\lambda^*(T^*) = \sum_{i=0}^7 b_i/T^{*i}. \quad (\text{A.2.3})$$

For b_i there are given values shown in Tab. A.2.1. The parameter T^* can be replaced by

$$T^* = \frac{kT}{\epsilon}, \quad (\text{A.2.4})$$

where $\epsilon/k = 251.196 \text{ K}$ with k as the Boltzmann constant $k = 1.380\,658 \cdot 10^{-23} \text{ JK}^{-1}$. For r in (A.2.2) it can be written

Table A.2.1: Values for the coefficient b_i in (A.2.3).

i	b_i	c_i
0	0.422 615 9	
1	0.628 011 5	$2.387\,869 \cdot 10^{-2}$
2	-0.538 766 1	4.350 794
3	0.673 594 1	-10.334 04
4	0.0	7.981 590
5	0.0	-1.940 558
6	-0.436 267 7	
7	0.225 538 8	

$$r = \left(\frac{2c_{int}}{5k} \right)^{1/2}, \quad (\text{A.2.5})$$

where

$$\frac{c_{int}}{k} = 1.0 + e^{-183.5/T} \sum_{i=1}^5 c_i (T/100)^{2-i}. \quad (\text{A.2.6})$$

The values for the coefficient c_i are given in Tab. A.2.1.

A.2.2 Nitrogen [2]

For the thermal conductivity of nitrogen the following equation exists:

$$\lambda(\rho, T) = \lambda_0(T) + \Delta\lambda_R(\rho). \quad (\text{A.2.7})$$

The term $\lambda_0(T)$ stands for the conductivity in the zero-density limit and $\Delta\lambda_R(\rho)$ for the residual thermal conductivity. $\lambda_0(T)$ is given by

$$\lambda_0(T) = \lambda_{tr} + \lambda_{in} \quad (\text{A.2.8})$$

with

$$\lambda_{tr} = -2.5F(1.5 - X_1) \quad (\text{A.2.9})$$

as the part due to the translational energy transfer and

$$\lambda_{in} = FX_2[c_{v0}(T)/(kN_A) + X_1] \quad (\text{A.2.10})$$

as the part due to the internal degrees of freedom of the molecule. Thereby X_1 and X_2 are adjustable parameters with $X_1 = 0.951\,852\,02$ and $X_2 = 1.020\,542\,2$. For F it can be written

$$F = kN_A\eta_0(T)/M. \quad (\text{A.2.11})$$

For η_0 and k , N_A and M see (A.1.8) and the corresponding explanation. The term c_{v0} in (A.2.10) represents the ideal isochoric heat capacity. It can be described by the following equations ((A.2.12)-(A.2.14)):

$$c_{v0} = R(B_i T^{i-4} + \frac{(B_8 UU(D+1))}{D^2}) - 1 \quad (\text{A.2.12})$$

with

$$U = \frac{B_9}{T} \quad (\text{A.2.13})$$

and

$$D = e^U - 1. \quad (\text{A.2.14})$$

The variables B_8 in (A.2.12) and B_9 in (A.2.13) are given with $B_8 = 0.100\,773\,735\,767 \cdot 10^1$ and $B_9 = 0.335\,340\,610 \cdot 10^4$. For the other parameters B_i in (A.2.12) the values are shown in Tab. A.2.2.

Table A.2.2: Values for the parameter B_i in (A.2.12).

i	B_i
1	$-0.837\,079\,888\,737 \cdot 10^3$
2	$0.379\,147\,114\,487 \cdot 10^2$
3	$-0.601\,737\,844\,275$
4	$0.350\,418\,363\,823 \cdot 10^1$
5	$-0.874\,955\,653\,028 \cdot 10^{-5}$
6	$0.148\,968\,607\,239 \cdot 10^{-7}$
7	$-0.256\,370\,354\,277 \cdot 10^{-11}$

The second term $\Delta\lambda_R(\rho)$ in (A.2.7) can be replaced by the following expression:

$$\Delta\lambda_R(\rho)/\lambda_c = \sum_{i=1}^4 C_i \chi^i, \quad (\text{A.2.15})$$

where λ_c is the critical thermal conductivity with $\lambda_c = 4.17$ and $\chi = \rho/\rho_c$ is the reduced density with $\rho_c = 314$. The values for C_i are given in Tab. A.2.3.

A.2.3 Methane [7]

For the thermal conductivity of methane the following equation exists:

$$\lambda = \lambda_0 + (F_0 + F_1\rho)\rho/(1 - F_2\rho) + \lambda_c. \quad (\text{A.2.16})$$

Table A.2.3: Values for C_i in (A.2.15).

i	C_i
1	3.337 354 2
2	0.370 982 51
3	0.899 134 56
4	0.169 725 05

Here the term λ_0 can be replaced by

$$\lambda_0 = 1000\eta_0(C_p^0 - 5R/2)[G_t(1) + G_t(2)\epsilon/kT], \quad (\text{A.2.17})$$

whereas for η_0 it can be referred to (A.1.13) with the corresponding explanations. For the coefficient $G_t(1)$ and $G_t(2)$ are the values given $G_t(1) = 1.346\,953\,698$ and $G_t(2) = -0.325\,467\,775\,3$. For ϵ/k it can be assumed $\epsilon/k = 174\,\text{K}$. The ideal gas specific heat C_p^0 is computed by

$$\frac{C_p^0}{R} = \sum_{n=1}^7 G_i(n)T^{(n-4)} + \frac{G_i(8)u^2e^u}{(e^u - 1)^2} \quad (\text{A.2.18})$$

with

$$u = \frac{G_i(9)}{T}. \quad (\text{A.2.19})$$

For the coefficient $G_i(n)$ are existing the following values, which are shown in Tab. A.2.4. The terms F_0 , F_1 and F_2 in (A.2.16) are given by the following

Table A.2.4: Values for the coefficient $G_i(n)$ in (A.2.18) and (A.2.19).

n	$G_i(n)$
1	-1.804 475 050 7 · 10 ⁶
2	7.742 666 639 3 · 10 ⁴
3	-1.324 165 875 4 · 10 ³
4	1.543 814 959 5 · 10 ¹
5	-5.147 900 525 7 · 10 ⁻²
6	1.080 917 219 6 · 10 ⁻⁴
7	-6.550 178 343 7 · 10 ⁻⁸
8	-6.749 005 617 1
9	3000

expressions:

$$F_0 = \sum_{n=1}^3 E_t(n)T^{(1-n)}, \quad (\text{A.2.20})$$

$$F_1 = \sum_{n=4}^6 E_t(n) T^{(1-n)} \quad (\text{A.2.21})$$

and

$$F_2 = \sum_{n=7}^8 E_t(n) T^{(1-n)}. \quad (\text{A.2.22})$$

For the coefficient $E_t(n)$ in (A.2.20) till (A.2.22) are existing values shown in Tab. A.2.5

Table A.2.5: Values for the coefficient $E_t(n)$ in (A.2.20) till (A.2.22).

n	$E_t(n)$
1	$0.232\,580\,081\,9 \cdot 10^{-2}$
2	$-0.247\,792\,799\,9$
3	$0.388\,059\,371\,3 \cdot 10^2$
4	$-0.157\,951\,914\,6 \cdot 10^{-6}$
5	$0.371\,799\,132\,8 \cdot 10^{-2}$
6	$-0.961\,698\,943\,4$
7	$-0.301\,735\,277\,4 \cdot 10^{-1}$
8	$0.429\,815\,338\,6$

A.2.4 Ethane [4]

The thermal conductivity for ethane is given in the following equation

$$\lambda(\rho, T) = \lambda_0(T) + \lambda_{ex}(\rho, T) + \lambda_{cr}(\rho, T). \quad (\text{A.2.23})$$

For λ_0 it can be written

$$\begin{aligned} \lambda_0(T) &= \frac{\eta_0(T)}{M_r u N_A} \left[\frac{15R}{4} + f_{int}(C_p^{id} - 5R/2) \right] \\ &= 0.276\,505 \eta_0(T) [3.75 - f_{int}(\tau^2 \phi_{\tau\tau}^{id} + 1.5)] \text{ mW} \cdot \text{m}^{-1} \cdot \text{K}^{-1} \end{aligned} \quad (\text{A.2.24})$$

where R represents the Gas constant with $R = 8.314\,472 \text{ J/mol} \cdot \text{K}$, N_A the Avogadro's number with $N_A = 6.022\,141\,79 \cdot 10^{23} \text{ mol}^{-1}$, M_r is the molecular weight and u is the unified atomic mass unit. For η_0 it can be referred to (A.1.14) in section A.1.3. The term C_p^{id} represents the (temperature dependent) ideal gas contribution to the molar isobaric heat capacity. For this and for the term $\tau^2 \phi_{\tau\tau}^{id}$ it is referred to [4]. The expression f_{int} is a dimensionless function describing the energy exchange. It is given as

$$f_{int} = f_1 + \frac{f_2}{t} \quad (\text{A.2.25})$$

with the coefficients $f_1 = 1.710\,414\,7$ and $f_2 = -0.693\,648\,2$.

For the excess thermal conductivity λ_{ex} it can be written

$$\begin{aligned}\lambda_{ex} &= \frac{P_c^{\frac{2}{3}} k^{\frac{5}{6}}}{T_c^{\frac{1}{6}} (M_r u)^{\frac{1}{2}}} \sum_{i=1}^7 j_i \delta^{r_i} \tau^{s_i} \\ &= 4.417\,866 \left[\sum_{i=1}^7 j_i \delta^{r_i} \tau^{s_i} \right] \text{ mW} \cdot \text{m}^{-1} \cdot \text{K}^{-1}\end{aligned}\quad (\text{A.2.26})$$

where k represents the Boltzmann constant with $k = 1.380\,658 \cdot 10^{-23} \text{ JK}^{-1}$. For δ and τ see the comments on (A.1.16) and (A.1.17) in section A.1.3. The values for the coefficients r_i , s_i and j_i are shown in Tab. A.2.6.

Table A.2.6: Values for the coefficients r_i , s_i and j_i from (A.2.26).

i	r_i	s_i	j_i
1	1	0	0.960 843 22
2	2	0	2.750 023 5
3	3	0	-0.026 609 289
4	4	0	-0.078 146 729
5	5	0	0.218 813 39
6	1	1.5	2.384 956 3
7	3	1	-0.751 139 71

For the term $\lambda_{cr}(\rho, T)$ it is given the following equation:

$$\begin{aligned}\lambda_{cr}(\rho, T) &= \frac{\Lambda k T \rho C_p}{6\pi\eta(\rho, T)\xi} F(\rho, T) \\ &= 1.55 \frac{\delta}{\tau} \frac{C_p}{\eta\xi} F(\delta, \tau) \text{ mW} \cdot \text{m}^{-1} \cdot \text{K}^{-1}.\end{aligned}\quad (\text{A.2.27})$$

The constant Λ has the value $\Lambda = 1.01$. The viscosity $\eta(\rho, T)$ is represented in (A.1.12) in section A.1.3. For ξ in (A.2.27) is given

$$\begin{aligned}\xi &= \xi_0 \Gamma_0^{\frac{-\nu}{\gamma}} \left(\frac{P_c}{\rho_c^2} \right)^{\frac{\nu}{\gamma}} \left[\rho \left(\frac{\partial \rho}{\partial P} \Big|_T - \frac{2T_c}{T} \frac{\partial \rho}{\partial P} \Big|_{T=2T_c} \right) \right]^{\frac{\nu}{\gamma}} \\ &= 0.428(\delta\tau)^{0.507} \left[(1 + 2\delta\phi_\delta^r + \delta^2\phi_{\delta\delta}^r)^{-1} - (1 + 2\delta\phi_\delta^r(\frac{1}{2}) + \delta^2\phi_\delta^r(\frac{1}{2}))^{-1} \right]^{0.507} \text{ nm.}\end{aligned}\quad (\text{A.2.28})$$

The critical exponents γ and ν are given with $\gamma = 1.242$ and $\nu = 0.63$. For ξ_0 stands the value $\xi_0 = 0.19 \text{ nm}$ and for Γ_0 stands $\Gamma_0 = 0.0563$. The term F from

(A.2.27) can be written as

$$F = \frac{2}{\pi} \left[e^{-q_D \xi [1 + (q_D \xi)^3 / (3\delta^2)]^{-1}} - 1 + \frac{C_p - C_V}{C_p} \left(\tan^{-1}(q_D \xi) + \frac{C_v}{C_p - C_v} q_D \xi \right) \right] \quad (\text{A.2.29})$$

Here for q_D^{-1} it is given the value $q_D^{-1} = 0.545 \text{ nm}$. For the molar isochoric heat capacity C_v and the molar isobaric heat capacity C_p it is referred to [4].

A.2.5 Propane [?]

For the thermal conductivity of propane exists the equation

$$\lambda(\rho, T) = \lambda_0(T) + \Delta\lambda_r(\rho, T) + \Delta\lambda_c(\rho; T). \quad (\text{A.2.30})$$

The term $\lambda_0(T)$ can be replaced by

$$\lambda_0(T) = A_1 + A_2 \left(\frac{T}{T_c} \right) + A_3 \left(\frac{T}{T_c} \right)^2, \quad (\text{A.2.31})$$

where A_i is a coefficient whose values are shown Tab. A.2.7. For $\Delta\lambda_r(\rho; T)$ it

Table A.2.7: Values for the coefficient A_i in (A.2.31).

i	$A_i [\text{Wm}^{-1}\text{K}^{-1}]$
1	$-1.24778 \cdot 10^{-3}$
2	$8.16371 \cdot 10^{-3}$
3	$1.99374 \cdot 10^{-2}$

can be written

$$\Delta\lambda_r(\rho; T) = \sum_{i=1}^5 \left(B_{i,1} + B_{i,2} \left(\frac{T}{T_c} \right) \right) \left(\frac{\rho}{\rho_c} \right)^i, \quad (\text{A.2.32})$$

with the coefficients B_i whose values are shown in Tab. A.2.8. Instead of $\Delta\lambda_c(\rho; T)$ the following equation can be used

$$\Delta\lambda_c(\rho, T) = \frac{C_1}{C_2 + |\Delta T_c|} \exp[-(C_3 \Delta \rho_c)^2]. \quad (\text{A.2.33})$$

Here ΔT_c and $\Delta \rho_c$ are given as $\Delta T_c = \frac{T}{T_c} - 1$ and $\Delta \rho_c = \frac{\rho}{\rho_c} - 1$. For the values of coefficient C_i see Tab. A.2.9.

Table A.2.8: Values for the coefficients B_i in (A.2.32).

i	$B_i [\text{Wm}^{-1}\text{K}^{-1}]$	
	$B_{i,1}$	$B_{i,2}$
1	$-3.511\,52 \cdot 10^{-2}$	$4.691\,95 \cdot 10^{-2}$
2	$1.708\,90 \cdot 10^{-1}$	$-1.486\,16 \cdot 10^{-1}$
3	$-1.476\,88 \cdot 10^{-3}$	$1.324\,57 \cdot 10^{-1}$
4	$5.192\,83 \cdot 10^{-2}$	$-4.856\,36 \cdot 10^{-2}$
5	$-6.186\,62 \cdot 10^{-3}$	$6.604\,14 \cdot 10^{-3}$

Table A.2.9: Values for the coefficient C_i in (A.2.33).

i	$C_i [\text{Wm}^{-1}\text{K}^{-1}]$
1	$3.664\,86 \cdot 10^{-4}$
2	$-2.216\,96 \cdot 10^{-3}$
3	$2.642\,13 \cdot 10^0$

A.2.6 Water[8]

The thermal conductivity for water is given in equation

$$\bar{\lambda} = \bar{\lambda}_0(\bar{T}) \cdot \bar{\lambda}_1(\bar{T}, \bar{p}) + \bar{\lambda}_2(\bar{T}, \bar{p}). \quad (\text{A.2.34})$$

In this connection it is used the dimensionless term for temperature T , pressure p , density ρ , thermal conductivity λ and the (symmetrized) compressibility $\bar{\chi}_T$ defined by the overline. They are given in the following:

$$\bar{T} = T/T^*, \quad (\text{A.2.35})$$

$$\bar{p} = p/p^*, \quad (\text{A.2.36})$$

$$\bar{\rho} = \rho/\rho^*, \quad (\text{A.2.37})$$

$$\bar{\lambda} = \lambda/\lambda^*, \quad (\text{A.2.38})$$

$$\bar{\chi}_T = \bar{p} \left[\frac{\partial \bar{\rho}}{\partial \bar{p}} \right]_{\bar{T}}^2 \quad (\text{A.2.39})$$

In this case the * stands for reference values which are close to but not identical with the critical constants of T , p and ρ . The reference values are given in Tab. A.2.10. For pressure p and temperature T are the following ranges of

Table A.2.10: Reference values for the variables T , p , ρ and λ .

variable	reference value
T^*	647.226 K
p^*	$22.115 \cdot 10^{-6}$ Pa
ρ^*	$317.763 \text{ kg} \cdot \text{m}^{-3}$
λ^*	$0.4945 \text{ W} \cdot \text{m}^{-1} \cdot \text{K}^{-1}$

validity given:

$$p \leq 400 \text{ MPa} \quad \text{for } 0^\circ\text{C} \leq T \leq 125^\circ\text{C} \quad (\text{A.2.40})$$

$$p \leq 200 \text{ MPa} \quad \text{for } 125^\circ\text{C} < T \leq 250^\circ\text{C} \quad (\text{A.2.41})$$

$$p \leq 150 \text{ MPa} \quad \text{for } 250^\circ\text{C} < T \leq 400^\circ\text{C} \quad (\text{A.2.42})$$

$$p \leq 100 \text{ MPa} \quad \text{for } 400^\circ\text{C} < T \leq 800^\circ\text{C} \quad (\text{A.2.43})$$

Based on (A.2.34) it can be written for the thermal conductivity in the dilute-gas limit $\bar{\lambda}_0(\bar{T})$

$$\bar{\lambda}_0(\bar{T}) = \frac{\sqrt{\bar{T}}}{\sum_{i=0}^3 \frac{L_i}{\bar{T}^i}} \quad (\text{A.2.44})$$

with the coefficient L_i , whose values are shown in Tab. A.2.11.

Table A.2.11: Values for the coefficient L_i in (A.2.44).

i	L_i
0	1.000 000
1	6.978 267
2	2.599 096
3	-0.998 254

The term $\bar{\lambda}_1(\bar{T}, \bar{\rho})$ in (A.2.34) can be written as

$$\bar{\lambda}_1(\bar{T}, \bar{\rho}) = \exp \left[\bar{\rho} \sum_{i=0}^4 \sum_{j=0}^5 L_{ij} \left(\frac{1}{\bar{T}} - 1 \right)^i (\bar{\rho} - 1)^j \right]. \quad (\text{A.2.45})$$

The values for the coefficient L_{ij} in (A.2.45) are shown in Tab. A.2.12.

The term $\bar{\lambda}_2(\bar{T}, \bar{\rho})$ in (A.2.34) accounts for an enhancement of the thermal con-

Table A.2.12: Values for coefficients L_{ij} in (A.2.45).

j	L_{0j}	L_{1j}	L_{2j}	L_{3j}	L_{4j}
0	1.329 304 6	1.701 836 3	5.224 615 8	8.712 767 5	-1.852 599 9
1	-0.404 524 37	-2.215 684 5	-10.124 111	-9.500 061 1	0.934 046 90
2	0.244 094 90	1.651 105 7	4.987 468 7	4.378 660 6	0.
3	0.018 660 751	-0.767 360 02	-0.272 976 94	-0.917 837 82	0.
4	-0.129 610 68	0.372 833 44	-0.430 833 93	0.0	
5	0.044 809 953	-0.112 031 60	0.133 338 49	0.0	

ductivity in the critical region and is defined by

$$\bar{\lambda}_2(\bar{T}, \bar{\rho}) = \frac{(55.071)(0.0013848)}{\bar{\eta}_0(\bar{T}) \cdot \bar{\eta}_1(\bar{T}, \bar{\rho})} \left(\frac{\bar{T}}{\bar{\rho}} \right)^2 \left(\frac{\partial \bar{p}}{\partial \bar{T}} \right)_{\bar{\rho}}^2 \bar{\chi}_T^{0.4678} \bar{\rho}^{\frac{1}{2}} \cdot \exp[-18.66(\bar{T}-1)^2 - (\bar{\rho}-1)^4]. \quad (\text{A.2.46})$$

The functions $\bar{\eta}_0(\bar{T})$ and $\bar{\eta}_1(\bar{T}, \bar{\rho})$ are those defined in (A.1.18) in section A.1.4.

A.3 Free Helmholtz Energy

A.3.1 Theory[9]

All thermodynamic properties of a pure substance can be derived from

$$\frac{f(\rho, T)}{RT} = \phi(\delta, \tau) = \phi^0(\delta, \tau) + \phi^r(\delta, \tau), \quad (\text{A.3.1})$$

where $R = 0.461\,518\,05 \text{ kJ kg}^{-1}\text{K}^{-1}$, $\delta = \rho/\rho_c$ and $\tau = T_c/T$ with $\rho_c = 322 \text{ kg m}^{-3}$ and $T_c = 647.096 \text{ K}$. Thereby it is used the appropriate combination of the ideal-gas part ϕ^0

$$\phi^o = \ln \delta + n_1^o + n_2^o \tau + n_3^o \ln \tau + \sum_{i=4}^8 n_i^o \ln \left[1 - e^{-\gamma_i^o \tau} \right] \quad (\text{A.3.2})$$

and the residual part ϕ^r of the dimensionless Helmholtz free energy and their derivatives

$$\begin{aligned}\phi^r = & \sum_{i=1}^{k_1} n_i \delta^{d_i} \tau^{t_i} + \sum_{i=k_1+1}^{k_2} n_i \delta^{d_i} \tau^{t_i} e^{-\delta^{c_i}} \\ & + \sum_{i=k_2+1}^{k_3} n_i \delta^{d_i} \tau^{t_i} e^{-\alpha_i(\delta-\epsilon_i)^2 - \beta(\tau-\gamma_i)^2} \\ & + \sum_{i=k_3+1}^{k_4} n_i \Delta^{b_i} \delta e^{-C_i(\delta-1)^2 - D_i(\tau-1)^2}.\end{aligned}\quad (\text{A.3.3})$$

with

$$\Delta = \{(1-\tau) + A_i[(\delta-1)^2]^{1/(2\beta_i)}\}^2 + B_i[(\delta-1)^2]^{a_i}. \quad (\text{A.3.4})$$

Relations between thermodynamic properties and ϕ^0 and ϕ^r and their derivatives are summarized in Tab. A.3.1.

Table A.3.1: Relations of thermodynamic properties to the ideal-gas part ϕ^0 and the residual part ϕ^r of the dimensionless Helmholtz free energy and their derivatives.

Property	Relation
pressure	$\frac{p(\delta,\tau)}{\rho RT} = 1 + \delta \phi_\delta^r$
isochoric heat capacity	$\frac{c_v(\delta,\tau)}{R} = -\tau^2(\phi_{\tau\tau}^0 + \phi_{\tau\tau}^r)$
isobaric heat capacity	$\frac{c_p(\delta,\tau)}{R} = -\tau^2(\phi_{\tau\tau}^0 + \phi_{\tau\tau}^r) + \frac{(1+\delta\phi_\delta^r - \delta\tau\phi_{\delta\tau}^r)^2}{1+2\delta\phi_\delta^r + \delta^2\phi_{\delta\delta}^r}$

For the coefficients n_i^0 , γ_i^0 from (A.3.2) and c_i , d_i , t_i , n_i , A_i , B_i , C_i , D_i , a_i , b_i , α_i , β_i , γ_i and ϵ_i from (A.3.3) are existing different values depending from the substances. In the following these values will be presented for some liquides and gases.

A.3.2 Water

For the limit k of the summator in (A.3.3) the following values are given for water:

- $k_1 = 7$
- $k_2 = 51$
- $k_3 = 54$
- $k_4 = 56$.

Table A.3.2: Values for n_i^o and γ_i^o in (A.3.2) for water.

i	n_i^o	γ_i^o
1	-8.320 446 482 01	
2	6.683 210 526 8	
3	3.006 32	
4	0.012 436	1.287 289 67
5	0.973 15	3.537 342 22
6	1.279 50	7.740 737 08
7	0.969 56	9.244 377 96
8	0.248 73	27.507 510 5

Table A.3.3: Values for the coefficients a_i , b_i , A_i , B_i , C_i , D_i , α_i , β_i , γ_i and ϵ_i from (A.3.3) and (A.3.4) for water.

i	a_i	b_i	A_i	B_i	C_i	D_i	α_i	β_i	γ_i	ϵ_i
52							20	150	1.21	1
53							20	150	1.21	1
54							20	250	1.25	1
55	3.5	0.85	0.32	0.2	28	700		0.3		
56	3.5	0.95	0.32	0.2	32	800		0.3		

Table A.3.4: Values for the coefficients n_i , d_i , t_i and c_i from (A.3.3) for water.

i	n_i	d_i	t_i	c_i
1	$1.253\,354\,793\,552\,3 \cdot 10^{-2}$	1	-0.5	
2	7.895 763 472 282 8	1	0.875	
3	-8.780 320 330 356 1	1	1	
4	3.180 250 934 541 8 $\cdot 10^{-1}$	2	0.5	
5	-2.614 553 385 935 8 $\cdot 10^{-1}$	2	0.75	
6	-7.819 975 168 798 1 $\cdot 10^{-3}$	3	0.375	
7	8.808 949 310 213 4 $\cdot 10^{-3}$	4	1	
8	-6.685 657 230 796 5 $\cdot 10^{-1}$	1	4	1
9	2.043 381 095 096 5 $\cdot 10^{-1}$	1	6	1
10	-6.621 260 503 968 7 $\cdot 10^{-5}$	1	12	1
11	-1.923 272 115 600 2 $\cdot 10^{-1}$	2	1	1
12	-2.570 904 300 343 8 $\cdot 10^{-1}$	2	5	1
14	-4.009 282 892 580 7 $\cdot 10^{-2}$	4	2	1
15	3.934 342 260 325 4 $\cdot 10^{-7}$	4	13	1
16	-7.594 137 708 814 4 $\cdot 10^{-6}$	5	9	1
17	5.625 097 935 188 8 $\cdot 10^{-4}$	7	3	1
18	-1.560 865 225 713 5 $\cdot 10^{-5}$	9	4	1
19	1.153 799 642 295 1 $\cdot 10^{-9}$	10	11	1
20	3.658 216 514 420 4 $\cdot 10^{-7}$	11	4	1
21	-1.325 118 007 466 8 $\cdot 10^{-12}$	13	13	1
22	-6.263 958 691 245 4 $\cdot 10^{-10}$	15	1	1
23	-1.079 360 090 893 2 $\cdot 10^{-1}$	1	7	2
24	1.761 149 100 875 2 $\cdot 10^{-2}$	2	1	2
25	2.213 229 516 754 6 $\cdot 10^{-1}$	2	9	2
26	-4.024 766 976 352 8 $\cdot 10^{-1}$	2	10	2
27	5.808 339 998 575 9 $\cdot 10^{-1}$	3	10	2
28	4.996 914 699 080 6 $\cdot 10^{-3}$	4	3	2
29	-3.135 870 071 254 9 $\cdot 10^{-2}$	4	7	2
30	-7.431 592 971 034 1 $\cdot 10^{-1}$	4	10	2
31	4.780 732 991 548 0 $\cdot 10^{-1}$	5	10	2
32	2.052 794 089 594 8 $\cdot 10^{-2}$	6	6	2
33	-1.363 643 511 034 3 $\cdot 10^{-1}$	6	10	2
34	1.418 063 440 061 7 $\cdot 10^{-2}$	7	10	2
35	8.332 650 488 071 3 $\cdot 10^{-3}$	9	1	2
36	-2.905 233 600 958 5 $\cdot 10^{-2}$	9	2	2
37	3.861 508 557 420 6 $\cdot 10^{-2}$	9	3	2
38	-2.039 348 651 370 4 $\cdot 10^{-2}$	9	4	2
39	-1.655 405 006 373 4 $\cdot 10^{-3}$	9	8	2
40	1.995 557 197 954 1 $\cdot 10^{-3}$	10	6	2
41	1.587 030 832 415 7 $\cdot 10^{-4}$	10	9	2
42	-1.638 856 834 253 0 $\cdot 10^{-5}$	12	8	2
43	4.361 361 572 381 1 $\cdot 10^{-2}$	3	16	3
44	3.499 400 546 376 5 $\cdot 10^{-2}$	4	22	3
45	-7.678 819 784 462 1 $\cdot 10^{-2}$	4	23	3
46	2.244 627 733 200 6 $\cdot 10^{-2}$	5	23	3
47	-6.268 971 041 468 5 $\cdot 10^{-5}$	14	10	4
48	-5.571 111 856 564 5 $\cdot 10^{-10}$	3	50	6
49	-1.990 571 835 440 8 $\cdot 10^{-1}$	6	44	6
50	3.177 749 733 073 8 $\cdot 10^{-1}$	6	46	6
51	-1.184 118 242 598 1 $\cdot 10^{-1}$	6	50	6
52	-3.130 626 032 343 5 $\cdot 10^1$	3	0	
53	3.154 614 023 778 1 $\cdot 10^1$	3	1	
54	-2.521 315 434 169 5 $\cdot 10^3$	3	4	
55	-1.487 464 085 672 4 $\cdot 10^{-1}$			
56	3.180 611 087 844 4 $\cdot 10^{-1}$			

A.3.3 Carbon Dioxide

For the limit k of the summator in (A.3.3) the following values are given for carbon dioxide:

- $k_1 = 7$
- $k_2 = 34$
- $k_3 = 39$
- $k_4 = 42$.

Table A.3.6: Values for n_i^o and γ_i^o in (A.3.2) for carbon dioxide.

i	n_i^o	γ_i^o
1	8.373 044 56	
2	-3.704 543 04	
3	2.5	
4	1.994 270 42	3.151 63
5	0.621 052 48	6.111 9
6	0.411 952 93	6.777 08
7	1.040 289 22	11.323 84
8	0.083 276 78	27.087 92

Table A.3.7: Values for the coefficients a_i , b_i , A_i , B_i , C_i , D_i , α_i , β_i , γ_i and ε_i from (A.3.3) and (A.3.4) for carbon dioxide.

i	a_i	b_i	A_i	B_i	C_i	D_i	α_i	β_i	γ_i	ε_i
35							25	325	1.16	1
36							25	300	1.19	1
37							25	300	1.19	1
38							15	275	1.25	1
39							20	275	1.22	1
40	3.5	0.875	0.7	0.3	10	275		0.3		
41	3.5	0.925	0.7	0.3	10	275		0.3		
42	3	0.875	0.7	1	12.5	275		0.3		

Table A.3.8: Values for the coefficients n_i , d_i , t_i and c_i from (A.3.3) for carbon dioxide.

i	n_i	d_i	t_i	c_i
1	$3.885\,682\,320\,316\,1 \cdot 10^{-1}$	1	0	
2	$2.938\,547\,594\,274\,0$	1	0.75	
3	$-5.586\,718\,853\,493\,4$	1	1	
4	$-7.675\,319\,959\,247\,7 \cdot 10^{-1}$	1	2	
5	$3.172\,900\,558\,041\,6 \cdot 10^{-1}$	2	0.75	
6	$5.480\,331\,589\,776\,7 \cdot 10^{-1}$	2	2	
7	$1.227\,941\,122\,033\,5 \cdot 10^{-1}$	3	0.75	
8	$2.165\,896\,154\,322\,0$	1	1.5	1
9	$1.584\,173\,510\,972\,4$	2	1.5	1
10	$-2.313\,270\,540\,550\,3 \cdot 10^{-1}$	4	2.5	1
11	$5.811\,691\,643\,143\,6 \cdot 10^{-2}$	5	0	1
12	$-5.536\,913\,720\,538\,2 \cdot 10^{-1}$	5	1.5	1
13	$4.894\,661\,590\,942\,2 \cdot 10^{-1}$	5	2	1
14	$-2.427\,573\,984\,350\,1 \cdot 10^{-2}$	6	0	1
15	$6.249\,479\,050\,167\,8 \cdot 10^{-2}$	6	1	1
16	$-1.217\,586\,022\,524\,6 \cdot 10^{-1}$	6	2	1
17	$-3.705\,568\,527\,008\,6 \cdot 10^{-1}$	1	3	2
18	$-1.677\,587\,970\,042\,6 \cdot 10^{-2}$	1	6	2
19	$-1.196\,073\,663\,798\,7 \cdot 10^{-1}$	4	3	2
20	$-4.561\,936\,250\,877\,8 \cdot 10^{-2}$	4	6	2
22	$-7.442\,772\,713\,205\,2 \cdot 10^{-3}$	7	6	2
23	$-1.739\,570\,490\,243\,2 \cdot 10^{-3}$	8	0	2
24	$-2.181\,012\,128\,952\,7 \cdot 10^{-2}$	2	7	3
26	$-3.744\,013\,342\,346\,3 \cdot 10^{-2}$	3	16	3
27	$1.433\,871\,575\,687\,8 \cdot 10^{-1}$	5	22	4
28	$-1.349\,196\,908\,328\,6 \cdot 10^{-1}$	5	24	4
29	$-2.315\,122\,505\,348\,0 \cdot 10^{-2}$	6	16	4
31	$2.105\,832\,197\,294\,0 \cdot 10^{-3}$	8	8	4
32	$-3.395\,851\,902\,636\,8 \cdot 10^{-4}$	10	2	4
33	$5.599\,365\,177\,159\,2 \cdot 10^{-3}$	4	28	5
34	$-3.033\,511\,805\,564\,6 \cdot 10^{-4}$	8	14	6
35	$-2.136\,548\,868\,832\,0 \cdot 10^2$	2	1	
36	$2.664\,156\,914\,927\,2 \cdot 10^4$	2	0	
37	$-2.402\,721\,220\,455\,7 \cdot 10^4$	2	1	
38	$-2.834\,160\,342\,399\,9 \cdot 10^2$	3	3	
39	$2.124\,728\,440\,017\,9 \cdot 10^2$	3	3	
40	$-6.664\,227\,654\,075\,1 \cdot 10^{-1}$			
41	$7.260\,863\,234\,989\,7 \cdot 10^{-1}$			
42	$5.506\,866\,861\,284\,2 \cdot 10^{-2}$			

A.3.4 Methane

For the limit k of the summator in (A.3.3) the following values are given for methane:

- $k_1 = 13$
- $k_2 = 36$
- $k_3 = 40$

Table A.3.9: Values for n_i^o and γ_i^o in (A.3.2) for methane.

i	n_i^o	γ_i^o
1	9.912 439 72	
2	-6.332 700 87	
3	3.001 6	
4	0.008 449	3.400 432 4
5	4.694 2	10.269 515 75
6	3.486 5	20.439 327 47
7	1.657 2	29.937 448 84
8	1.411 5	79.133 519 45

Table A.3.10: Values for the coefficients α_i , β_i , γ_i and ϵ_i from (A.3.3) and (A.3.4) for methane.

i	α_i	β_i	γ_i	ϵ_i
37	20	200	1.07	1
38	40	250	1.11	1
39	40	250	1.11	1
40	40	250	1.11	1

Table A.3.11: Values for the coefficients n_i , d_i , t_i and c_i from (A.3.3) for methane.

i	n_i	d_i	t_i	c_i	i	n_i	d_i	t_i	c_i
1	$4.368 \cdot 10^{-2}$	1	-0.5		21	$-1.932 \cdot 10^{-2}$	1	5	2
2	$6.709 \cdot 10^{-1}$	1	0.5		22	$-1.106 \cdot 10^{-1}$	2	5	2
3	-1.766	1	1		23	$9.953 \cdot 10^{-2}$	3	5	2
4	$8.582 \cdot 10^{-1}$	2	0.5		24	$8.548 \cdot 10^{-3}$	4	2	2
5	-1.207	2	1		25	$-6.151 \cdot 10^{-2}$	4	4	2
6	$5.120 \cdot 10^{-1}$	2	1.5		26	$-4.292 \cdot 10^{-2}$	3	12	3
7	$-4.000 \cdot 10^{-4}$	2	4.5		27	$-1.813 \cdot 10^{-2}$	5	8	3
8	$-1.248 \cdot 10^{-2}$	3	0		28	$3.446 \cdot 10^{-2}$	5	10	3
9	$3.100 \cdot 10^{-2}$	4	1		29	$-2.386 \cdot 10^{-3}$	8	10	3
10	$1.755 \cdot 10^{-3}$	4	3		30	$-1.159 \cdot 10^{-2}$	2	10	4
11	$-3.172 \cdot 10^{-6}$	8	1		31	$6.642 \cdot 10^{-2}$	3	14	4
12	$-2.240 \cdot 10^{-6}$	9	3		32	$-2.372 \cdot 10^{-2}$	4	12	4
13	$2.947 \cdot 10^{-7}$	10	3		33	$-3.962 \cdot 10^{-2}$	4	18	4
14	$1.830 \cdot 10^{-10}$	1	0	1	34	$-1.387 \cdot 10^{-2}$	4	22	4
15	$1.512 \cdot 10^{-1}$	1	1	1	35	$3.389 \cdot 10^{-2}$	5	18	4
16	$-4.289 \cdot 10^{-1}$	1	2	1	36	$-2.927 \cdot 10^{-3}$	6	14	4
17	$6.894 \cdot 10^{-2}$	2	0	1	37	$9.325 \cdot 10^{-5}$	2	2	
18	$-1.408 \cdot 10^{-2}$	4	0	1	38	-6.287	0	0	
19	$-3.063 \cdot 10^{-2}$	5	2	1	39	$1.271 \cdot 10^1$	0	1	
20	$-2.970 \cdot 10^{-2}$	6	2	1	40	-6.424	0	2	

A.3.5 Nitrogen

For the limit k of the summator in (A.3.3) the following values are given for nitrogen:

- $k_1 = 6$
- $k_2 = 32$
- $k_3 = 36$

Table A.3.12: Values for n_i^o and γ_i^o in (A.3.2) for nitrogen.

i	n_i^o	γ_i^o
1	9.912 644	
2	-6.333 133	
3	3.001 6	
4	0.008 449	3.400 664
5	4.694 2	10.270 22
7	1.657 2	29.939 49
8	1.411 5	79.138 92

Table A.3.13: Values for the coefficients α_i , β_i , γ_i and ϵ_i from (A.3.3) and (A.3.4) for nitrogen.

i	α_i	β_i	γ_i	ϵ_i
33	20	325	1.16	1
34	20	325	1.16	1
35	15	300	1.13	1
36	25	275	1.25	1

Table A.3.14: Values for the coefficients n_i , d_i , t_i and c_i from (A.3.3) for nitrogen.

i	n_i	d_i	t_i	c_i
1	0.924 803 575 275	1	0.25	0
2	-0.492 448 489 428	1	875	0
3	0.661 883 336 938	2	0.5	0
4	-0.192 902 649 201 · 10 ¹	2	875	0
5	-0.622 469 309 629 · 10 ⁻¹	3	375	0
6	0.349 943 957 581	3	0.75	0
7	0.564 857 472 498	1	0.5	1
8	-0.161 720 005 987 · 10 ¹	1	0.75	1
9	-0.481 395 031 883	1	2	1
10	0.421 150 636 384	3	1.25	1
11	-0.161 962 230 825 · 10 ⁻¹	3	3.5	1
12	0.172 100 994 165	4	1	1
13	0.735 448 924 933 · 10 ⁻²	6	0.5	1
14	0.168 077 305 479 · 10 ⁻¹	6	3	1
15	-0.107 626 664 179 · 10 ⁻²	7	0	1
16	-0.137 318 088 513 · 10 ⁻¹	7	2.75	1
17	0.635 466 899 859 · 10 ⁻³	8	0.75	1
18	0.304 432 279 419 · 10 ⁻²	8	2.5	1
19	-0.435 762 336 045 · 10 ⁻¹	1	4	2
20	-0.723 174 889 316 · 10 ⁻¹	2	6	2
21	0.389 644 315 272 · 10 ⁻¹	3	6	2
22	-0.212 201 363 910 · 10 ⁻¹	4	3	2
23	0.408 822 981 509 · 10 ⁻²	5	3	2
24	-0.551 990 017 984 · 10 ⁻⁴	8	6	2
25	-0.462 016 716 479 · 10 ⁻¹	4	16	3
26	-0.300 311 716 011 · 10 ⁻²	5	11	3
27	0.368 825 891 208 · 10 ⁻¹	5	15	3
28	-0.255 856 846 220 · 10 ⁻²	8	12	3
29	0.896 915 264 558 · 10 ⁻²	3	12	4
30	-0.441 513 370 350 · 10 ⁻²	5	7	4
31	0.133 722 924 858 · 10 ⁻²	6	4	4
32	0.264 832 491 957 · 10 ⁻³	9	16	4
33	0.196 688 194 015 · 10 ²	1	0	2
34	-0.209 115 600 730 · 10 ²	1	1	2
35	0.167 788 306 989 · 10 ⁻¹	3	2	2
36	0.262 767 566 274 · 10 ⁴	2	3	2

Appendix A

Density of carbon dioxide

A fast way to estimate densities of fluids relating to thermodynamic boundary conditions is to read them out of a matrix. The following tables present the density of carbon dioxide at different temperatures and pressures. All density values are calculated from Equation ?? in section ??.

Table A.0.1: Thermodynamic and transport properties of pure carbon dioxide.

temper- ature [K]	density [kg · m ⁻³]	viscosity [Pa · s]	thermal conductivity [W · m ⁻¹ · K ⁻¹]	isobaric heat capacity [J · kg ⁻¹ · K ⁻¹]	isochoric heat capacity [J · kg ⁻¹ · K ⁻¹]
pressure 50 000 Pa					
260	1.0219	$1.30569 \cdot 10^{-5}$	0.015272	808.451	616.125
280	0.948101	$1.40429 \cdot 10^{-5}$	0.0174424	828.953	637.371
300	0.884342	$1.50176 \cdot 10^{-5}$	0.0197164	849.17	658.116
310	0.855599	$1.55004 \cdot 10^{-5}$	0.0208841	859.085	668.238
320	0.82868	$1.59799 \cdot 10^{-5}$	0.0220682	868.842	678.174
330	0.803413	$1.64562 \cdot 10^{-5}$	0.0232661	878.43	687.918
340	0.779651	$1.69291 \cdot 10^{-5}$	0.0244753	887.841	697.465
350	0.75726	$1.73986 \cdot 10^{-5}$	0.0256937	897.07	706.813
360	0.736127	$1.78646 \cdot 10^{-5}$	0.0269192	906.114	715.963
370	0.716145	$1.83271 \cdot 10^{-5}$	0.0281503	914.973	724.916
380	0.697224	$1.8786 \cdot 10^{-5}$	0.0293853	923.65	733.676
390	0.679281	$1.92413 \cdot 10^{-5}$	0.0306229	932.145	742.246
400	0.662241	$1.96931 \cdot 10^{-5}$	0.0318621	940.463	750.631
420	0.630611	$2.05859 \cdot 10^{-5}$	0.0343408	956.581	766.863
440	0.601873	$2.14643 \cdot 10^{-5}$	0.0368149	972.037	782.414
460	0.575645	$2.23285 \cdot 10^{-5}$	0.0392794	986.867	797.323
480	0.551612	$2.31786 \cdot 10^{-5}$	0.0417309	1001.11	811.629
pressure 101 300 Pa					
260	2.07878	$1.30614 \cdot 10^{-5}$	0.0152981	814.394	618.485
280	1.92694	$1.4047 \cdot 10^{-5}$	0.0174666	833.412	639.048
300	1.79619	$1.50215 \cdot 10^{-5}$	0.0197389	852.622	659.347
310	1.73736	$1.55041 \cdot 10^{-5}$	0.0209059	862.151	669.304
320	1.68231	$1.59836 \cdot 10^{-5}$	0.0220893	871.581	679.103
330	1.63069	$1.64597 \cdot 10^{-5}$	0.0232865	880.891	688.731
340	1.58218	$1.69325 \cdot 10^{-5}$	0.0244951	890.062	698.181
350	1.5365	$1.74019 \cdot 10^{-5}$	0.0257129	899.083	707.447
360	1.49341	$1.78678 \cdot 10^{-5}$	0.0269379	907.947	716.527
370	1.4527	$1.83302 \cdot 10^{-5}$	0.0281685	916.648	725.419
380	1.41416	$1.8789 \cdot 10^{-5}$	0.029403	925.185	734.127
390	1.37763	$1.92443 \cdot 10^{-5}$	0.0306402	933.558	742.652
400	1.34295	$1.9696 \cdot 10^{-5}$	0.0318788	941.767	750.997
420	1.27861	$2.05886 \cdot 10^{-5}$	0.0343568	957.701	767.165
440	1.22019	$2.14669 \cdot 10^{-5}$	0.0368301	973.008	782.666
460	1.16689	$2.2331 \cdot 10^{-5}$	0.039294	987.717	797.535
480	1.11807	$2.3181 \cdot 10^{-5}$	0.0417448	1001.86	811.809
pressure 500 000 [Pa]					
260	987305	0.000120005	0.123914	2343.51	933.987
280	9.75683	$1.40855 \cdot 10^{-5}$	0.0176661	870.631	652.546
300	9.04555	$1.50566 \cdot 10^{-5}$	0.0199231	880.965	669.163
310	8.73047	$1.55379 \cdot 10^{-5}$	0.0210833	887.174	677.773
320	8.43811	$1.6016 \cdot 10^{-5}$	0.0222605	893.818	686.456
330	8.16591	$1.64909 \cdot 10^{-5}$	0.023452	900.772	695.157
340	7.9117	$1.69626 \cdot 10^{-5}$	0.0246552	907.935	703.829
350	7.67364	$1.7431 \cdot 10^{-5}$	0.025868	915.23	712.437
360	7.45015	$1.78959 \cdot 10^{-5}$	0.0270883	922.6	720.957
370	7.23986	$1.83574 \cdot 10^{-5}$	0.0283144	930.002	729.369
380	7.04158	$1.88153 \cdot 10^{-5}$	0.0295448	937.4	737.664
390	6.85425	$1.92698 \cdot 10^{-5}$	0.0307781	944.771	745.831
400	6.67696	$1.97208 \cdot 10^{-5}$	0.0320131	952.094	753.865
420	6.34932	$2.0612 \cdot 10^{-5}$	0.0344842	966.539	769.522
440	6.05311	$2.14891 \cdot 10^{-5}$	0.0369514	980.654	784.626
460	5.7839	$2.23521 \cdot 10^{-5}$	0.0394098	994.393	799.184
480	5.53807	$2.32011 \cdot 10^{-5}$	0.0418555	1007.73	813.209

Table A.0.2: Thermodynamic and transport properties of pure carbon dioxide.

temper- ature [K]	density [kg · m ⁻³]	viscosity [Pa · s]	thermal conductivity [W · m ⁻¹ · K ⁻¹]	isobaric heat capacity [J · kg ⁻¹ · K ⁻¹]	isochoric heat capacity [J · kg ⁻¹ · K ⁻¹]
pressure 1 000 000 [Pa]					
260	484.996	$3.22842 \cdot 10^{-5}$	0.0437718	$-4.03066 \cdot 10^7$	$-4.03162 \cdot 10^7$
280	20.1993	$1.41505 \cdot 10^{-5}$	0.0179484	925.18	670.92
300	18.5794	$1.51144 \cdot 10^{-5}$	0.020179	920.888	682.167
310	17.8778	$1.55926 \cdot 10^{-5}$	0.021328	921.92	688.895
320	17.2343	$1.60681 \cdot 10^{-5}$	0.0224951	924.327	696.045
330	16.6411	$1.65406 \cdot 10^{-5}$	0.0236774	927.775	703.489
340	16.0919	$1.70101 \cdot 10^{-5}$	0.0248722	932.003	711.12
350	15.5813	$1.74764 \cdot 10^{-5}$	0.0260773	936.813	718.855
360	15.105	$1.79395 \cdot 10^{-5}$	0.0272905	942.06	726.635
370	14.6594	$1.83993 \cdot 10^{-5}$	0.02851	947.634	734.419
380	14.2414	$1.88557 \cdot 10^{-5}$	0.0297342	953.449	742.173
390	13.8482	$1.93087 \cdot 10^{-5}$	0.0309617	959.438	749.875
400	13.4775	$1.97583 \cdot 10^{-5}$	0.0321913	965.548	757.506
420	12.7959	$2.06472 \cdot 10^{-5}$	0.0346526	977.976	772.506
440	12.1832	$2.15221 \cdot 10^{-5}$	0.0371111	990.492	787.102
460	11.629	$2.23832 \cdot 10^{-5}$	0.0395616	1002.94	801.262
480	11.1249	$2.32306 \cdot 10^{-5}$	0.0420003	1015.23	814.972
pressure 2 000 000 [Pa]					
260	49.9138	$1.34352 \cdot 10^{-5}$	0.0166775	1212.96	743.312
280	484.296	$3.31634 \cdot 10^{-5}$	0.0458792	$2.48814 \cdot 10^7$	$2.48811 \cdot 10^7$
300	39.4201	$1.52863 \cdot 10^{-5}$	0.0207908	1020.61	711.165
310	37.6448	$1.57521 \cdot 10^{-5}$	0.0219043	1005.92	713.172
320	36.0628	$1.62169 \cdot 10^{-5}$	0.0230406	996.207	716.641
330	34.6388	$1.66803 \cdot 10^{-5}$	0.0241959	990.08	721.169
340	33.3462	$1.71417 \cdot 10^{-5}$	0.0253667	986.588	726.447
350	32.1647	$1.76009 \cdot 10^{-5}$	0.0265502	985.061	732.246
360	31.0785	$1.80576 \cdot 10^{-5}$	0.0277439	985.03	738.412
370	30.0748	$1.85117 \cdot 10^{-5}$	0.0289457	986.158	744.837
380	29.1433	$1.89629 \cdot 10^{-5}$	0.0301537	988.19	751.438
390	28.2755	$1.94112 \cdot 10^{-5}$	0.0313664	990.932	758.154
400	27.4643	$1.98565 \cdot 10^{-5}$	0.0325823	994.235	764.936
420	25.9885	$2.07377 \cdot 10^{-5}$	0.035019	1002.07	778.562
440	24.6778	$2.16061 \cdot 10^{-5}$	0.0374561	1011.03	792.108
460	23.5036	$2.24616 \cdot 10^{-5}$	0.0398878	1020.65	805.451
480	22.444	$2.3304 \cdot 10^{-5}$	0.0423097	1030.67	818.515
pressure 5 000 000 [Pa]					
260	484.996	$3.22843 \cdot 10^{-5}$	0.0437719	$-4.03065 \cdot 10^7$	$-4.03162 \cdot 10^7$
280	484.355	$3.3168 \cdot 10^{-5}$	0.0458847	$2.48814 \cdot 10^7$	$2.48812 \cdot 10^7$
300	128.398	$1.67234 \cdot 10^{-5}$	0.0241513	1802.53	852.579
310	116.129	$1.69404 \cdot 10^{-5}$	0.0247884	1524.61	815.079
320	107.216	$1.72404 \cdot 10^{-5}$	0.0256003	1378.56	795.617
330	100.221	$1.75839 \cdot 10^{-5}$	0.0265141	1289.01	785.046
340	94.4783	$1.79531 \cdot 10^{-5}$	0.0274953	1229.37	779.631
350	89.6193	$1.83384 \cdot 10^{-5}$	0.0285245	1187.55	777.393
360	85.4182	$1.87345 \cdot 10^{-5}$	0.0295894	1157.25	777.266
370	81.7263	$1.91376 \cdot 10^{-5}$	0.0306814	1134.89	778.631
380	78.44	$1.95453 \cdot 10^{-5}$	0.0317943	1118.22	781.088
390	75.4845	$1.9956 \cdot 10^{-5}$	0.0329235	1105.78	784.357
400	72.8036	$2.03683 \cdot 10^{-5}$	0.0340655	1096.54	788.239
420	68.1036	$2.11944 \cdot 10^{-5}$	0.0363764	1084.99	797.287
440	64.0937	$2.20185 \cdot 10^{-5}$	0.0387101	1079.77	807.425
460	60.6128	$2.28374 \cdot 10^{-5}$	0.0410548	1078.69	818.168
480	57.55	$2.36491 \cdot 10^{-5}$	0.0434022	1080.38	829.21

Appendix A

List containing all benchmarks

*nw = not working, nf = no file found, NA = all timesteps done
but no calculation time given in .txt file,
!= computing time > 10min(Computer : 2 * 1.2GHz, 2GB RAM)*

Chapter	Author	Dim	Comment	Repository	t (s)	Lars
2	NB					
2.2			Heat Transport (T)	T\TDIFF	59	
2.3			Linear heat diffusion Linear heat diffusion in a wall	T\TDiff-wall	303	
2.4						
2.6			Radial heat diffusion	T\T_1D_axi	11	
2.7			Heat transport in a fracture	T\Ogata-Banks	63	
			Heat transport in fracture- matrix systems	T\Lauwerier	837!	
2.8	Blöcher G. and Cacace M.	3	Heat transport in fracture- matrix systems: 3D case	T\2units2faults	(XXX)	
2.9			Heat transport with tem- perature dependend fluid properties	T\HT_var_density_1D	5	
NA			Yaws viscosity model	T\Viscosity	1	
NA			Periodic BC with advection	HT\ht_sat.line	nf	
NA			Periodic BC with advec- tion& infiltration in unsat- urated porous medium	HT\ht_unsat.line	nf	
3	FS					
3.2.1		1	Saturated flow in isotropic medium	H\sat_1d\H_sat_flow_1d	0	
3.2.2		2	Saturated flow in anisotropic medium	H\sat_2d\H_sat_flow_K_ortho	135	
3.2.3		2	Saturated flow in a hetero- geneous medium	H\HetGWF_low\2D1P- GWF_low	10	

	NB	Fluid	Property	Functions	
3.3.1	2	Confined aquifer, source term	constant	GROUNDWATER_FLOW\q_quad	
3.3.2	3	Confined aquifer, source term	channel	GROUNDWATER_FLOW\q_hkx	GROUNDWATER_FLOW\riv4_quad
3.3.3	2	Confined aquifer, sink term	channel	GROUNDWATER_FLOW\riv12pris	GROUNDWATER_FLOW\riv12hex
3.3.4	1	Confined aquifer, problem	Theis's	\H\Theis_1D\h_quad_axisym	12
	2	Time variant flow		\H\Theis_2D\Theis_quad_2d	329
3.4				\GROUNDWATER_FLOW\transient_flow	4
3.5	2	Unconfined aquifer		GROUNDWATER_FLOW\uc0quad	
	3			GROUNDWATER_FLOW\uc0ri	
				GROUNDWATER_FLOW\uc0pris	
4					
4.3.1	1	isothermal phase flow	CO2-single	FLUID_PROPERTIES\H_CO28	
4.3.2	1	non-isothermal flow	single phase	FLUID_PROPERTIES\HT_EQ8	
4.3.3	1	non-isothermal flow	two-phase	FLUID_PROPERTIES\	nw
				H2T_MCWHORTER_PMSNW	
5	AKS			Richards Flow (H)	

5.2.1	1	Infiltration in homogeneous soil	H_US\wet\h_us_line_warrick	19				
	2		H_US\wet\h_us_line_halm	275				
			H_US\wet\h_us_quad	92				
			H_US\wet\h_us_tri_freebc	43				
5.2.2	1	Infiltration in homogeneous soil (ST\BC)	H_US\wet\h_us_line_forsyth	523				
5.2.3	1	Infiltration in homogeneous soil (BC\BC)	H_US\wet\h_us_line_celia	202				
5.2.4	1	Transient infiltration in homogeneous soil	H_US\wet\transient	575				
5.2.5	1	Non-uniform IC in heterogeneous soil	H_US\wet\1d_ho	0				
??			H_US\h_us_drainage	144				
5.3		Dual continua	H_US\dual\dual_vl	69				
5.3.1			H_US\dual\dual_van	1651!				
5.3.2			H_US\RSM\at_5	!!!				
5.4		Regional soil model						
6	YW							
6.2.1	1	Surface flow (H)						
	2	1-D precipitation runoff	OVERLAND_FLOW\govin_lin20					
6.2.2	2	2-D precipitation runoff	OVERLAND_FLOW\govin_qi321					
	2		OVERLAND_FLOW\gian_tri10					
6.2.3	2	Infiltration excess overland flow	OVERLAND_FLOW\gian_quad					
			OVERLAND_FLOW\wool_quad					
8	PCH							
8.2	1	Fluid Momentum (H)	FLUID_MOMENTUM\1d_linel					
	2		FLUID_MOMENTUM\1d_tri1					

		Deformation (M)	
9	UJG	Isotropic elasticity	
9.2		Plane strain with uniform loading	M\m_drift
9.2.1	2	Excavation in homogeneous media	M\m_excav
9.2.2	2	Excavation in heterogeneous media	M\m_drift_init
9.2.3	2	Elastic cube	M\m_brick]
9.2.4	3	Uniaxial compression,	M\elasticity\ M_e_displacement3DU
9.2.5	3	Uniaxial compression, strain driven	48
9.2.6	3	Uniaxial compression, stress driven	M\elasticity\ M_e_stress_3DU 543
9.2.7	2	Triaxial test, nonlinear model (Lubby1)	M\m_triax_lubby1
9.3		Transverse isotropic elasticity	376
9.3.1	2	Tensile test 2D	M\m_e_transiso_2D 0
9.3.2	3	Tensile test 3D	M\elasticity\ M_e_transiso_3D 22
9.4	3	Excavation in homogeneous media	M\excavation\ 1703!
9.5		3DEX\ 3D_excav	
9.5.1	2	Elasto-plasticity Von Mises plasticity	M\m_mises
			83

9.5.2	2	Drucker-Prager plasticity,	M\m_sdc	27
9.5.3	2	Cam-Clay plasticity	M\m_cc_quad.s	18
9.5.4	2	Rotational hardening plasticity	M\m_cc_tri.s	18
9.6	Creep	Creep of cylindrical sample	M\creep\m_crp_tri	49
9.6.1	2	Creep in salt rock	M\creep\m_crp_bgr	!!!
9.6.2	2		M\creep\uc_creep01	840
9.6.3	2	Transient and stationary creep model	M\creep\m_triax_lubby2	613
10		Mass transport (C)		
10.2	MDL	1	Solute transport with decay	C\decay\hc_decay_1Du
10.3			Solute transport with sorption	
10.3.1	MDL	1	Solute transport with sorption, Henry	C\sorption\henry\hc_sorp_henry_1D
10.3.2	MDL	1	Solute transport with sorption, Freundlich	C\sorption_Freundlich\HC_sorp_freundl_1D
10.3.3	MDL	1	Solute transport with sorption, Langmuir	C\sorption_Langmuir\HC_sorp_langmuir_1D
10.3.4	MDL	1	Solute transport with sorption and decay	C\sorption_decay\HC_decay_sorp_henry_1Du
10.4			Solute transport by diffusion	

10.4.1		1	Diffusion: model	axisymmetric	C\Diffusion\Diff_HTO_test	153
10.4.2		2	Diffusion in an anisotropic medium	C\Diffusion\diff_aniso	14	
10.4.3		2	Solute transport with ma- trix diffusion	C\matrix_diffusion\	164	
10.4.4	SB	1	Solute transport with cation exchange	OGS_vs-picnic C\ion_exchange\pqc1	164 126	
10.4.5	GK	1	Precipitation \ dissolution	C\Calcite_gems C\Calcite_pqc	94 54	
10.5		1	Conservative transport	C\1d_analyt\1d_line	32	
10.5.1	SB	1	1D reactive and conserva- tive transport	C\1d_analyt\1d_hex C\1d_analyt\1d_pri C\1d_analyt\1d_quad C\1d_analyt\1d_tet C\1d_analyt\1d_tri C\2d_analyt\2D_quad C\2d_analyt\2D_tri C\hecn+n+restart	376 365 98 539 108 406 261 592	
10.5.2	SB	2	2D conservative transport	2D conservative transport	406	
10.5.3	SB	2	2D Conservative transport in heterogeneous media	2D Conservative transport in heterogeneous media	261	
10.6	FS	2	Radial flow and conserva- tive transport	Radial flow and conserva- tive transport	592	
10.6.1			Theis-Problem	Theis-Problem	nf	
10.6.2			Conservative transport in radial flow	Conservative transport in radial flow	nf	

10.7	SB							
10.7.1		Reactive transport						
		Xylene degradation with multiple Monod kinetics	C:\1d_xylene_degradation					67
10.7.2		TCE and DCE degradation	C:\1d_TCEauffEisen					906
10.7.3		CHC degradation with isotopic fractionation	C:\1d_isofrac					144
10.7.4		Degradation network	C:\1d_degradationnetwork					!!!
10.7.5		Mixing controlled bioreactive transport	C:\monod2d\rt1					2727!
10.8		Conservative mass transport in unsaturated medium						nf
11	PCH	Random Walk Particle Tracking (H)	RWPT\Veri1000					
11.2		2						!!!
12	PCH		Anisotropy (H,C,HC)					
12.2		2						!!!
12.3		2						Anisotropy\permeability Anisotropy\moleculardiffusion!!!
13	JOD		Surface\subsurface flow coupling					
13.2.1		Horton flow	COUPLED_FLOW\wool_lines\&up					
13.2.2		Dunne flow	COUPLED_FLOW					117
			groundwater not coupled					
			yet\abduLlab					
13.2.3		Aquifer recharge from channel	COUPLED_FLOW\riv1_quad&oup					
13.2.4		Flood at channel junction	COUPLED_FLOW\biFork1_coup					
			COUPLED_FLOW\biFork2_coup					

14	WX						
14.2							
14.2.1		1	Saturated Consolidation	HM\hm_tri	10		
14.2.2		3	Poro-elastic column	HM\hm_foot_tri	19		
14.2.3		2	Poro-elastic cube	HM\hm_foot_tet	217		
14.2.4		2	Plastic consolidation	HM\hm_cc_tri_s	NA		
14.3		2	Dynamic consolidation	HM\hm_dyn_tri	45		
14.3.2		2	Unsaturated Consolidation	HM\hm_unsat			
14.3.3		2	Liakopoulos Experiment	HM\hm_linearSwelling			
14.4		2	Decovalex HM test case	HM\LinearSwelling	20		
14.4.2		2	Two-phase-flow consolidation	HM\LinearSwelling	88		
15	NW						
15.2.1		2	Thermo-elastic plate, plane strain	TM\tm2d	3		
15.2.2		3	Thermo-elastic cube	TM\tm3d	176		
15.2.3		3	Homogeneous material	TM\tm_01_3du	73		
15.2.4		3	Composite material	TM\tm_02_3du	184		
15.2.5		2	Hollow cylinder	TM\tm_axi	3		
16	WW						
16.1.4		2	Thermo Mechanical Consolidation(THM) DECOVALEX Task (THM)	THM\THm_decov	485		
17	WW		Non isothermal two-phase flow consolidation				

17.3		2	TH2M\th2m_quad	207
18	PCH	THC-Processes DECOVALEX (THC)	Task 4	nf
19	PCH	Density-Dependent Flow (HC, THC) The Elder Problem	DENSITY- DEPENDENT_FLOW\elder DENSITY- DEPENDENT_FLOW\elder_2d	!!!
19.2		3		
19.2		2	The Elder Problem	!!!
20	PCH	Isothermal Two Phase Flow (HH)	MULTIPHASE\BuckleyLeverett@ MULTIPHASE\McWhorterP@ MULTIPHASE\KueperProblem@ PS	
20.1.5		1	Buckley-Leverett problem	
20.1.6		1		
20.1.7		2		
		2		MULTIPHASE\KueperProblem@82!!!
??	WW		PcPnw	
??			H2\BuckleyLeverett	13
??			H2\Liakopoulos	208(tet)
			H2\McWhorter	86
21	NW	Numerics		
21.1		Discrete features		
21.1.1		1	Liquid flow in a single inclined feature	Numerics\DISCRETE_FEATURES\ InclinedFeature\H_incline_45r_line

		H_incline_45r_quad	0
		Numerics\SUPG\	0
21.2.1	2	Steady-state heat transport	
	1	in a fracture	
22.2.2	1	Transient heat transport in	T_adv_diff_steady_SUPG_line
		a fracture	T_adv_diff_transient_SUPG_line96

Bibliography

- [1] A. Fenghour, W.A. Wakeham, and V. Vesovic. The Viscosity of Carbon Dioxide. *Journal of Physical and Chemical Reference Data*, 27:31–44, 1998.
- [2] K. Stephan, R. Krauss, and A. Laesecke. Viscosity and thermal conductivity of nitrogen for a wide range of fluid states. *Journal of Physical and Chemical Reference Data*, 16(4), 1987.
- [3] D. G. Friend, J. F. Ely, and H. H. Ingham. Thermophysical properties of methane. *Journal of Physical and Chemical Reference Data*, 18(2), 1989.
- [4] D. G. Friend, H. Ingham, and J. F. Ely. Thermophysical properties of ethane. *Journal of Physical and Chemical Reference Data*, 20(2), 1991.
- [5] International Association for the Properties of Water and Steam. *Release on the IAPWS Formulation 2008 for the Viscosity of Ordinary Water Substance*, 2008.
- [6] V. Vesovic and W.A. Wakeham. The transport properties of carbon dioxide. *Journal of Physical and Chemical Reference Data*, 19(3):763–807, 1990.
- [7] B. A. Younglove and J. F. Ely. Thermophysical properties of fluids. ii. methane, ethane, propane, isobutane, and normal butane. *Journal of Physical and Chemical Reference Data*, 16(4), 1987.
- [8] International Association for the Properties of Water and Steam. *Revised Release on the IAPWS Formulation 1985 for the Thermal Conductivity of Ordinary Water Substance*, 2008.
- [9] K. Watanabe and R. B. Dooley. Release on the IAPWS Formulation 1995 for the Thermodynamic Properties of Ordinary Water Substance for General and Scientific Use. The International Association for the Properties of Water and Steam, 1996.
- [10] K.P. Kroehn. *Simulation von Transportvorgaengen im klueftigen Gestein mit der Methode der Finiten Elemente*. PhD thesis, Institute of Fluid Mechanics, Hannover University, 1991.

- [11] J Wollrath. *Ein Stroemungs- und Transportmodell fuer klueftiges Gestein und Untersuchungen zu homogenen Ersatzsystemen.* PhD thesis, Institute of Fluid Mechanics, Hannover University, 1990.
- [12] R. Helmig. *Theorie und Numerik der Mehrphasenstroemungen in gekluftet-poroesen Medien.* PhD thesis, Institute of Fluid Mechanics, Hannover University, 1993.
- [13] H. Shao. *Simulation von Stroemungs- und Transportvorgaengen im geklufteten poroesen Medien mit gekoppelten Finite-Elementund und Rand-Element-Methoden.* PhD thesis, Institute of Fluid Mechanics, Hannover University, 1994.
- [14] T. Lege. *Modellierung des Kluftgestein als geologische Barriere fuer Deponien.* PhD thesis, Institute of Fluid Mechanics, Hannover University, 1995.
- [15] O. Kolditz. *Stoff- und Waermetransport im Kluftgestein.* Habilitation, Institute of Fluid Mechanics, Hannover University, 1996.
- [16] O. Kolditz, R. Ratke, H.-J. Diersch, and W. Zielke. Coupled groundwater flow and transport: 1. Verification of variable density flow and transport models. *Advances in Water Resources*, 21:27–46, 1998.
- [17] M. Schulze-Ruhfus. *Adaptive Verfeinerung und Vergroeberung gekoppelter 1D/2D/3D Elemente.* Diploma thesis, Institute of Fluid Mechanics, Hannover University, 1996.
- [18] C. Barlag. *Adaptive Methoden zur Modellierung von Stofftransport im Kluftgestein.* PhD thesis, Institute of Fluid Mechanics, Hannover University, 1997.
- [19] C. Thorenz. Model adaptive simulation of multiphase and density driven flow in fractured and porous media. Dissertation, Bericht Nr. 62, Institut für Strömungsmechanik und Elektronisches Rechnen im Bauwesen, 2001.
- [20] R. Kaiser. Gitteradaption für die Finite-Elemente-Modellierung gekoppelter Prozesse in klüftig-porösen medien. Dissertation, Bericht Nr. 63, Institut für Strömungsmechanik und Elektronisches Rechnen im Bauwesen, 2001.
- [21] A. Habbar. Direkte und inverse Modellierung reaktiver Transportprozesse in klüftig-porösen medien. Dissertation, Bericht Nr. 65, Institut für Strömungsmechanik und Elektronisches Rechnen im Bauwesen, 2001.
- [22] M. Kohlmeier. *Coupling of thermal, hydraulic and mechanical processes fro geotechnical simulations of partially saturated porous media.* PhD thesis, Institute of Fluid Mechanics, Hannover University, 2006.

- [23] T. Rother. Geometric modelling geo-systems. Dissertation, Bericht Nr. 64, Institut für Strömungsmechanik und Elektronisches Rechnen im Bauwesen, 2001.
- [24] S. Moenckes. *Grid generation for simulation of flow and transport processes in fractured porous media*. PhD thesis, Institute of Fluid Mechanics, Hannover University, 2004.
- [25] O. Kolditz and S. Bauer. A process-oriented approach to computing multi-field problems in porous media. *Journal of Hydroinformatics*, 6:225–244, 2004.
- [26] W. Wang and O. Kolditz. Object-oriented finite element analysis of thermo-hydro-mechanical (thm) problems in porous media. *Int. J. Numerical Methods in Engineering*, 68:doi:10.1002/nme.1770, 2007.
- [27] I. Engelhardt. *Experimental and numerical investigations with respect to the material properties of geotechnical barriers*. PhD thesis, University of Tübingen, 2003.
- [28] J. de Jonge. *Contributions to computational geotechnics: Non-isothermal flow in low-permeable porous media*. PhD thesis, GeoHydrology and HydroInformatics, Center for Applied Geosciences, Tuebingen University, 2004.
- [29] R. Walsh. *Numerical modeling of THM coupled processes in fractured porous media*. PhD thesis, GeoHydrology and HydroInformatics, Center for Applied Geosciences, Tuebingen University, 2007.
- [30] M. Beinhorn. *Contributions to computational hydrology: Non-linear flow processes in subsurface and surface hydrosystems*. PhD thesis, GeoHydrology and HydroInformatics, Center for Applied Geosciences, Tuebingen University, 2005.
- [31] C. Beyer. *Applied numerical modeling of saturated / unsaturated flow and reactive contaminant transport: evaluation of site investigation strategies and assessment of environmental impact*. PhD thesis, GeoHydrology and HydroInformatics, Center for Applied Geosciences, Tuebingen University, 2007.
- [32] B. Miles. *Practical approaches to modeling natural attenuation processes at LNAPL contaminated sites*. PhD thesis, GeoHydrology and HydroInformatics, Center for Applied Geosciences, Tuebingen University, 2007.
- [33] H. Tenzer. *Comparison of the exploration and evaluation techniques of Hot Dry Rock Enhanced Geothermal sites at Soultz-sous-Forêts and Urach Spa in the framework of the geomechanical facies concept*. PhD thesis, GeoHydrology and HydroInformatics, Center for Applied Geosciences, Tuebingen University, 2006.

- [34] T. Kalbacher. *Geometric modelling and 3-D visualization of hydrogeological systems: Software design and application.* PhD thesis, GeoHydrology and HydroInformatics, Center for Applied Geosciences, Tuebingen University, 2006.
- [35] J. Gronewold. *Entwicklung eines Internet-Informationssystems zur Modellierung natuerlicher Rueckhalte- und Abbauprozesse im Grundwasser.* PhD thesis, GeoHydrology and HydroInformatics, Center for Applied Geosciences, Tuebingen University, 2006.
- [36] C. Chen. *Integrating GIS methods for the analysis of geosystems.* PhD thesis, GeoHydrology and HydroInformatics, Center for Applied Geosciences, Tuebingen University, 2006.
- [37] S. Bauer. *Process based numerical modelling as a tool for aquifer characterization and groundwater quality evaluation.* Habilitation, GeoHydrology and HydroInformatics, Center for Applied Geosciences, Tuebingen University, 2006.
- [38] C.I. McDermott. *Reservoir Engineering and System Analysis: Hydraulic, Thermal and Geomechanical Coupled Processes in Geosystems.* Habilitation, GeoHydrology and HydroInformatics, Center for Applied Geosciences, Tuebingen University, 2006.
- [39] G. Kosakowski. *Transport in fractured media: Concepts, Models, and Applications.* Habilitation, GeoHydrology and HydroInformatics, Center for Applied Geosciences, Tuebingen University, 2007.
- [40] C.-H. Park, C. Beyer, S. Bauer, and O. Kolditz. Using global node-based velocity in random walk particle tracking in variably saturated porous media: Application to contaminant leaching from road constructions. *Environmental Geology*, DOI: 10.1007/s00254-007-1126-7, 2007.
- [41] O. Kolditz, Y. Du, C.M. Brger, J.-O. Delfs, M Hess, W. Wang, B van der Grift, and C te Stroet. Development and application of a compartment approach for hydro-system analysis to the beerze-reuzel catchment (meuse basin). *J Environmental Pollution*, 148(3):855–866, 2007.
- [42] M. Xie, S. Bauer, O. Kolditz, T. Nowak, and H. Shao. Non-isothermal multicomponent reactive transport in partially saturated porous media. *J. Contaminant Hydrology*, 83:122–147, 2006.
- [43] W. Wang, G. Kosakowski, and O. Kolditz. A parallel finite element scheme for thermo-hydro-mechanical (thm) coupled problems in porous media. *Computers & Geosciences*, in revision, 2008.
- [44] Frieder Häfner, Dietrich Sames, and Hans-Dieter Voigt. *Wärme- und Stofftransport: Mathematische Methoden.* Springer, Berlin, 1992.

- [45] O. Kolditz. *Strömung, Stoff- und Wärmetransport im Kluftgestein.* Borntraeger-Verlag, Berlin-Stuttgart, 1997.
- [46] R E Glover. Transient ground water hydraulics monograph. Water resources publications, Fort Collins, CO, 1978.
- [47] Johannes Diderik van der Waals. *Over de Continuiteit van den gas- en vloeistofstoestand.* Sijthoff, Leiden, 1873.
- [48] Otto Redlich and J. N. S. Kwong. On the Thermodynamics of Solutions. v. An Equation of State. Fugacities of Gaseous Solutions. *Chemical Reviews*, 44:233–244, 1949.
- [49] D.Y. Peng and D.B. Robinson. A new two-constant equation of state. *Ind. Eng. Chem. Fundam.*, 15:59–64, 1974.
- [50] R. Span and W. Wagner. A new Equation of State for Carbon Dioxide Covering the Fluid Region from the Triple-Point Temperature to 1100 K at Pressures up to 800 MPa. *Journal of Physical and Chemical Reference Data*, 25(6):1509–1596, 1996.
- [51] Roland Span. *Eine neue Fundamentalgleichung für das fluide Zustandsgebiet von Kohlendioxid bei Temperaturen bis zu 1100 K und Drücken bis zu 800 MPa.* VDI Verlag, Düsseldorf, 1993.
- [52] R. Span, E.W. Lemmon, R.T. Jacobsen, W. Wagner, and A.Yokozeki. A Reference Equation of State for the Thermodynamic Properties of Nitrogen for Temperatures from 63.151 to 1000K and Pressures to 2200MPa. *J. Phys. Chem. Ref. Data*, 29:1361–1431, 2000.
- [53] Andreas Prüß and Wolfgang Wagner. *Eine neue Fundamentalgleichung für das fluide Zustandsgebiet von Wasser für Temperaturen von der Schmelzlinie bis zu 1273 K bei Drücken bis zu 1000 MPa.* VDI Verlag, Düsseldorf, 1995.
- [54] W. Wagner and A. Prüß. The IAPWS formulation 1995 for the thermodynamic properties of ordinary water substance for general and scientific use. *Journal of Physical and Chemical Reference Data*, 31(2), 2002.
- [55] D. Bücker and W. Wagner. A reference equation of state for the thermodynamic properties of ethane for temperatures from the melting line to 675 K and pressures up to 900 MPa. *J. Phys. Chem. Ref. Data*, 35:205–266, 2006.
- [56] Ulrich Setzmann and Wolfgang Wagner. A new equation of state and tables of thermodynamic properties for methane covering the range from the melting line to 625 K at pressures up to 1000 MPa. *J. Phys. Chem. Ref. Data*, 20:1061–1155, 1991.

- [57] P. A. Forsyth, Y. S. Wu, and K. Pruess. Robust numerical methods for saturated-unsaturated flow with dry initial conditions in heterogeneous media. *Advances in Water Resource*, 18:25–38, 1995.
- [58] K. Rathfeder and L. M. Abriola. Mass conservative numerical solutions of the head-based richards equation. *Water Resource Research*, 30:2579–2586, 1994.
- [59] Tomas Vogel. Personal communication. Technical Report 2006-23, Civil Engineering, CTU, Prague, 2007.
- [60] Gerke H. H. and van Genuchten M. T. A dual-porosity model for simulating the preferential movement of water and solutes in structured porous media. *Water Resources Research*, 29(2):305–320, 1993.
- [61] Y Du, C M Bürger, J O Delfs, O Kolditz, B van der Grift, and C te Stroet. Development of a regional soil model for the Beerze-Reuzel area (Meuse). Technical Report 2006-23, Center for Applied Geoscience, University of Tübingen, 2006.
- [62] R Therrien, R G McLaren, E A Sudicky, and S M Panday. Hydrosphere, a three-dimensional numerical model describing fully-integrated subsurface and surface flow and solute transport. Technical report, Université Laval and University of Waterloo, 2004.
- [63] J.E. VanderKwaak. *Numerical simulation of flow and chemical transport in integrated surface-subsurface hydrologic systems*. PhD thesis, University of Waterloo, Ontario, Canada, 1999.
- [64] P.Y. Julien. *River mechanics*. Cambridge University Press, Cambridge, 2002.
- [65] R. S. Govindaraju, S. E. Jones, and M.L. Kavvas. On the diffusion wave model for overland flow 1. solution for steep slopes. *Water Resources Research*, 24(5):734–744, 1988.
- [66] P Di Giacomo, P E Todini, and P Lamberti. A conservative finite elements approach to overland flow: The control volume finite element formulation. *Journal of Hydrology*, 175:267–291, 1996.
- [67] R E Smith and D A Woolhiser. Overland flow on an infiltrating surface. *Water Resources Research*, 7(4):899–913, 1971.
- [68] H D Voigt and M Lauterbach. Druckaufbaumessungen an Gas-Sonden. Technical report, Zentrales Geologisches Institut, Berlin, 1985. Haefner et al. Geohydrodynamische Erkundung von Erdöl-, Ergas- und Grundwasserlagerstaetten.
- [69] M Muskat. *The flow of homogenous fluids through porous media*. J.W. Edwards Inc., Ann Arbor, Michigan, 1nd edition, 1937.

- [70] I.S. Leibenzon. *The flow of natural fluids in porous media (in Russian)*. Gostekizdat, 1947.
- [71] V.I. Aravin and S. N. Numerov. *Theory of fluid flow in undeformable porous media*. Israel Program for Scientific Translations, 1965.
- [72] W. Wang and O. Kolditz. Object-oriented finite element analysis of thermo-hydro-mechanical (thm) problems in porous media. *Int. J. Numerical Methods in Engineering*, 69(1):162–201, 2007.
- [73] C I McDermott, A L Randriamanjatosoa, H Tenzer, and O Kolditz. Simulation of heat extraction from crystalline rocks: The influence of coupled processes on differential reservoir cooling. *Geothermics*, 35(3):321–344, 2006.
- [74] R C Reid, J M Prausnitz, and B E Poling. *The properties of liquids and gases*. McGraw-Hill, 1988.
- [75] A I Zografas, W A Martin, and J E Sunderland. Equations of properties as a function of temperature for seven fluids. *Computer Methods in Applied Mechanics and Engineering*, 61:177–187, 1987.
- [76] N B Vargaftik, J K Vinogradov, and V S Jargin. *Handbook of physical properties of liquids and gases: Pures substances and mixtures*. Begell House, Redding, 1996.
- [77] C. I. Voss and W. R. Souza. Variable density flow and solute transport simulation of regional aquifers containing a narrow fresh-water-saltwater transition. *Water Resources Research*, 23:1851–1866, 1987.
- [78] H. J. G. Diersch and O. Kolditz. Coupled groundwater flow and transport: 2. thermohaline and 3d convection system. *Advances in Water Resources*, 21:401–425, 1998.
- [79] P. Knabner and P. Frolkvić. Consistent velocity approximation for finite volume or element discretizations of density driven flow in porous media. *Int. Conf. on Computational Methods in Water Resources, CMWR*, 1:93–100, 1996.
- [80] P. Frolković. Consistent velocity approximation for density driven flow and transport. Technical report, 1998. In:Van Keer R. et al., editors ACOMEN98. Maastricht: Shaker:603-611.
- [81] G. T. Yeh. On the computation of darcian velocity and mass balance in the finite-element modeling of groundwater-flow. *Water Resources Research*, 17:1529–1534, 1981.
- [82] R. Mosé, P. Siegel, P. Ackerer, and G. Chavent. Application of the mixed hybrid finite element approximation in a groundwater flow model: Luxury or necessity? *Water Resources Research*, 30(11):3001–3012, 1994.

- [83] C. H. Park. *Saltwater intrusion in coastal aquifers*. PhD thesis, Georgia Institute of Technology, Atlanta, Georgia, USA, 2004.
- [84] C. Cordes and W. Kinzelbach. Continuous groundwater velocity field and path lines in linear, bilinear, and trilinear finite elements. *Water Resources Research*, 28(11):2903–2911, 1992.
- [85] E. Schneid, P. Knabner, and F. Radu. A priori error estimates for a mixed finite element discretization of the richards' equation. *Numerische Mathematik*, 98(2):353–370, 2004.
- [86] J Korsawe and G. Starke. A least-squares mixed finite element method for biot's consolidation problem in porous media. *SIAM Journal on Numerical Analysis*, 43(1):318–339, 2005.
- [87] IBM and OpenDX. *IBM Visualization Data Explorer, User's Manual*. Yorktown, Heights, New York, USA, 1997.
- [88] K.-H. Lux. *Gebirgsmechanischer Entwurf und Felderfahrungen im Salzkavernenbau: Ein Beitrag zur Entwicklung von Prognosemodellen für den Hohlraumbau im duktilen Salzgebirge*. Ferdinand Enke Verlag, Stuttgart, 1984.
- [89] J. Schröder. Theoretische und algorithmische Konzepte zur phänomenologischen Beschreibung anisotropen Materialverhaltens. Dissertation, 1996.
- [90] M. Kohlmeier. Coupling of thermal, hydraulic and mechanical processes for geotechnical simulations of partially saturated porous media. Dissertation, 2006.
- [91] M. Fiolka. Theorie und Numerik volumetrischer Schalenelemente zur Delaminationsanalyse von Faserverbundlaminaten. Dissertation, Berichte des Instituts für Mechanik 2008/2, 2008.
- [92] E. Ramm, E. Rank, R. Rannacher, K. Schweizerhol, E. Stein, W. Wendland, G. Wittum, P. Wriggers, and W. Wunderlich. *Error-controlled Adaptive Finite Elements in Solid Mechanics*. Wiley, England, 2003.
- [93] I.S. Sandler and J.P. Wright. Strain softening. In S. Nemat, R. Asaro, and G. Hegemier, editors, *Theoretical foundations for Large Scale Computations of Nonlinear Behavior*, pages 285–315. Matinus Nijhoff, Netherlands, 1984.
- [94] R. I. Borja. A finite element model for strain localization analysis of strongly discontinuous fields based on standard Galerkin approximation. *Computer Methods in Applied Mechanics and Engineering*, 190:1529–1549, 2000.

- [95] D. Sheng, S. W. Sloan, and H. S. Yu. Aspects of finite element implementation of critical state models. *Computational Mechanis*, 26:185–196, 2000.
- [96] Z. Hou. Untersuchungen zum Nachweis der Standsicherheit für Untertagedeponien im Salzgebirge. Dissertation, 1997.
- [97] Z. Hou. Geomechanische Planungskonzepte für untertägige Tragwerke mit besonderer Berücksichtigung von Gefügeschädigung, Verheilung und hydromechanischer Kopplung. Habilitation, 2002.
- [98] Z. Hou and K.-H. Lux. Ein neues Stoffmodell für duktile Salzgesteine mit Einbeziehung von Gefügeschädigung und tertiärem Kriechen auf der Grundlage der Continuum-Damage-Mechanik. *Geotechnik*, 21(3):259–263, 1998.
- [99] W. Hummel, U. Berner, E. Curti, F.J. Pearson, and T. Troenen. *The Nagra/PSI Chemical Thermodynamic Data Base 01/01*. Universal Publishers, 2002.
- [100] B.V. Van Breukelen, D. Hunkeler, and F. Volkering. Quantification of sequential chlorinated ethene degradation by use of a reactive transport model incorporating isotope fractionation. *Environ. Sci. Technol.*, 39(11):4189–4197, 2005.
- [101] D.R. Aguilera, P. Jourabchi, C. Spiteri, and P. Regnier. A knowledge-based reactive transport approach for the simulation of biogeochemical dynamics in earth systems. *Geochemistry, Geophysics, Geosystems*, 6:Q07012, 2005.
- [102] P. Regnier, J.P. O’Kane, C.I. Steefel, and J.P. Vanderborgh. Modeling complex multi-component reactive-transport systems: towards a simulation environment based on the concept of a knowledge base. *Applied Mathematical Modelling*, 26:913–927, 2002.
- [103] Urs von Gunten and Jürg Zobrist. Biogeochemical changes in groundwater-infiltration systems: Column studies. *Geochimica et Cosmochimica Acta*, 57:3895–3906, 1993.
- [104] Dirk Schäfer, Wolfgang Schäfer, and Wolfgang Kinzelbach. Simulation of reactive processes related to biodegradation in aquifers. 2. model application to a column study on organic carbon degradation. *Journal of Contaminant Hydrology*, 31:187–209, 1998.
- [105] Martin Thullner, Philippe Van Cappellen, and Pierre Regnier. Modeling the impact of microbial activity on redox dynamics in porous media. *Geochimica et Cosmochimica Acta*, 69(21):5005–5019, 2005.

- [106] Florian Centler, Haibing Shao, Cecilia de Bias, Chan-Hee Park, Pierre Regnier, Olaf Kolditz, and Martin Thullner. Geosysbrns - a flexible multidimensional reactive transport model for simulating biogeochemical subsurface processes. *submitted to Computers & Geosciences*, 00:0000, 2009.
- [107] Olaf A. Cirpka and Albert J. Valocchi. Two-dimensional concentration distribution for mixing-controlled bioreactive transport in steady state. *Adv Water Resour*, 30:1668–1679, 2007.
- [108] Olaf A. Cirpka and Albert J. Valocchi. Reply to comments on two-dimensional concentration distribution for mixing-controlled bioreactive transport in steady state by h. shao et al.
- [109] Haibing Shao, Florian Centler, Cecilia de Bias, Martin Thullner, and Olaf Kolditz. Comments on "two-dimensional concentration distribution for mixing-controlled bioreactive transport in steady state" by o. a. cirpka and a. j. valocchi. *Adv Water Resour*, 32:293–297, 2009.
- [110] J. Bear. *Hydraulics of groundwater*. McGraw-Hill, New York, 1979.
- [111] W. Kinzelbach. *Groundwater Modelling*. Elsevier, Amsterdam, 1986.
- [112] A F B Tompson and L W Gelhar. Numerical simulation of solute transport in three-dimensional randomly heterogeneous porous media. *Water Resources Research*, 26(10):2451–2562, 1990.
- [113] E. M. LaBolle, G. E. Fogg, and A. F. B. Tompson. Random-walk simulation of transport in heterogeneous porous media: Local mass-conservation problem and implementation methods. *Water Resources Research*, 32(3):583–593, 1996.
- [114] W. Kinzelbach. The random-walk method in pollutant transport simulation. *NATO ASI Ser, Ser.(C224)*:227–246, 1988.
- [115] H. Hoteit, R. Mose, A. Younes, F. Lehmann, and Ph. Ackerer. Three-dimensional modeling of mass transfer in porous media using the mixed hybrid finite elements and the random-walk methods. *Mathe. Geology*, 34(4):435–456, 2002.
- [116] A. Ogata and R. B. Banks. A solution of the differential equation of longitudinal dispersion in porous media. Technical report, Washington, D.C., 1961.
- [117] A E Hassan and M M Mohamed. On using particle tracking methods to simulate transport in single-continuum and dual continua porous media. *Journal of Hydrology*, 275(3-4):242–260, 2003.
- [118] Thomas Harter and Sonja Wagner. Colloid transport and filtration of *Cryptosporidium parvum* in sandy soils and aquifer sediments. *Environ. Sci. Technol.*, 34:62–70, 2000.

- [119] William P. Johnson, Karen A. Blue, and Bruce E. Logan. Modeling bacterial detachment during transport through porous media as a residence-time-dependent process. *Water Resour. Res.*, 31:2649–2658, 1995.
- [120] A S Abdul and R W Gilham. Laboratory studies of the effects of the capillary fringe on streamflow generation. *Water Resour. Res.*, 20(6):691–698, 1984.
- [121] O Gunduz and M M Aral. River networks and groundwater flow: a simultaneous solution of a coupled system. *Journal of Hydrology*, 301:216–234, 2005.
- [122] R. W. Lewis, P. J. Roberts, and B. A. Schrefler. Finite element modelling of two-phase heat and fluid flow in deforming porous media. *Transport in Porous Media*, 4:319–334, 1989.
- [123] O. Kolditz. *Computational methods in environmental fluid mechanics*. Graduate Text Book, Springer Science Publisher, Berlin, 2002.
- [124] M. Murad and A. Loula. Improved accuracy in finite element analysis of Biot's consolidation problem. *Comput. Methods Appl. Mech. Engrg.*, 95:359–382, 1992.
- [125] R. W. Lewis and B. A. Schrefler. *The finite element method in the static and dynamic deformation and consolidation of porous media*. Wiley, 1998.
- [126] J. Birkholzer, J. Rutqvist, E. Sonnenthal, and D. Barr. Decovalex-thmc project, task d: Long-term permeability/porosity changes in the edz and near field due to thm and thc processes in volcanic and crystalline-bentonite systems. Technical Report 2008:45, SKI, Stockholm, 2008.
- [127] J. Rutqvist. Coupling thermal-hydrological-mechanical analysis within the framework of DECPVALEX-THMC, Task D_THM, step 1: Model inception. Technical report, Earth Sciences Division, Lawrence Berkeley National Laboratory, USA, 2005.
- [128] W. Wang, M. Datcheva, U.J. Görke, Kolditz O., and T. Schanz. Model validation for swelling pressure in expansive porous media. Technical Report 2008-XX, Helmholtz Centre for Environmental Reserach - UFZ, Leipzig, 2008.
- [129] D. Barr, J. Birkholzer, J. Rutqvist, and E. Sonnenthal. Draft description for DECOVALEX-THMC task D: Long-term permaebility/porosity changes in edz and near field, due to THM and THC processes in volcanic and crystalline-bentonite systems. Technical report, Earth Sciences Division, Lawrence Berkeley National Laboratory, USA, 2004.
- [130] W. Wang, M. Xie, O. Kolditz, T. Nowak, H. Kunz, and H Shao. Modeling thm coupled problems of task d of the decovalex project. Geoproc2006, nanjing, Centre for Applied Geosciences, University of Tbingen, May 2006.

- [131] J. Rutqvist, J. T. Birkholzer, M. Chijimatsu, K. Kolditz, Q. Liu, Y. Oda, W. Wang, and C. Zhang. Results from an international simulation study on coupled thermal, hydrological, and mechanical (thm) processes near geological nuclear waste repositories. In K. Morgan et. al., editor, *Proceedings of the 11th International High-Level Radioactive Waste Management Conference (IHLRWM)*, pages 755–762. American Nuclear Society, 2006.
- [132] L. Sanavia, F. Pesavento, and B. A. Schrefler. Finite element analysis of non-isothermal multiphase geomaterials with application to strain localization simulation. *Trans. Amer. Math. Soc.*, 37(4):331–348, 2006.
- [133] A. Liakopoulos. Retention and distribution of moisture in soils after infiltration has ceased. *Bull. Intern. Assoc. Scientific Hydrology*, 10:58–69, 1965.